

# PEM Water Electrolysis at Elevated Temperatures

**Hansen, Martin Kalmar**

*Publication date:*
2012

*Document Version*
Publisher's PDF, also known as Version of record

Technical University of Denmark

# PEM Water Electrolysis at Elevated Temperatures

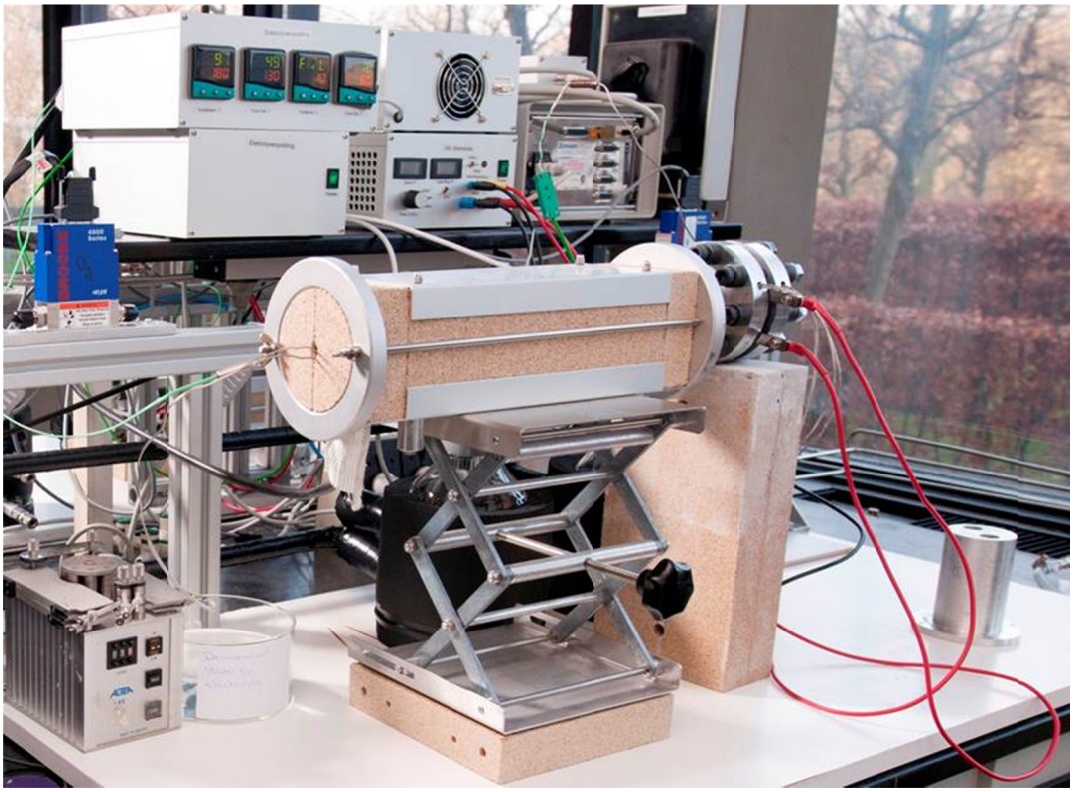

Ph.D. Thesis
Martin Kalmar Hansen
March 2012

# PEM water electrolysis at elevated temperatures

Ph.D. Thesis by Martin Kalmar Hansen

Proton Conductors Section
Department of Energy Conversion and Storage
Technical University of Denmark

Supervisor:

Professor Niels J. Bjerrum

Co-supervisors:

Senior scientist Erik Christensen
Associate professor Jens Oluf Jensen

Date of submission
30th of March 2012

DTU Energy Conversion
Department of Energy Conversion and Storage

This Ph.D. study has been financed by:

1/3 from Danish Hydrogen and Fuel Cell Academy
1/3 from Dean Scholarship – Technical University of Denmark
1/3 from DTU Chemistry

Affiliated projects:

WELTEMP - EU (Project number 212903)
HyCycle - Danish Council for Strategic Research (2104-07-0041)

Supervisors:

Professor Niels J. Bjerrum - DTU Energy Conversion
Senior scientist Erik Christensen - DTU Energy Conversion
Associate professor Jens Oluf Jensen - DTU Energy Conversion

**"I am a Bear of Very Little Brain, and long words Bother me."**
**- Winnie the Pooh**

## Abstract

Global warming and the accelerating depletion of fossil based fuels have catalysed a tremendous surge in the development of alternative and sustainable energy sources *e.g.* wind-, solar- and hydropower. Common for most of these alternative energy sources is that they at times provide more power than needed and hence it has become acute to be able to store the energy. Hydrogen has been identified as a suitable energy carrier and water electrolysis is one way to produce it in a sustainable and environmentally friendly way.

In this thesis an introduction to the subject (chapter 1) is given followed by a literature review of the field of water electrolysis (chapter 2), with a focus on proton exchange membrane (PEM) electrolysis.

In chapter 3 a short description of the experimental techniques used for synthesis of catalyst and characterisation of the components in the electrolysis cell is given. This is followed in chapter 4 by a description of the electrolysis setups and electrolysis cells used during the work. Two different setups were used, one operating at atmospheric pressure and another that could operate at elevated pressure so that liquid water electrolysis could be performed at temperature above 100 °C.

It was found that the gas diffusion layer on the anode side played an important role for the electrolyser performance. Different thicknesses and types, *i.e.* a single layer- and double layer type, were tested. Chapter 5 presents a characterisation of the gas diffusion layers, using parameters such as porosity and resistance which were supported by images acquired using scanning electron microscopy (SEM).

In chapters 6 and 7 the results of the steam electrolysis and pressurised water electrolysis, respectively, are presented and discussed. The steam electrolysis was tested at 130 °C and atmospheric pressure, whereas the pressurised water electrolysis was performed at 120 °C and 3 bar. For the steam electrolysis three different electrolytes were used. Chapter 6 is divided into subchapters in which the results are presented and discussed before a comparison between them is given. First phosphoric acid

doped membranes of polybenzimidazole - poly[2,2'(*m*-phenylene)-5,5'-bibenzimidazole] (PBI) were used as electrolyte. Reasonably good short-term results were achieved using this membrane reaching a current density of 775 $mA \cdot cm^{-2}$ at a cell voltage of 1.84 V. The durability of phosphoric acid doped PBI however was quite poor only lasting few hours in the setup used. Afterwards a range of different phosphoric acid doped commercial Nafion® and ternary phosphoric acid doped composite Nafion® membranes were tested. The performance was not as good as for the PBI system; only 310 $mA \cdot cm^{-2}$ at 1.7V for the best ternary composite membrane. The durability, on the other hand, was greatly improved and test was run for approximately 70 hours (constant voltage of 1.7 V) with a 0.17 $mA \cdot h^{-1}$ decline in performance. Finally, a new class of perfluorosulfonic acid (PFSA) membranes were tested. This was Aquivion™, which is a short side chained PFSA membrane. Aquivion™ was also tested doped with phosphoric acid. It showed better mechanical properties, larger uptake of phosphoric acid and hence improved performance. The best result achieved was 775 $mA \cdot cm^{-2}$ at 1.8 V. Aquivion™ also showed quite promising durability features running for approximately 760 hours (constant current density of 400 $mA \cdot cm^{-2}$) with a 0.023-0.04 $mV \cdot h^{-1}$ decline in performance over the last 660 hours. For the pressurised water electrolysis the best result obtained was for an Aquivion™ membrane with a current density of 2125 $mA \cdot cm^{-2}$ at 1.85 V.

An attempt was made to quantify the significance of various parameters such as membrane electrode assembly (MEA) technique (chapter 6), binder content in anode (chapter 6), anode catalyst loading (chapter 6), gas diffusion layer (chapter 5 and 6) and flow patterns (chapter 4, 6 and 7). The different machined flow patterns used are described in chapter 4, and the results with the different patterns are shown and discussed in chapters 6 and 7.

Chapter 8 is devoted to a general discussion and the conclusions and outlook are given in chapter 9. It seems obvious that further effort should be put into characterisation and development of a more sophisticated anode electrode structure. Only when this parameter is optimised and performing at a high level, will it be possible to really quantify the importance of the other parameters under full single cell electrolysis tests.

# Resumé

Den globale opvarmning og udsigten til at de fossile brændsler slipper op har katalyseret en kæmpe udvikling af alternative og bæredygtige energikilder f.eks. vind-, sol- og vandkraft. Disse alternative energikilder har dét tilfælles at de til tider leverer mere energi end der er brug for. Derfor er det blevet yderst vigtigt at kunne opbevare energien. Hydrogen er blevet identificeret som en passende energibærer, og vandelektrolyse er en både bæredygtig og miljøvenlig måde at producere hydrogen på.

I denne afhandling bliver der givet en generel introduktion til emnet (kapitel 1), fulgt op at en gennemgang af litteraturen vedrørende vandelektrolyse (kapitel 2), med fokus på protonledende membran (PEM) elektrolyse.

I kapitel 3 bliver de benyttede eksperimentelle teknikker til syntese af katalysator og karakterisering af elektrolysecelle komponenterne gennemgået ganske kortfattet. Efterfølgende er der i kapitel 4 en beskrivelse af de elektrolyseopstillinger og elektrolyseceller, der er blevet benyttet. To forskellige elektrolyseopstillinger blev benyttet, en hvor trykket var atmosfærisk, og en anden der kunne anvendes ved forhøjede tryk, således at vand kunne holdes på flydende form selv ved temperaturer over 100 °C.

Det blev fundet, at gasdiffusionslaget på anode siden spillede en yderst vigtig rolle. Forskellige tykkelser og typer, enkeltlag og dobbeltlag, blev undersøgt. I kapitel 5 bliver karakterisering af gasdiffusionslagene præsenteret, parametre såsom porøsitet og modstand blev benyttet til evaluering disse. Skanning elektron mikroskopibilleder blev brugt til at anskueliggøre de undersøgte parametre.

I kapitel 6 og 7 bliver de respektive resultater for dampelektrolyse og vandelektrolyse præsenteret og diskuteret. Dampelektrolysen blev udført ved 130 °C og atmosfærisk tryk, hvorimod vandelektrolysen blev udført ved 120 °C og 3 bar. Ved dampelektrolyseforsøgene blev forskellige elektrolytter brugt, og kapitel 6 er inddelt i underkapitler, hvori resultaterne for de forskellige elektrolytter bliver præsenteret og diskuteret før en sammenligning bliver foretaget. Først blev fosforsyre dopet polybenzimidazole -

poly[2,2'(*m*-phenylene)-5,5'-bibenzimidazole] (PBI) membraner benyttet som elektrolyt, relativt gode polariseringsresultater blev opnået. En strømtæthed på 775 $mA \cdot cm^{-2}$ ved en cellespænding på 1,84 V var det bedste resultat, men langtidsholdbarheden af de fosforsyre dopede PBI MEAer var meget besværet med driftstider på et par timer i den testede opstilling. Efterfølgende blev en række fosforsyredopede kommercielle Nafion® og ternære fosforsyredopede komposit Nafion® membraner testet. Elektrolyseperformance var ikke så god som for PBI, bare 310 $mA \cdot cm^{-2}$ ved 1,7 V for den bedst ydende ternære kompositmembran. Holdbarheden var dog stærkt forbedret og elektrolysetest blev udført i omtrent 70 timer med kun et lille fald i ydeevnen (0.17 $mA \cdot h^{-1}$, ved konstant spænding på 1,7 V). Til slut blev en ny type perfluoret sulfonsyre (PFSA) membraner testet. Aquivion™, som er en PFSA membran med korte sidekæder, blev testet dopet med fosforsyre. Aquivion™ udviste forbedrede mekaniske egenskaber og et større optag af fosforsyre, derfor blev der opnået bedre elektrolysator performance. Det bedst opnåede resultat var 775 $mA \cdot cm^{-2}$ ved en cellespænding på 1,8 V. Aquivion™ udviste også ret lovende langtidsholdbarhed med kun en mindre nedgang i ydeevne over en periode på ca. 760 timer (mellem 0.023 og 0.04 $mV \cdot h^{-1}$ de sidste 660 timer med en konstant strømtæthed på 400 $mA \cdot cm^{-2}$). For tryksat vandelektrolyse blev den bedste performance opnået med en Aquivion™ membran, strømtætheden var i dette tilfælde 2125 $mA \cdot cm^{-2}$ ved 1,85 V.

Vigtigheden af flere forskellige elektrolyseparametre blev undersøgt blandt andet: Teknik til membran elektrode samling (MEA) (kapitel 6), binder indhold i anoden (kapitel 6), anode katalysator loading (kapitel 6), gasdiffusionslag (kapitel 5 og 6) og flowmønster (kapitel 4, 6 og 7). De forskellige maskinfræsede flowmønstre bliver beskrevet i kapitel 4, mens resultaterne for de forskellige mønstre bliver vist og diskuteret i kapitel 6 og 7.

Kapitel 8 er viet til en generel diskussion. Konklusionen og perspektivering bliver givet i kapitel 9. Det fremgår klar fra de opnåede resultater at fremtidig forskning i emnet skal koncentreres omkring udvikling og karakterisering af en mere sofistikeret anode elektrodestruktur. Det er først når denne parameter er optimeret til en høj performance at det er muligt kvantificere vigtigheden af de resterende parametre i en rigtig elektrolysecelle.

# Preface

The work presented in this Ph.D. thesis was carried out at the Technical University of Denmark (DTU) from March 2009 to March 2012 first in Department of Chemistry and later, due to the formation of a new department at DTU, in Department of Energy Conversion and Storage.

There are many people towards whom I am very grateful. First of all I would like to direct huge thanks to my supervisors. Professor *Niels J. Bjerrum* for giving me the chance to explore the exciting field of PEM water electrolysis, he has guided me safely through the mine fields of the Ph.D. study. Dr. *Jens Oluf Jensen* and Dr. *Erik Christensen* for many fruitful discussions and for practical help getting started in the lab making electrolysis tests. I would also like to thank Dr. *Jens von Barner* for taking a huge interest in my work and helping with fulfilling many of the formal requirements for the Ph.D. study at DTU. Special gratitude should also be directed to Dr. *Qingfeng Li* for many discussions about the electrolysis MEAs and especially the membranes. I would like to thank **all** the former and present members of the group and Danish Power Systems for making my time here in the Proton Conductors section interesting and fun. They have always been ready to lend a helping hand or provide much appreciated advice. I would in particular like to direct a special thanks to Dr. *David Aili*, who has provided me with the polymeric material needed for the electrolysis experiments, and much of the characterisation of these in this thesis are provided by him. Furthermore he was an invaluable help during the proof-reading of the thesis. I would also like to thank Ph.D. students *Carsten B. Prag* and *James A. Mugabi* for their great help with proof-reading. I would like to thank *Chao Pan* for providing me with cathodes. I would also like to thank guest Ph.D. student *Junyuan Xu* for a good cooperation doing electrolysis measurements. I also owe *Lisbeth Molzen* gratitude for the results we obtained during her bachelor project.

I am very thankful for the help the administrative and technical staff have provided me with. I would like to mention: *The workshop at DTU Chemistry*, *Alex Lisbjerg*, *Claus B. Mortensen*, *Steen Blichfeldt*, *Mo Hongling Sønnichsen*, *Sinh Hy Nquyen*, *Astrid Schøneberg*, *Lise Lotte Berring*, *Carl Erik Foverskov*, *Kirsten Munkgaard Thomsen*, *Jette Nilsson* and *Mette Hansen*.

I acknowledge the WELTEMP and HyCycle partners for good cooperation during the project. I would like to thank our partners at NTNU (Norway) for providing me with $IrO_2$ catalyst which I used during my experiments. I would also like to thank Professor *Karel Bouzek* from ICTP (Czech Republic) for making my short but very fruitful stay in his group possible. During the week I stayed there I managed to not only make pressurised electrolysis measurements, I also got invaluable inspiration for the creation of our own pressurised setup at DTU. I would like to thank Dr. *Martin Paidar* and Ph.D. student *Petr Mazur* (both ICTP) for their great help during my stay and for the great discussions we have had on the topic. I would like to acknowledge Tantaline A/S and Dr. *Søren Eriksen* for providing the tantalum coated felt.

I would like to acknowledge HyFC Acadamy, DTU Chemistry and DTU for financing my Ph.D. project.

During my Ph.D. study I also spent three and a half months at Professor Robert Savinells group at Case Western Reserve University, Cleveland Ohio. It was a stay I deeply cherish and I am grateful to both Professor *Robert Savinell* and associate professor *Jesse Wainright* for their guidance and help during my stay abroad. I am grateful towards graduate student *Tyler Petek* with whom I spent many fun hours in lab and who has helped with the proof-reading of my thesis.

I would also like to acknowledge the great help with experiments that late *Viktor Bandur* provided.

Finally I am grateful to my family, at times I have been stressed and distant but they have always supported and believed in me, for that I will always be thankful!

I hope you will enjoy reading this thesis and you will be both inspired and enlightened afterwards. Just remember: **"The more you know, the more you realize you know nothing." – *Socrates***

Martin Kalmar Hansen
March 30th 2012
Technical University of Denmark, Kgs. Lyngby

# List of contents

# List of abbreviations

| | |
|---|---|
| AEC | Alkaline electrolysis cell |
| AQU-MEA | MEA with Aquivion™ as membrane |
| ATO | Antimony doped tin oxide |
| BET | Brunauer-Emmett-Teller |
| BPP | Bipolar plate |
| CCM | Catalyst coated membrane |
| CNC | Computerised numerically controlled |
| Co(dmg) | Boron-capped trix(glyoximate) cobalt complex |
| CVD | Chemical vapour deposition |
| DMAc | Dimethylacetamide |
| DTU | Technical University of Denmark |
| $E_{EMF}$ | Electromotive force voltage |
| EMF | Electromotive force |
| $E_{rev}$ | Reversible voltage |
| $E_{TN}$ | Thermo-neutral voltage |
| EW | Equivalent weight |
| GDE | Gas diffusion electrode |
| GDL | Gas diffusion layer |
| GNF | Graphitic nano-fibres |
| HHV | Higher heating value |
| HPA | Heteropolyacid |
| I-R | Impregnation-reduction |
| ICTP | Institute of Chemical Technology Prague |
| LHV | Lower heating value |
| LIQ-MEA | MEA tested in pressurised setup, liquid water |
| LSGM | Strontium for lanthanum and magnesium for gallium doped $LaGaO_3$ |

| | |
|---|---|
| MEA | Membrane electrode assembly |
| MoPA | Molybdophosphoric acid |
| MWCNT | Multi-walled carbon nano-tubes |
| NAF-MEA | MEA with Nafion® as membrane |
| NTNU | Norwegian University of Science and Technology |
| OSV | Open circuit voltage |
| PA | Phosphoric acid |
| PBI | Polybenzimidazole - poly[2,2'(m-phenylene)-5,5'-bibenzimidazole] |
| PBI-MEA | MEA with PBI as membrane |
| PEEK | Poly(etheretherketone) |
| PEM | Proton exchange membrane |
| PEMEC | Proton exchange membrane electrolysis cell |
| PES | Poly(ether sulfone) |
| PFSA | Perfluorosulfonic acid |
| POX | Partial oxidation |
| PPS | Poly phenylene sulfide |
| PSA | Pressure swing adsorption |
| PSU | Polysulfone |
| PTFE | Polytetrafluoroethylene |
| PVC | Polyvinyl chloride |
| PVD | Physical vapour deposition |
| RH | Relative humidity |
| SEM | Scanning electon microscopy |
| SHE | Standard hydrogen electrode |
| SMR | Steam methane reforming |
| SnP | Tin pyrophosphate |
| SO | Solid Oxide |
| SOEC | Solid Oxide Electrolysis cell |
| SOFC | Solid oxide fuel cell |
| SPEEK | Sulfonated poly(etheretherketone) |

| | |
|---|---|
| SPSf-co-PPSS) | Polysulfone copolymer poly(phenylene sulphide sulfone) |
| SR | Steam reforming |
| SSC | Short side chain |
| $T_g$ | Glass transition temperature |
| TPA | Tungstophosphoric acid |
| TSiA | Tungstosilicic acid |
| WC | Tungsten carbide |
| WGS | Water-gas shift |
| XRPD | X-ray powder diffraction |
| YSZ | Yttria stabilised zirconia |
| Zr-CNO | Partially oxidised zirconium carbonitrides |
| ZrP | Zirconium phosphate ($Zr(HPO_4)_2 \cdot nH_2O$) |
| $\varepsilon_E$ | Energy efficiency |
| $\varepsilon_F$ | Faradaic efficiency |

# 1 Introduction

In today's world there is a great concern about global warming [1], which can be ascribed to an increase in the carbon dioxide ($CO_2$) level released to the atmosphere [2, 3]. During the last decades the $CO_2$ level has kept increasing [4] as more and more humans inhabit the world and the demand for energy and material goods goes up and have reached an unprecedented high level [5, 6]. Several initiatives have been made to reduce the level of human made $CO_2$ emissions *e.g.* the Kyoto Protocol and recently the European Commission (March 2011) have launched an ambitious plan to reduce the $CO_2$ emissions to 25% below the 1990 level by 2020. The European Commission is not allowing the member nations to buy $CO_2$ quotas in third world countries. This means that a reduction in the $CO_2$ emissions internally in the European Union must at least partly be gained by changing from using fossil fuels to more environment friendly technologies. It is assumed that a greater electrification of the society is needed, in this context the hydrogen society fits in beautifully. Electricity from environmentally friendly sources (*e.g.* hydro power, wind turbines and solar panels) can be stored as hydrogen during periods of low electricity demand and released again during periods with large demands. To realise the 'Hydrogen Society', a safe and environmentally friendly way of producing hydrogen is necessary. One way to produce clean hydrogen is from electrolysis. If the power needed for the water splitting comes from renewable sources it provides clean and environmental friendly hydrogen.

Water electrolysis can be made from several different electrolysis technologies, where the three most prominent are: Alkaline electrolysis, proton exchange membrane (PEM) electrolysis and solid oxide (SO) electrolysis [7]. Of these technologies the alkaline technology is, by far, the most mature technology, the least developed technology is the SO electrolysis technology which mostly still are on research scale. PEM electrolysers have reached the commercial market, but only for small scale niche applications. PEM electrolysers provide several advantages compared to alkaline electrolysers. PEM electrolysers are safer compared to the alkaline electrolysers since they use a solid electrolyte instead of circulation of a highly alkaline electrolyte [8], they provide hydrogen of higher purity (99.99%) [9] due

to better gas separation and they can be made more compact since high current densities (between 1-2 $A \cdot cm^{-2}$) are possible [10], finally it is also possible to produce pressurised gases directly (70 bar [11], 130 bar [12] and 138 bar [13] have been reported) and even differential pressurisation (systems with approximately 20 bar [14] and 70 bar [15] pressure difference between the anode and cathode (high pressure side)) have been reported.

Compared to SO electrolysers PEM electrolysers also have some benefits. The lower operating temperature of PEM systems means less demand on uniformity of thermal expansion coefficients in the construction materials [16]. Furthermore the PEM electrolyser system of plant is also much simpler, most SO electrolysers are run with recirculation of gases [17-22] (oxygen or air to anode and hydrogen to cathode) to ensure the integrity of the electrodes.

PEM electrolysers are often based on perflourosulfonic acid (PFSA) type membranes [8] the most common being Nafion®. The proton conductivity of PFSA type membranes is very dependent on the water content and temperature is limited to temperatures below 100 °C [23] at ambient pressure due to dehydration of the membrane. Dehydration results in significant loss of proton conductivity in the membranes. It has been proposed that raising the temperature to above 100 °C will be beneficial [23]. First of all, the elevated temperature will improve the electrode kinetics and thus reduce the overpotentials which are connected to kinetic limitations. Secondly, the total thermodynamic energy requirement for the water splitting ($\Delta H$) is lowered from 284 $kJ \cdot mol^{-1}$ (liquid water, 80 °C) to 243 $kJ \cdot mol^{-1}$ for steam electrolysis at 130 °C. Furthermore, the reversible voltage, as calculated from the Gibbs free energy change ($\Delta G$), is reduced slightly by raising the temperature from 80 °C (1.18 V, liquid water) to 130 °C (1.16 V, steam). The decrease in supplied electrical energy should be compensated with an increase in the heat added to the system, however this heat is expected to be taken from the waste heat produced due to Ohmic loss in the system. This heat could also be used for preheating and evaporation of the feed water.

An elevated temperature is also advantageous for PEM systems operated in fuel cell mode [24]. In fuel cell technology the challenge with an increase in operation temperature was solved by replacing water as the proton conducting phase in the membrane with phosphoric acid (PA), which exhibits high

anhydrous proton conductivity and has very low vapour pressure [25]. For example, PA doped polybenzimidazole - poly[2,2'(*m*-phenylene)-5,5'-bibenzimidazole] (PBI) can be used at operation temperatures up to 200 °C [24, 26, 27] since its proton conductivity mechanism is not (like in traditional PFSA membranes) completely dependent on the presence of water within the membrane matrix. Another way to improve the electrolysis performance of PFSA membranes at elevated temperatures is to improve their hydration characteristics through the incorporation of hygroscopic inorganic fillers, such as $SiO_2$ [28, 29] or $TiO_2$ [30] or by pressurising the system in order to keep the membrane well hydrated [28-31].

Aquivion™ is another type of polymer in the PFSA family, which differs from Nafion® in terms of the equivalent weight and the length of the sulfonic acid terminated side chains. Compared to the conventional Nafion® membranes, this type of PFSA membranes exhibits considerably higher softening temperatures [32] which should naturally facilitate the electrolysis operation at elevated temperatures. Its high elastic modulus has also been identified as the sole reason for its superior performance in $H_2/O_2$ PEM fuel cells [33, 34].

Increasing the temperature and replacing water as the proton carrier with PA naturally result in harsher conditions within the cell. Hence highly corrosion resistant materials are needed for the cell hardware. Traditionally, titanium is used for this purpose in low temperature PEM electrolysis [9, 35]. However, recent work within our group [36] has shown that titanium has a very high corrosion rate in PA at elevated temperatures. In order to simulate the conditions in an operating electrolysis cell based on a PA doped membrane, the corrosion currents were determined in 85 wt% PA at 120 °C and potentials up to 1.1 V *vs.* a standard hydrogen electrode (SHE). Under these conditions the corrosion current of titanium was determined to be 6.3 $mA \cdot cm^{-2}$, which according to Faraday's Law corresponds to a corrosion rate of 73 $mm \cdot year^{-1}$ [36]. For comparison, the corrosion current density of tantalum under these conditions was determined to $6.3 \cdot 10^{-5}$ $mA \cdot cm^{-2}$ which gives a corrosion rate of under $1 \cdot 10^{-3}$ $mm \cdot year^{-1}$ [36]. Similar extremely low corrosion rates of less than $1 \cdot 10^{-2}$ $mm \cdot year^{-1}$ for Ta have been determined at temperatures up to 150 °C in 85 wt% PA and at potentials as high as 2.27 V *vs.* SHE [37]. The excellent corrosion resistance of tantalum in aggressive acidic media is due to a protective oxide surface layer, $Ta_2O_5$, that is naturally formed on the surface but only in very thin layers (3 nm

[38]). However, such oxide layers have a low electronic conductivity and hence the performance of the tantalum coated cell components may be dramatically reduced if too thick oxide layers are formed.

Other aspects in PEM electrolysis are the gas diffusion layer (GDL) and the flow pattern. The GDL has been a subject that has received much attention in fuel cell applications. There has also been focus on the GDL in the field of electrolysis, *e.g.* Grigoriev *et al.* [9] investigated the effect of the porosity of the GDL in water electrolysis. Another important property for the GDL is the contact resistance between it and the bipolar plate (BPP). Zhang *et al.* [39] reported that up to 59% of the total power loss in a PEM fuel cell can be ascribed the contact resistance between GDL and BPP. It could be assumed that the same, to some extent, is valid for an electrolysis cell. Further research effort has been put into describing this phenomenon [40].

It is clear that even though PEM electrolysis at elevated temperatures is a technology that has promising aspects to it, it is also a novel area where little research effort has been dedicated until now. Hence many tasks were ahead at the beginning of this project, one being the construction of a functioning and reliable electrolysis setup enabling electrolysis test. Many aspects concerning the setup had to be evaluated and changed as more experience and knowledge was gained *e.g.* design of evaporator, the out-let of produced gases and different designs of flow patterns. Other tasks were to test materials used in the membrane electrode assembly: Different types of membranes were evaluated in real electrolysis applications, new types of gas diffusion layers were also tested as well as different anode loadings, different binder content in the anode and different assembly procedures such as direct assembly in cell *vs.* hot pressing before cell assembly.

The project goal of the WELTEMP project (a water electrolysis project under the European Union's 7$^{th}$ framework programme, coordinated by DTU) and hence the goal of this study, was to make a membrane electrode assembly (MEA) which in single cell electrolysis test had a performance of 1 $A \cdot cm^{-2}$ at a cell voltage of 1.55 V. The electrolysis cell should be operated at elevated temperature between 120 and 200 °C and either under atmospheric or pressurised conditions.

# 2 Literature review

## 2.1 Historical review of water electrolysis

The history of electrolysis dates back to the end of the 18th century (1789) where it was first reported by two Dutchmen, namely Adriaan Paets van Troostwijk and Johan Rudolph Deiman [41, 42]. The experiment done by van Troostwijk and Deiman was by the standards of today quite simple. They used a glass tube sealed in one end with a gold wire going through the sealing. The tube was completely filled with water and another gold wire was brought into close proximity of the first gold wire (the one going through the sealing) from the open end of the tube. An electrical charge (provided from a Leyden jar [42]) was run through the gold wires and gases were evolved from the two wires. Earlier in 1784 Cavendish [43] had reported that igniting by an electric spark, a mixture of hydrogen (inflammable air) and air (common air) in a volume ratio 423:1000 $H_2$:Air [43] (2:1 $H_2$:$O_2$), would explode, leaving approximately 80% of the initial volume of the air and hydrogen. In other words, Cavendish described the combustion of hydrogen in air with the formation of water. The gas mixture made by van Troostwijk and Deiman in 1789 was also explosive and left only water, hence the two Dutchmen had successfully split water into hydrogen and oxygen [41].

In 1799 the Italian physicist Alessandro Volta invented the 'Electric Pile' or 'Voltaic Pile' [44, 45]. Already the year after in 1800 the English scientists William Nicholson and Anthony Carlisle [44, 46] also observed that water could be split with application of an electric current. However, using a direct current source, the 'Electric Pile' invented by Volta, made it possible to separate the evolved gases [46]. From these first observations of the electrolysis principle in 1789 [42] and the successful evolution of separated hydrogen and oxygen in 1800 [46] to modern PEM electrolysis cells as they are known today, much research has gone into the field.

In 1966 the first PEM electrolyser was built by General Electric[47], as part of their development of PEM fuel cells [8] *e.g.* for the American space program. PEM electrolysers were of great interest both for NASA and for military applications *e.g.* for situations where a production of oxygen was of the

essence. It could be applications like space crafts or submarines [48] where the crew are reliant on a steady supply of oxygen to survive. The PEM electrolyser has the advantage over alkaline electrolysers that it has no caustic liquid electrolyte improving the safety. PEM electrolysers also operates at much higher current densities which ensures that much smaller units are needed to provide the necessary amount of gases, which is of crucial importance for space missions and for submarines. Since the initial work by General Electric in the 1950s and 60s, Japan has put a large effort into the area with their Sunshine Project in the 1980s [49] followed in the 1990s with the WE-NET project [50]. In the European Union projects like GenHyPEM [31] (started in 2005) and WELTEMP (started in 2008) have been financed to improve the PEM electrolyser technology. The research effort has since the development of PEM electrolysers constantly been focused on improving the performance of PEM water electrolyser and finding new suitable and cheaper materials in order to make the PEM technology more cost-competitive than alkaline electrolysers and other hydrogen production technologies.

## 2.2 Introduction to important electrochemistry

In electrochemistry the electrode where the oxidation takes place is always called the anode and the electrode where the reduction takes place is called the cathode [51]. So in an electrolysis cell the electrodes are named differently compared to a fuel cell. The anode is where the oxygen evolution is taking place, and the cathode is where the hydrogen generation is going on.

So for electrolysis with an acidic electrolyte, *e.g.* PEM:

| | | |
|---|---|---|
| Anode: | $H_2O(l/g) \rightarrow \frac{1}{2}O_2(g) + 2H^+ + 2e^-$ | (R- 2-1) |
| Cathode: | $2H^+ + 2e^- \rightarrow H_2(g)$ | (R- 2-2) |
| Total: | $H_2O(l/g) \rightarrow H_2(g) + \frac{1}{2}O_2(g)$ | (R- 2-3) |

And for fuel cell (PEM):

Anode: $H_2(g) \rightarrow 2H^+ + 2e^-$ (R- 2-4)

Cathode: $½O_2(g) + 2e^- + 2H^+ \rightarrow H_2O(l/g)$ (R- 2-5)

Total: $H_2(g) + ½\ O_2(g) \rightarrow H_2O(l/g)$ (R- 2-6)

### 2.2.1 Thermodynamics

The reversible voltage ($E_{rev}$) for water electrolysis at room temperature and ambient pressure is 1.23V [52, 53], but for different temperatures and pressure it can be calculated from equations (2-1) and (2-2) [51]. In equation (2-1) the reversible voltage is determined by the Gibbs free energy at a given condition, *i.e.* given temperature and pressure, divided by the number of electrons taking part in the reaction (here z equals 2) and the Faraday constant (F).

$$E_{rev} = - \frac{\Delta_r G}{z \cdot F} \tag{2-1}$$

A quantity known as the electromotive force (EMF) is often used. This quantity is used to evaluate the thermodynamic properties of the cell reaction, thus it can be seen from the potential of cell reaction ($E_{EMF}$) if the process is spontaneous or not. A positive $E_{EMF}$ is defined as a spontaneous reaction and thus the Gibbs free energy corresponding to this is negative. Following this convention all voltages given ought to be negative, but since it goes against the tradition in literature, the following voltages will be given as positive.

From the Nernst equation (2-2), the reversible voltage at given conditions can be calculated. If the partial pressures are known then the potential can be determined from equation (2-2) where the temperature and partial pressures of the reactants and the product are included, as well as the standard Gibbs free energy for the water electrolysis reaction (R- 2-1).

$$E = - \frac{\Delta_r G^\circ}{z \cdot F} - \frac{R \cdot T}{z \cdot F} \cdot \ln\left(\frac{a_{H_2} \cdot a_{O_2}^{½}}{a_{H_2O}}\right) \quad (2\text{-}2)$$

R is the gas constant, T is the actual temperature and $a_x$ is the activity of species x. The activities of the species are often substituted with the partial pressures. It should be noted that the change in Gibbs free energy of course is dependent on the phase of water.

If the partial pressures of the reactants and products are unknown the Gibbs free energy can be calculated from following equation.

$$\Delta_r G = \Delta_r H - T \cdot \Delta_r S \quad (2\text{-}3)$$

The enthalpy (H) and entropy (S) for the reactants and products at a given temperature is calculated from equation (2-4) and (2-5) respectively.

$$H = H^\circ + C_p \cdot \Delta T \quad (2\text{-}4)$$

$$S = S^\circ + C_p \cdot \ln\left(\frac{T}{T^\circ}\right) \quad (2\text{-}5)$$

Where $\Delta T$ is the temperature difference between the temperature (T) where the reaction takes place and the standard temperature ($T^o$) and $C_p$ is the heat capacitance for a given species. It is assumed that the heat capacitance does not vary with pressure or temperature.

The thermodynamics values used for calculating the reversible voltage below are taken from the online version of CRC Handbook of Chemistry and Physics 91st Ed. [54]. They are given in appendix 1 together with the calculations.

The reversible voltage for an electrolysis cell at 130 °C and 1 bar calculated from equation (2-1) is 1.16 V, the electromotive force for the same conditions is -1.16 V showing that electrolysis of water is a non-spontaneous reaction that needs energy applied to proceed.

Another often used value is the thermo-neutral voltage ($E_{TN}$), which is the voltage at which the cell neither releases heat to nor require heat from the surroundings. It is given as equation (2-6):

$$E_{TN} = - \frac{\Delta_r H}{z \cdot F} \tag{2-6}$$

From equations (2-1) and (2-6) it is, as mentioned above, possible to calculate the temperature dependence of the reversible- and thermo-neutral voltages. These voltages are shown in figure 2.1 as a function of temperatures, from 0 °C to 250 °C.

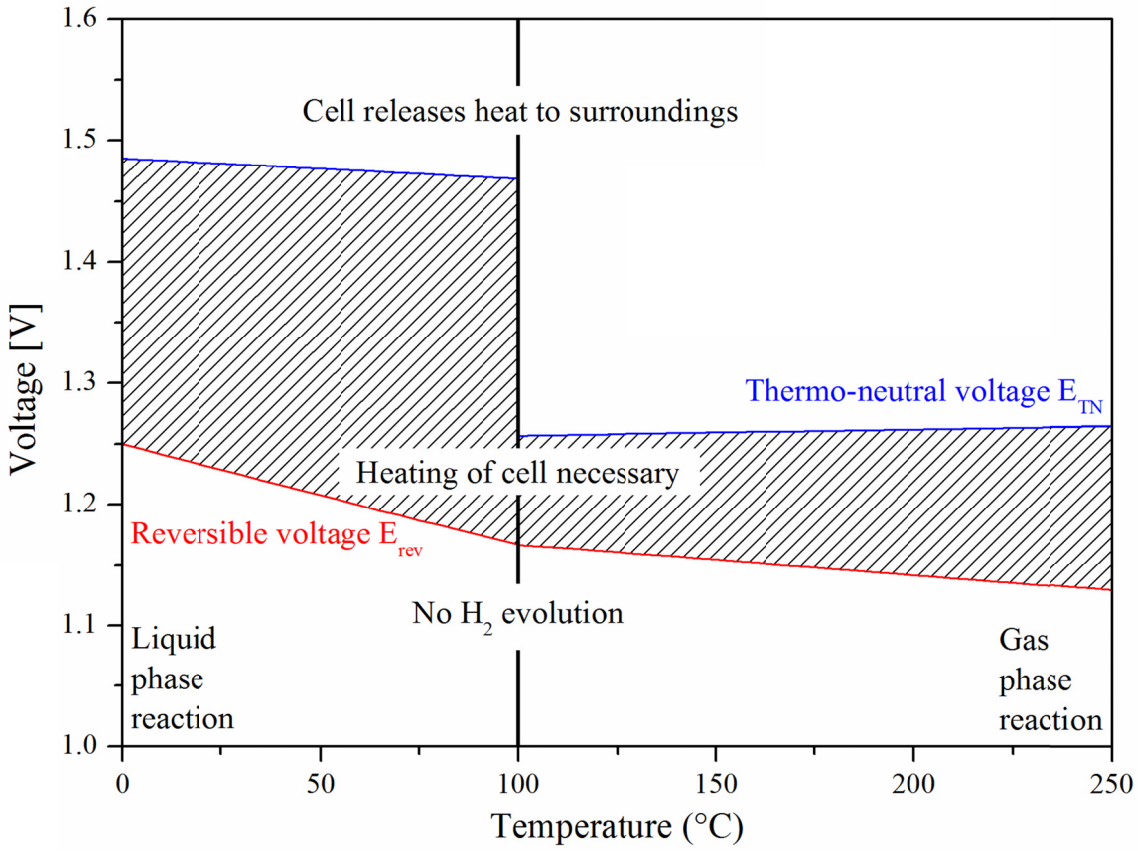


**Figure 2.1: The reversible- and thermo-neutral voltages as a function of temperature.**

If the Nernst equation (2-2) is used to calculate the reversible voltage, the voltage is very dependent on the partial pressures in the system. Table 11.5 (See section 11) has listed the $E_{rev}$ for a number of different partial pressures.

### 2.2.2 Kinetics

It is well known that even when the thermodynamics is favourable (which is not the case for water electrolysis, where an applied voltage is needed) chemical reactions do usually not proceed at a measurable rate. The cause of this is of course kinetics. For a chemical reaction to proceed an activation barrier must be overcome; this barrier can be small or large. The energy required to overcome this barrier is called the activation energy.

From the Arrhenius expression it is known that the chemical reaction rate is dependent on both the temperature and activation energy.

$$k = A \cdot e^{\left(\frac{-E_A}{R \cdot T}\right)} \tag{2-7}$$

In equation (2-7) the Arrhenius expression is shown where k is the rate constant, A is the frequency factor [51], $E_A$ is the activation energy, R and T are still the gas constant and temperature respectively. It is clear from the Arrhenius expression that the rate constant k increases (the reaction rate increases), as the temperature goes up and/or the activation energy goes down. This means that to increase the reaction rate the temperature can be increased or a catalyst can be introduced, since catalysts lower the activation energy.

The cell voltage of a working electrochemical cell is never the theoretical reversible value; there will always be other contributions to the voltage. Equation (2-8) shows the contributions to the total measured cell voltage of an electrolysis cell.

$$E_{cell} = E_{rev} + \eta_{anode} + \eta_{cathode} + I \cdot R \quad (2\text{-}8)$$

Where $\eta_x$ is the overvoltage for the electrodes and I is the current and R the resistance.

It can be seen from equation (2-8) that there are several contributions to the cell voltage. Apart from the reversible voltage which is controlled by the thermo-dynamics, the cell voltage also depends on kinetics. The kinetics of the electrode reactions, particularly at the anode, led to a so-called activation overvoltage (η). Transport of protons through the electrolyte and contact resistances between cell parts also lead to an ohmic resistance contribution to the cell voltage. Moreover when large currents are applied to the cell, the electrode reactions can take place so fast that the transport of reactant/product to and from the electrodes leads to mass transport limitations (not included in equation (2-8)). In figure 2.2 an idealised representation of how the cell voltage is depending on the current is shown. These types of curves are often called polarisation curves or I-U curves.

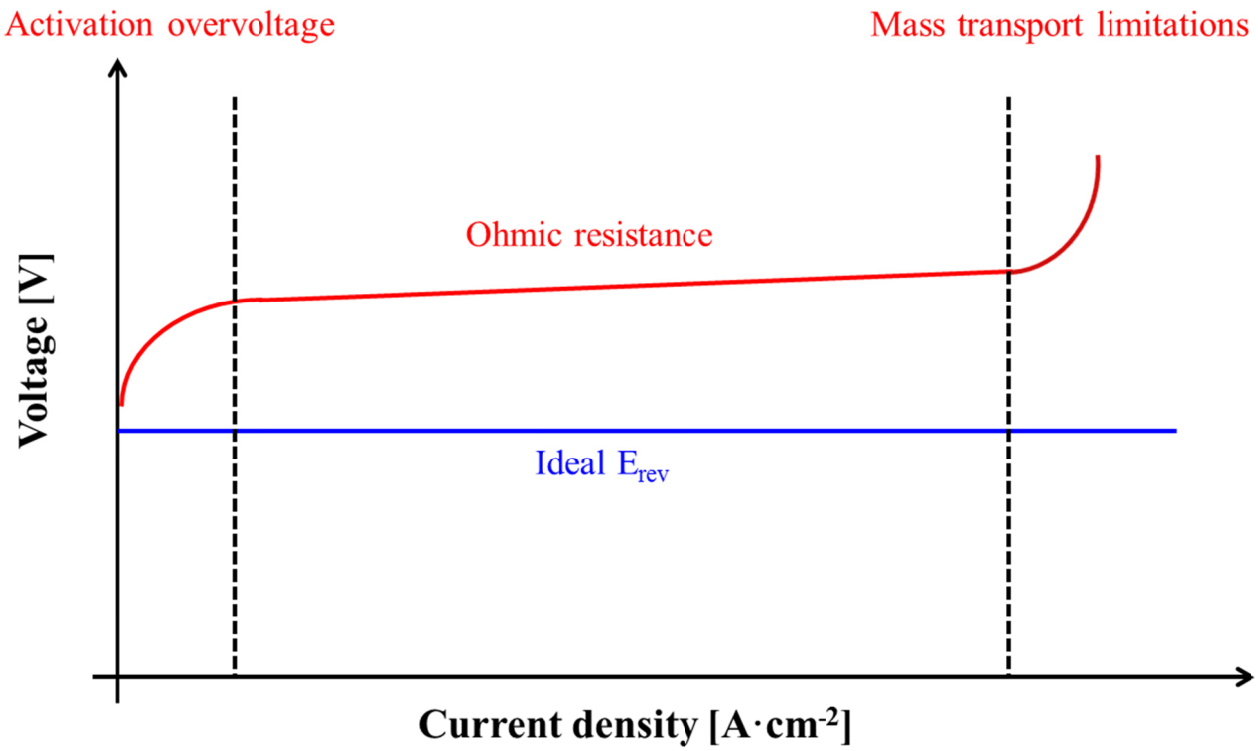


**Figure 2.2: Polarisation curve for an electrolysis system (red) and the ideal reversible voltage (blue).**

Figure 2.2 shows how a polarisation curve for an electrolysis system consists of the three parts mentioned above. In each of these three parts the overall cell voltage increase is more dependent on the contribution from one contributor than the remaining two contributors. The three parts are consequently named after the main contributor. In the low current density range the increase in cell voltage is mostly affected by the electrode kinetics, hence this range is called the activation overvoltage range. At intermediate current densities the ohmic resistance has the largest influence on the cell voltage increase, whereas at large current densities it is the mass transportation of reactants and products to and from the electrodes respectively which mainly contributes to the cell voltage increase. In the figure it is also shown how the ideal reversible voltage is not dependent on the current density.

To describe the kinetic relationship at equilibrium between the current density and the cell voltage the Butler-Volmer equation can be used. In a simplified reaction where an oxidant (O) is reduced and a reductant (R) is oxidised without any mass transport limitation the Butler-Volmer equation can be expressed as seen in equation (2-9).

$$\begin{aligned} I &= I_0 \cdot \left[ e^{-\alpha \cdot f \cdot \eta} - e^{(1-\alpha) \cdot f \cdot \eta} \right] \\ I_0 &= F \cdot A \cdot k^0 \cdot C_O^{*(1-\alpha)} \cdot C_R^{*\alpha} \\ f &= \frac{F}{R \cdot T} \end{aligned} \tag{2-9}$$

In equation (2-9) $I_0$ is the exchange current (at equilibrium no net current is running, but an equal current is running in both the forward and backward direction, $I_0$ equal one of these), $\alpha$ is the transfer or symmetry coefficient (which tells about how much the applied potential is affecting the symmetry between the forward and backward reaction), $\eta$ is the overpotential (stating the difference in potential from equilibrium potential), A is the electrode area, $k^0$ is the standard rate constant and C* is the bulk concentration of the species. F, R and T are as usual the Faraday constant, gas constant and temperature.

At large overpotentials where the electrode reaction takes place irreversible, the Butler-Volmer equation can be further reduced and it takes a Tafel-like character. In equation (2-10) the Tafel equation is given.

$$\eta = a + b \cdot \log(i) \tag{2-10}$$

This Tafel-like character is exploited when trying to break the polarisation curve down into contributions from the activation governed region and the ohmic governed region. In equation (2-8) it was stated that the cell voltage is related to the electrode overvoltages and the IR contribution. Hence a popular way to express the cell voltage is by saying that it can be seen as the collected overvoltage for both electrodes expressed by means of the Tafel equation added the IR contribution. As seen in equation (2-11) [55, 56].

$$E_{cell} = a + b \cdot \log(I) + I \cdot R \tag{2-11}$$

Separating the ohmic and activation contributions to the cell voltage is hence possible by regression of experimentally acquired cell voltages against the current and the logarithmic current.

### 2.2.3 Efficiency

The efficiency of an electrolysis cell can be calculated in various ways, however it should first be clarified whether the efficiency in question is voltage efficiency or current (or faradaic) efficiency.

The current/faradaic efficiency ($\varepsilon_F$) is defined as the real hydrogen production (number of moles hydrogen, $n_R$) at a given current compared to the theoretically possible hydrogen production at the same current, see equation (2-12).

$$\varepsilon_F = \frac{n_R}{n_T} \tag{2-12}$$

The theoretical number of moles hydrogen, $n_T$, produced can be calculated from Faraday's law, see equation (2-13):

$$n_T = \frac{I \cdot t}{z \cdot F} \tag{2-13}$$

Where $n_T$ is the theoretic amount of produced hydrogen in mol, I is the current in A, t is the time in s, z is the number of electrons taking part in the reaction and F is Faraday's constant.

In the case of voltage efficiency ($\varepsilon_V$), the efficiency is defined as the theoretical required voltage to produce a given amount of hydrogen compared to the actual used voltage. The voltage efficiency can be calculated using both the reversible voltage [52] as from equation (2-1) or the thermo-neutral voltage [52] as from equation (2-6) in both cases the values are a function of temperature and pressure as indicated in equations (2-2) to (2-5). Furthermore, in both cases, the voltage efficiency can either be calculated using the higher heating value (HHV) or the lower heating value (LHV). The HHV corresponds to reaction in reaction scheme (R- 2-3) where water is in its liquid form, hence the LHV corresponds to water in gas phase. In equation (2-14) is given the formulas for the voltage efficiency:

$$\varepsilon_V = \frac{E_{rev}}{E_{cell}} \text{ or } \varepsilon_V = \frac{E_{TN}}{E_{cell}} \tag{2-14}$$

$E_{cell}$ is the actual cell voltage in V, whereas the $E_{rev}$ and $E_{TN}$ are functions of temperature and pressure, $E_{cell}$ also depends of current see figure 2.2. Furthermore it is clear from equation (2-14) and figure 2.2 that it is necessary to carefully define how the voltage efficiency is calculated, otherwise it is impossible to extract any meaning from the value. In table 2.1 the voltage efficiencies in percentage calculated for an imaginary electrolysis cell operated at 1 $A \cdot cm^{-2}$ and 1.55 V at 130 °C and atmospheric pressure are shown (project goal). The reversible- and thermo-neutral voltages are calculated using equations (2-1), (2-6) and (2-3) to (2-5).

**Table 2.1: Voltage efficiencies calculated for a fictive electrolysis cell with a cell voltage of 1.55 V (1 A·cm$^{-2}$) operated at 130 °C and atmospheric pressure.**

| | $\varepsilon_{V,HHV}$ [%] | $\varepsilon_{V,LHV}$ [%] |
|---|---|---|
| $E_{rev}$ | 73.7 | 74.8 |
| $E_{TN}$ | 94.4 | 81.2 |

The voltage efficiency percentages changes quite a lot especially by using the HHV or LHV especially for efficiencies calculated from the thermo-neutral voltage, see table 2.1. Energy efficiency can be calculated simply by multiplying the voltage- and faradaic efficiency.

## 2.3 Hydrogen production

Hydrogen is the most abundant elements in the Universe. Actually, hydrogen constitutes around 75 wt.% [57] of the total mass in the Universe and 90 % [57] on an atomic basis. However, on Earth hydrogen is very rarely found in its free form. Most often hydrogen is bounded either as hydrocarbons or in water. Many technologies exist from which it is possible to produce hydrogen. Many of these are mostly experimental and have not yet found commercial use. In table 2.2 a number of hydrogen production technologies are listed. The production technologies are divided into columns depending on the hydrogen source *i.e.* hydrocarbons or water.

**Table 2.2: Hydrogen production technologies.**

| Hydrocarbons | Water |
|---|---|
| Steam reforming [58-61] | Electrolysis |
| Partial Oxidation [58-60] | Thermolysis [62, 63] |
| Gasification [59, 60, 64] | Thermochemical [63, 65, 66] |
| Pyrolysis [59, 64, 67] | Photolytic [60, 68, 69] |
| Fermentation [59, 70] | Photobiological [60, 70] |
| Enzymatic [71, 72] | Photoelectrochemical [60, 73, 74] |
| Microbial electrolysis cells [75, 76] | |

Table 2.2 does not show the extent of application of the different technologies, however approximately 96 % [59] of the hydrogen is produced from hydrocarbons with steam reforming of natural gas being the most widespread technology [77]. The remaining approximately 4 % [59, 77] of the world's

hydrogen production comes from water electrolysis, leaving almost nothing to the more exotic techniques listed in table 2.2, most of which are still in the development phase [60].

Since steam reforming (SR) of methane is the most widely spread technology used for hydrogen production a brief account of the technology is appropriate. The difference between SR and partial oxidation (POX) of methane lies in the oxidant [61], where SR uses steam as oxidant, POX uses oxygen. In reaction schemes (R- 2-7) and (R- 2-8) the reactions for SR and POX respectively are shown.

SR: $CH_4 + H_2O \rightleftharpoons CO + 3H_2$ (R- 2-7)

POX: $CH_4 + \frac{1}{2}O_2 \rightleftharpoons CO + 2H_2$ (R- 2-8)

To increase the hydrogen yield, the steam reforming reaction is often coupled with the water-gas shift (WGS) reaction where carbon monoxide is further reacted with more water to give carbon dioxide and hydrogen, see (R- 2-9).

WGS: $CO + H_2O \rightleftharpoons CO_2 + H_2$ (R- 2-9)

The steam methane reforming (SMR) reaction is very energy demanding as it is strongly endothermic ($\Delta_r H = 206$ kJ·mol$^{-1}$) [78]. Often the inlet temperature in steam reforming reactors is in the range of 450-650 °C [79] and the outlet temperature of the product gases is in the range of 700-950 °C [79]. Typically nickel supported catalysts *e.g.* nickel supported on alumina or spinel [80, 81] are used to catalyse the reaction. A typical gas composition after the SMR reaction is: 70-72 % $H_2$, 6-8 % $CH_4$, 8-10 % CO and 10-14 % $CO_2$ based on dry gases [82]. When further reacted through the WGS reaction ( at around 300-400 °C) the gas composition of the product gas is: 71-75 % $H_2$, 4-7 % $CH_4$, 1-4 % CO and 15-35 % $CO_2$ [82] also based on a dry gas composition.

It is clear that the steam reforming process of natural gas is not the way to produce clean and sustainable hydrogen for use in PEM fuel cells. The CO content in the product stream from the WGS reaction is still too high to be fed to low temperature PEM fuel cells, which demand CO levels under 10

ppm [61, 83] and for high temperature (up to 200 °C) PEM fuel cells the accepted CO level is increased up to 1-3 % for PA doped PBI fuel cells operated at 200 °C [84] and maximum 1 % for PA doped PBI fuel cells operated at 150 and 175 °C [84]. It seems that the preferred temperature to run durability test of PBI-based high temperature PEM fuel cells at is 160 °C [85, 86]. Hence it seems reasonable to assume that the CO level should not exceed 1 % in practical high temperature PEM fuel cell applications. This means that further purification of the product gas stream from SR and WGS often is necessary. A commonly used process for industrial cleaning of the product gases from SR and WGS is the pressure swing adsorption (PSA) process [82, 87]. In general a PSA unit consist of three different adsorbent layers [88]. The first layer is often made of alumina or a silica gel. The function of the first layer is mainly to absorb water from the gas stream. The second layer consists of activated carbon onto which CO, $CO_2$, $CH_4$ and sulphur traces are adsorbed. The third and last layer consists of zeolites which have improved adsorption capabilities towards CO, $N_2$ and other trace species. The purity of the gas is determined by the number of PSA columns in the unit the hydrogen is led through, often the number of columns vary between 4 and 12 [89]. A 10 column PSA unit is capable to clean a hydrogen off gas stream from steam reforming and WGS to a purity of 99.999 % [89].

Ryland *et al.* [90] estimate that producing 1 ton of hydrogen by the SMR process requires energy corresponding to 11 tons of $CO_2$, hence it is clear that hydrogen produced by steam methane reforming is by no standards sustainable nor environmentally friendly. Clean and environmentally friendly hydrogen can be produced by water electrolysis as long as the electricity comes from sustainable energy sources such as wind-, solar- or hydropower.

## 2.4 The electrolysis cell

An electrolysis cell consists of several elements. It has an electrolyte, two electrodes (an anode and a cathode) and two gas diffusion layers. The electrolyte and electrodes (often with the GDL included) are called the membrane electrode assembly. An electrolysis cell also consists of gaskets, two flow plates (or in the case of stacks bipolar plates), and finally there are two endplates. In figure 2.3 a schematic exploded view of a cross section of an electrolysis cell is shown.

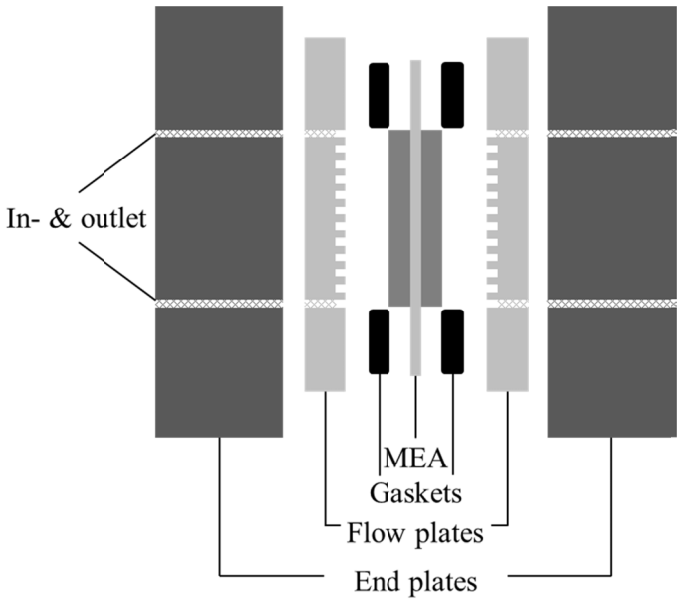


**Figure 2.3: Schematic exploded view of electrolysis cell cross section.**

The type of electrolysis cell is – like in the case of fuel cells – defined from the type of electrolyte. There are three major kinds of electrolysis cells: 'Alkaline', 'Proton Exchange Membrane/Polymer Electrolyte Membrane' and 'Solid Oxide'. Some general requirements can be set up to be met in order to be a good electrolyte (table 2.3) and a good electrode/catalyst (table 2.4). The requirement for the electrolyte is taken from PEM fuel cell systems, but the points are valid also for the PEM electrolyser and the two other types of electrolysers.

**Table 2.3: General requirements for electrolyte [8, 24, 27]**

| Property | Incentive |
|---|---|
| Chemically stable | During electrolysis the electrolyte has to withstand harsh conditions like elevated temperatures, elevated potentials, extreme pHs and reactive species ($O_2$, $H_2$, etc.). |
| Mechanically stable | The electrolyte should preferably be very thin to reduce ohmic loss. At the same time it needs to preserve its mechanical strength and to keep its dimensional integrity. |
| Gastight | The electrolyte need low permeability of $O_2$ and $H_2$ to ensure high gas purity and for safety reasons. |
| Ionic conductivity | High ionic conductivity to reduce ohmic resistance. |
| Electrical insulating | To avoid short circuiting the electrodes. |
| Price | In order to commercialise the cost of the electrolyte need to be minimised. |

The requirements listed in table 2.3 are general and not all the points are of equal relevance for all types of electrolysers. In an alkaline electrolysis cell the electrolyte traditional is a liquid and hence not gastight, but the requirement of gas separation is still valid and a separator must be added to the system.

**Table 2.4: General requirements for electrodes for technical applications [16, 91]**

| Property | Incentive |
|---|---|
| High surface area of catalyst | To increase the performance |
| Good electrocatalytic properties | To enhanced kinetics enhances performance |
| High electronic conductivity | In order to transport electrons to/from the electrode reaction |
| Sufficient porosity and pore size | To facilitate transportation of reactant and products |
| Long-term mechanical and chemical stability | Stability of both catalyst and electrode at elevated temperatures and potentials |
| Minimize gas bubble problems | High coverage of electrode lowers performance |
| Enhanced selectivity | More relevant for more complex reactions |
| Availability and low cost | Important for commercialisation |
| Health safety | Preferably as low toxicity as possible |

A point that is also very important for the electrodes is that it should be compatible with the electrolyte. An example of this is for instance solid oxide electrolysis cells (SOECs) where the thermal expansion coefficient should be similar to that of the electrolyte, otherwise the cell will be destroyed under heating and cooling since the expansion and contraction of the parts will be different and the material will fail [16].

An electrocatalyst is like an ordinary catalyst; a material which can accelerate a reaction without being consumed during the reaction, *i.e.* the catalyst lower the activation energy for a reaction to take place. An electrocatalyst is a catalyst for a reaction where a net charge transfer takes place [92], which means that electronic conductivity is essential for electrocatalysts.

In a strict definition of an electrocatalyst the catalytic particles of the electrode should influence the rate of the electrode reaction [93] *i.e.* the kinetic and mechanistic effect on the bonds formed by the reactants, product and/or intermediates with the electrode surface [91]. Trasatti gives a broader meaning of the term electrocatalyst, which comes from a practical point of view. If a material gives a

lower overpotential due to better conductivity it can still be considered a better electrocatalyst, although the kinetics and mechanism of the electrode reaction are unchanged [91].

### 2.4.1 Alkaline electrolysis

As mentioned in the previous section, the name of the electrolysis technology originates from the type of electrolyte. The electrode reactions and the schematic structure of an alkaline electrolyser can be seen in figure 2.4.

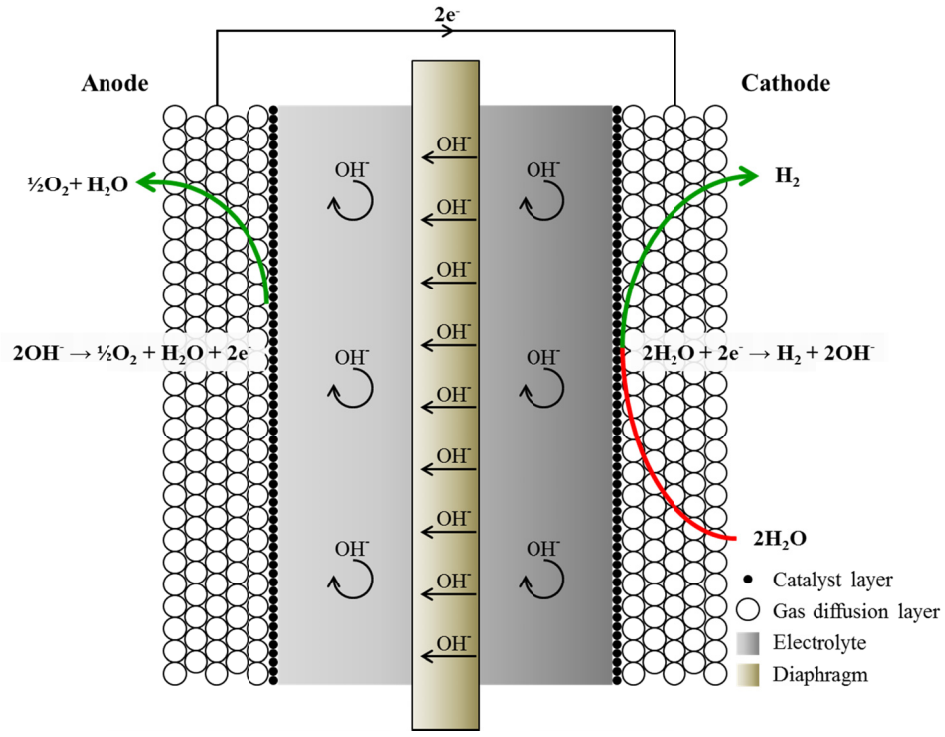


**Figure 2.4: Schematic representation of an alkaline electrolysis cell.**

From figure 2.4 it can be seen that the reactant, water, is fed to the cathode side of the electrolysis cell. At the cathode the water is dissociated into protons and hydroxide ions, the protons are reduced to hydrogen, and the hydroxide ions are transported across the electrolyte. On the anode side the hydroxide ions are oxidised to oxygen under formation of water. On both sides of the diaphragm the electrolyte is recirculated in order to keep a constant hydroxide concentration. The gradient colour of the electrolyte symbolises how the hydroxide ions are formed at the cathode (darker grey colour) and consumed at the anode (lighter grey).

In an alkaline electrolysis cell the electrolyte is a strongly alkaline liquid solution. For commercial alkaline electrolysis the maximal conductivity of KOH is at a concentration around 30 wt.% [94], depending on the temperature. At 25 °C the optimal concentration has been reported to be 27 wt.% and increasing to between 30 and 35 wt.% as the temperature is increased to 100 °C [95, 96]. Most often commercial alkaline electrolysers operate at temperatures around 80 °C [94]. As mentioned above, the electrolyte should separate the produced gases from each electrode, but with a liquid electrolyte as KOH, it is necessary to use a separator or diaphragm. This should fulfil the same requirements as a solid electrolyte (see table 2.3). The most common diaphragm in alkaline electrolysis cells has historically been made of porous white asbestos ($Mg_3Si_2O_5(OH)_4$) [97], but there are several drawbacks by using a white asbestos diaphragm, the obvious being it's toxicity leading to asbestosis and lung cancer [98]. In a basic solution the corrosion rate of white asbestos is dependent on temperature – higher temperatures leading to faster corrosion – which means that increasing the efficiencies of the electrolyser by elevating the temperature is a problem when using this kind of diaphragm [97].

Due to these issues other materials have been tested for use as diaphragms, *e.g.* composite of potassium titanate ($K_2TiO_3$) fibres and polytetraflouroethylene (PTFE) [99], poly phenylene sulfide [97], PTFE (as felt and as woven) [97], polysulfone [97] and asbestos coated with polysulfone [97]. During the last decade or so considerable amount of research has been put into developing hydroxide conducting polymers suitable for alkaline water electrolysis [100]. Recently Li *et al.* [101] reported very promising results with a hydrocarbon based polymeric membrane in a zero gap (*i.e.* zero distance between electrodes and electrolyte) alkaline electrolysis cell (AEC) with 4 M NaOH feed to both electrodes. They reached 1 $A \cdot cm^{-2}$ at 2.12 V with no decline of performance observed during a 10 day durability test [101].

For electrodes the most common materials are steel plates with some kind of Ni treatment. It could for instance be Ni-plating [53, 102], since nickel is corrosion resistant in alkaline media and because it is a fairly low cost metal [102]. Different metals like cobalt [103], iron [104] and vanadium [105] are used as additives to the electrodes. Cobalt is added to the anode, while iron and vanadium are used at the cathode. It was found that iron and vanadium can reactivate the cathode [104, 105]. The reactivation of

the cathode is promoted by ions of iron or vanadium in solution rather than metal incorporated in an alloy [104, 105]. The deactivation of the cathode are ascribed a formation of nickel hydride [104], which iron and vanadium can reverse.

### 2.4.2 Solid Oxide electrolysis

Where AEC systems have been commercial for decades, solid oxide electrolysis cells (SOECs) are still only under development. Building on top of solid oxide fuel cell (SOFC) considerable effort is put into this field. In figure 2.5 the schematic structure of an SOEC can be seen and the electrode reactions are given for both anode and cathode. The colour gradient in the electrolyte is used to symbolise the oxide ions are moving from the cathode to the anode.

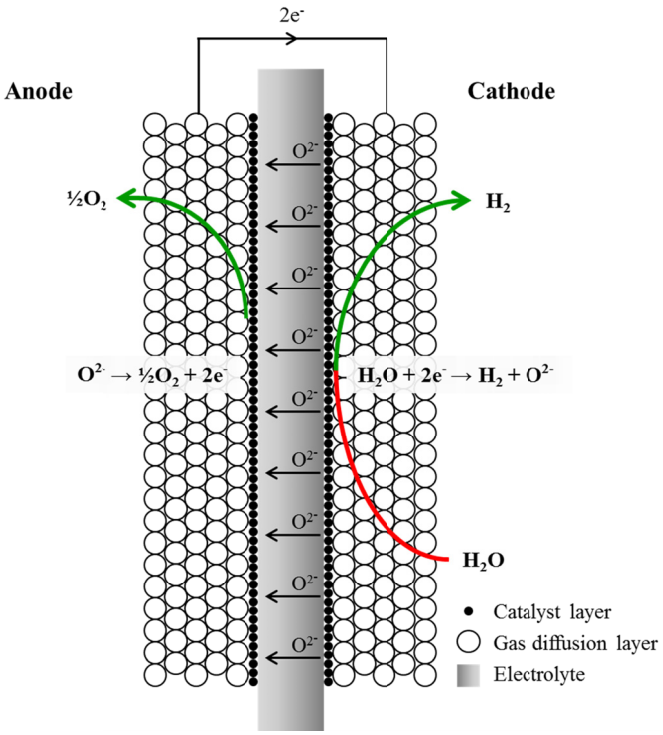


**Figure 2.5: Schematic representation of a solid oxide electrolysis cell.**

As in the AEC the reactant is fed to the cathode. Protons from the dissociated water are reduced to hydrogen, and oxide ions are transported across the oxide ion conducting electrolyte. On the anode side the oxide ions are oxidized to oxygen. SOECs are as SOFCs operated at very high temperatures between 600 °C and 1000 °C [17, 18, 106-108], but temperatures above 800 °C seems to be most

common. In SOECs the most common electrolyte is (as in SOFCs) yttria ($Y_2O_3$) stabilised zirconia ($ZrO_2$) (YSZ) [16, 109]. Other stabilised zirconia electrolytes are also used, *e.g.* Scandia ($Sc_2O_3$) stabilised zirconia which has higher ionic conductivity than YSZ, but suffers from higher cost and lower stability. The ionic conductivity of the stabilised zirconia electrolytes is very dependent on operating temperature. To achieve reasonable conductivities the temperature should be in the higher temperature range (from 800 °C and up). In the lower temperature range 600-800 °C doped $LaGaO_3$ (LSGM) was found to exhibit good conductivity [16]. Dopants could be strontium (Sr) for lanthanum (La) and magnesium (Mg) for gallium (Ga) hence shortened LSGM [16, 106]. LSGM has as mentioned above good conductivity in the lower temperature range and has superior conductivities compared to YSZ in the high temperature range. One reason to the limited use of LSGM as electrolytes in SOEC is that it has a tendency to react with nickel in the electrode and form lanthanum nicklates [16, 109, 110]. Other electrolytes used are made from ceria based oxides [16, 109] and other stabilised zirconia compounds than mentioned above [16].

Typical anodes used in SOEC are perovskite structured mixed oxides such as lanthanum strontium manganite (LSM) in a composite electrode with YSZ [109]. Other anodes such as $LaSrFeO_3$ [16, 109] and $LaSrCoO_3$ [16, 109] have been tested in composite anodes with YSZ. Similarly, a range of materials have been tested for the cathode in SOECs and the state-of-the-art cathode has been identified as a Ni-YSZ cermet [16, 109] (a cermet is a composite material of ceramic and metal). Other cathode materials which have been tested are Ni/samaria doped ceria composite electrodes and titanate/ceria ($LaSrTiO_3$/CeLaO) electrodes [109].

An often used procedure when testing SOECs is to keep a constant supply of hydrogen to the cathode and oxygen or air (could be synthetic air) to the anode [17-22]. The amount of hydrogen compared to water on the cathode is varied and it can be low amounts as ~ 8 vol% [22] and as high as 80 vol% [17]. This procedure of recirculating the gases to keep a constant flow of hydrogen and oxygen to ensure the right gas composition of the respective electrodes complicate the setup further and adds another challenge and cost to the overall design of the electrolysis cell/stack.

### 2.4.3 PEM electrolysis

Proton exchange membrane electrolysis cells (PEMECs) have been commercialised for years now, but they are mostly used in laboratories or other small scale applications since the size and hence the production capacity is small compared to commercial AEC plants. Contrary to the AEC and SOEC technologies the reactant (water) is fed to the anode side of the electrolysis cell in PEMECs, a schematic structure of a PEMEC and the electrode reactions are shown in figure 2.6. Again the colour gradient of the electrolyte is used to symbolise that the proton are formed at the anode and transported to the cathode.

Most PEMEC uses a PFSA (*e.g.* Nafion®) type membrane in which the proton conductivity is strongly dependent on the water content in the membrane [111]. Hence PEMECs (and PEMFCs) using PFSA membranes are almost exclusively operated at temperatures below 100 °C, at ambient pressure [111], although it is known that raising the temperature can facilitate both the electrode kinetics and lower the thermodynamic requirements for water splitting [23]. Much effort is put into developing new electrolyte materials that can be used at intermediated temperatures between 100-200 °C. This thesis is focused on PEM water electrolysis at elevated temperature (130 °C) and ambient pressure, but since only little work has been reported in this area until now an in-depth literature review of the different materials used in low temperature water PEMEC will be given in the following sections.

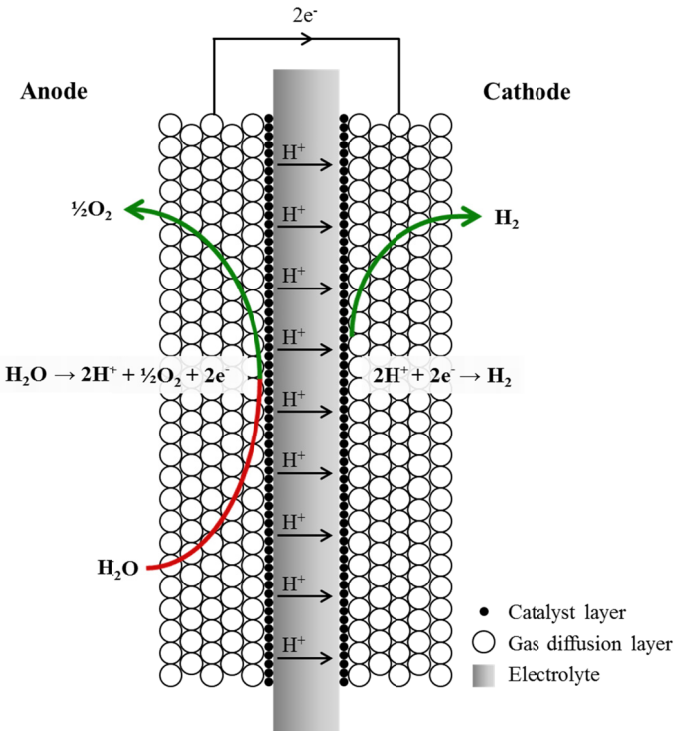


**Figure 2.6: Schematic representation of a proton exchange membrane electrolysis cell.**

## 2.5 Membranes

The, by far, most commonly used membranes for PEM water electrolysis are perflourosulfonic acid membranes. These consist of a perflourinated polymeric backbone (polytetrafluoroethylene) having ether bonded perflourinated side branches. These side branches are terminated with sulfonic acid groups. The most well-known membrane in the PFSA family is the Nafion® membrane from DuPont™. In figure 2.7 is shown a schematic representation of the chemical structure of Nafion®.

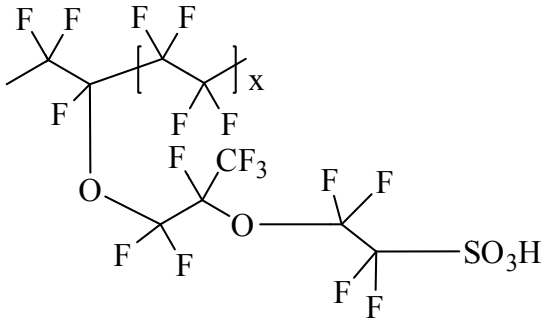


**Figure 2.7: Schematic of the chemical structure of Nafion®.**

Nafion® membranes are named with a three or four ciphered code after Nafion®, *e.g.* Nafion® 212 and Nafion® 1135. The two first numbers gives information about the degree of sulfonation of the membrane, commonly known as the equivalent weight (EW) [32]. The EW is defined as the mass of the dry polymer per sulfonic acid group [112]. The 21 in Nafion® 212 means that the membrane has an EW of 2100 g per sulfonic acid group and the 11 in Nafion® 1135 means it has an EW of 1100 g per sulfonic acid group. The last (two) cipher(s) in the three (or four) ciphered code gives information about the thickness of the membrane. The number(s) tell(s) how many multiplies of a thousandth of an inch (approximately 25 microns) the membrane thickness is [32]. Hence a Nafion® 212 membrane will have a thickness of 0.002 inch or approximately 50 microns and the Nafion® 1135 membrane has a thickness of 0.0035 inch or approximately 87.5 microns. As mentioned above the vast majority of PEM water electrolysis test has been conducted using Nafion® membranes as electrolyte. The most commonly used are: Nafion® 115 [9, 29-31, 113-132] and Nafion® 117 [8, 11, 23, 31, 48, 52, 133-149], but also other types of Nafion® are used like: Nafion® 1035 [150-152], Nafion® 112 [126, 153-155], Nafion® 1135 [126, 156], Nafion® 1110 [13] and Nafion® 212 [157-160].

Another commercially available brand of PFSA typed membranes is Aquivion™ from Solvay Solexis. Aquivion™ also consists of a PTFE like backbone, and like Nafion® it has sulfonic acid terminated side branches. However, in contrast to Nafion® the Aquivion™'s side chains are shorter, hence it is called a short side chain (SSC) [32] PFSA membrane. In figure 2.8 the chemical structure of the Aquivion™ polymer is shown.

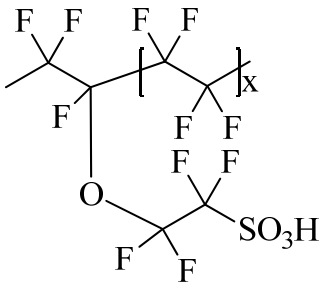


**Figure 2.8: Chemical structure of Aquivion™.**

The difference in side chain length between Nafion® and Aquivion™ means that Aquivion™ has a higher degree of sulfonation. Typically the EW of SSC PFSA membranes like Aquivion™ is in the

range of 750-850 g per sulfonic acid group. The short side chains of the polymer give SSC-PFSA membranes a more structured composition *i.e.* higher crystallinity compared to traditional PFSA membranes [32, 34]. It is this increase in crystallinity that prevents SSC-PFSA membranes to dissolve in water even though they have such high degrees of sulfonation [32]. SSC-PFSA is found to exhibit great dimensional stability [33], this and their improved ability to retain water in the higher temperature range [34] has made them an interesting class of membranes to use in the pursuit on increasing the operating temperatures on both fuel cells and electrolysers.

Other membranes than Nafion® have also been tested in water electrolysis, since Nafion® membranes and other PFSA membranes are relatively expensive, which could be limiting to commercialising. The focus for alternatives to PFSA membranes has mostly been towards sulfonated membranes which are not fluorinated or only partly fluorinated. One example is sulfonated poly(etheretherketone) SPEEK [23, 148] or variations of SPEEK eg. crosslinking [148], blend membranes with other polymers [161] and composite membranes with heteropolyacids (HPAs), both crosslinked [147, 148, 162] and not [149]. In figure 2.9 is a schematic representation of SPEEK shown.

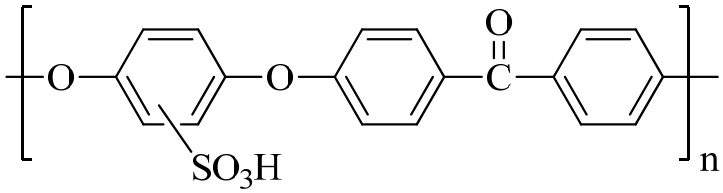


**Figure 2.9: Schematic of the chemical structure of SPEEK.**

Composite membranes of crosslinked SPEEK and HPAs perform especially well compared to a traditional PFSA membrane like Nafion® 117. Lee *et al.* [147] used three different kinds of heteropolyacids tungstophosporic acid (TPA, $H_3PW_{12}O_{40}\cdot nH_2O$), molybdophosphoric acid (MoPA, $H_3PMo_{12}O_{40}\cdot nH_2O$) and tungstosilicic acid (TSiA, $H_4SiW_{12}O_{40}\cdot nH_2O$). With membranes of similar thickness (approximately 180 μm) they reached cell voltages around 1.75 V [147] at a current density of 1 $A\cdot cm^{-2}$ (80 °C and atmospheric pressure) for all the three SPEEK/HPA and the Nafion® 117 reference membrane. Woo *et al.* [162] got similar voltages in the range of 1.7-1.8 V at 1 $A\cdot cm^{-2}$ (80 °C and atmospheric pressure) testing SPEEK/MoPA and SPEEK/TPA using a Nafion® 117 membrane as electrolyte in the reference MEAs.

Another example is sulfonated block copolymer of polysulfone and poly(phenylene sulphide sulfone), abbreviated SPSf-co-PPSS. Jang *et al.* [149] tested a composite membrane of SPSf-co-PPSS and TPA against a SPEEK/TPA membrane and a Nafion® 117 reference membrane. Their investigations showed that the SPSf-co-PPSS/TPA composite membrane had a marginally lower cell voltage (1.83 V, at 1 $A \cdot cm^{-2}$) [149] compared to Nafion® 117 (1.85 V, at 1 $A \cdot cm^{-2}$) [149], the SPEEK/TPA composite had a marginally higher cell voltage with 1.9 V also at 1 $A \cdot cm^{-2}$ [149].

All the sulfonated membranes mentioned above (including of course the PFSA membranes) have in common that they are highly dependent on the water content to have sufficiently high proton conductivity [111]. The water content of the membrane in an electrolysis cell operating below 100 °C is easily controlled since the cell is fed with liquid water and hence continuous wetting will be ensured. To operate at temperatures above 100 °C the retention of water in the membrane needs to be improved, or the system needs to be pressurised to keep the water in the liquid phase.

Some groups have tried to tackle the dehydration problem of the PFSA membranes by making PFSA composite membranes consisting of a PFSA membrane and inorganic filler with hygroscopic and mechanical stabilising properties. Both Antonucci *et al.* [29] and Xu *et al.* [28] have approached this by adding $SiO_2$ as the inorganic filler. Antonucci *et al.* [29] used an in-house made Nafion®-$SiO_2$ composite membranes with a $SiO_2$ content of 3 wt.%. With this membrane they improved the performance of the electrolysis cell considerably at 120 °C and atmospheric pressure. With a Nafion® 115 membrane as a reference electrolyte they achieved a current density of approximately 250 $mA \cdot cm^{-2}$ at a cell voltage of 1.8 V [29], but with the Nafion-$SiO_2$ composite membrane a current density of approximately 450 $mA \cdot cm^{-2}$ [29] was achieved at the same cell voltage. Obviously a considerable improvement was achieved by improving the water retention and mechanical properties of the membrane.

Xu *et al.* [28] tested a commercially available PFSA-silica membrane with a thickness of 60 μm. The performance of the membrane was tested using elevated pressures, up to 4 bar, when temperature was elevated above 100 °C, up to 130 °C. The electrolysis measurements were not compared to a reference

membrane without any inorganic filler in it. Hence it is impossible to distinguish between the contribution from the silica filler and the elevated pressure. However Antonucci *et al.* [29] found that also at elevated pressures the addition of $SiO_2$ had a tremendous influence on the performance. Going from approximately 600 $mA \cdot cm^{-2}$ at 1.8 V [29] to around 1700 $mA \cdot cm^{-2}$ at 1.8 V [29] at a temperature of 120 °C and an absolute pressure of 3 bar.

Baglio *et al.* [30] tested a composite membrane with $TiO_2$ (3 wt.%) as inorganic filler, in this case Nafion® 115 was used as reference material and improvements in performance were observed for electrolysis test done at 120 °C both at atmospheric pressure and 3 bar absolute pressure. At 120 °C and atmospheric pressure an increase in current density from around 275 $mA \cdot cm^{-2}$ at 1.8 V to approximately 700 $mA \cdot cm^{-2}$ at the same voltage was observed for the Nafion® 115 reference and the Nafion®-$TiO_2$ composite respectively. Although in the case of the Nafion®-$TiO_2$ system [30] the increase in performance was not as distinct as in the case with the Nafion®-$SiO_2$ from Antonucci *et al.* [29] when increasing the total pressure to 3 bar. The current density for the Nafion®-$TiO_2$ membrane at 1.8 V was approximately 1100 $mA \cdot cm^{-2}$ at 120 °C and 3 bar absolute pressure whereas it was approximately 600 $mA \cdot cm^{-2}$ at 1.8 V for the Nafion® 115 at the same conditions. In table 2.5 the characteristics for the three presented composite systems are listed.

**Table 2.5: Characteristics of PFSA composite MEAs and their current densities at the standard thermoneutral (TN) voltage (1.48 V) and at 1.7 V at 120 °C.**

| | Electrolyte Thickness [μm] | Anode [$mg \cdot cm^{-2}$] | Cathode [$mg \cdot cm^{-2}$] | Pressure [bar] | $i_{TN}$ [$mA \cdot cm^{-2}$] | $i_{1.7V}$ [$mA \cdot cm^{-2}$] |
|---|---|---|---|---|---|---|
| Antonucci *et al.* [29] | Nafion®-$SiO_2$ 120 | $IrO_2$ 5 | Pt/C 0.8 | 1 | 250 | 425 |
| Antonucci *et al.* [29] | Nafion®-$SiO_2$ 120 | $IrO_2$ 5 | Pt/C 0.8 | 3 | 250 | 1200 |
| Xu *et al.* [28] | PFSA-$SiO_2$ 60 | $Ru_{0.7}Ir_{0.3}O_2$ 2.5 | Pt/C 0.6 | 3 | 650 | 1475 |
| Baglio *et al.* [30] | Nafion®-$TiO_2$ 110-120 | $IrO_2$ 5 | Pt/C 0.8 | 1 | 350 | 575 |
| Baglio *et al.* [30] | Nafion®-$TiO_2$ 110-120 | $IrO_2$ 5 | Pt/C 0.8 | 3 | 375 | 875 |

A different class of membrane much used in high temperature fuel cell operation is the phosphoric acid doped polybenzimidazole membrane, see figure 2.10.

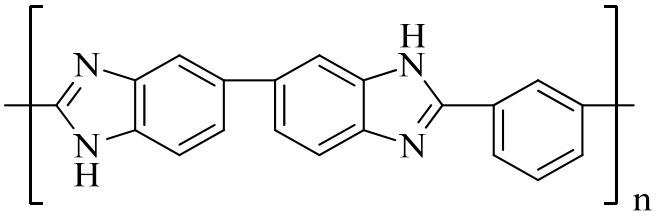


**Figure 2.10: Schematic of the chemical structure of PBI.**

PA doped PBI was first proposed as electrolyte for high temperature fuel cells in 1995 by Wainright *et al.* [26], and since then numerous groups have published high temperature fuel cell results using PA doped PBI. By February 2012 605 articles have been published within this field (indexed on Web of Knowledge using "polybenzimidazoles" and "fuel cell" as search phrase). Despite the great success as electrolyte in high temperature fuel cells, to the best of the author's knowledge, no one has tried using PA doped PBI as electrolyte in water electrolysis at elevated temperatures.

### 2.5.1 Proton transport in proton exchange membranes

In general the proton conductivity of proton exchange membranes follow either or both of two major routes, these being the vehicle mechanism [111, 163-166] and the Grotthuss mechanism [165-172].

The vehicle mechanism operates as the name imply by transporting the proton on a carrier (vehicle) molecule [166], in the case of most low temperature fuel cells and electrolysers (most often PFSA electrolytes as Nafion®) these carrier molecules are water molecules. The proton is carried as different water complexes such as the hydronium ion ($H_3O^+$), the Zundel ion ($H_5O_2^+$) or the Eigen ion ($H_9O_4^+$) [111]. The transport of the positive proton on its water carrier complex ion is a typical example on an electro-osmotic flow, where the charged species is moving in the direction of the applied potential.

Proton transport with the Grotthuss mechanism comes from a transport of a more or less common network of protons in the proton conducting media. In the case of electrolysis using PA doped membranes both of the PFSA type and PBI at elevated temperature and ambient pressure, the PA acts as the proton conducting media. When protons flow into the membrane at the anode side, it is not those

specific protons that are transported through the membrane, but rather a rearrangement of the protons in the PA phase allowing for protons on the cathode side of the membrane to reach the cathode and be reduced to free hydrogen.

The proton transport under anhydrous conditions are dominated by the Grotthuss mechanism, Ma *et al.* [170] found that for PA doped PBI the humidity has a dominant effect on the proton transport. The rate of proton transfer between species in PA doped PBI was found to be: $H_3PO_4(H_2PO_4^+)$…H-O-H > $H_3PO_4$…$H_2PO_4^+$ > N-$H^+$…$H_2PO_4^-$ > N-$H^+$…H-O-H > N-$H^+$…N-H [170]. Furthermore, both Ma *et al.* [170] and He *et al.* [168] have shown that increased PA content in PBI membranes increases the proton conductivity of the membrane.

## 2.6 Electrodes

### 2.6.1 Anode

The anode electrocatalyst is in PEM electrolysers most often an oxide of a noble metal like iridium or ruthenium or mixtures thereof. In 1984 Trasatti [91] presented a paper giving an overview over some electrocatalysts used for oxygen and chlorine evolution. He presented the data in a so-called volcano plot where the electrocatalytic overpotential towards oxygen evolution was plotted as a function of the transition enthalpy of going from the lower to the higher oxidation number. Figure 2.11 shows the volcano plot from reference [91]. It is clear that $RuO_2$ has the highest activity towards oxygen evolution since it has the lowest overpotential. However $RuO_2$ is not stable in the oxygen evolution reaction [173], it is further oxidised to its highest oxidation number, Ru(VIII), $RuO_4$ is a liquid at room temperature. The melting point of $RuO_4$ is around 25 °C [174, 175] and the boiling point is approximately 130 °C [174, 175]. Hence under normal water electrolysis conditions of 80 °C $RuO_2$ will not be suitable for application since it will be corroded away [94]. Nonetheless some groups present work using $RuO_2$ as oxygen evolution catalyst [154, 176] mostly in order to compare with other mixed oxides.

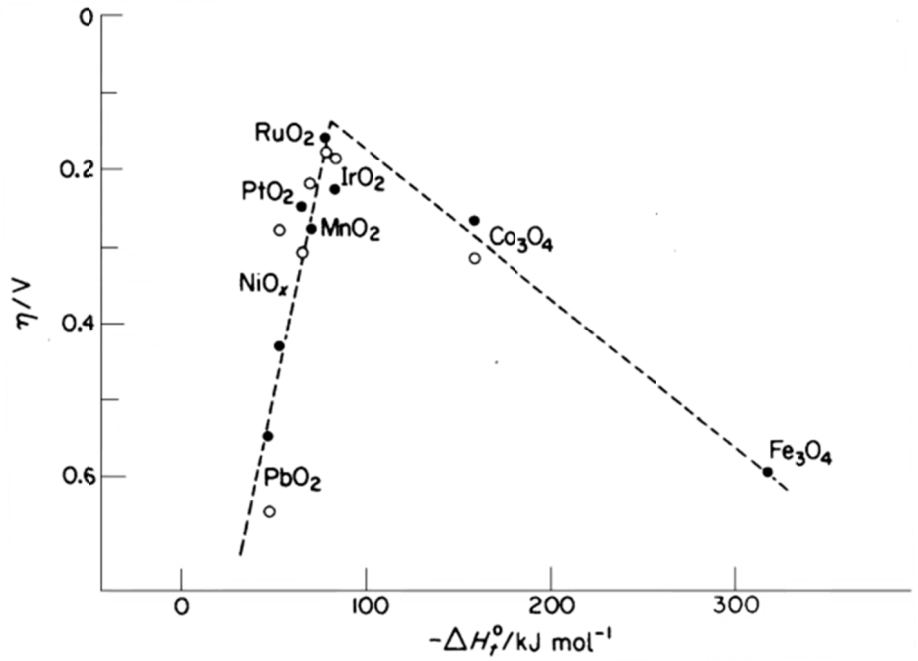


**Figure 2.11: Vulcano plot for some metal oxides in the oxygen evolution reaction. Overpotential *vs.* transition enthalpy going from lower to higher oxidation state. The open circles are for reaction in alkaline media and the filled circles are for reaction in acidic media. Taken from [91].**

$IrO_2$ on the other hand is less active towards the oxygen evolution reaction but it is far more stable [173] so it has been used extensively on its own [29, 30, 115, 116, 119-122, 128, 134, 139, 142, 144, 154, 160] or in order to stabilise the $RuO_2$ [173] as a mixed oxide with ruthenium $Ir_xRu_{1-x}O_2$ [28, 113, 116, 128, 136, 150-152, 154, 177]. Other mixed oxides have also been used such as $Ir_xSn_{1-x}O_2$ [113, 123], $Ir_xTa_yO_2$ [136], $Ir_xRu_yTa_zO_2$ [116, 128] and $Ir_xRu_{1-x}Mo_yO_z$ [151].

In the case of $Ir_xSn_{1-x}O_2$ it was found that $SnO_2$ did not have a beneficial influence on the performance of the electrolysis cell. In both cases [113, 123] it was found that the cell voltage at a given current density was increased as the content of $SnO_2$ was increased. Marshall *et al.* [123] found that the cell voltage at 1 $A \cdot cm^{-2}$ was increased by 42 mV with 20 mol% Sn in the mixed oxide and by 165 mV for a 80 mol% Sn content. Similar results were found by Mayousse *et al.* [113], who tested iridium-tin mixed oxides with tin contents of 30 and 50 mol%, which had an increase in the cell voltage of around 100 and 125 mV respectively at a current density of 1 $A \cdot cm^{-2}$. So the only beneficial effect of adding $SnO_2$ to the anode seems to be to lower the cost by 'diluting' the precious active species [123].

The addition of $Ta_2O_5$ to mixed oxides of $Ir_xRu_yTa_zO_2$ or $Ir_xTa_yO_2$ does not seem to have a significant negative influence on the performance. Marshall *et al.* [128] obtained more or less similar cell voltages for $Ir_{0.6}Ru_{0.2}Ta_{0.2}O_2$ and $Ir_{0.8}Ru_{0.2}O_2$, indicating that at least part of the iridium can be replaced with tantalum, in a mixed oxide containing ruthenium, without losing catalytic activity. However the same does not seem to be the case for at mixed oxide of just tantalum and iridium. Marshall *et al.* [116] did not compare $IrO_2$ and $Ir_xTa_yO_2$ directly in real PEM electrolysis applications, however polarisation tests in a liquid electrolyte of 0.5 M $H_2SO_4$ revealed that $Ir_{0.7}Ta_{0.3}O_2$ had higher potentials than $IrO_2$ [116].

Cheng *et al.* [151] found that adding molybdenum oxide to $Ir_{0.4}Ru_{0.6}O_2$ improved the performance in real PEM electrolysis testing. An $Ir_{0.4}Ru_{0.6}Mo_xO_y$ with a Mo content of 40 mol% of the total metal content had a cell voltage 40 mV lower than $Ir_{0.4}Ru_{0.6}O_2$ at 1 $A \cdot cm^{-2}$ [151], at higher current densities the difference was even more pronounced with approximately 150 mV at 2 $A \cdot cm^{-2}$ [151]. Cheng *et al.* [151] explained the improvement in performance with the smaller particle size of the $Ir_{0.4}Ru_{0.6}Mo_xO_y$ compared to $Ir_{0.4}Ru_{0.6}O_2$, hence increasing the effective catalytic active area of the anode.

Table 2.6 summarises the MEA characteristics, MEA performance and electrolysis testing temperatures for the different anode catalysts described above.

**Table 2.6: MEA data, MEA performance and electrolysis temperature for different anode catalysts.**

| | Anode [$mg \cdot cm^{-2}$] | Cathode [$mg \cdot cm^{-2}$] | Electrolyte | U [V] 1 $A \cdot cm^{-2}$ | Temp. [°C] |
|---|---|---|---|---|---|
| Marshall *et al.* [123] | $IrO_2$ [2] | Pt [0.4] | Nafion® 115 | 1.61 | 80 |
| Marshall *et al.* [123] | $Ir_{0.8}Sn_{0.2}O_2$ [2] | Pt [0.4] | Nafion® 115 | 1.65 | 80 |
| Marshall *et al.* [123] | $Ir_{0.2}Sn_{0.8}O_2$ [2] | Pt [0.4] | Nafion® 115 | 1.78 | 80 |
| Mayousse *et al.* [113] | $IrO_2$ [2.5][a] | Pt [0.5] | Nafion® 115 | 2.3 | RT |
| Mayousse *et al.* [113] | $Ir_{0.7}Sn_{0.3}O_2$ [2.5][a] | Pt [0.5] | Nafion® 115 | 2.39 | RT |
| Mayousse *et al.* [113] | $Ir_{0.5}Sn_{0.5}O_2$ [2.5][a] | Pt [0.5] | Nafion® 115 | 2.43 | RT |
| Cheng *et al.* [151] | $Ir_{0.4}Ru_{0.6}Mo_xO_y$ [1.5][b] | Pt [0.4] | Nafion® 1035 | 1.61 | 80 |
| Cheng *et al.* [151] | $Ir_{0.4}Ru_{0.6}O_2$ [1.5] | Pt [0.4] | Nafion® 1035 | 1.65 | 80 |
| Marshall *et al.* [128] | $Ir_{0.6}Ru_{0.2}Ta_{0.2}O_2$ [2] | Pt [0.4] | Nafion® 115 | ~1.60 | 80 |
| Marshall *et al.* [128] | $Ir_{0.8}Ru_{0.2}O_2$ [2] | Pt [0.4] | Nafion® 115 | ~1.60 | 80 |

Cathode catalysts were Pt/C with Pt content between 20 and 46.1 wt.% in all cases.
[a] Targeted loading 2.5 $mg \cdot cm^{-2}$, actual loading between 2 and 3 $mg \cdot cm^{-2}$.
[b] Mo content 40 mol%.

Other commonly used electrocatalysts for the oxygen evolution reaction in PEM electrolysers are Ir-black [9, 23, 114, 117, 118, 131, 153, 154, 161, 178] and Pt [8, 135, 140, 143, 145, 147-149, 179]. More 'exotic' electrocatalysts tested are: Pt-Ni [162], Pt-Co [138, 162], Pt-Ru-Ni [162], Pt-Ru-Co [138, 162], Pt-Ru [135], Pt-Ir [135], and Co-Ru [138]. Woo *et al.* [162] achieved reasonable cell voltages around 1.7-1.8 V at 1 $A \cdot cm^{-2}$ with Pt-Ni, Pt-Co, Pt-Ru-Ni, Pt-Ru-Co as anode catalysts and Pt as cathode.

In addition non-noble species have also been tested as anode in PEM electrolysers, Matsuzawa *et al.* [180] tested partially oxidised zirconium carbonitrides (Zr-CNO) and achieved a cell voltage of 2.6 V at 1 $A \cdot cm^{-2}$ at 80 °C using 0.9 $mg \cdot cm^{-2}$ Zr-CNO (with a degree of oxidation of 0.07) on the anode, Pt on the cathode and a Nafion® membrane as electrolyte.

The anode consists not only of the electrocatalyst, but also an ionic conducting component to facilitate the transport of ions. For this an ionomer of the same type as the polymeric membrane material is used. Wei *et al.* [161] found that using an ionomer (Nafion®) very different from the membrane material (SPEEK/poly(ether sulfone) (PES) blend) gave a very poor electrolyser performance, attributed to an interfacial resistance between the electrode layer and the membrane [161].

The amount of the ionic conducting ionomer (also called binder material) is varied greatly. From 5 wt.% [9, 123, 128] to 40 wt.% [126] commonly binder contents of 25 wt.% [150-152, 159, 160] and 33 wt.% [29, 30, 119-122, 130, 177] are used. Ma *et al.* [126] found that lowering the binder content from 40 wt.% to 10 wt.% markedly improved the performance. In a polarisation test the cell voltage was lowered by approximately 200 mV at 700 $mA \cdot cm^{-2}$ [126] at 30 °C, using a loading of 3.5 $mg \cdot cm^{-2}$ Ir-black and a Nafion® 1135 membrane by going from a ionomer binder content of 40 wt.% to 10 wt.%.

### 2.6.2 Cathode

On the cathode the electrocatalyst is very often Pt, either as Pt-black or as supported Pt on carbon (Pt/C). A commonly used catalyst support is Vulcan XC-72R carbon, which is carbon black with a very high surface area. The high surface area combined with the high electronic conductivity of carbon gives it excellent properties for a catalyst supporting material. The content of Pt in Pt/C varies from 20 wt.% [123] to 70 wt.% [114]. Other support materials tested for the electrocatalyst of the electrolyser cathode are graphitic nano-fibres (GNFs) [131] and multi-walled carbon nano-tubes (MWCNT) [138].

Other tested cathode electrocatalysts are: Pd/C [52, 114, 118, 132], $RuO_2$ [114], Pt-Ir [137], Pt/$TiO_2$-MWCNT [138], Co-Ru/$TiO_2$-MWCNT [138], Co-Ru-Pt/$TiO_2$-MWCNT [138], Co-Pt/$TiO_2$-MWCNT [138], Pt/GNF [131], Pt-Pd/GNF [131]. Electrocatalysts without noble metals have also been tested in PEM water electrolysis, some examples are boron-capped trix(glyoximato) cobalt complexes (shorted by authors to Co(dmg) [52] and tungstosilicic acide hydrate ($\alpha$-$H_4SiW_{12}O_{40}$) [52].

Millet *et al.* [52] tested the two non-noble cathode catalysts, and found that the cobalt complex (Co(dmg)) in itself did not have a pronounced catalytic activity. In an electrolyser test using a Nafion® 115 as electrolyte, Ir-black as anode (2.5 $mg \cdot cm^{-2}$) and 1 $mg \cdot cm^{-2}$ Co(dmg) without supporting material as cathode gave a cell voltage that was approximately 450 mV higher at 500 $mA \cdot cm^{-2}$ [52] (90 °C, 1 bar) compared to a similar reference MEA (cell voltage approximately 1.65 V at 500 $mA \cdot cm^{-2}$) using Pt (unsupported - 1 $mg \cdot cm^{-2}$) as electrocatalyst. However using a supporting material as carbon black (Vulcan XC72) the cell voltage of the Co(dmg)/C (1 $mg \cdot cm^{-2}$) was now reduced to only approximately 200 mV [52] higher than the reference MEA. $H_4SiW_{12}O_{40}$ on the other hand shows more promising catalytic properties. Millet *et al.* [52] found that using a cathode loading of 0.8 $mg \cdot cm^{-2}$ of unsupported $H_4SiW_{12}O_{40}$ only gave an increase in cell voltage of approximately 50 mV at 1 $A \cdot cm^{-2}$ [52] (90 °C, 1 bar) compared to a reference MEA using unsupported Pt as cathode (loading not specified).

Also carbon black supported palladium Pd/C has shown reasonable activity. Millet *et al.* [52] found that a MEA with a 0.7 $mg \cdot cm^{-2}$ of 40 wt.% Pd/C cathode (anode Ir-black 2 $mg \cdot cm^{-2}$, electrolyte Nafion® 115, 90 °C and 1 bar) only had a voltage of approximately 25 mV [52] higher at 1 $A \cdot cm^{-2}$ than

a reference MEA using 0.7 mg·cm$^{-2}$ 40 wt.% Pt/C (approximately 1.68 V at 1 A·cm$^{-2}$). The same was observed by Grigoriev *et al.* [118] who also found that a MEA with a 0.7 mg·cm$^{-2}$ 40 wt.% Pd/C cathode (anode Ir-black 2.4 mg, electrolyte Nafion® 115, 90 °C and 1 bar) had a cell voltage approximately 25 mV [118] higher than the reference MEA with 0.7 mg·cm$^{-2}$ 40 wt.% Pt/C cathode (ca. 1.68V at 1 A·cm$^{-2}$).

The effect of the supporting layer was investigated by Grigoriev *et al.* [131] comparing carbon black (Vulcan® XC-72) with graphitic nano-tubes. In a MEA using Nafion® 115 as electrolyte and 2.0 mg·cm$^{-2}$ Ir-black as anode tested at 90 °C and 1 bar, a 0.8 mg·cm$^{-2}$ 40 wt.% Pt/C cathode was compared to a 0.8 mg·cm$^{-2}$ 40 wt.% Pt/GNF cathode. The Pt/GNF cathode had a cell voltage 50 mV [131] lower than the Pt/C reference (1.72 V [131]) at 1 A·cm$^{-2}$. The improvement was attributed to the micro-structure of the electrocatalysts made with GNFs having improved electronic and ionic conductivity and having a more optimal shape and distribution of pores [131].

In table 2.7 the MEA data, MEA performance and electrolysis testing temperatures are summarised for the different cathode materials compared above.

**Table 2.7: MEA data, MEA performance and electrolysis temperature for different cathode catalysts.**

| | Cathode [mg·cm$^{-2}$] | Anode [mg·cm$^{-2}$] | Electrolyte | U [V] 1 A·cm$^{-2}$ | Temp. [°C] |
|---|---|---|---|---|---|
| Millet *et al.* [52] | Co(dmg) [1] | Ir black [2.5] | Nafion® 115 | - [a] | 90 |
| Millet *et al.* [52] | Co(dmg)/C [1] | Ir black [2.5] | Nafion® 115 | ~2.1 | 90 |
| Millet *et al.* [52] | Pt [1] | Ir black [2.5] | Nafion® 115 | ~1.8 | 90 |
| Millet *et al.* [52] | α-$H_4SiW_{12}O_{40}$ [0.8] | Ir black [2.5] | Nafion® 115 | ~1.84 | 90 |
| Millet *et al.* [52] | Pd/C 40 wt.% [0.7] | Ir black [2.0] | Nafion® 115 | ~1.7 | 90 |
| Millet *et al.* [52] | Pt/C 40 wt.% [0.7] | Ir black [2.0] | Nafion® 115 | ~1.68 | 90 |
| Grigoriev et al. [118] | Pd/C 40 wt.% [0.7] | Ir black [2.4] | Nafion® 115 | ~1.7 | 90 |
| Grigoriev et al. [118] | Pt/C 40 wt.% [0.7] | Ir black [2.4] | Nafion® 115 | ~1.68 | 90 |
| Grigoriev et al. [131] | Pt/GNF 40 wt.% [0.8] | Ir black [2.0] | Nafion® 115 | 1.67 | 90 |
| Grigoriev et al. [131] | Pt/C 40 wt.% [0.8] | Ir black [2.0] | Nafion® 115 | 1.72 | 90 |

[a] ~2.05 V at 0.5 A·cm$^{-2}$.

### 2.6.3 Manufacturing procedures

The nanoparticles of Pt (in the case of the cathode) and oxides (for the anode) can be prepared in several different ways. One of the more common methods for the synthesis of nano-size oxides are the Adams fusion method [181]. Other methods are the colloid method and the sulphite-complex route.

A version of the Adams fusion method often used is described by Marshall *et al.* [182]. The synthesis route is given for $IrO_2$, but can easily be adapted to other pure oxides or mixed oxides. A chloride precursor salt ($H_2IrCl_6 \cdot nH_2O$) was dissolved in isopropanol under magnetic stirring for 1-2 hours at room temperature (until complete dissolution). Then finely ground $NaNO_3$ was mixed with the solution and the mixture was heated to 70 °C under air, and kept at this temperature until completely dry. The salt mixture was calcined in a preheated furnace at 500 °C for a certain period of time (30 min, for small amounts) to evaporate $NO_x$. The furnace was subsequently cooled slowly down to room temperature. Then the resulting salt-$IrO_2$ mixture was washed several times in demineralised water to remove the remaining salts. The black $IrO_2$ was separated by centrifugation and finally dried in air at 90 °C.

Marshall *et al.* [182] also described the colloid method (also called modified polyol method). The precursor salt was added to ethylene glycol, the solution was magnetically stirred and heated to reflux using a protective $N_2$ atmosphere. The solution was stirred for two hours until the colloid had been formed. Afterwards the pH of the solution was adjusted to 2.5 using 0.1 M NaOH and then stirred for additionally 10 minutes. Adjusting the pH ensured better separation of the colloid and the glycol. Separation of the colloid was done centrifugally and the colloid was washed several times in deionised water. The colloid was dispersed ultrasonically in acetone and dried in air at 60 °C before being annealed in air at 500 °C for 30 minutes (small portions) to oxidise the iridium to $IrO_2$.

Siracusano *et al.* [120] used a sulfite complex route to make $IrO_2$. Again a chloride precursor salt was used to achieve a sulfite precursor salt. The $IrCl_4 \cdot nH_2O$ was dissolved in distilled water, $Na_2CO_3$ was used to adjust the pH to 7. $NaHSO_3$ was then added to the solution and $Na_6Ir(SO_3)_4$ precipitates, the precipitate is filtered and subsequently washed by distilled water to remove traces of chloride. The Ir-

sulfite complex was suspended in distilled water under stirring followed by a decomposing from adding 40% $H_2O_2$ solution drop-wise (gas evolution) to the complex solution kept at 80 °C. The colloidal $IrO_x$ was filtered, washed and dried at 80 °C, finally the dry powder was calcined under air.

Pure metals are often made simply by reducing their chloride salts using $NaBH_4$ [154]. The metal precipitates and are washed repeatedly to remove the chloride.

## 2.7 Membrane Electrode Assembly preparation

The membrane electrode assembly consists of the membrane and the two electrodes. There are two different ways the electrodes can be prepared. Either they can be attached to the membrane and making a so-called catalyst coated membrane (CCM) [154, 158] electrode, or they can be attached to the gas diffusion layer making a gas diffusion electrode (GDE) [183]. Supported platinum on carbon black on a wet-proofed carbon cloth is a well-known example of a GDE from both the fuel cell and electrolysis (as cathode) world.

In the case of the CCM the electrodes can be prepared in several different ways. The electrodes can be attached to the membrane by an impregnation-reduction technique (I-R technique) [147] where the membrane is impregnated with a precursor salt (*e.g.* $Pt(NH_3)_4Cl_2$, in the case of a Pt electrode) and subsequently reduced. Millet *et al.* [143] soaked a Nafion® membrane in its protonated form in a $Pt(NH_3)_4Cl_2$ solution, the protons in the membrane were then cation exchanged with the platinum. Subsequently the platinum exchanged membrane was reduced by soaking it in a $NaBH_4$ solution (see also section 2.6.3). Both these processes were done at room temperature and it was found that the platinum predominately precipitated near the surfaces on the membrane [143]. The phenomenon was explained by the fact that platinum cations near the surface were reduced first to metallic Pt when immersed in the $NaBH_4$ solution. This made a chemical potential gradient hence the platinum cations would diffuse to the surface while sodium ions would diffuse back into the membrane to ensure electroneutrality [143]. Millet *et al.* [143] reported that the penetration depth of the precipitated metallic platinum could be controlled by the concentration of the reducing solution. Lower

concentrations of $NaBH_4$ [143] would give a more localised precipitation of Pt at the membrane surface. The I-R technique was used frequently in the late 80s and the beginning of the 90s by the lab of Millet *et al.* [8, 135, 143] and Aldebert *et al.* [140]. More recently the labs of Jang *et al.* [148, 149], Lee *et al.* [147] and Woo *et al.* [162] have also used the I-R technique to make CCMs.

Another widely used technique to form CCMs is to make a catalyst ink of catalyst (*e.g.* $IrO_2$), a ionomer binder (often Nafion® is used, since the majority of PEM electrolysers use Nafion® membranes as electrolyte) and a dispergent (*e.g.* isopropanol [128, 152] or ethanol [28]). The ink can be applied directly to the membrane by a spraying procedure [122, 177] or by brushing the catalytic ink onto the membrane [126]. The ink can also be sprayed to another substrate first (*e.g.* PTFE [159] or silicone-rubber [153]) and then hot-pressed to membrane according to the decal method [153, 159], a method described by Wilson *et al.* [184] in 1992 for PEM fuel cell applications.

The catalyst can also be applied to the membrane by sputtering [179], but the sputtering technique is most commonly applied to sputter the catalyst layer on the gas diffusion layer making a GDE [129, 144]. Making GDE is often very similar to making CCM. A catalytic ink, like described above is sprayed to the gas diffusion layer instead of the membrane [9, 52, 118] or brushed onto the GDL [117].

Finally the MEA procedure also often includes a hot pressing step where the GDLs are hot pressed to the catalyst coated membrane [159], or the GDE are hot pressed to membrane and first there making the complete MEA [117]. Several different temperatures and pressures are applied, however for Nafion® MEAs the most commonly used temperatures are between 125 °C [128] and 140°C [151], since this is in the range of the glass transition temperature. Common pressures are between 2 MPa [128] and 10 MPa [151]. The hot pressing time is usually longer for lower temperatures *e.g.* 10 minutes for 125 °C [128] and shorter for higher temperatures *e.g.* 3 minutes for 135 °C [157]. However the membrane and electrodes can also be assembled in the electrolysis cell, so the MEA first is formed when clamping the cell together [121, 122]. This procedure can, however, potentially be problematic for cells operating at 80 °C *i.e.* well below the glass transition temperature of Nafion® membranes.

On the anode side carbon cloth cannot be used as GDL since it will be corroded severely over time. Few research groups uses carbon cloth as GDL anyway, but try to protect it by *e.g.* sputtering it with titanium [144] or plate it with gold [115]. The most commonly used material for anode gas diffusion layer is titanium *e.g.* as Ti-sinter [9, 128] or Ti-grid [136, 177] or Ti-mesh [119, 120].

# 3 Description of experimental techniques

## 3.1 Synthesis of anode catalyst

The synthesis of $IrO_2$ was based on the Adams fusion procedure by Marshall *et al.* [182] described in section 2.6.3. A normal batch size for the catalyst preparation would be using approximately 3 g of the precursor salt.
The reaction schemes for the Adams fusion synthesis of $IrO_2$ can be seen in (R- 3-1) and (R- 3-2).

$$H_2IrCl_6 \cdot 4H_2O + 6NaNO_3 \rightarrow 6NaCl + Ir(NO_3)_4 + 2HNO_3 \quad \text{(R- 3-1)}$$

$$Ir(NO_3)_4 \xrightarrow{500\ °C} IrO_2 + 4NO_2 + O_2 \quad \text{(R- 3-2)}$$

As a precursor salt, dihydrogen hexachloroiridate(IV)hydrate, $H_2IrCl_6 \cdot 4H_2O$ (Alfa Aesar – 99 % metal base) was used. The precursor salt was stored and weighed in a protected argon atmosphere (glove box) to keep its nominal level of hydration. The hexachloroiridate was brought into complete solution by magnetically stirring (2-3 hours) in approximately 78 mL of 2-propanol (Riedel de Häen, puriss) which equals a concentration of $8 \cdot 10^{-2}$ mol·L$^{-1}$. After dissolution of the iridium salt a large surplus (approximately 25 times the stoichiometry) of finely ground sodium nitrate was added to the solution a little at the time. After the addition of $NaNO_3$, the mixture was magnetically stirred at 70 °C in air until completely dry, for a portion of this size, drying time was around 5-6 hours.

When completely dry the salt mixture was ground finely (to ease the evaporation of $NO_x$) and placed in a preheated furnace (500 °C) for 4-5 hours to ensure the complete decomposition of the $Ir(NO_3)_4$. The furnace was slowly cooled to room temperature after which the iridium oxide was washed 3 times in large quantities of demineralised water. The separation of $IrO_2$ and water was done by centrifuging. The washed $IrO_2$ was dried in air at 90 °C before X-ray powder diffraction and $N_2$ adsorption/desorption analysis to determine the Brunauer-Emmett-Teller (BET) surface area. A typical yield of this synthesis was 97-99%.

## 3.2 Powder X-ray diffraction

The $IrO_2$ was characterised using X-ray powder diffraction (XRPD). The XRPD was done on a Bruker AXS D8 Advance Diffractometer with a wave length of 1.5406 Å (Cu-anode, $\alpha_1$-value). The $IrO_2$ samples were examined in a 2θ range from 20 ° to 80 °. The step size was 0.02 °/step each step lasting 2.5 second giving a measurement time of approximately 2 hours per diffractogram. The measurements were all done at room temperature.

Powder X-ray diffractograms gives information about the structure of the crystallites in the sample. They can be used to confirm the identity of the material. There are several key elements in a diffractogram, one is the position and size of the peaks in the diffractogram. This is used to determine the dimension of the unit cell of the sample and hence the crystal structure of the sample. The relative intensities of the peaks tell which atoms the sample consists of since the scattering of X-rays are dependent on atomic weight (heavier atoms have higher scattering). Both of these characteristics give a clear indication if the sample is the correct species. From the width of peaks a quantitative estimation of the crystallite sizes can be determined. As a rule of thumb the wider a peak is, the smaller is the crystallite size. From the Debye-Scherrer equation a quantitative size can be calculated. The Debye-Scherrer equation is given here as equation (3-1).

$$T = \frac{C \cdot \lambda}{B \cdot \cos\theta} \tag{3-1}$$

T is the thickness of the crystallites, C is the Scherrer constant (dependent on crystallite geometry) [185], λ is the wave length of the X-rays, θ is the Bragg angle and B is the full-width at half-maximum of the peak given in radians [186].

## 3.3 Nitrogen adsorption/desorption

The nitrogen adsorption and desorption were used to determine the BET surface area. The adsorption/desorption was performed on a Micromeritics Gemini FlowPrep 060 Degasser and a Micromeritics Gemini 2375 instrument, using nitrogen as the adsorbate. Adsorption was done using liquid nitrogen to cool the sample (the adsorbent) down. In nitrogen adsorption/desorption nitrogen is physisorbed (physically adsorbed) to the surface of the particles and by knowing the size of each nitrogen molecule (0.162 $nm^2$ at 77 K [187]) the surface area can be calculated from the adsorbed volume of $N_2$. The BET surface area is calculated from a multilayer adsorption and then extrapolating the data back to a case where only a monolayer of nitrogen had physisorbed to the surface.

First the sample was heated under vacuum to desorb any contaminant *e.g.* water (this was done in the Micromeritics Gemini FlowPrep 060 Degasser). Then the sample was cooled using liquid nitrogen. Nitrogen was admitted into the sample holder in controlled increments (in the Micromeritics Gemini 2375 BET instrument) allowing for the pressure to equilibrate. It was then possible to calculate the gas quantities adsorbed to the surface. Each adsorbed gas volume at a given pressure of nitrogen (keeping the temperature constant) defined the adsorption isotherm. This isotherm was then used to calculate the aforementioned BET surface area. The more gas introduced to the sample holder the higher the coverage of nitrogen would be.

At some point the coverage will exceed a monolayer, so to calculate the BET surface area an adequate range on the adsorption isotherm should be chosen (often in the range of 0.05 to 0.35 of the relative pressure between the actual pressure p and the saturated pressure $p_0$ [188]) and the BET equation can be used to calculate the volume of the monolayer. The BET equation is given in equation (3-2) [189].

$$\frac{P}{V\cdot(p_0-p)} = \frac{1}{V_m\cdot c} + \frac{c-1}{V_m\cdot c}\cdot\frac{p}{p_0} \tag{3-2}$$

V is the volume of gas adsorbed at a given pressure, p is the gas pressure, $p_0$ is the saturated vapour pressure of the liquid at the operating temperature, $V_m$ is the volume equivalent to an adsorbed monolayer and c is the BET constant.

Plotting experimental data in the form of $p/V \cdot (p_0-p)$ against the relative pressure $p/p_0$ often have a linear relationship in the aforementioned pressure range (0.05-0.35), so by evaluating the slope and the intercept, $V_m$ and a the BET constant c can be determined. Since the BET surface area is calculated from a mathematical model a whole range of assumptions has to be taken into account for it to be valid [187].

- There is a dynamic equilibrium between the adsorbate and the adsorbent, *i.e.* the rate of adsorption and desorption in any layer are equal.
- In the first layer all the molecules adsorb on adsorption sites with equivalent properties.
- The molecules in the first adsorption layer acts as adsorption sites for molecules in the subsequent layers.
- Any interaction between adsorbants is ignored
- Adsorption/desorption conditions are equal for all layers except the first layer.
- Adsorption energy for the molecules in the second and higher layers is equal to the condensation energy.
- The multilayer grows to infinite thickness when the pressure is equal to the saturation pressure.

## 3.4 Scanning electron microscopy

Scanning electron microscopy (SEM) is used to show the surface topology of a specimen and, in the case of ion beam cut samples, how the cross section of a sample looks. In this project SEM has been used to investigate the gas diffusion layers. SEM is a very useful technique to look at surfaces in very high resolution. Resolutions down to 1-2 nm are possible with new high performance microscopes [190]. In this project a Carl Zeiss EVO MA10 microscope was used for acquiring the SEM images. Cross sections of the gas diffusion layers were made using a Hitachi E-3500 ion mill.

SEM images are generated by scanning an electron beam across the surface of the sample. During this scanning secondary and backscattered electrons are emitted from the sample. The intensity of the backscattered electrons is dependent of the atoms they are scattered from so atoms with higher atomic number will give more backscattering. Hence the brighter an area is on a backscattered SEM image the higher the relative atomic number compared to the rest of the image. It is the secondary electrons (electrons that are emitted from the atoms, when the incident electron beam hits the sample) that gives SEM pictures their depth. Areas with holes or edges will have fewer secondary electrons that reach the detector compared to raised areas. Therefore holes or edges will look darker compared to raised areas.

Scanning electron microscopy needs high vacuum so the electron beam is not scattered before hitting the sample and the secondary- and back scattered electrons are not scattered before hitting the detector. Furthermore the sample needs to be electronically conducting to avoid charge accumulation on the surface of the sample. If the sample is not conducting by itself it can be coated with different metals, *e.g.* platinum or gold, to become conducting. In this project all the samples were electronic conducting so no additional sample preparation was necessary prior to the scan. The samples were cut into pieces of approximately 1 $cm^2$ and fastened to the sample holder with carbon tape.

## 3.5 Porosity determination

The porosity of the gas diffusion layer is another important characteristic and it was determined on a Micromeritic AccuPyc 1330 gas pycnometer. The sample size was approximately 0.3 $cm^3$. First, the geometric volume of the sample was found by measuring the sample dimensions. In the pycnometer the true volume was found by filling the sample chamber with a gas (helium) to a pre-set pressure and afterwards expanding the gas over into a second empty chamber calculating the sample volume from the pressure in the second chamber. The pycnometer gives an average of the sample density from 5 measurements.

When the geometric volume and the true sample volume are known, the porosity can be calculated as the difference between these according to equation (3-3).

$$\text{Porosity} = \frac{V_{geometric} - V_{true}}{V_{geometric}} \quad (3\text{-}3)$$

## 3.6 Resistance measurements

Resistance measurements were performed on the gas diffusion layers to see whether the contact and bulk resistance were below the maximum limit (10 $m\Omega \cdot cm^2$ [191]) proposed by DOE for fuel cell GDLs and bipolar plates. The measurements were done on an in-house built setup consisting of a power supply providing a direct current, and a multi-meter (Keithley 175 Autorange Multimeter) to measure the voltage at a given current, a vertical hand screw to apply pressure to the samples, a strain gauge (Nordic Transducer MD1010R) to measure the applied force and an in-house build PTFE holder to keep the sample specimen in place.

The measurements were done at room temperature using a typical four point setup (two points for applying the current and two points for measuring the voltage). The force used during measurements was between 0.1 and 3.0 MPa, the force was raised in increments of 0.1 MPa. A direct current of 100 mA was applied to the sample and the voltage was recorded at peak force. The samples were cut into 1 $cm^2$ pieces and sandwiched between two pieces of rectangular (1.5 x 4 cm) tantalum foil (0.3 mm thick, 99.9% Goodfellow). Prior to measurement the surfaces of the tantalum foils and the sample were cleaned by rinsing with ethanol. The two tantalum foils were laid perpendicular to each other with the 1 $cm^2$ sample sandwiched between them giving a contact area of 1 $cm^2$. The tantalum foils and the sample were kept in place by the in-house made PTFE holder. Spacers made from PTFE were used to keep the foils electrically insulated from the pressure system. Figure 3.1 shows an exploded view of the sample holder and setup. A photograph of the entire resistance setup is shown in figure 3.2.

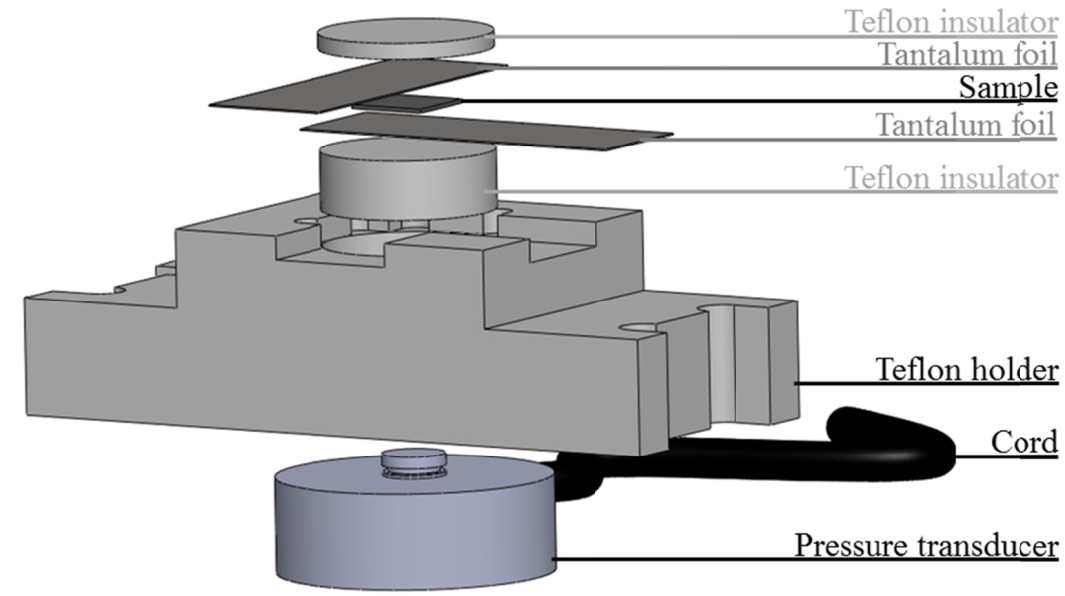


**Figure 3.1: Exploded view of the resistance measurement setup.**

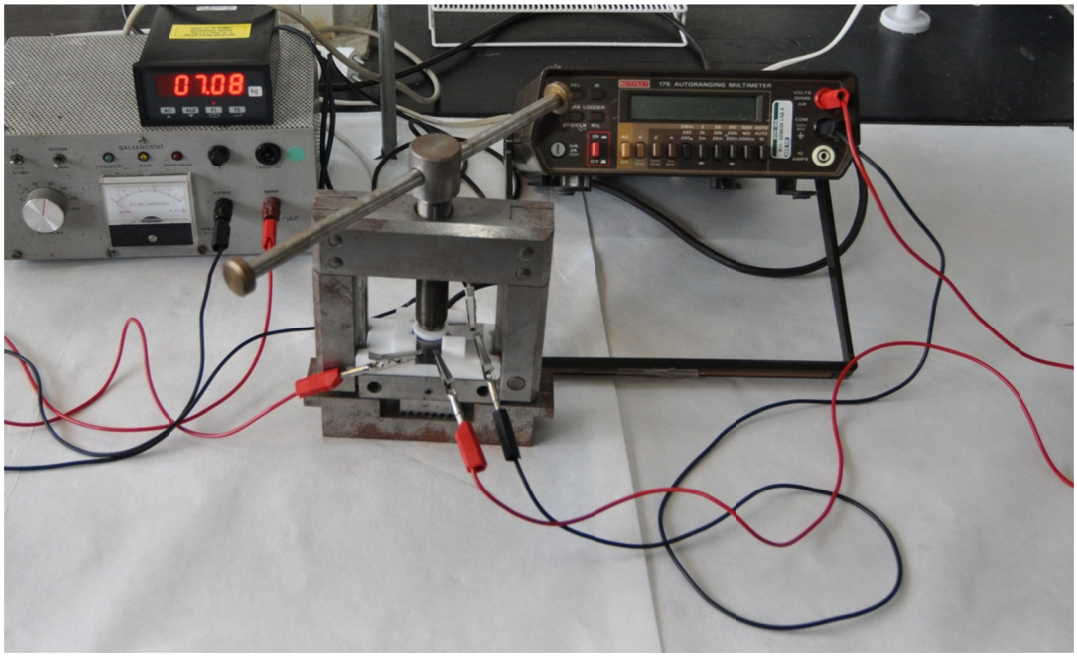

**Figure 3.2: Photograph of the resistance setup.**

## 3.7 Mechanical strength of membranes

The mechanical properties of the membranes were measured using a modified Testometric Micro 350 machine. The samples were heated in a metallic chamber that enclosed the membrane sample and the holders that were used to fix the membrane sample. The membrane samples were shaped as a 'dog-bone' and prepared by stamping using a punch die and a hydraulic press. The length and width of the sample were 30 mm and 2 mm respectively. The data was recorded as stress-strain curves measuring the force required to obtain a fixed strain from elongation of the sample. The elongation rate was 10.00 $mm \cdot min^{-1}$, giving a stress rate of 3.33 $min^{-1}$.

The tensile stress ($\sigma$) and the tensile strain ($\varepsilon$) were calculated from the stress-strain data. The tensile stress was calculated using equation (3-4) [192].

$$\sigma = \frac{F}{A} \tag{3-4}$$

F is the measured force and A is the cross sectional area of the sample.

The tensile elongation was calculated using equation (3-5).

$$\varepsilon = \frac{\Delta L}{L^0} \cdot 100\ \% \tag{3-5}$$

Where $\Delta L$ and $L^0$ are the dimensional change in sample length and initial sample length respectively.

Young's modulus (E) is defined as the initial slope of the stress-strain curve and can hence be calculated using equation (3-6).

$$E = \frac{\sigma}{\varepsilon} \tag{3-6}$$

Young's modulus provides information about the material's resistance to deformation and is a commonly used quantity for characterising materials' strength.

Each membrane type was tested 4-5 times and it is the average values with standard deviation which are reported.

## 3.8 Electrode preparation

The anodes were made individually for each MEA. The electrodes either had a geometric area of 10 or 11.6 $cm^2$, hence they were in some cases a bit bigger than the flow area (10 $cm^2$). This was done deliberately to avoid mechanical failure of the membrane due to stress coming from the reactant flow if the MEA was not aligned perfectly. During the initial experiments this problem with alignment, was observed and hence the choice of slightly larger electrodes resulted. To calculate the current density the geometric area of the anode was used, even though it is possible that in the case of 11.6 $cm^2$ parts were not fully accessible (Further discussion of the subject can be found in chapter 8). The ink was manually air sprayed directly onto the GDL which was kept at 130 °C. The spraying procedure was optimised (stepwise spraying, keeping the GDL as dry as possible) to prevent the ink from deep penetrating into the GDL. The ink consisted of $IrO_2$ (made either in a thermolysis process, and provided from Norwegian University of Science and Technology (NTNU) or made in-house by the Adams Fusion method, as described in section 3.1), an ionomer binder (Aquivion™ D83-06A, Solvay Solexis or Nafion® D521 Dispersion, DuPont™) and 2-propanol (puriss, Riedel de Häen) or ethanol (96 Vol%, KEMETYL) as dispergent. The weight ratio between $IrO_2$ and the 2-propanol (or ethanol) was kept constant *i.e.* there was approximately 100 times more 2-propanol than $IrO_2$. After spraying the catalyst onto the GDL the anode was doped with a solution consisting of 1.5 wt.% aqueous PA and glacial acetic acid in a 1:1 weight ratio. Later it was found that this ratio between aqueous PA and glacial acetic acid was too high and it was changed to PA:Glacial acetic acid 1:9 weight ratio, using more of this mixture to achieve the same PA post doping level (0.1-0.2 $mg \cdot cm^{-2}$), but with a better distribution over the electrode area. The loadings of $IrO_2$ were between 1.0 and 3.5 $mg \cdot cm^{-2}$ and the ionomer binder content was varied between 5 and 30 wt.%. In some case the anode was of the CCM type. In these

cases the catalyst layer was sprayed onto a piece of PTFE, which was kept at 130 °C using a metal template to ensure the correct electrode area during the manual air spraying. Afterwards the electrode was doped in the same way as the GDE and transferred to the membrane using the decal method of hot pressing it onto the membrane.

The cathodes were prepared in large sheets with a typical area of 600 $cm^2$. The ink was manually air sprayed onto the pre-treated non-woven carbon cloth at 80-110 °C in steps in order to avoid deep penetration of the ink into the GDL. The ink consisted of an in-house made 40 wt.% Pt/C catalyst, a Nafion® ionomer (D521 Dispersion DuPont™) and ethanol (96 Vol%, KEMETYL) as dispergent. The platinum loading was about 0.8 $mg \cdot cm^{-2}$ and the Nafion® ionomer loading about 0.3 $mg \cdot cm^{-2}$. The cathodes were punched out in to discs with a geometric area of 10 or 11.6 $cm^2$ using a hydraulic press.

## 3.9 Polarisation measurements

The electrolysis tests were performed at 130 °C under ambient pressure. Water was fed by a peristaltic pump (Alitea –XV), 0.25 $mL \cdot min^{-1}$ (approximately double the consumption of water at 20 A), through an evaporator at 180 °C. Water from the exit hydrogen flow was collected in a condenser flask at 5°C and the remaining flow of hydrogen was monitored by mass flow meter (Brooks 4800 Series). The cell was powered by an in-house made current source.
The cell was heated to the operating temperature before steam was supplied to the cell in order to avoid condensation of water in the cell. To achieve steady state behaviour an upstart period of 20 minutes was applied. Measurements for the polarisation data were then done by current step potentiometry with the steady state voltage recorded 10 minutes after each current was set.

# 4 Electrolysis setup

In this project, electrolysis was performed on two different systems: One was operated in steam mode, *i.e.* 130 °C and atmospheric pressure; and the other could be pressurised so that water would be kept in its liquid form even at elevated temperatures. As part of this project, the construction of both the steam and pressurised electrolysis setups were carried out. However, the pressurised setup was completed so late that only a few measurements were performed on it. Most of the pressurised measurements were performed on a similar setup (which inspired the design of the pressurised setup at DTU) at Department of Inorganic Technology at Institute of Chemical Technology Prague (ICTP).

## 4.1 Steam setup

The steam electrolysis setup was fairly simply, consisting of an in-house made power supply, an in-house made temperature controller, an in-house made data collection box, a peristaltic pump (Alitea – XV) equipped with a medical grade polyvinyl chloride (PVC) tubing with an inner diameter of 1.42 $mm^2$ (Mikrolab), two mass flow meters (Brooks 4800 series), two in-house constructed condensation units, two 225 W heating rods (RS Components), two type K thermocouples, an in-house made evaporator and an in-house made electrolysis cell. In figure 4.1 a schematic overview of the steam electrolysis setup is shown. In the schematic overview the connections between the different units are indicated. The pipes used in the setup are all of the 316L stainless steel type and all the fittings were 316L Swagelok® fittings.

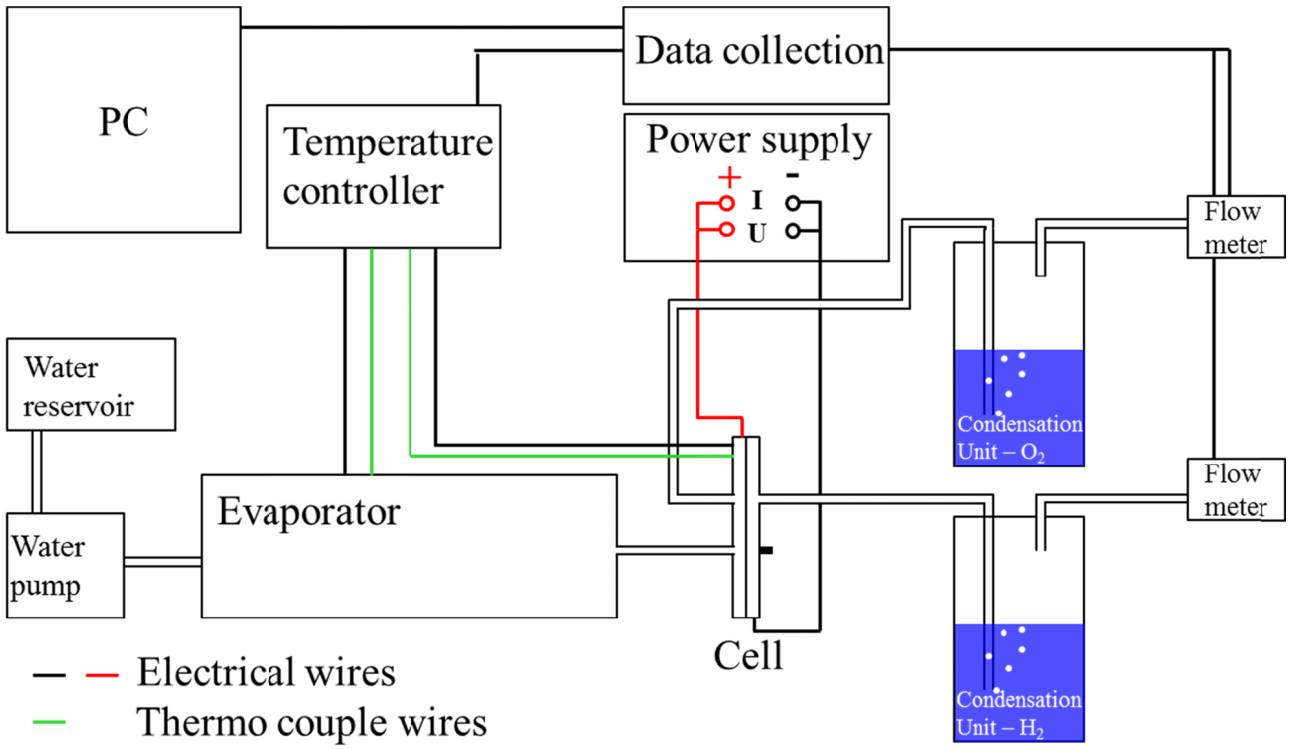


**Figure 4.1: Schematic overview of the steam electrolysis setup.**

The power supply could only control the current and provide currents of up to 20 A *i.e.* 1.72 $A \cdot cm^{-2}$ (using 11.6 $cm^2$ electrodes) in this setup. The power supply could be controlled both manually via a knob on the front panel, or remotely via the in-house coded software. The power supply was connected to the cell with four wires, meaning that the cell was operated in a typical four point setup. Two of the wires were used for supplying the current to the cell, and the other two were used to measure the cell voltage.

The temperature controller box was constructed to manage two electrolysis setups. Hence, it had four individual temperature controllers (CAL9400). In each setup the cell temperature and the temperature of the evaporator were controlled. The electrolysis cell was heated by two 225 W heating rods (one in each end plate) and controlled by one type K thermocouple in one of the end plates. The evaporator was heated using a 208 W heating tape from HTS/Amptek® and a type K thermocouple to measure the temperature.

The data collection box was connected to the power supply, the temperature controller box, the two flow meters and a computer as illustrated in figure 4.1. The current, voltage, temperature and hydrogen and oxygen flow were saved as function of time.

The peristaltic pump was connected to the evaporator via the PVC tubing. The PVC tube was placed on a small capillary pipe which was connected to the evaporator in two different configurations which will be described below. The other end of the PVC tubing was simply put into a glass beaker full of demineralised water which acted as a water reservoir.

Two different versions of the evaporator were tested. Both versions were inspired by the evaporator design used by Ph.D. student Anton Vassiliev (DTU Energy Conversion). Both designs consisted of a 250 mm long 316L stainless steel pipe with an outer diameter of 19 mm. On the outside of the pipe the type K thermocouple was fixed with heat resistant aluminium tape. The heating tape was coiled around the steel pipe with the thermocouple between it and the pipe. In each end was a Swagelok® fitting and a copper ring was used as sealing. The pipe was filled with stainless steel balls to get a better transfer of energy from the pipe to the water. The difference between the two versions was in how the water was led into the big steel pipe through the capillary piping.

In the first version the capillary pipe was just fixed in the Swagelok® fitting so the water entered the evaporator in droplets onto the inner walls of the pipe and on the steel balls. In the second version of the evaporator the capillary tube was going through the fitting and approximately 50 mm into the steel balls. The reason for this change in evaporator design was that the first design did not give a steady continuous supply of steam. The water droplets came out of the capillary tubing placed in the fitting and hit the pipe wall and the balls. This gave pulses in the steam supply corresponding to the pump speed. In the second design the water was heated/evaporated already while it still was in the capillary tube (since the capillary tube was heated to the same temperature as the rest of the evaporator). This gave a much steadier supply of steam at the same pump speed, and overall also made the temperature of the evaporator more stable. Both evaporator types were insulated by vermiculite. A block of vermiculite was drilled through so the evaporator could lie inside. The ends of the insulation block

were also made from vermiculite with holes to let the pipe to the cell and the capillary tube to the pump through. Figure 4.2 is a schematic illustration of the two evaporator concepts.

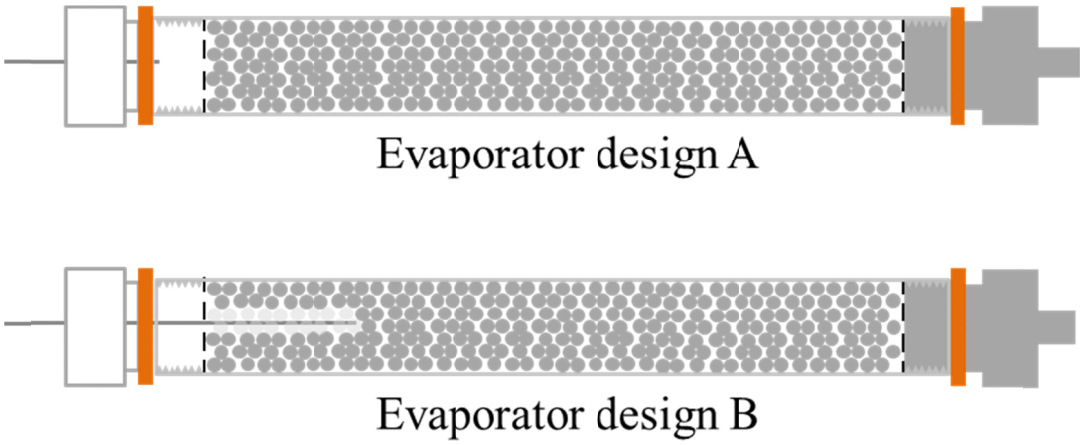


**Figure 4.2: The two evaporator designs tested. Design A is without the longer capillary tube. Design B is with the longer capillary tube.**

As seen in figure 4.1 there were the two mass flow meters connected to the system after the gas had passed through the condensation units. The condensation unit was an in-house made glass bottle equipped with a cooling spiral through which cooled water (5 °C) was circulated. This glass bottle was approximately half-filled with demineralised water. A cooling system was designed for this purpose. A 50 L isolated container was equipped with a cooler (Haake EK12 unit) and a circulation pump. Cooled water was circulated to the four systems built. Each system had its own connection. The cooled water was first let into the condensation unit on the anode side. The outlet from the anode side was connected to the inlet on the cathode side of the condensation unit. Finally, the outlet from the cathode condensation unit was connected back to the 50 L reservoir where the water was cooled down to 5 °C again. Each condensation unit could be emptied without disconnecting it from the cooling system. The gas from the electrolysis cell was led through the chilled water in the condensation unit after which the gas, now with a fixed very low water content, was led through the mass flow meter.

The electrolysis cell consisted, as shortly described in section 2.4, of two end plates and two flow plates. The end plates were constructed out of aluminium with two holes in the edge, one for the heating rod and one for the thermocouple. Through the end plates were ten holes, eight for the bolts

that were used for cell assembly and two for the in- and outlets. The in- and out-lets were fitted with Swagelok® fittings, so they could be connected to the rest of the system. In figure 4.3 an exploded view of the electrolysis cell used for testing is depicted.

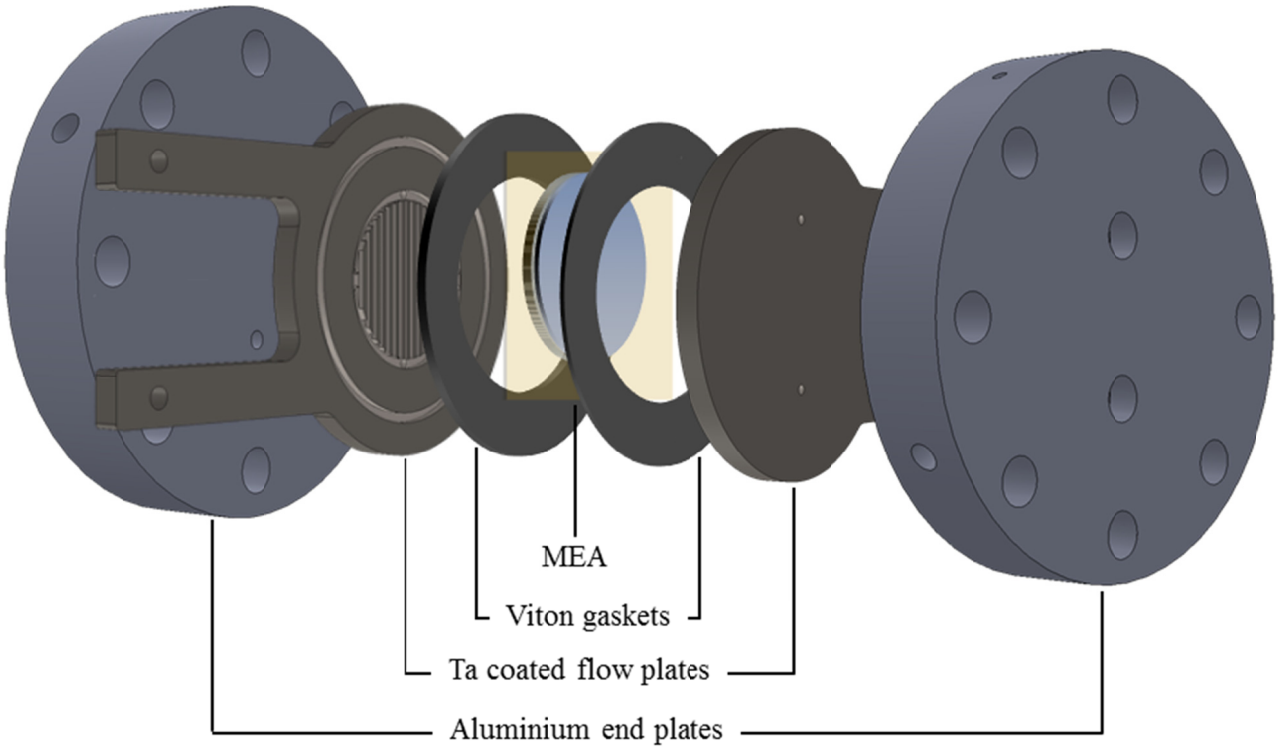


**Figure 4.3: Schematic exploded view of the electrolysis cell used for the experiments.**

The flow plate was fixed to the aluminium end-plate by Viton® (a fluoroelastomer, DuPont™). Since Viton® gets sticky when heated, it was possible to use it as an insulating adhesive between the plates. By heating the flow plate and end-plate with a shape cut sheet of Viton® in between under pressure it was possible to make the plates stick together. The temperature used was 135 °C, pressing it together using a total force of 2000 kg. The 'sandwich' was kept under pressure for 10-15 minutes, subsequently it was cooled down to room temperature while keeping the force at approximately 2000 kg. To keep the holes in the end-plate aligned with the in- and out-lets in the flow plate two guide pins were used. After it was cooled down the guide pins were carefully removed since the adhesion between the plates and the Viton® was not sufficiently sturdy until it had been used a couple of times in the electrolysis cell (where it in similar fashion is heated and cooled under pressure). The flow plates were machined from

316L stainless steel, in-house, on a computerised numerically controlled (CNC) milling machine. Before use in the electrolyse cell they were coated with tantalum in a chemical vapour deposition (CVD) process by Tantaline®. This coating is of the utmost importance since, the stainless steel in itself is not sufficiently corrosion resistant to withstand the harsh conditions. The flow plates were coated with a tantalum layer of approximately 50 μm.

Four different machined designs of the flow pattern on the flow plates were tested. Commonly for all four of them were that they had a 10 $cm^2$ (35.7 mm in diameter) round flow pattern area and that the in- and outlet holes were located in the top and bottom of the flow pattern. Figure 4.4 presents a schematic illustration of the four tested machined flow patterns. The reason for the flow pattern being round was that it then would be easier, later on, to pressurise the system since O-rings could be used for sealing.

The first flow pattern tested was flow pattern A which has a waffle pattern with flow channels going both horizontally and vertically. The width and depth of the channels were 2 mm. This flow pattern was not optimal neither when it came to distributing the reactant (steam) flow or distributing the force from the flow plate to the MEA. The next flow pattern tested was pattern B, which had an asymmetric spiral shape. It was inspired by the traditional serpentine flow pattern used in square fuel cells which ensure that the reactant is distributed to the entire electrode area. Furthermore it was found that it gave a better force distribution to the MEA with less sharp corners. The width and the depth of the flow channel were also in this case 2 mm. Some drawbacks with the spiral pattern were that it gave a very long flow channel compared to the other flow designs. Also, the geometry was more complicated to machine. The two last flow patterns (patterns C and D) were designed with parallel vertical flow channels. They both had an outer distribution channel around the perimeter of the flow area with a width of 2 mm and a depth of 1.5 mm. At the horizontal mid axis of the flow patterns the depth of the distribution channel was changed to 0.2 mm. This was done to avoid that the gases predominantly were running from the inlet to the outlet in the distribution channel. However, having shallow passages allow small gas volumes to pass, hence avoiding places with stagnant flow.

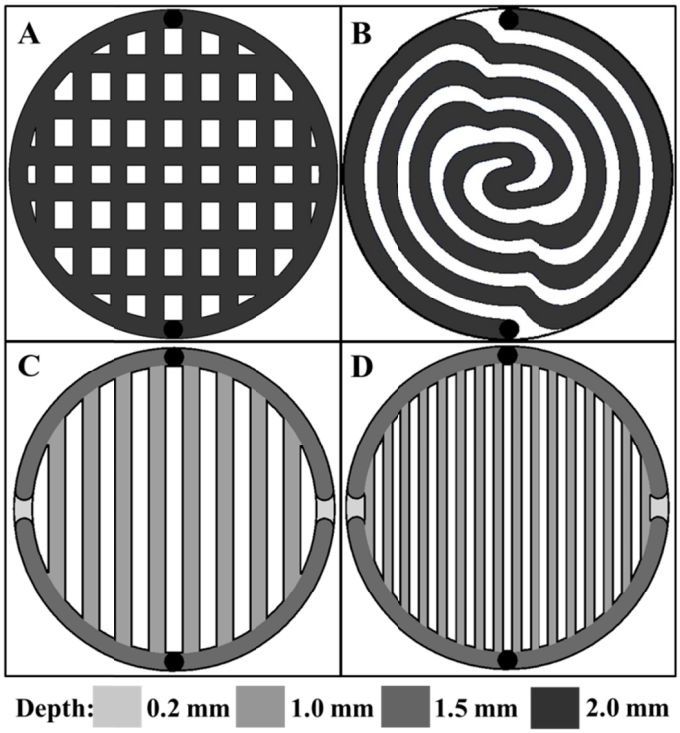


**Figure 4.4: Schematic illustrations of the four tested machined flow patterns. In- and out let are marked with black in the top and bottom perimeter of the flow pattern. The land area (ribs) is white, while the channels are marked with different shades of grey corresponding to different channel depths. The diameters of all the flow patterns are 35.7 mm.**

The flow channels in both pattern C and D had a depth of 1 mm, but in flow pattern C the channel width was 2 mm, where it was 1 mm in flow pattern D. In table 4.1 the physical characteristics of the four different flow patterns tested during this work is summarised.

**Figure 4.5: Photograph of the four machined flow patterns. The diameter on all the flow areas is 35.7 mm. ©fagpress**

Figure 4.5 shows a photograph of the four tested machined flow patterns. On the flow plates can also be seen the holes through which bolts are used to fix wires for current supply and voltage reading.

**Table 4.1: Summary of the physical characteristics of the different machined flow patterns**

| | | Channel dimension [mm] | | | Land [mm] | Area [$mm^2$] | |
|---|---|---|---|---|---|---|---|
| # | Flow design | Width | Depth | Max. Length | Width | Channel | Land |
| A | Waffle | 2 | 2 | 34 | 2 | 763 | 232 |
| B | Asym. Spiral | 2 | 2 | ~290 | 2 | 608 | 387 |
| C | Straight | 2 | 1 | 34 | 2 | 594 | 401 |
| D | Straight | 1 | 1 | 34 | 1 | 593 | 402 |

## 4.2 Pressurised setup

The pressurised system designed here at DTU was in many aspects similar to the steam electrolysis setup. Following hardware in the pressurised system was identical to the steam electrolysis setup, power supply, temperature controller, data collection unit, mass flow meters, heating rods, evaporator (although it in this configuration is functioning as a water heater, since pressure was kept sufficiently high to keep the water in the liquid phase), thermocouples and condensation units.

New for the pressurised electrolysis setup was the addition of two pressure tanks (Swagelok®, 1 L 304L stainless steel with inner PTFE coating), two back pressure valves (Brooks SLA5820A), a Fluid-o-tech magnetic gear pump (MG204XPB17) with a 316L stainless steel housing and poly(etheretherkethone) (PEEK) as the material for the gear. Furthermore, the pressurised electrolysis setup needed a controller box (Brooks Model 0154 Read Out & Control unit) to control the two back pressure valves and a power supply to power the pump (in-house made with manually voltage control *i.e.* control of the pump flow). In figure 4.6 a schematic illustration of the pressurised part of the electrolysis setup is shown. The electrolysis cell and the water heater were connected in the same way to the rest of the electrolysis hardware as illustrated in figure 4.1. For clarification this part is omitted in figure 4.6.

The pressurised system was built so the anode pressure tank also acted as a water reservoir for the electrolysis cell. The tank could contain 1 L of demineralised water. This amount of water would make

it possible to electrolyse for approximately 148 hours at the maximum possible current in this system, 20 A, assuming that no water is lost from the anode side, *e.g.* via the produced oxygen. This assumption is probably not very likely. However the tank should contain enough water to electrolyse continuously for around 100 hours at reasonable current densities. As it can be seen on from figure 4.6 and figure 4.7, the anodic pressurised tank was connected with a clear tube of polysulfone (PSU) (drilled through from a solid rod of PSU) allowing visual determination of the water level inside the pressurised tank.

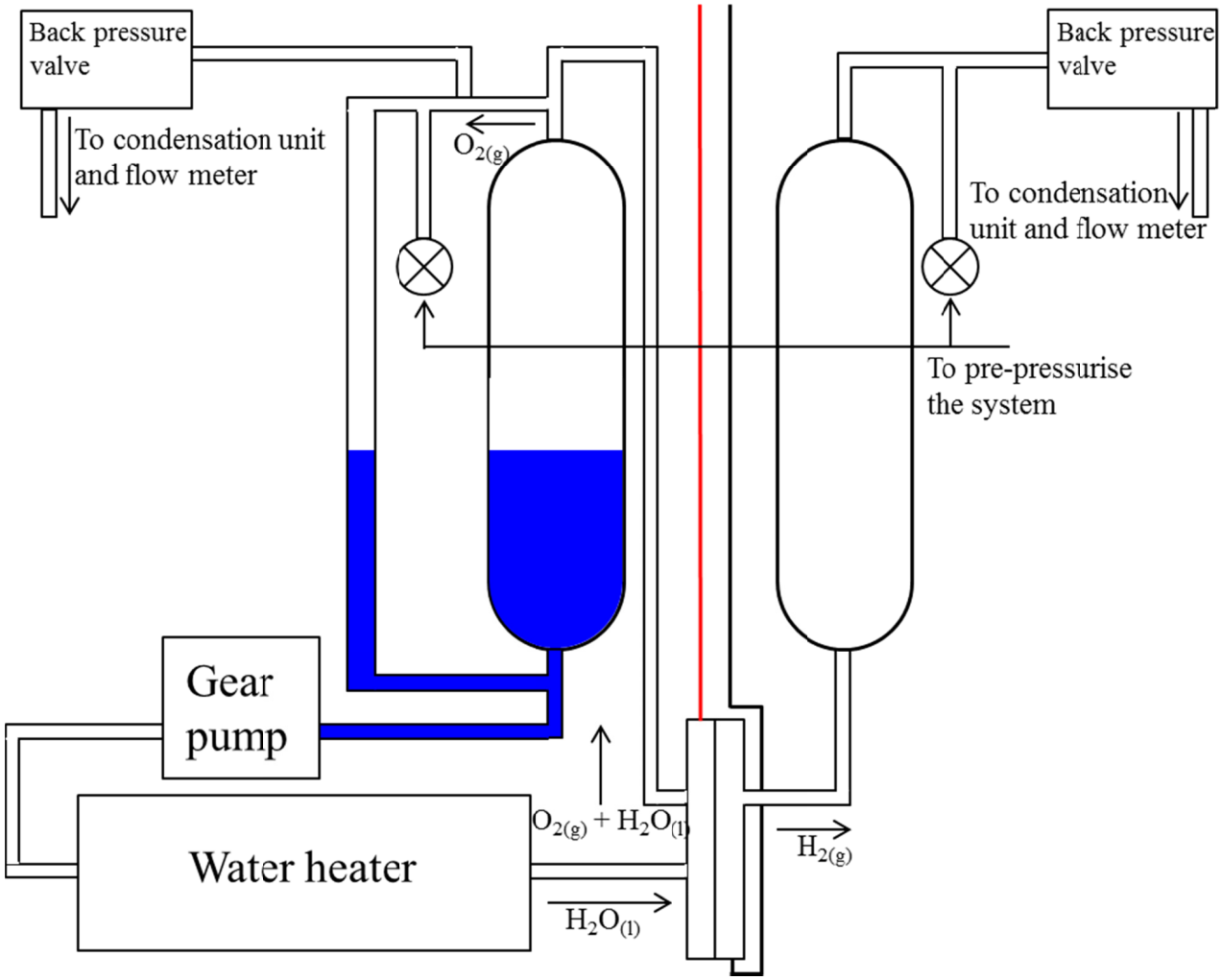


**Figure 4.6: Schematic illustration of the pressurised electrolysis setup.**

On the anode side the feed water was pumped into the electrolysis cell after being heated in the water heater. The produced oxygen and the over-stoichiometry water fed to the cell were separated in the

pressurised tank on the anode side. The water/oxygen mixture was led into the pressure tank through a drilled-through Swagelok® T-fitting in a 6 mm stainless steel tube. In the pressurised tank the water returned to the reservoir and the oxygen bubbled up towards to the T-fitting and out to the back pressure valve. In figure 4.8 a schematic illustration of the in- and out-let connections of both the anodic and cathodic pressure tanks is shown. On the cathode side only small amounts of water were expected (coming from the water drag through the membrane, during electrolysis). The produced hydrogen and the water were led into the cathodic pressure tank by the pressure from the evolved hydrogen.


**Figure 4.7: Photograph of the pressurised electrolysis system. ©fagpress**

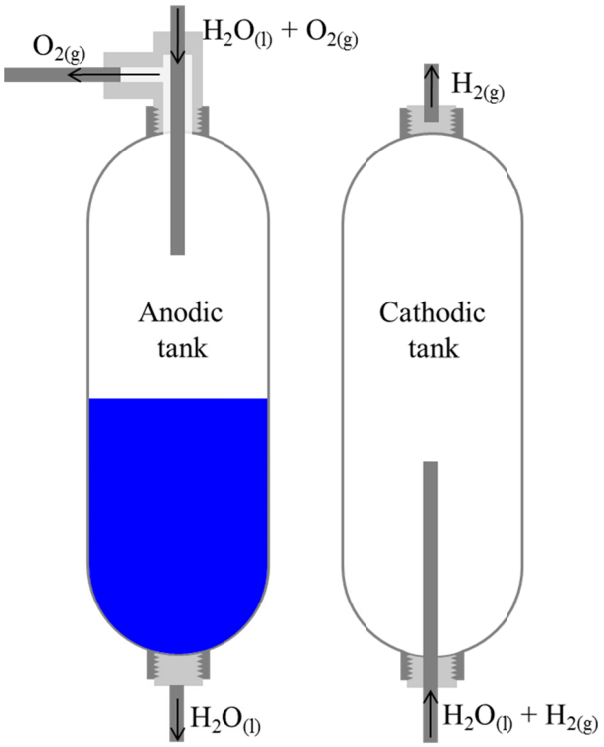


**Figure 4.8: Schematic close-up illustration of the pressurised tanks in the pressurised electrolysis setup. Illustrating in- and outlet to the tanks.**

In the middle of the cathodic tank the water and the hydrogen were separated. The hydrogen rose to the top of the tank where it went through the outlet tube to the back pressure valve. The water collected in the bottom of the tank, and had to be emptied after the completion of each electrolysis test. After the back pressure valves, the oxygen and hydrogen on the anode and cathode side, respectively, went through the condensation units, like in the steam electrolysis setup before the flow rates were measured by the mass flow meters.

As mentioned in the beginning of this chapter, the pressurised setup was finished so late in the Ph.D. study that only very few experiments were carried out on it. The pressurised measurements presented in this thesis were done on the setup shown in figure 4.9. The ICTP pressurised setup was very similar to the constructed DTU pressurised setup. The biggest difference between the two systems was that at DTU electronic back pressure valves were used while it at ICTP were manually controlled valves. Also at ICTP PTFE tubing was used to connect the different parts of the electrolyser setup, this limited the

working temperature and pressure to 120 °C and 3 bar total pressure. Finally at ICTP a large diaphragm pump (ProCam DS 15/72) was used.

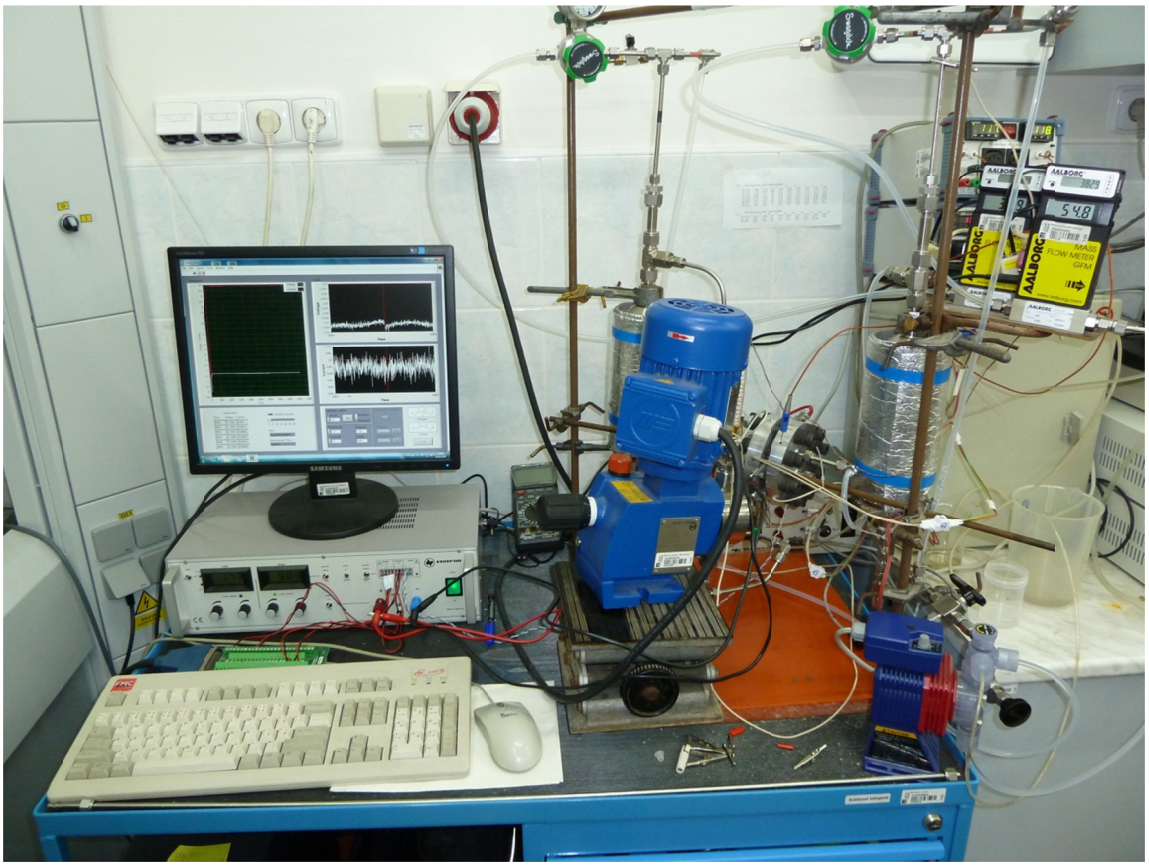


**Figure 4.9: Pressurised electrolysis setup at ICTP equipped with the round DTU electrolysis cell.**

The fittings and the PSU tube in the DTU pressurised setup were chosen to be able to stand elevated temperatures and pressures. The tanks were certified to 124 bar, however the back pressure valves were not certified to higher pressures than 10 bar. A pressure of 10 bar enables the heating of the water to approximately 175 °C, while still being in its liquid phase (see figure 4.10).

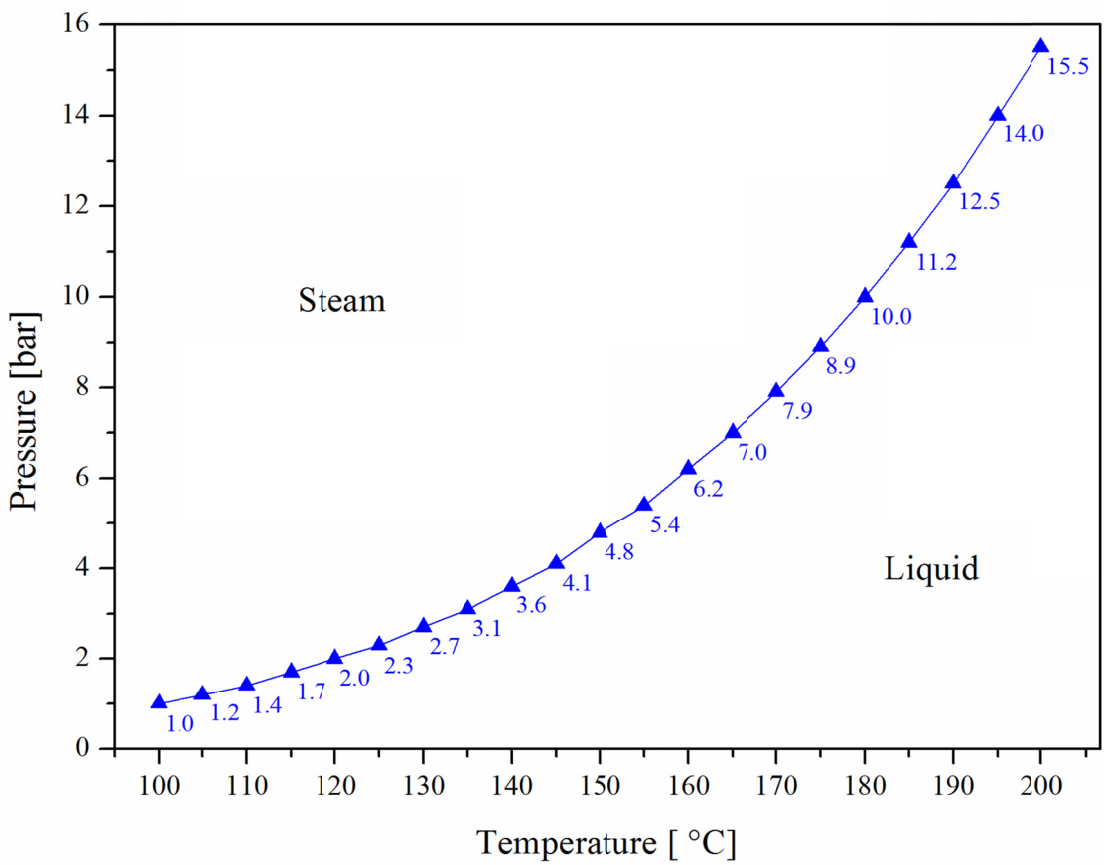


**Figure 4.10: Saturated water vapour pressure as function of temperature (calculated from Antoine equation [193], see Appendix 2).**

A more likely candidate to determine the maximum operating temperature in the system is the PEEK used as the gear in the gear pump. The manufacturer specify a working range for PEEK up to 120 °C, but this is for working against a pressure of 20 bar. Since the pump was not pumping up against a pressure, the temperature can probably be raised further for extended periods of time without the PEEK being too soft to transport water through the pump head. Temperatures of 130 °C, which is the temperature the steam electrolysis measurement were done at, should be easily achievable. However, whether or not it is possible raising the temperature to the 175 °C (which is the temperature that is limited by the back pressure valves) is still a matter of controversy.

# 5 Gas diffusion layers. Results and discussion

PEM electrolysis at elevated temperatures presents many design challenges. Beside the choice of an electrolyte membrane, the design of gas diffusion layer and the flow plates are challenges of critical importance to the overall performance of the cell. The GDL is a subject that has not only received a lot of attention in fuel cell applications, but also in electrolysis applications. When it comes to materials, titanium is the most common either as porous felt [35] or as sinter [9]. Grigoriev *et al.* [9] conducted a study to quantify the effect of the porosity of the GDL in water electrolysis. Another important property for the GDL is the contact resistance between it and the bipolar plate (BPP). Zhang *et al.* [39] reported that up to 59% of the total power loss in a PEM fuel cell can be attributed to the contact resistance between GDL and BPP. This seems as a quite high percentage, however it is seem believable that the contact resistance also contributes significantly to the total power loss for an electrolysis cell. Further research effort has been put into describing this phenomenon [40].

The use of titanium in this work was not possible. Previous work [36] within the group has revealed that titanium has a very high corrosion rate in an environment similar to the conditions used during electrolysis in this work. The corrosion phenomenon was examined in 85 wt.% phosphoric acid at 120 °C and potentials up to 1.1 V *vs.* SHE. The corrosion current for titanium was found to be 6.3 mA, which corresponds approximately to a corrosion rate of 73 $mm \cdot year^{-1}$ as calculated using Faraday's Law. The corrosion rate for tantalum was by comparison much lower. It was found that tantalum had a corrosion current of $6.3 \cdot 10^{-5}$ mA which gives a corrosion rate of under $1 \cdot 10^{-3}$ $mm \cdot year^{-1}$ [36]. The work done within the group was further confirmed by Kouril *et al.* [37] who found similar extremely low corrosion rates for tantalum of less than $1 \cdot 10^{-2}$ $mm \cdot year^{-1}$. This very low corrosion rate was determined at temperatures up to 150 °C in 85 wt.% PA and at potentials as high as 2.27 V *vs.* SHE [37].

The excellent corrosion resistance of tantalum in aggressive acidic media is due to its protective oxide surface layer, $Ta_2O_5$, which is naturally formed on the surface as a very thin layer (3 nm [38]). However such an oxide layer has a relatively low electronic conductivity, hence the performance of the tantalum coated cell components may be dramatically reduced if too thick an oxide layer is formed

For the aim of a better performance and longer durability especially for high temperature operation, tantalum was selected as a coating material for both the flow pattern and gas diffusion layers in this study. The tantalum film has strong adherent ability to many metal substrates. Moreover, tantalum has a lower electrical resistivity (12.2 μΩ·cm, at 273 K) [54] than titanium (39 μΩ·cm, at 273 K) [54]. In short, the excellent corrosion resistance, formation of dense and adherent oxide films and lower electrical resistivity make tantalum a promising material for anode applications in PEM electrolysers at elevated temperatures. The main barrier for using tantalum in this connection is the high cost of the metal.

To reduce the tantalum cost, a thin and dense tantalum surface coating was prepared on both GDL and flow plates in the present work. The tantalum coating procedure was done by chemical vapour deposition (CVD). CVD can be defined as the deposition of a solid on a heated surface from a chemical reaction in the vapour phase [194]. The solid that is deposited on the substrate (the heated surface) comes from the precursor. The precursor can be many different gaseous species at the reaction temperature, often in the case of general CVD it is a halide of the wanted metal. In the case of tantalum-CVD the most common precursor is $TaCl_5$ [195], which have a boiling point of 242 °C [196]. The precursor is carried to the substrate by a carrier gas. The carrier gas can be either inert or reactive. If the carrier gas is reactive, it will take part in the chemical reaction which facilitates the deposition [196]. An example of a reactive carrier gas is $H_2$, which in the case of tantalum-CVD reduces the $Ta^{5+}$ to $Ta_{(S)}$. Often it is most beneficial if the reactive carrier gas does not react with the precursor until the precursor is adsorbed to the substrate, otherwise nucleation of the solid can give rise to defects and poor adhesion to the substrate. This can be minimised by controlling the pressure (low pressure will lower the risk of gas phase reactions) [196].

Some of the advantages using CVD as opposed to *e.g.* physical vapour deposition (PVD) techniques are: CVD is not restricted to line-of-sight coatings [194] – that means that even advanced geometries can be coated and CVD often has a high deposition rate compared to PVD [194]. CVD like any other technique also has some disadvantages, some of them are: CVD often requires high temperatures –

which can restrict choice of substrates and CVD often use hazardous and toxic precursors, which also gives rise to similar hazardous and toxic by-products [194].

## 5.1 Porosity results GDLs

Two different types of felt were tested. The first was a single layer type of felt which had the same fibre thickness (8 μm or 12 μm) throughout the whole felt. The other felt type was a double layer type which consisted of one half with thin steel fibres (8 μm) and the other half with 12 μm thick fibres. The single layer felt was tested in two different overall thicknesses – 0.2 mm and 0.5 mm, whereas the double layer felt only was tested with an overall thickness of 0.5 mm. Moreover, the felts were CVD coated with tantalum in different batches. Two batches were examined in detail, they were named batch 1 and 2. Batch 1 had a higher degree of tantalum coating and rougher surface with a sort of dendrite structure on the surface of the individual fibres, whereas batch 2 had a thinner and smoother tantalum coating (see figure 5.2).

The porosity of the felts was calculated by taking into consideration the pycnometer result for the 'true' volume; and the apparent volume as determined by a simple geometric calculation: See equation (3-3). The pristine stainless steel felt had a porosity of 82 %, which was in agreement with the information from the supplier. Data used for the porosity calculations and corresponding porosities for a few selected sheets can be seen in table 5.1.

**Table 5.1: GDL porosity calculated from pycnometer data.**

| | Stainless steel felt | Tantalum coated stainless steel felt | | |
|---|---|---|---|---|
| | Pristine | Batch 1 | | Batch 2 |
| Nominal thickness | 0.5 mm | 0.2 mm | 0.5 mm | 0.5 mm |
| Length [mm] | 35.5 | 32.7 | 39 | 35 |
| Width [mm] | 16.5 | 14.9 | 17 | 17 |
| Thickness [mm] | 0.5 | 0.28 | 0.5 | 0.5 |
| Volume geometric [$mm^3$] | 292.9 | 136.4 | 331.5 | 297.5 |
| Volume pycnometer [$mm^3$] | 52.3 | 91.1 | 183.1 | 82.1 |
| Porosity [%] | 82 | 33 | 45 | 72 |

After the tantalum coating of the stainless steel felt, the porosity decreased as expected, for both batches. The porosity of batch 1 was considerably lower with 33 % and 45 % for the 0.2 and 0.5 mm respectively, than for batch 2 which had a porosity of 72 %. Grigoriev *et al.* [9] reported that the

optimal porosity for a liquid electrolyser should be between 30 % and 50 %, though their experiments and calculations were done on sintered spherical titanium particles which pack in a more ordered way, whereas the felt has a very random order. This random order will undoubtedly have an influence on the pore sizes, which is another important parameter. The importance of the pore sizes is possibly of less importance in the case of steam electrolysis. Electrolysis using liquid water is more sensible to blockage of pores in GDL than steam electrolysis since the transport of steam is less restricted than liquid water.

It was found that there were quite large differences in the amount of tantalum coating from sheet to sheet within the same batch, and even across the same sheet (either 10 x 10 cm or 15 x 15 cm) considerable variation of the tantalum coating and hence the porosity could be measured.

Thick (0.5 mm) double layer felt and thin (0.2 mm) single layer felt coated with tantalum in batch 1 showed these kinds of variations. In table 5.2 the masses and standard deviations of pristine and tantalum coated felt discs (11.6 $cm^2$), both of the single- and double layer felt types with 0.2 mm and 0.5 mm thicknesses, respectively, are summarised. Each column represents a unique sheet of felt. Furthermore the standard deviation is in each case divided by the average mass, to give a percentage of deviation. The data series consists either of 4 or 9 sets of data corresponding to a 10 x 10 cm or a 15 x 15 cm sheet, respectively.

**Table 5.2: Masses of discs of different felt types: Pristine and coated with tantalum.**

| Felt type | S.L. | S.L. | | D.L. | |
|---|---|---|---|---|---|
| Batch | Pristine | 1 | 1 | 1 | 1 |
| Sheet # | A | B | C | D | E |
| Nominal thickness | 0.5 | 0.2 | 0.2 | 0.5 | 0.5 |
| Average mass [g] | 0.81 | 2.03 | 1.98 | 4.02 | 3.64 |
| Std. deviation [g] | 0.008 | 0.03 | 0.13 | 0.18 | 0.13 |
| Percentage [%] | 0.1 | 2 | 7 | 4 | 4 |

As it can be seen from table 5.2 the pristine felt is quite uniform, with a percentage-wise deviation in mass of approximately 0.1 %. By comparison the percentage-wise deviation in mass of the tantalum coated discs is in the range between 2 and 7 % on the same sheet. Comparing two different sheets of

felt of the same type and from the same batch gives an average mass difference of 0.38 g, *i.e.* up to approximately 10 % difference in mass for the discs used as anode GDL.

To investigate if the difference in porosity of the tantalum coated felt could be extracted from the average mass of the felt, the porosity was determined for three individual sheets of 0.2 mm single layer felt and 0.5 mm double layer felt. In table 5.3 the porosity and standard deviation values for the two felt types are listed.

**Table 5.3: Porosities of single- and double layer felt.**

| | D.L. | S.L. |
|---|---|---|
| Porosity [%] | 40 | 34 |
| Std. deviation [%] | 5 | 5 |

As it can be seen from table 5.2 and table 5.3 there is a reasonably good accordance between the percentage-wise mass deviation and the deviation in porosity.

## 5.2 Interfacial contact resistance results

High electronic conductivity of the GDL and BPP and good interfacial contact between these two are of utmost importance in order to achieve good performance [197]. In order to investigate whether the tantalum coated stainless steel felt can be used as a gas diffusion layer in an electrolysis cell, the resistance of the felt was measured. Figure 5.1 shows the resistance measured as a function of clamping pressure, the resistance was the sum of bulk resistance of the felt and the interfacial resistance between the coated felt (both sides) and tantalum foils mimicking the tantalum coated flow plates. For both batches of tantalum coated felts, varying coating amounts were tested. In batch 1, with a thicker tantalum coating, were both single- and double layer felts tested. From batch 2 was only tested a single layer felt. The resistance of three samples from each type were measured and the averages and the corresponding standard deviations for both batches and thicknesses are depicted in figure 5.1.

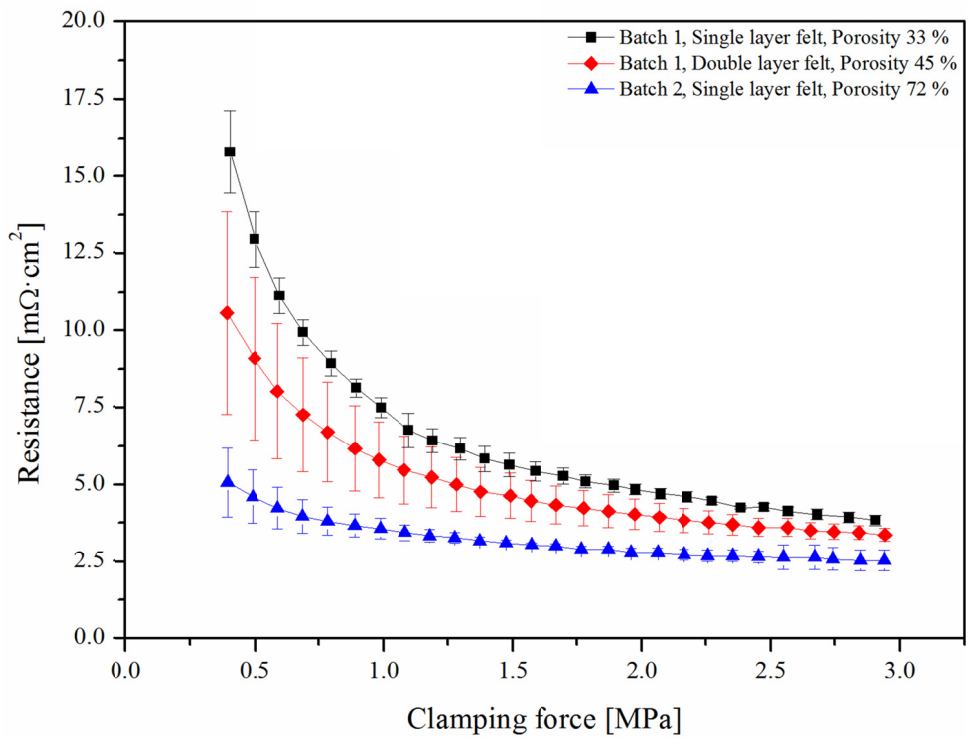


**Figure 5.1: Resistance as function of clamping force for tantalum coated stainless steel felt, measured at room temperature.**

From figure 5.1 it can be seen that the total resistance of the single layer felt, with the thinner tantalum coating (Batch 2), was lower than that for felts with the thicker coatings (Batch 1). This can be explained by the fact that the fibres with the thicker tantalum coating were stiffer and more rigid. Consequently, the higher total resistance of the thicker coated felt can be explained by a higher interfacial contact resistance since fewer felt fibres were in contact with the tantalum foils. As the clamping force was increased the resistance diminished as more fibres came into contact with the tantalum foil. The same can be observed for the two felts of different thickness from batch 1. Since the amount of tantalum deposited on the fibres in the 0.2 mm felt was larger the stiffness was greater and more force was required to get an equal number of fibres in contact with the tantalum foils. Hence the measured contact resistance can differ from samples which can be deformed, *e.g.* membranes, to follow the surface of the GDL.

At clamping forces above 2 MPa both batches of tantalum coated felt exhibited very low resistance in the 3-5 $m\Omega \cdot cm^2$ range. For comparison, DOE has proposed a limit of 10 $m\Omega \cdot cm^2$ for the bipolar plates including the contact resistance between GDL and BPP [191]. Hence the values for the resistance found in this work are below the DOE target. Thus, it was concluded that the naturally occurring oxide layer of $Ta_2O_5$, which gives tantalum its excellent corrosion resistance, was not hindering a sufficient electrical conductivity of the GDL. Tantalum coated felt was hence found suitable for use as GDL in acidic steam PEM electrolysis.

## 5.3 Scanning electron microscopy results

SEM images were acquired for pristine, and tantalum coated felt from both batches of CVD coating. These images are presented in figure 5.2.

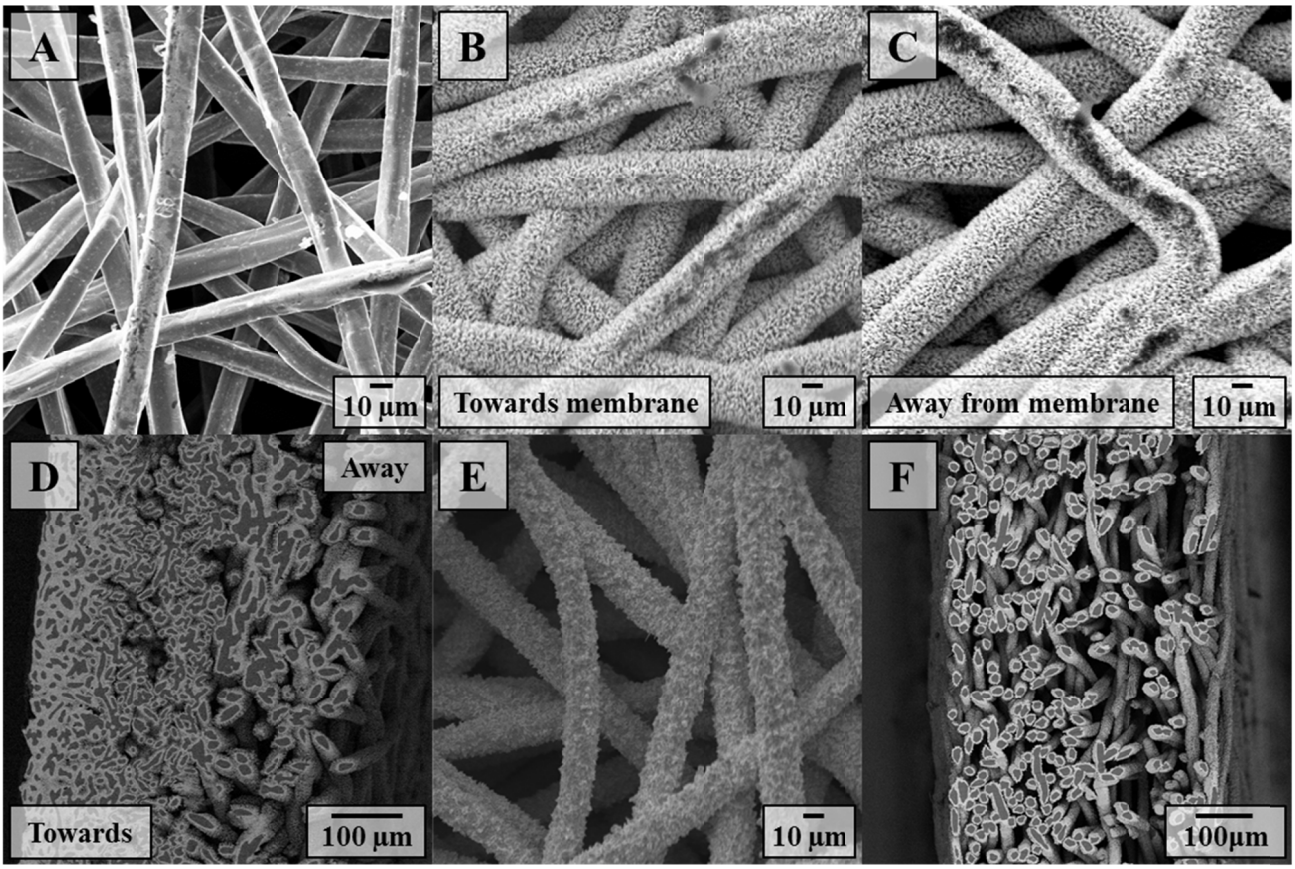


**Figure 5.2: SEM images of tantalum coated felt. A - Pristine felt, B-D – double layer felt from batch 1 and E-F – Single layer felt fra batch 2. All the felt 0.5 mm thick. Cross sections in D and F are made by ion-milling.**

The porosity data were clearly supported by the images. The felt with the thinner coating (batch 2, figure 5.2E and F) obviously had a much more open structure than the double layer felt with the thicker tantalum coating (batch 1, figure 5.2B-D). Similarities in both appearance and porosity can be observed between the thinly coated felt and the pristine stainless steel felt with a porosity of 72 % and 82 % respectively (see table 5.1). The porosity of the more dense structure of the thickly coated felt (batch 1) was 45 % (table 5.1). Another apparent difference between the two felt batches was the surface topology of the tantalum coating on the stainless steel fibres. This combination of the differences in porosity and surface topology can possibly have a significant influence on the penetration depth of the catalyst ink into the felt. It would be expected that the ink penetrated more deeply into the depicted single layer felt with the thinner tantalum coating (batch 2), since it had a more open structure. As observed from figure 5.2E the fibres of the single layer felt (batch 2, thinner coating) did also have a smoother surface than the double layer felt with the thicker coating (batch 1). Moreover, the combination of a more dense side (the individual fibres are closer together) and the rougher surface of the fibres (the dendrites) give rise to an increase in the number of contacts points between the GDL and the membrane and the GDL and the BPP/flow plate which results in a lower interfacial contact resistance.

Further on, an attempt was also made to smoothen the surface of the tantalum coated felt discs used for anodes GDLs by roll milling before spraying the catalyst ink onto them. This of course had an influence on the porosity of the felt depending on how much the felt was compressed in an attempt to flatten it. By compressing a piece of tantalum coated felt from approximately 0.29 mm to 0.24 mm the porosity of the felt decreased from 30 % to 16 %. This change in porosity can also be observed on cross section SEM images of a piece of felt before and after roll milling in figure 5.3.

In figure 5.3 the cross sections and top views of the felt before roll milling (image A and B respectively) and the same felt after roll milling (C and D respectively) are depicted. By comparing images A and C in figure 5.3 it can be noticed that the fibres in the felt are more densely packed corresponding with the measured porosity. However roll milling also had an effect on the surface characteristics of the tantalum coating of the individual fibres. In images B and D it can be seen that the

dendrites on the fibre surface gets flattened where the rolls in the roll mill have been in contact with the felt.

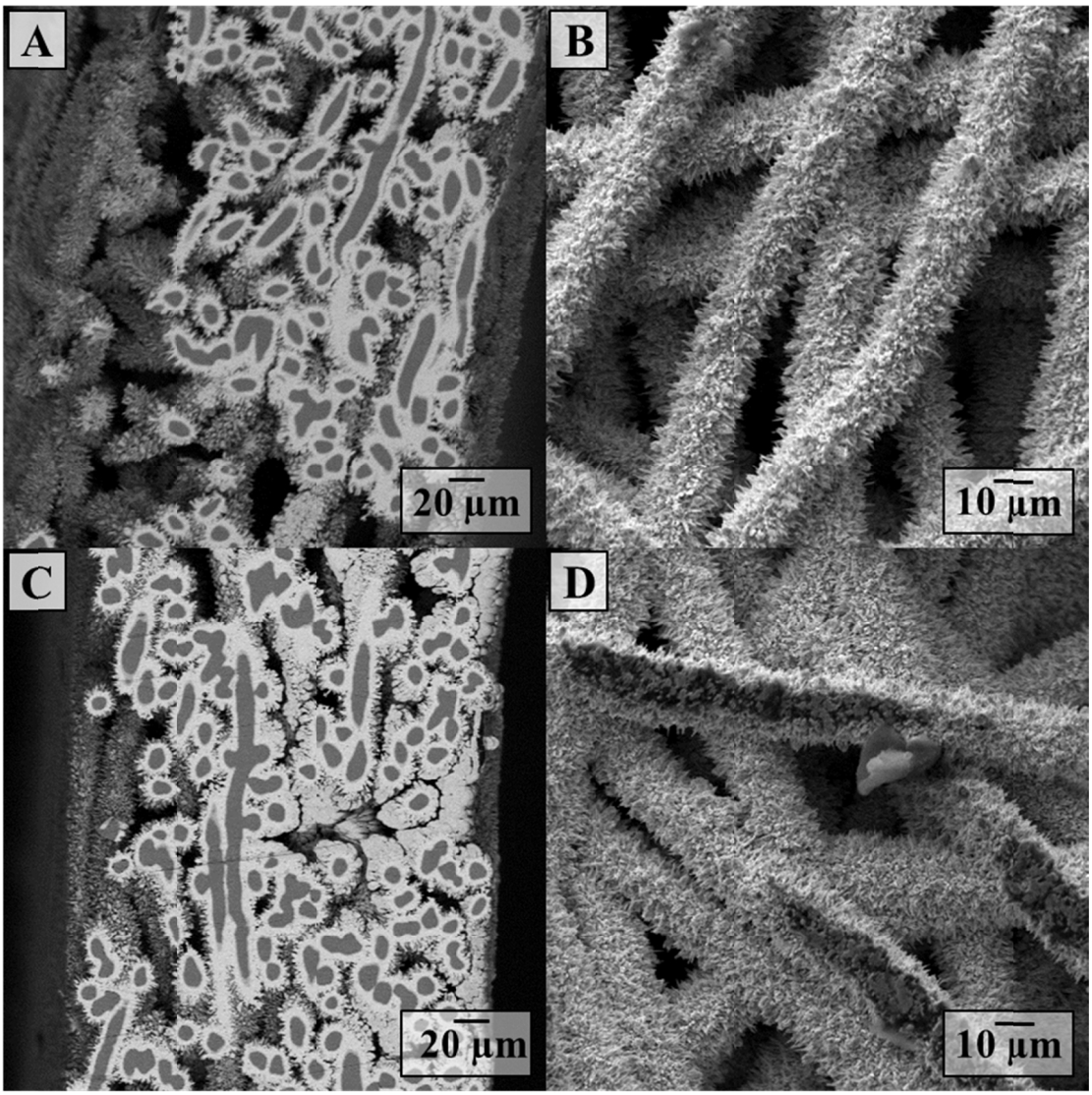


**Figure 5.3: SEM images of, A and B felt before roll milling. C and D after roll milling. Cross sections in A and C are made by ion-milling.**

The flattening of the dendrites on the fibres in image D in figure 5.3 does not seem too extensive. However, if the surface topology is extensively altered, such that it gets significantly smoother, it risks changing the properties of the catalyst particle dispersion and hence lowering the catalytic area and the number of contact points between the GDE and membrane.

## 5.4 Summary GDLs

It was found that even though the variation in mass of discs punched out from the same sheet of pristine felt was negligible (0.1 %) the variation for tantalum coated felt was significant and in the range of 2 to 7 %. Besides the variation in mass on the same sheet of felt there also was a considerable variation between sheets of felt. Here the percentage-wise difference in average mass between discs from different sheets of felt could be up to 10 %. As with the variation of mass a considerable variation of porosity was also observed. The standard deviation between felts of same type and batch tantalum coating was around 5 %, meaning that the difference in porosity in some cases were 10 percentage points.

Furthermore, a marked difference in the appearance of the tantalum coating was observed between different batches. It was found that the tantalum coating could vary from a quite smooth surface of the felt fibres, to very shaggy with dendrites on the fibre surface. There was a connection between the porosity and the topology of the tantalum coating on the fibres. High porosity gave thinner and smoother coatings whereas lower porosity gave coatings with surface dendrites. All this comes down to the CVD process and should of course be optimised.

Irregularities of the tantalum coated felt could be smoothened by roll milling, although porosity was sacrificed and the tantalum dendrites on the fibre were flattened. A larger fraction of the porosity could potentially be lost, even to such a degree that it would become a problem. Moreover changing the tantalum topology on the fibres can give fewer contact points between the GDE and the membrane and a worse catalyst particle distribution on the GDL, *i.e.* leading to worse electrolyser performance.

# 6 Steam electrolysis. Result and discussion

Many different aspects concerning steam electrolysis have been tested. In order to separate between these many factors this chapter has been divided into subchapters depending on which membrane or composite membrane system was used as electrolyte. In general three different membranes or composite membrane systems were used. First phosphoric acid doped PBI membranes was tested as electrolytes, later on were: PA doped Nafion® membranes, composite systems of Nafion® and zirconium phosphate ($Zr(HPO_4)_2 \cdot nH_2O$, ZrP) and Nafion®, ZrP and PA tested. In the end electrolytes of the commercially available short side chain PFSA membrane Aquivion™ doped with PA were tested under steam electrolysis conditions.

A great deal of different MEAs were tested. In table 13.1 (Appendix 3) an overview of all the presented MEAs is given to aid the reader.

## 6.1 Phosphoric acid doped PBI membranes

Some of the results from this section are presented in the article titled: *Phosphoric acid doped membranes based on Nafion®, PBI and their blends – Membrane preparation, characterization and steam electrolysis testing* in International Journal of Hydrogen Energy. The article is attached as paper I in chapter 14.

### 6.1.1 Membrane preparation

Phosphoric acid doped PBI membranes were prepared in-house from a 5 wt.% PBI in dimethylacetamide (DMAc) solution. The procedure with minor changes was briefly described by Pan *et al.* [198]. The PBI polymer was kindly supplied by Danish Power Systems®. The PBI/DMAc solution was cast onto a glass sheet and the DMAc was subsequently evaporated by heat treatment. First it was kept for 1 hour at 60 °C, then the temperature was raised to 80 °C and kept at this temperature for another hour before the temperature was increased to 100 °C. The temperature was

kept at 100 °C for four hours before it was increased to 120 °C, this temperature was kept overnight (usually 14 hours).

The cast membrane was then boiled in demineralised water for 1 hour to remove any solvent residuals and eventually LiCl. After the membrane had been boiled it was dried at 180 °C for 1 hour to remove the absorbed water and the last traces of DMAc. The membrane was then doped in 85 wt.% PA at room temperature for at least 14 days. This gave a doping level (mol of PA per repeating unit of PBI polymer) of 10. Better doping was achieved when the PBI membrane was wetted by demineralised water before immersing in PA.

### 6.1.2 Electrolysis tests

All the electrolysis tests using PBI membranes were, unless otherwise mentioned, PA doped PBI membranes with a doping level of 10. The doped membranes had a thickness of approximately 80 μm. The cathodes had a platinum loading of 0.7 $mg \cdot cm^{-2}$ (in-house made 40 wt.% Pt/C catalyst), a PBI binder loading of 0.14 $mg \cdot cm^{-2}$ and a PA loading of 0.98 $mg \cdot cm^{-2}$. The MEA were hot pressed for 10 minutes at 135 °C with a pressure of approximately 6 MPa.

**Phosphoric acid doping of anode**

During the initial electrolysis experiments it proved very hard to get any measureable electrolysis performance. A possible reason that the first experiments showed very poor performance could be that the ionic conductivity of the anode was not sufficient, since the doping of the anode relied on excess PA from the doped membrane. To test the hypothesis four MEAs with different anodes were prepared. Two of the anodes were of the catalyst coated membrane type, made by the decal method. The remaining two were of the GDE type. Both methods for anode preparation were described above in section 3.8. In each of these two series one of the anodes were doped with PA before being hot pressed. As anode gas diffusion layers single layer stainless steel felts with nominal thicknesses of 0.2 mm (PBI-MEA1 and 2) and 0.5 mm (PBI-MEA3 and 4) were used. The flow plates used were the waffle-

like flow pattern (PBI-MEA1 and 2) and the straight 1 mm channels pattern (PBI-MEA3 and 4) as described in section 4.1 (Pattern A and D respectively, see figure 4.4 and table 4.1).

**Table 6.1: MEA characteristics for MEAs used in comparison of importance of PA doping of anode.**

| | Anode | | | | |
|---|---|---|---|---|---|
| MEA # | $IrO_2$ [mg·cm$^{-2}$] | Binder Nafion® [wt.%] | PA doping [mg·cm$^{-2}$] | GDL thickness [mm] | Type |
| PBI-MEA1 | 1.28 | 1.8 | - | 0.2 | CCM |
| PBI-MEA2 | 4.13 | 4.8 | 2 | 0.2 | CCM |
| PBI-MEA3 | 1.14 | 5.4 | - | 0.5 | GDE |
| PBI-MEA4 | 1.01 | 5.3 | 0.72 | 0.5 | GDE |
| | Constant for the above PBI-MEAs | | | | |
| Cathode | 0.7 mg·cm$^{-2}$ Pt, 0.14 mg·cm$^{-2}$ PBI and 0.98 mg·cm$^{-2}$ PA | | | | |
| Membrane | PA doped PBI, doping level 10 thickness approximately 80 µm | | | | |

As it can be seen from table 6.1 there are more differences between the anodes in PBI-MEA1 and 2 than just the post doping of the anode with phosphoric acid. Both the catalyst loading and the amount of ionomer binder in the anodes differ. Hence PBI-MEA3 and 4 were prepared to verify the findings from PBI-MEA1 and 2. In figure 6.1 the polarisation curves for the four MEAs, which differ in terms of the anode preparation procedure (PA doping of anode *vs*. no doping of anode), are depicted.

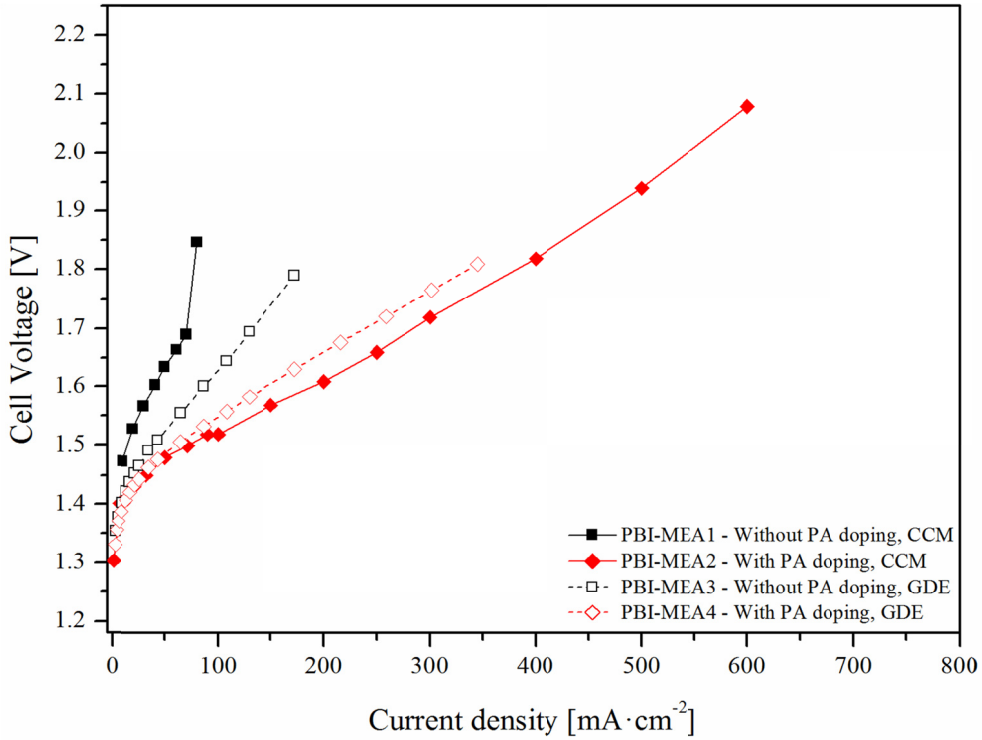


**Figure 6.1: Polarisation curves of PBI based cells for comparison of the importance of PA doping in anode (see table 6.1), tested at 130 °C and ambient pressure.**

The comparison between PBI-MEA1 and 2 is subject to uncertainty due to the above mentioned differences. However, since most of the MEAs without PA post doping of the anode were showing considerably lower performance, the conclusion that PA doping of the anode before assembly of the MEA is crucial for performance seems valid. Especially since the comparison between PBI-MEA3 and 4 also revealed considerably better performance in the PA doped case. It is clear from figure 6.1 that the MEAs without any PA doping (PBI-MEA1 and 3) have a considerably reduced performance compared to their respective counterparts which had their anode doped with PA before hot pressing. The polarisation curves should be compared in pairs, such that the PBI-MEA1 and 2 with solid markers and lines are compared to each other since they are of the same anode type, CCM, and they used the same thickness GDL. Likewise for PBI-MEA3 and 4.

The reduced performance can be seen to originate from an increase in the ohmic resistance, most likely from the anodic catalyst layer. Ohmic resistance contributions are often attributed to the membrane resistance and the contact resistances between parts in the MEA and between the MEA and the cell

components. In this case the increase in ohmic resistance is attributed to the lack of ionic conductivity in the un-doped anodes (PBI-MEA1 and 3). In the case of PBI-MEA1 another difference compared to PBI-MEA2 can be observed, the cell voltages at low current densities are considerably higher, in good correlation with the fact that PBI-MEA1 has a lower catalyst loading on the anode side, hence the active catalyst area is lower. Even at low current densities (below 100 $mA \cdot cm^{-2}$) the ionic transport in the anode of PBI-MEA1 was so restricted that a large increase in the voltage could be observed at small increases in the cell current. PBI-MEA3 and 4 on the other hand, which had similar anode catalyst loading, showed no apparent difference in the activation governed current density range, only differing in the overall system resistance. It is clear from figure 6.1 that the constriction in conductivity is relevant for both electrode preparation methods. The reason PBI-MEA1 and 3 are not completely inactive is, as mentioned above, that part of the free PA in the membrane will penetrate into the anode and hence ensure proton conductivity.

**Anode type - CCM *vs*. GDE**

Preparing the anode on a substrate and transferring it to the membrane by the decal method proved difficult. Hence two different MEA preparation methods were explored. With method one the anode was prepared as a GDE (PBI-MEA5) and with method two the anode was transferred to the membrane according to the decal method giving a CCM electrode (PBI-MEA2). As anode gas diffusion layer a 0.2 mm thick single layer stainless steel felt coated with tantalum was used. As flow pattern the waffle-like pattern as described in section 4.1 (See figure 4.4 and table 4.1) was used. The anodes were in both cases doped with PA before use in the MEA. The doping level of PA was in these early experiments around 2 $mg \cdot cm^{-2}$ of PA. In table 6.2 the catalyst loadings, binder contents and electrode types (CCM or GDE) for the anodes and the cathode and membrane characteristic are listed.

**Table 6.2: MEA characteristics for MEAs used in comparison of different anode types.**

| | Anode | | | |
|---|---|---|---|---|
| MEA # | $IrO_2$ [$mg \cdot cm^{-2}$] | Binder Nafion® [wt.%] | PA doping [$mg \cdot cm^{-2}$] | Electrode type |
| PBI-MEA2 | 4.13 | 4.8 | 2 | CCM |
| PBI-MEA5 | 3.08 | 5.4 | 2 | GDE |
| Constant for the above PBI-MEAs | | | | |
| Cathode | 0.7 $mg \cdot cm^{-2}$ Pt, 0.14 $mg \cdot cm^{-2}$ PBI and 0.98 $mg \cdot cm^{-2}$ PA | | | |
| Membrane | PA doped PBI, doping level 10 thickness approximately 80 μm | | | |

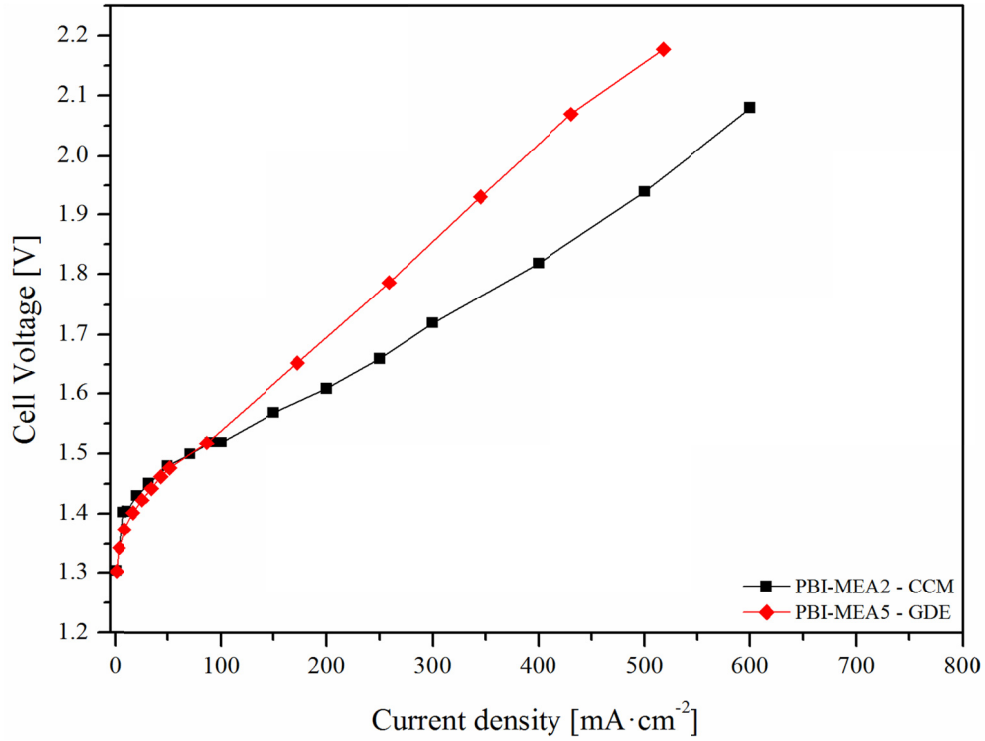


**Figure 6.2: Polarisation curves of PBI based cells for the comparison of different anode types (see table 6.2), tested at 130 °C and ambient pressure.**

In figure 6.2 the polarisation curves for the two different MEAs are shown. As expected it can be seen that the MEA with the CCM anode (PBI-MEA2) has a lower resistance compared to the MEA with the GDE (PBI-MEA5). This was expected since most often a better contact between electrode and membrane is achieved using the CCM technique. Although there is a considerable difference in the anode catalyst loading (PBI-MEA2 having the highest loading) this does not seem to, significantly, influence the polarisation behaviour in the activation governed current density range. The sole difference in performance originates from the increased ohmic resistance.

One drawback of using the decal method of applying the electrode to the membrane was that often the transfer from the original substrate (in this case a sheet of PTFE) to the membrane was quite poor, and much work could be dedicated finding the optimal transfer conditions. On the other hand making a GDE was quite simple and the catalyst was not left behind on a substrate when hot pressed to the membrane. Because of the easier manufacturing procedure of GDE this technique was preferred even though it gave slightly worse results.

**Ionomer in anode**

Other research groups have observed that a mismatch between the ionomer in the electrode and the membrane can have severe consequences for the electrolysis performance. As mentioned in section 2.6.1 Wei *et al.* [161] found that using Nafion® as ionomer in the anode instead of the same ionomer as the membrane (SPEEK/PES) increased the cell voltage. The voltage increased from approximately 1.525 V at a current density of 150 $mA \cdot cm^{-2}$ [161] (identical ionomer and membrane) to approximately 2.0 V at 150 $mA \cdot cm^{-2}$ [161] when Nafion® was used as ionomer together with the SPEEK/PES membrane.

In this study it was investigated whether deterioration in performance of similar magnitude could be observed when using a different ionomer binder than the membrane. Two MEAs were made one with a PBI/PA mixture as the ionomer binder/proton conductor (PBI-MEA6) and one with Nafion® as binder (PBI-MEA5) both using a PA doped PBI membrane. The anode gas diffusion layers (0.2 mm thick single layer felt) and the flow patterns (waffle-like) were identical to the above tested. The anodes were in both cases made as GDE, since controlling the nominal catalyst loading was much easier with this method. The ink was sprayed to the felt GDLs as described in section 3.8. The anode with the PBI/PA mixture as binder/proton conductor was not doped before hot pressing of the MEA since it already contained PA in the catalyst layer. In the MEA using Nafion® as anode binder, the anode was doped with approximately 2 $mg \cdot cm^{-2}$ of PA before hot pressing. In table 6.3 MEA characteristics, e.g. the catalyst loading, binder and binder content for the anodes used in the investigation of importance of uniformity between binder ionomer and membrane polymer are listed.

**Table 6.3: MEA characteristics for MEAs used in comparison of different anode ionomers.**

| | Anode | | | |
|---|---|---|---|---|
| MEA # | $IrO_2$ [$mg \cdot cm^{-2}$] | Binder [wt.%] | PA doping [$mg \cdot cm^{-2}$] | Electrode type |
| PBI-MEA5 | 3.08 | Nafion® 5.4 | 2.06 | GDE |
| PBI-MEA6 | 3.71 | PBI 2.3 | 0.14 | GDE |
| Constant for the above PBI-MEAs | | | | |
| Cathode | 0.7 $mg \cdot cm^{-2}$ Pt, 0.14 $mg \cdot cm^{-2}$ PBI and 0.98 $mg \cdot cm^{-2}$ PA | | | |
| Membrane | PA doped PBI, doping level 10 thickness approximately 80 µm | | | |

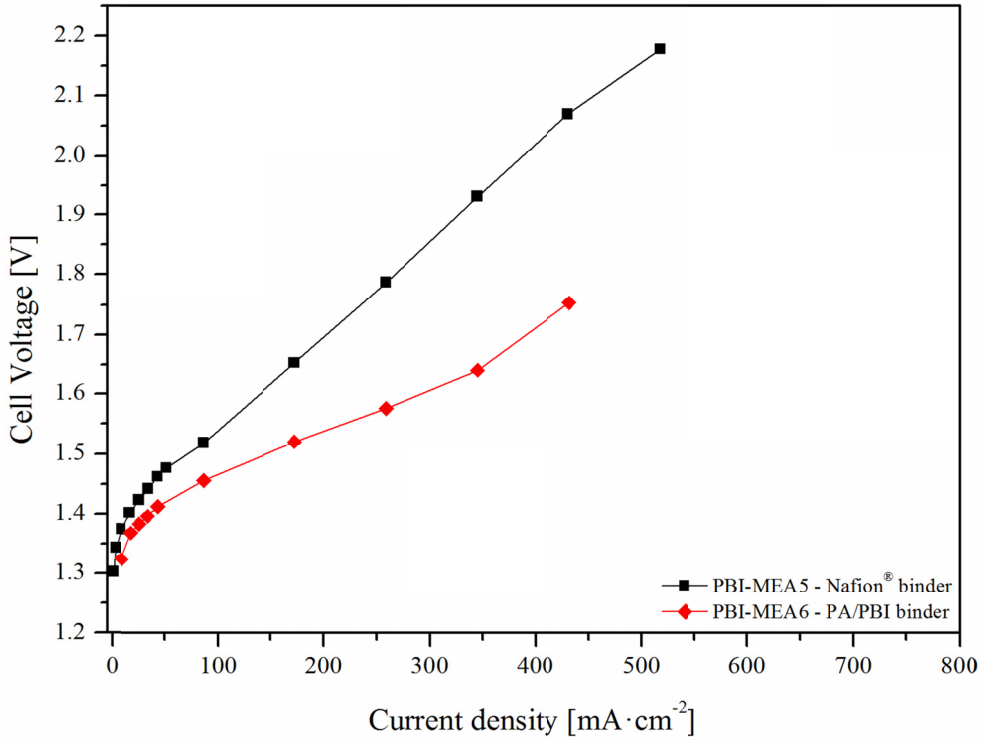


**Figure 6.3: Polarisation curves of PBI based cells for comparison of ionomer in anode (see table 6.3), tested at 130 °C and ambient pressure.**

From figure 6.3 it is clear that there is a difference between the two MEAs with different proton conducting phases in the anode electrode layer. At a current density of 258 mA·cm$^{-2}$ the cell voltage of the MEA with PBI/PA as binder (PBI-MEA6) was approximately 210 mV lower (1.58 V) than the MEA with Nafion® as binder (PBI-MEA5).

It should be stated that even though the electrolyser performance is affected by the choice of binder, other factors could also have attributed to the difference. The slightly higher catalyst loading of PBI-MEA6 can partly explain the lower voltage, since it is evident that PBI-MEA6 has lower activation overvoltage. Nevertheless the major improvement originates from a lower overall ohmic resistance in PBI-MEA6. The lower ohmic resistance can possibly be ascribed to better ionic compatibility from the same type of polymer in anode and membrane respectively. However it can also be argued that the reason for the improved conductivity of PBI-MEA6 is not solely from the PBI binder, but from better distribution of PA in the anode. The total loading of PA in the anode of PBI-MEA6 is approximately an order of magnitude lower, however since it was mixed with the ink and sprayed onto the GDL the

distribution is most likely much better. The reason that electrolysis performance can be observed for PBI-MEA5 is likely to be an effect of the large loading of PA in the anode, since most of the ionic conductivity comes from the PA content as seen above in figure 6.1.

From figure 6.3 it can furthermore be seen that even though the electrolysis performance is worse when using a Nafion® ionomer as binder it still is possible to achieve fairly high current densities without an abrupt increase in voltage like found by Wei *et al.* [161]. When comparing the behaviour of the polarisation curve of PBI-MEA5 in figure 6.3, with the behaviour of the MEA in Wei *et al.*'s study [161] (Nafion® binder and SPEEK/PES membrane), it is clear that it is not the same kind of restriction in electrolyser performance which can be observed. In the case of Wei *et al.* [161] 150 $mA \cdot cm^{-2}$ seemed to be the maximum current density that the MEA could be applied, since at this current density the cell voltage increased almost vertically indicating transport limitations of some kind. In the case of PBI-MEA5 the situation was different. Here a general higher ohmic resistance was observed, however not an abrupt increase in voltage. Hence in this case it seems likely that the transport properties of the anode is not as restricted as the case from Wei *et al.* [161] likely due to the large amount of PA in the anode, as mentioned earlier.

**Best performing PA doped PBI membrane**

It was found that increasing the $IrO_2$ loading of the anode in the PBI/PA membrane MEAs gave fairly good electrolyser performance even with Nafion®/PA as binder and ionic conductor in the anode. The anode was of the GDE type with an $IrO_2$ loading of 9.97 $mg \cdot cm^{-2}$ and a Nafion® binder content of 5.2 wt.%. The GDE was doped with PA before being hot pressed to the membrane, the PA content on the anode was 0.95 $mg \cdot cm^{-2}$. The GDL in the GDE was likewise the earlier tested MEAs a 0.2 mm thick tantalum coated single layer stainless steel felt. Like the previous measurements the flow pattern was of the waffle-like type (flow pattern A as shown in figure 4.2).

**Table 6.4: MEA characteristics for the best performing PBI-MEA.**

| Anode | | | | |
|---|---|---|---|---|
| MEA # | $IrO_2$ [mg·cm$^{-2}$] | Binder Nafion® [wt.%] | PA doping [mg·cm$^{-2}$] | Electrode type |
| PBI-MEA7 | 9.97 | 5.2 | 0.95 | GDE |
| Constant for the above PBI-MEA | | | | |
| Cathode | 0.7 mg·cm$^{-2}$ Pt, 0.14 mg·cm$^{-2}$ PBI and 0.98 mg·cm$^{-2}$ PA | | | |
| Membrane | PA doped PBI, doping level 10 thickness approximately 80 µm | | | |

The key characteristics for the PBI-MEA7 are listed in table 6.4 and in figure 6.4 the polarisation curve and total i·r-voltage contribution for PBI-MEA7 are shown. Furthermore, an estimated i·r-voltage contribution from the membrane is plotted in the figure (i being the current density and r the area specific resistance). This data is estimated for a PA doped PBI membrane (doping level 11) with a proton conductivity of $9 \cdot 10^{-2}$ S·cm$^{-1}$ at 130 °C with a relative humidity (RH) of 16-18 % as found by Aili *et al.* [199]. The data for the i·r-voltage contribution was found as described in section 2.2.2 by doing regression on the data, assuming that the polarisation data can be described by the following equation (6-1) [55, 56], which is as equation (2-11) just substituting the current and resistance with current density and area specific resistance respectively.

$$U_{Cell} = U_{Act} + U_{Ohmic} = (a + b' \cdot \log(i)) + (i \cdot r) \tag{6-1}$$

In equation (6-1) the cell voltage is divided into two voltage contributions, these being the voltages which are controlled by the activation of the electrode reactions and the ohmic resistance respectively. In some cases the cell voltage would also be affected by mass transport limitations, and equation (6-1) would simply consist of one more term. In figure 2.2 (Section 2.2.2) the schematic representation of this mass transport limitation concept was shown as the last part of a polarisation curve with the three regions. In the polarisation curve in figure 2.2 the first two current densities range the cell voltage are dominated by activation overvoltage and ohmic resistance respectively.

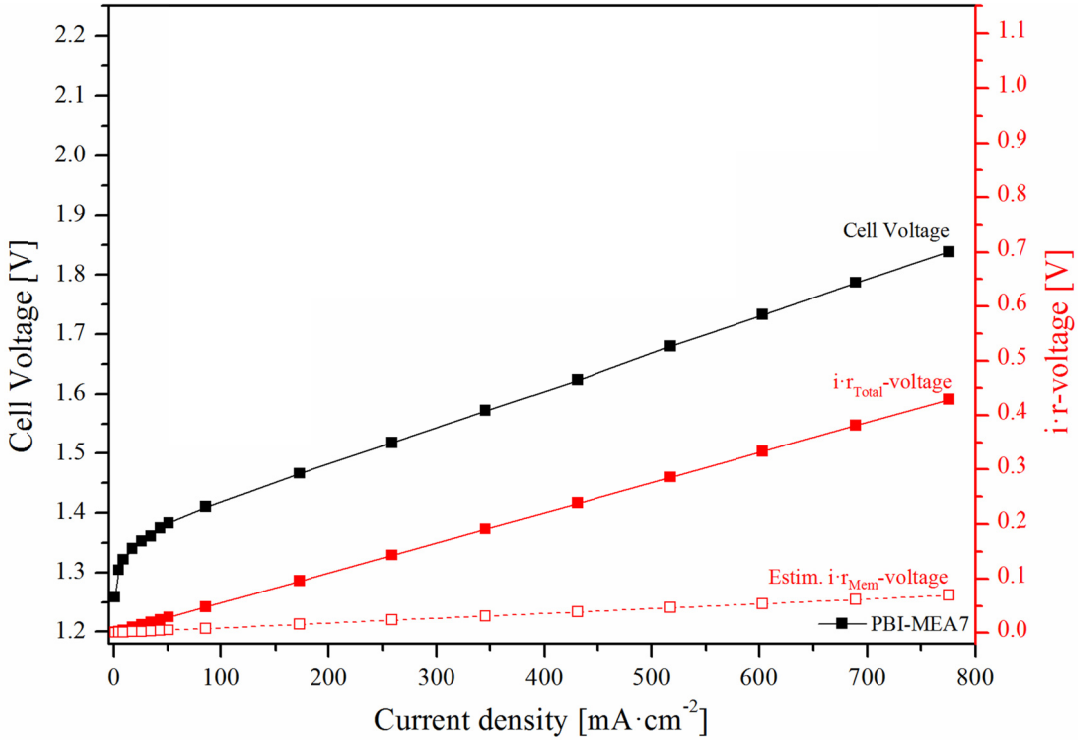


**Figure 6.4: Polarisation curve and i·r-voltages for the best performing PBI-MEA – PBI-MEA7 (see table 6.4), tested at 130 °C and ambient pressure.**

From figure 6.4 it is clear that it was possible to achieve relatively good steam electrolysis results with MEAs based on phosphoric acid doped PBI membranes at a temperature of 130 °C and atmospheric pressure, even when Nafion®/PA was used as proton conducting phase in the electrode. However, it should be noted that the anode loading of $IrO_2$ is extremely high in this case with almost 10 mg·cm$^{-2}$. Nevertheless, it is encouraging that the concept of PEM steam electrolysis is possible and reasonably good performance can be achieved. It is clear both from the polarisation curve and the total i·r-voltage curve that a large part of the overvoltage can be ascribed the total ohmic contribution. Moreover it is very clear that a large part (around 80 %) of the ohmic resistance cannot be attributed the membrane resistance, given that the $9 \cdot 10^{-2}$ S·cm$^{-1}$ conductivity can be assumed valid. The electrolysis testing conditions matched the conditions under which the conductivity was found when it came to temperature, however the water activity was quite different under actual electrolysis testing. During electrolysis test the water activity is higher which should lead to improved proton conductivity, as mentioned in section (2.5.1) making up for the slightly lower doping level of the PBI membranes used during the electrolysis tests. Hence the used proton conductivity for the estimated membrane

contribution is probably relatively correct. The main part of the ohmic resistance for PBI-MEA7 must be attributed to other factors like contact resistances and resistance in the electrodes. The electrode resistance could eventually be due to the discrepancy between the membrane and ionomer used as binder in the anode as found above.

**Durability of PBI-MEAs**

It was found that the durability of the PBI-MEAs in this setup was not sufficient. All the MEAs failed already after a short period of time due to severe membrane failure. Most PBI-MEAs failed already after around 6-10 hours. An example of an electrolysis run with a MEA that failed is illustrated by PBI-MEA8. The MEA used the same kind of anode GDL, the same cathode, the same waffle-like flow pattern and hot pressing procedure as the previously described MEAs. The PBI membrane was in this case considerably thicker than the previously tested ones. The PA doped membrane had a thickness of approximately 180 μm. However the casting and doping procedure were identical to the procedures given in section 6.1.1, *i.e.* it had a doping level of PA of approximately 10. The anode was made after the GDE method with subsequent PA doping, the doping of the anode was 2.1 $mg \cdot cm^{-2}$. Table 6.5 lists characteristic anode features.

**Table 6.5: MEA Characteristics for a typical failed PBI-MEA.**

| Anode | | | | |
|---|---|---|---|---|
| MEA # | $IrO_2$ [$mg \cdot cm^{-2}$] | Binder Nafion® [wt.%] | PA doping [$mg \cdot cm^{-2}$] | Electrode type |
| PBI-MEA8 | 2.79 | 5.1 | 2.1 | GDE |
| Constant for the above PBI-MEA | | | | |
| Cathode | 0.7 $mg \cdot cm^{-2}$ Pt, 0.14 $mg \cdot cm^{-2}$ PBI and 0.98 $mg \cdot cm^{-2}$ PA | | | |
| Membrane | PA doped PBI, doping level 10 thickness approximately 180 μm | | | |

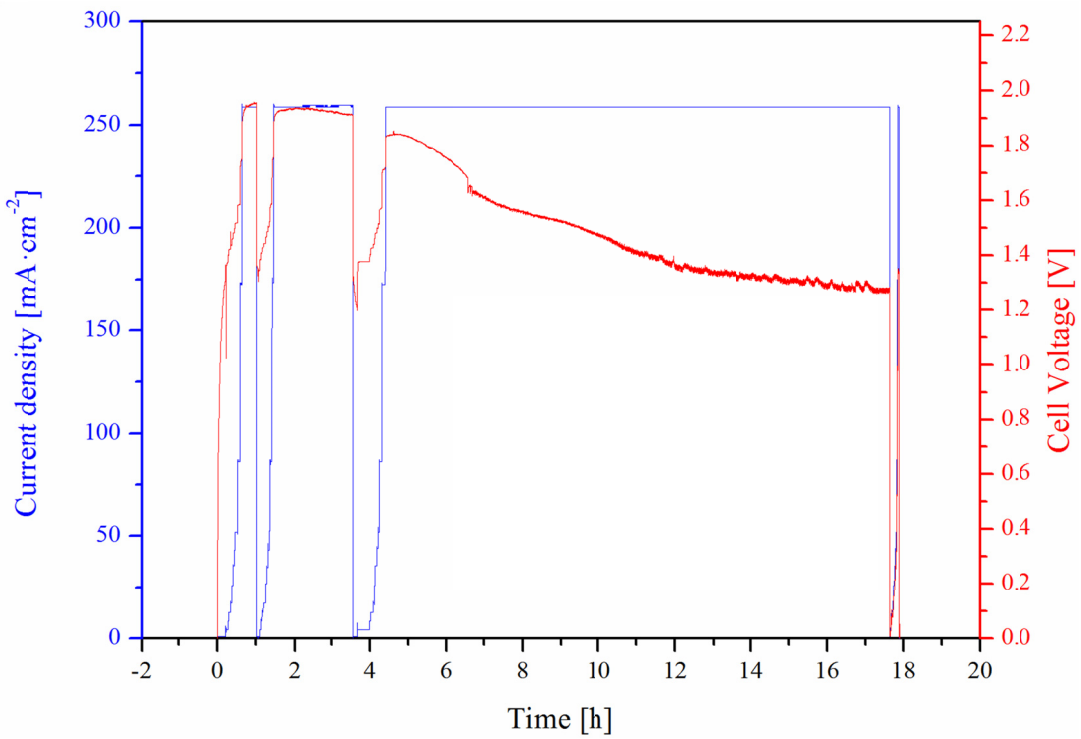


**Figure 6.5: Current density and cell voltage as a function of time for a typical failed PBI-MEA – PBI-MEA8 (see table 6.5), tested at 130 °C and ambient pressure.**

The voltage curve (red) in figure 6.5 clearly shows that at around 2 hours the voltage starts to decrease considerably, *i.e.* indicating that the membrane already started to fail at this time. The reason for the membrane failure is not completely understood. A possible explanation could be lack of chemical stability of the PA doped PBI membrane at the harsh oxidative conditions during electrolysis at elevated temperatures. Linkous [200] reported that PBI had thermohydrolytic stability problems especially under oxidative conditions. Linkous proposed the degradation could be due to hydrolysis of the imidazole ring [200]. However, the failure could also be caused by uneven current density distribution over the electrode area leading to local hot spots, where very high current densities are predominant, hence simply burning the membrane because of the high temperature. The cause of these hot spots could be due to mechanical factors such as the roughness of the anode GDL and the force distribution from the cell assembly. For instance if the anode GDL is very rough and some parts of the electrode area are compressed harder than others, it would be likely that the threads of the tantalum coated stainless steel felt could be pressed so hard towards the soft membrane that areas on the membrane become very thin. These areas with thinner membrane would then conduct the majority of

the current *i.e.* leading to local hot spots. Another possible reason could be that the distribution of ionomer in the catalyst ink was not completely homogenous. This and the possibility of a non-homogenous distribution of PA in the doping step could also lead to areas with better ionic conductivity *i.e.* hot spots.

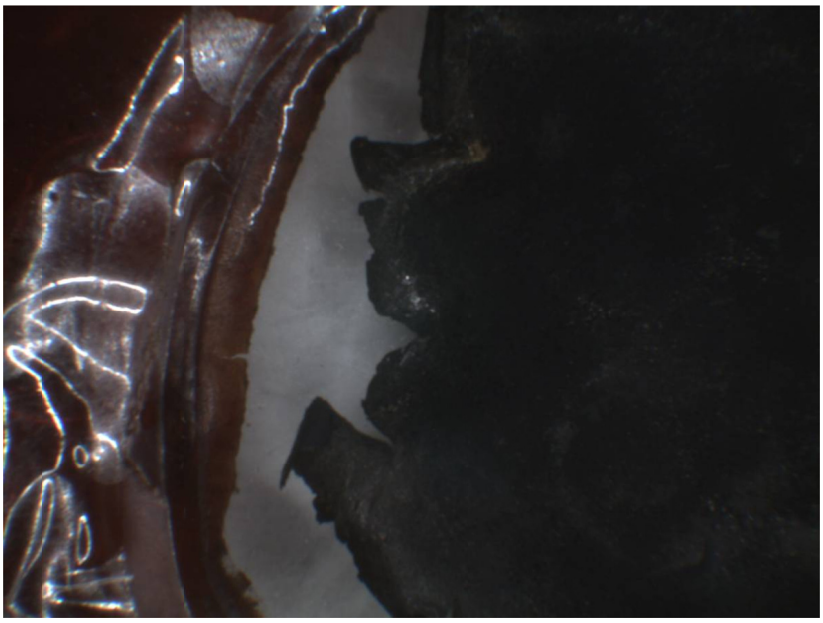

**Figure 6.6: Photograph of membrane after disassembly of PBI-MEA8 after electrolysis test.**

Figure 6.6 shows a photograph of the PBI membrane after the electrolysis test of PBI-MEA8. In order to avoid further damage the membrane, the electrodes were peeled off very carefully. It can be seen that a large area of the membrane along the edge of the electrode has disappeared. The example chosen is one of the most extreme cases of membrane failure observed. However the MEA was also allowed continued testing around 16 hours after the first sign of membrane failure could be observed from the decrease in voltage. As mentioned above the reason for the membrane failure in the PBI-MEAs is not fully understood, and further work ought to be devoted this subject to clarify the issue.

### 6.1.3 Summary

The electrolysis testing of MEAs with PBI membranes showed that it is possible to achieve reasonable short term electrolysis performance of PBI-MEAs with high anode catalyst loading. No long term durability of the PBI-MEAs could be achieved since all MEAs failed within hours of electrolysis

initiation. It was furthermore found that doping of the anode with PA was crucial to get sufficient performance of the MEA. In other words the major part of the ionic conductivity in the electrode came from the PA it was doped with.

Finally it was also shown that electrodes prepared from the catalyst coated membrane technique gave a slight improvement of electrolyser performance, which could be explained by the fact that the interfacial resistance between the electrode and membrane was lower when the anode was transferred to the membrane via the decal method. However the transfer of the catalyst layer from the supporting material (PTFE) to the membrane was not optimal, which made it very hard to control the anode loading. So from a practical point of view the electrode manufacturing procedure for GDE was simpler and gave considerably better reproducibility, hence this was the electrode manufacturing technique which mainly was further pursued.

## 6.2 Nafion® composite membranes

The poor durability of PBI membranes under the steam electrolysis conditions used, with life times in the range of few hours, spawned the need of new membrane materials as electrolyte. In literature Savinell *et al.* [201] reported already back in 1994 that doping Nafion® with phosphoric acid could give reasonably ionic conducting membranes. Although, the ionic conductivity was still partly dependent on the water activity in the gases, this should be of less concern under electrolysis conditions where steam continuously is fed to the cell. It is well-known, as shown in the literature study (section 2.5), that PFSA membranes are tried and tested for low temperature water electrolysis, having shown excellent durability lasting for several thousands of hours [8]. The excellent durability of Nafion® and the possibility of imbibing PA to ensure proton conductivity at elevated temperatures, made PA doped Nafion® an obvious candidate for further testing. ZrP has been identified to improve both the water retention and the mechanical characteristics of the membrane [202], indicating imbibing the Nafion® membrane with this inorganic filler as a possible route to steam electrolysis based on PFSA membranes.

The membrane preparation, membrane conductivity tests and mechanical strength tests were mainly performed by Dr. David Aili at the Technical University of Denmark, Kgs. Lyngby Denmark. Further results within this subject can be examined in details in the Ph.D. thesis of Dr. David Aili [203].

Experiments with the decal method of transferring the anode to the membrane were conducted by Lisbeth Molzen at the Technical University of Denmark, Kgs. Lyngby Denmark, as part of her bachelor study.

Parts of the results from this section is presented in the article titled: *Phosphoric acid doped membranes based on Nafion®, PBI and their blends – Membrane preparation, characterization and steam electrolysis testing* in International Journal of Hydrogen Energy. The article manuscript is attached as paper I in chapter 14.

### 6.2.1 Membrane preparations

Nafion® membranes used during this study were purchased from Ion Power Inc©. Before any further treatment (*e.g.* PA doping) the membranes were pre-treated by the standard procedure for PFSA membranes. First they were treated in 3 wt.% $H_2O_2$ at 80 °C for 1 hour, this was done to oxidise and wash out any impurities and potential residues of solvent from the manufacturing procedure of the membrane. Subsequently the membranes were boiled in demineralised water and then 0.5 $mol \cdot L^{-1}$ $H_2SO_4$ for 2 hours and 1 hour respectively. Before storage in demineralised water, the membranes were rinsed and boiled for several hours in demineralised water.

Phosphoric acid doped membranes were doped by immersing the pre-treated membrane in 85 wt.% PA for approximately 16 hours at 150 °C in a beaker fitted loosely with a watch's glass to avoid contamination of the PA solution. The PA content of the doped membrane was measured on a weight basis by drying the membrane prior and after PA doping at 100 °C *in vacuo* until constant weight. The PA content was then calculated as the gained weight of PA divided by the weight of the PA doped membrane and given in wt.%.

Composite membranes of Nafion® and ZrP were made by a cation-exchange of pre-swollen membrane (done by refluxing the membrane in an 1:1 (vol./vol.) MeOH:$H_2O$ solution at 80 °C for 1 hour). The pre-swollen membrane was ion-exchanged with Zr(IV) ions (from $ZrOCl_2$ hydrochloric acid solutions) in various concentrations at 80 °C for varying periods of time. The zirconium phosphate was precipitated in the membrane by immersing the treated membrane in a 1.0 $mol \cdot L^{-1}$ PA solution at 80 °C for 12 hours. Finally the membranes were boiled in demineralised water to remove excess acid and ZrP precipitated on the surface.

Composite membranes of Nafion®, ZrP and PA were initially made by making the Nafion®-ZrP composite membrane as described above and then doping it according to the above described procedure. However, since ZrP is partly soluble in hot concentrated PA [204] the major fraction of the ZrP was most likely dissolved and washed out during this process. Therefore, the ternary composites were prepared by doping the Nafion® membranes in a hot phosphoric acid solution which had been saturated with ZrP. However the content of ZrP in the ternary composites was hence unknown and unfortunately no further work to determine this was done. Nevertheless, the ZrP content could roughly be estimated from the solubility of ZrP in hot PA and assuming the same composition of PA/ZrP in the doped membrane as found by this rough estimate.

### 6.2.2 Mechanical strength

Mechanical strength tests of the different composite PFSA membranes were carried out at 130 °C as described in section 3.7. Each type of membranes was tested 4-5 times and the reported values are averages for Young's moduli, elongations at break and tensile stresses at break, where such measurements were possible. If a value is omitted, it is because it was not practically possible to measure it by the used system. For example a membrane could be so soft at the temperature in question, that its elongation was longer than the range of the machine. The Young's moduli are given in MPa and are calculated using equation (3-6) the tensile stress at break and the elongation at break are read off the stress strain curves. In table 6.6 the values for the tested membranes are listed.

**Table 6.6: Summary of mechanical strength properties of PA doped- and ternary PA doped composite Nafion® membranes at 130 °C and ambient atmosphere.**

| | Approx. Thickness [µm] | Young's modulus [MPa] | Elongation at break [%] | Tensile stress at break [MPa] |
|---|---|---|---|---|
| Nafion® 212 + PA | 57 | 4.5 ± 0.6 | > 800 | - |
| Nafion® 212 + PA + ZrP | 56 | 3.9 ± 0.3 | > 800 | - |
| Nafion® 115 + PA | 140 | 5.1 ± 0.4 | 695 ± 75 | 6.8 ± 2 |
| Nafion® 115 + PA + ZrP | 138 | 5.4 ± 0.3 | 666 ± 52 | 6.7 ± 0.9 |

As can be seen from table 6.6 there were no significant differences in Young's moduli for the four different types of PA doped Nafion® membranes. It can be seen as expected that the Young's moduli for the Nafion® 115 type membranes were a bit higher than the thinner Nafion® 212, since Nafion® 115 is extrusion cast while Nafion® 212 is dispersion cast. In general extrusion cast membranes have higher degree of crystallinity and thus improved mechanical properties compared to solution cast membranes [203]. However the difference in Young's moduli was very small, and could be within the experimental uncertainty of these experiments. The uncertainty of the measurements reflects that the setup was not well suited for measuring on very soft samples. Furthermore it is possible that the strain rate (0.333 $min^{-1}$) of the sample was not optimal for testing under these conditions, although it lies within the range (although the high end) of strain rates reported in literature. Fujimoto *et al.* [205] used a strain rate of 0.167 $min^{-1}$, Tang *et al.* [206] and Werner *et al.* [207] used a strain rate of 0.2 $min^{-1}$, Liu *et al.* [208] tested five different strain rates: 0.025, 0.07, 0.12, 0.3 and 0.7 $min^{-1}$ and Kundu *et al.* [209] used a very low strain rate of 0.0005 $min^{-1}$. However all these strain rates were used at temperatures between room temperature and 85 °C *i.e.* well below the glass transition temperature ($T_g$) of Nafion®. The $T_g$ for Nafion with EW of 1100 $g \cdot eq^{-1}$ is normally reported in the range 100-120 °C in the protonated form. Page *et al.* [112] reported a $T_g$ of approximately 100 °C, while Osborn *et al.* [210] found a softening temperature of ~ 110 °C and Li *et al.* [211] reported a $T_g$ value of 124 °C.

The reason for the surprising similarity in mechanical strength between Nafion® 115 and 212 could come from a plasticising effect of PA in the membrane. This plasticising effect is believed to be due the swelling of the membrane, hence lowering the attractive forces between the macromolecules in the membrane [212, 213]. The same trend has been observed for melt extruded Nafion® 117 which had a significant loss of mechanical strength as the hydration level was increased [202]. This phenomenon was also ascribed to the swelling of the membrane *i.e.* weaker coulombic forces between molecules

[202]. Aili [203] reported that the PA content in Nafion® 115 after doping for 16 hours at 150 °C in 85 wt.% PA was 25.7 wt.% whereas it only was 19.5 wt.% in Nafion® 212 doped under the same conditions. Hence the higher PA content in Nafion® 115 could cause the more pronounced decrease in expected mechanical strength compared to Nafion® 212.

Even though only a small difference in Young's moduli was seen between the Nafion® 115 and 212 based membranes it is clear from the tensile stress at break in table 6.6 that the Nafion® 115 based membranes have more mechanical strength as the strain is increased.

### 6.2.3 Electrolysis tests

Electrolysis tests were performed on three different kinds of commercially available Nafion® membranes Nafion® 115, Nafion® 212 and Nafion® 211. Additionally a few tests using in-house cast Nafion® membranes were performed. All the tested Nafion® MEAs used a GDE cathode with a platinum loading of approximately 0.7 $mg \cdot cm^{-2}$ (40 wt.% Pt/C) on non-woven carbon cloth. For the cathode an additional backing layer of 0.2 mm thick tantalum coated steel felt was used between the flow plate and the cathode GDE to ensure a uniform pressure on the carbon cloth GDL. As flow pattern either the waffle-like or the asymmetric spiral pattern, which are both depicted in figure 4.4 as pattern A and pattern B respectively, was used. None of the tested MEAs were hot pressed before cell assembly, *i.e.* they were all assembled directly in the cell.

#### Nafion® 115 composite membranes

First Nafion® 115 membranes were tested in three different systems. The tested systems were Nafion® 115 doped with PA, a composite membrane of Nafion® 115 and ZrP and finally a ternary composite membrane of Nafion® 115 and ZrP doped with PA.

The MEA with the composite Nafion® 115 ZrP membrane (NAF-MEA1) had an anode loading of 3.19 $mg \cdot cm^{-2}$ $IrO_2$ and a binder content of 5.5 wt.% Nafion® ionomer. The anode was doped with

approximately 0.5 mg·cm$^{-2}$ PA before cell assembly. The anode GDL was tantalum coated steel felt with a thickness of 0.2 mm. The thickness of the Nafion® 115 and ZrP composite membrane was approximately 225 µm. The characteristics for the anode and electrolyte for NAF-MEA1 are listed in table 6.7. NAF-MEA1 was tested in a cell using the asymmetric spiral flow pattern.

**Table 6.7: Characteristics for MEA with Nafion® 115 and ZrP composite membrane.**

| MEA # | Anode | | | Electrolyte | |
|---|---|---|---|---|---|
| | $IrO_2$ [mg·cm$^{-2}$] | Binder Nafion® [wt.%] | PA [mg·cm$^{-2}$] | Electrolyte type | Thickness [µm] |
| NAF-MEA1 | 3.19 | 5.5 | 0.5 | Nafion® 115 + ZrP | 225 |

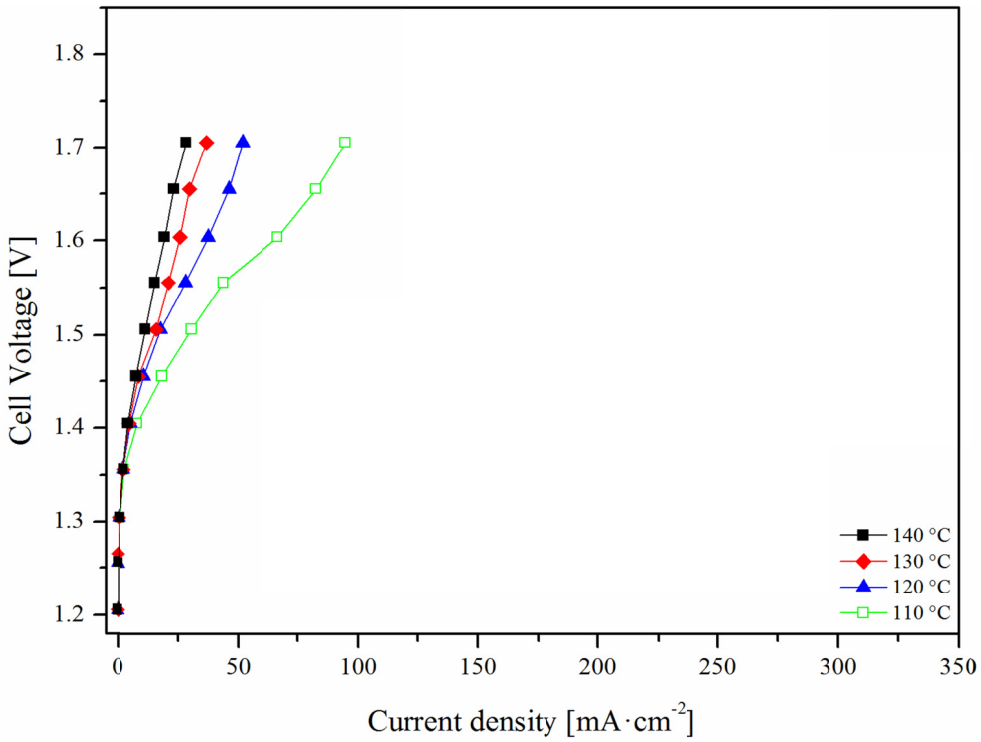


**Figure 6.7: Polarisation curves for NAF-MEA1 (see table 6.7) at different temperatures from 110 to 140 °C, at ambient pressure.**

From figure 6.7 it is clear that the performance of NAF-MEA1 was temperature dependent. This is also what would be expected since there is no substitute for water as proton conducting media, hence the MEA is very much dependent on its ability to retain water. The ZrP has two roles in the composite material. First it should act as inorganic filler and hence improve the mechanical strength of the membrane. Secondly, ZrP has hygroscopic properties, hence it should improve the membranes water

retaining abilities *i.e.* increase the ionic conductivity of the membrane. It is clear from figure 6.7 that lowering the temperature from 140 °C to 110 °C gives an improvement in performance, at a cell voltage of 1.7 V the current density was increased from 33 $mA \cdot cm^{-2}$ to 110 $mA \cdot cm^{-2}$ for 140 °C and 110 °C respectively. The performance improvement was achieved by a lowering of the ohmic resistance in the cell which could be due to two contributions. Firstly better mechanical properties of the membrane at 110 °C *i.e.* better structural integrity of the interface between the electrodes and the membrane. Secondly the decrease in ohmic resistance could definitely also be attributed to the better ionic conductivity of the membrane at lower temperatures due to the higher water activity in the membrane at lower temperatures.

Next were two MEAs with PA doped Nafion® 115 membranes tested, one of them being a ternary composite with ZrP. The MEA with a PA doped Nafion® 115 membrane (NAF-MEA2) had an anode loading of 3.03 $mg \cdot cm^{-2}$ $IrO_2$, the binder content in the anode was 5.4 wt.% Nafion® and the anode was doped with approximately 0.8 $mg \cdot cm^{-2}$ PA before cell assembly, the GDL was a 0.2 mm thick tantalum coated stainless steel felt. The thickness of the PA doped Nafion® membrane was approximately 165 μm. The ternary MEA with the PA doped composite membrane of Nafion® and ZrP (NAF-MEA3) was like the two above mentioned Nafion based MEAs using a 0.2 mm tantalum coated stainless steel felt as GDL. The $IrO_2$ loading of the anode was 3.35 $mg \cdot cm^{-2}$ and the Nafion® binder content was 5.4 wt.%. The anode had a post-doping level of PA of approximately 0.9 $mg \cdot cm^{-2}$. The membrane thickness of the phosphoric acid doped composite membrane was approximately 175 μm.

In table 6.8 the anode and electrolyte characteristics for NAF-MEA1-3 are summarised. NAF-MEA1 was tested using the asymmetric spiral pattern while both NAF-MEA2 and 3 were tested using the waffle-like flow pattern.

**Table 6.8: Characteristics for MEAs with Nafion® 115 membrane.**

| MEA # | Anode | | | Electrolyte | |
|---|---|---|---|---|---|
| | $IrO_2$ [$mg \cdot cm^{-2}$] | Binder Nafion® [wt.%] | PA [$mg \cdot cm^{-2}$] | Electrolyte type | Thickness [μm] |
| NAF-MEA1 | 3.10 | 5.5 | 0.5 | Nafion® 115 + ZrP | 225 |
| NAF-MEA2 | 3.03 | 5.4 | 0.8 | Nafion® 115 + PA | 165 |
| NAF-MEA3 | 3.35 | 5.4 | 0.9 | Nafion® 115 + PA + ZrP | 175 |

In figure 6.8 the polarisation curves for NAF-MEA1-3, tested at 130 °C and atmospheric pressure, are presented.

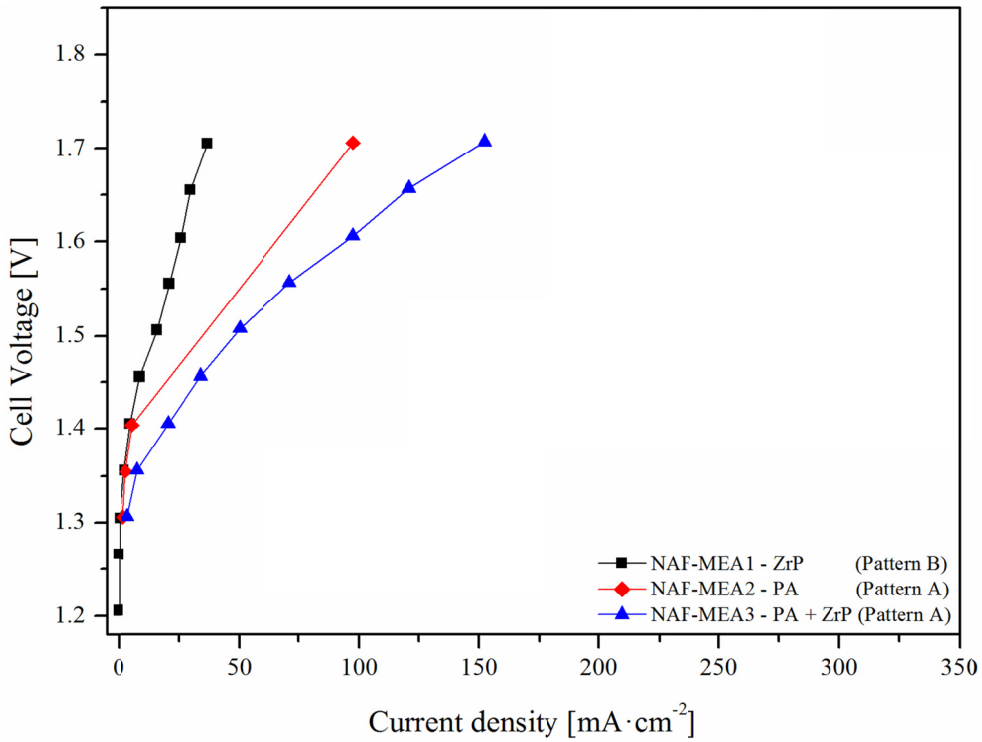


**Figure 6.8: Polarisation curves for the three Nafion® 115 based MEAs (see table 6.8). Tested at 130 °C and ambient pressure.**

From figure 6.8 it is seen that doping the membrane with PA had a positive influence on the electrolysis performance. The current density of NAF-MEA2 (Nafion® 115 doped with PA) is 97 $mA \cdot cm^{-2}$ at 1.7 V compared to 37 $mA \cdot cm^{-2}$ at the same voltage for NAF-MEA1 (Nafion® 115 + ZrP composite MEA). The performance was further improved using a ternary PA doped Nafion® 115 + ZrP composite membrane. NAF-MEA3 had a current density of 152 $mA \cdot cm^{-2}$ at 1.7 V. The improvement of electrolyser performance between NAF-MEA2 and 3 could be caused by the better dimensional stability of the membrane in NAF-MEA3. However it could also be the result of NAF-MEA3 having a better water retaining capability due to the ZrP (as described by Bauer *et al.* [202]), *i.e.* part of the proton conductivity takes part through the vehicle mechanism where water act as a carrier of protons through the membrane and not only follows the Grotthuss mechanism where the PA network conducts the protons.

The three Nafion® 115 based MEAs were tested using two different flow patterns and it could be argued whether the polarisation curves can be compared to each other since there it a large difference in the flow patterns. NAF-MEA3 was tested using both flow patterns and the resulting polarisation curves are shown in figure 6.9.

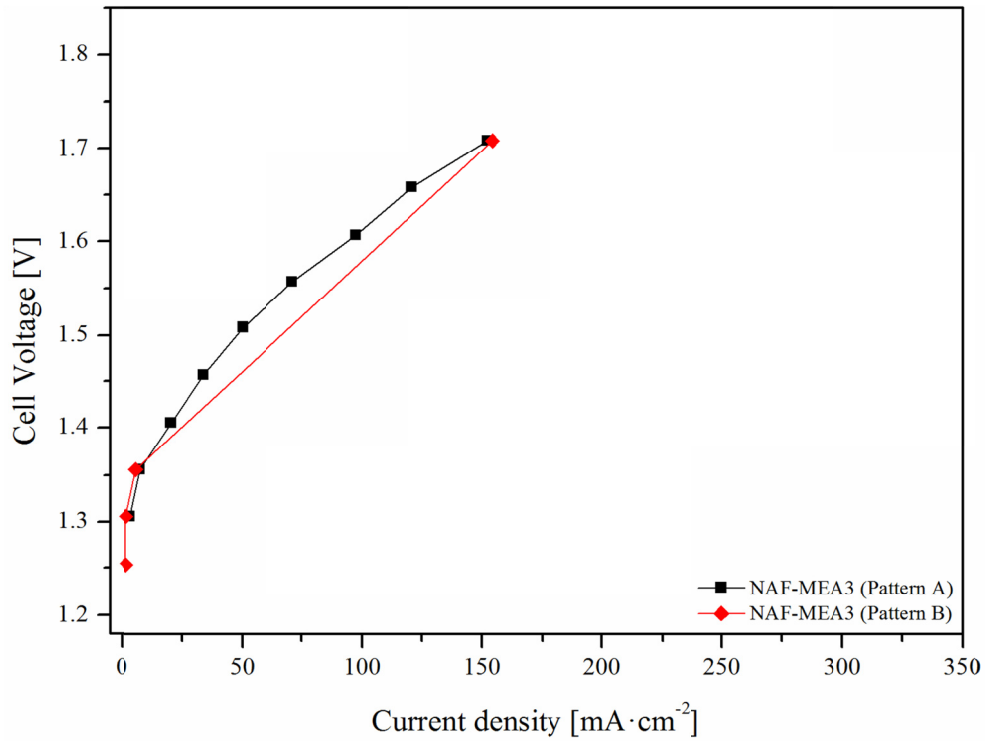


**Figure 6.9: Polarisation curves for NAF-MEA3 using two different flow patterns (see table 6.8), tested at 130 °C and ambient pressure.**

As it can be seen in figure 6.9 the polarisation curve for the asymmetric spiral flow pattern only has a few points, the reason being the measurement with the spiral flow pattern was used to test the durability of the MEA. However it is clear that the data points are overlapping for the two flow patterns, hence it is reasonable to compare the electrolysis data in figure 6.8 since no apparent difference in electrolyser performance can be distinguished. Nonetheless there is good reason to changing the flow pattern from the waffle-like type to the asymmetric spiral pattern. The force from the flow plate is more evenly distributed to the GDL using the spiral pattern compared to the waffle-like pattern *i.e.* the risk of ruining the MEA is less with the spiral pattern.

**Nafion® 212 composite membranes**

The next Nafion® membranes tested were a thinner version of Nafion® with an EW of 2100 $g \cdot eq^{-1}$, Nafion® 212 doped with PA and PA doped ternary composite Nafion® 212 and ZrP system. The non-doped Nafion® 212 and ZrP composite was omitted since the preliminary results from the Nafion® 115 and ZrP composite strongly indicated that the conductivity of these composites was quite poor at the operating conditions used in this study.

The PA doped Nafion® 212 (NAF-MEA4) had a $IrO_2$ loading of 3.39 $mg \cdot cm^{-2}$ with a Nafion® binder content of 5.1 wt.% and was post doped with approximately 0.3 $mg \cdot cm^{-2}$ PA. The GDL for the anode GDE was also 0.2 mm tantalum coated stainless steel felt. The membrane had a thickness of approximately 75 μm after the PA doping.

The Nafion® 212 + ZrP + PA ternary composite membrane (NAF-MEA5) also had a membrane thickness of approximately 75 μm. The anode loading was 3.05 $mg \cdot cm^{-2}$ $IrO_2$ with a Nafion® binder content of 5.0 wt.%. The post doping with PA gave a PA loading of 0.4 $mg \cdot cm^{-2}$. The gas diffusion layer was again of the 0.2 mm tantalum coated single layer felt type.

Both NAF-MEA4 and 5 were assembled directly in the cell, and tested with the spiral pattern at 130 °C and atmospheric pressure. In table 6.9 the characteristics for NAF-MEA4 and 5 are listed and figure 6.10 shows their polarisation curves.

**Table 6.9: Characteristics for MEAs with Nafion® 212 membrane.**

| MEA # | Anode $IrO_2$ [$mg \cdot cm^{-2}$] | Anode Binder Nafion® [wt.%] | PA [$mg \cdot cm^{-2}$] | Electrolyte Electrolyte type | Electrolyte Thickness [μm] |
|---|---|---|---|---|---|
| NAF-MEA4 | 3.39 | 5.1 | 0.3 | Nafion® 212 + PA | 75 |
| NAF-MEA5 | 3.05 | 5.0 | 0.4 | Nafion® 212 + PA + ZrP | 75 |

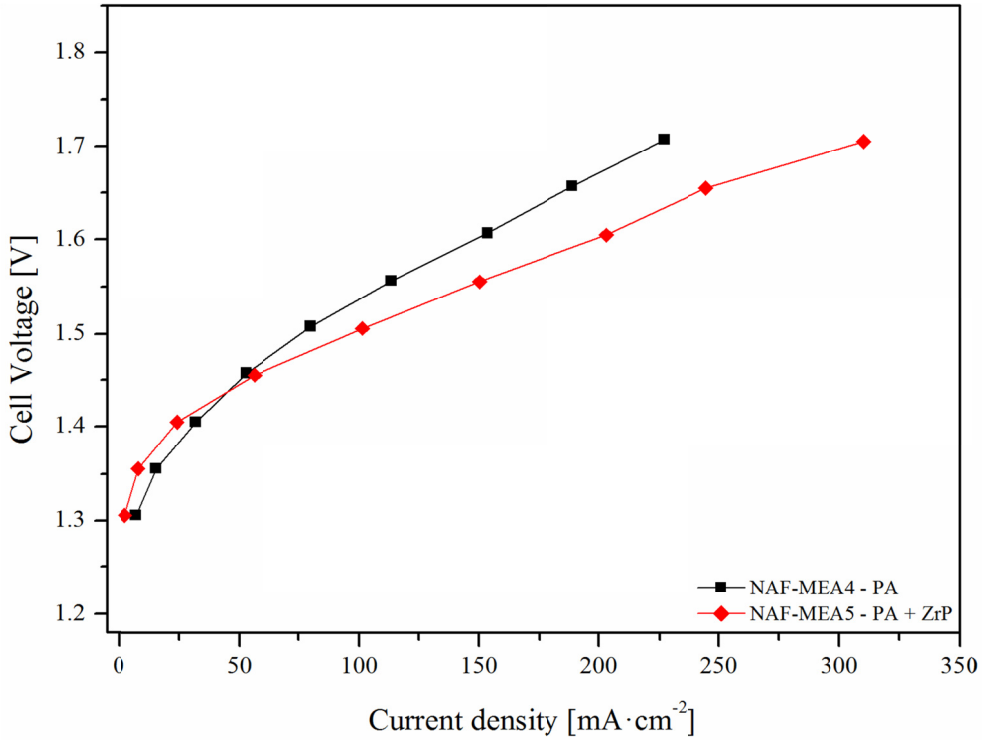


**Figure 6.10: Polarisation curves for Nafion® 212 MEAs (see table 6.9), tested at 130 °C and ambient pressure.**

In figure 6.10 the same trend as seen for the electrolyser performance for the Nafion® 115 based MEAs (see figure 6.8) is observed. The electrolyser performance got improved by the addition of ZrP to the membrane (NAF-MEA5). As it was the case for the Nafion® 115 the improvement of the electrolyser performance is due to lower ohmic resistance in the electrolysis cell. The same explanations as for Nafion® 115 based MEAs are still valid, the improvements are due to improved mechanical properties and better water retention.

### Nafion® 211 composite membranes

Finally MEAs of commercially available Nafion® 211 were tested. Nafion® 211 has the same equivalent weight as Nafion® 212, however the membrane thickness is much thinner. In this study the ternary composite membranes with Nafion® 211 had a thickness around 25 µm. Only MEAs using the ternary composite Nafion® 211 membrane were tested, since experimental evidence from the tests of

Nafion® 115 and 212 showed that the phosphoric acid doped composite membranes had the best electrolyser performance.

The MEA with the Nafion® 211 + ZrP and PA composite membrane (NAF-MEA6) had an anode loading of 3.22 mg·cm$^{-2}$ $IrO_2$, the Nafion® binder content in the anode was 5.7 wt.% and the doping level of post doped PA was 0.3 mg·cm$^{-2}$. The anode GDL was of the usual tantalum coated single layer felt type with a nominal thickness of 0.2 mm. The assembly of the MEA was done in the cell without prior hot pressing. NAF-MEA6 was tested using the spiral flow pattern at 130 °C and atmospheric pressure. Table 6.10 lists the anode and electrolyte characteristics for NAF-MEA6 and in figure 6.11 the polarisation curve for the electrolysis test is depicted.

**Table 6.10: Characteristics for MEA with Nafion® 211 membrane.**

| MEA # | Anode $IrO_2$ [mg·cm$^{-2}$] | Anode Binder Nafion® [wt.%] | PA [mg·cm$^{-2}$] | Electrolyte Electrolyte type | Electrolyte Thickness [µm] |
|---|---|---|---|---|---|
| NAF-MEA6 | 3.22 | 5.7 | 0.3 | Nafion® 211 + PA + ZrP | 25 |

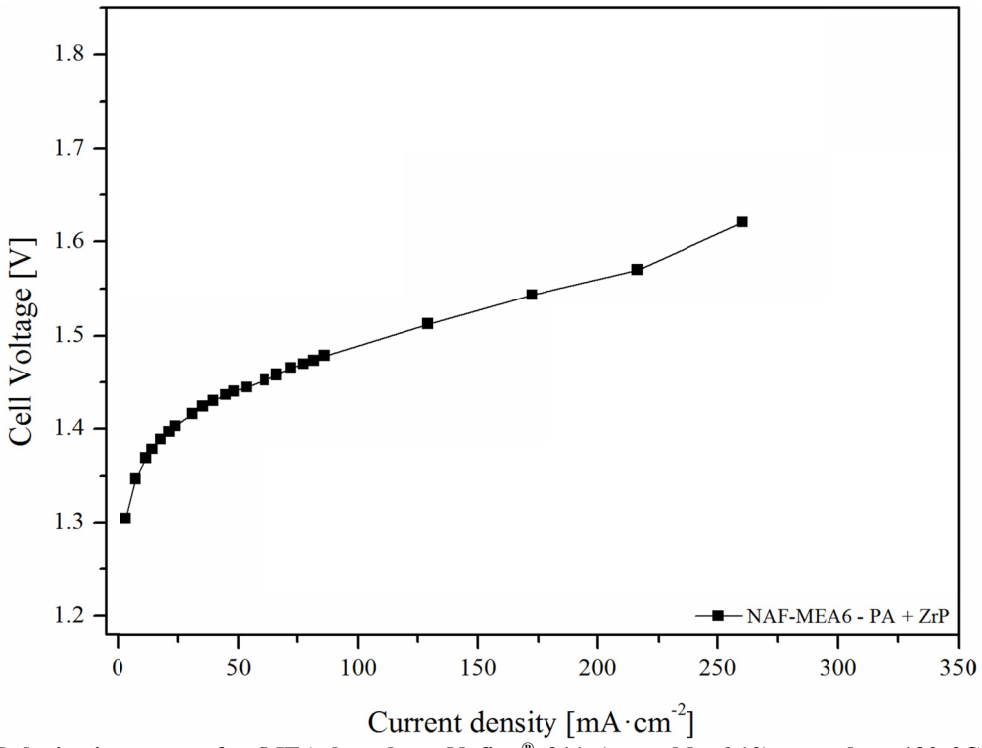


**Figure 6.11: Polarisation curve for MEA based on Nafion® 211 (see table 6.10), tested at 130 °C and ambient pressure.**

The polarisation curve for NAF-MEA6 in figure 6.11 is quite flat, since it is thinner than the previously tested membranes *i.e.* the contribution to the total ohmic resistance of the electrolysis cell from the ionic conductivity is lower.

**Comparison of different ternary PA doped Nafion® + ZrP composite membranes**

The difference in steepness of the slope for the polarisation curves for the three ternary composite membranes using different commercially available Nafion® membranes can be seen directly in figure 6.12.

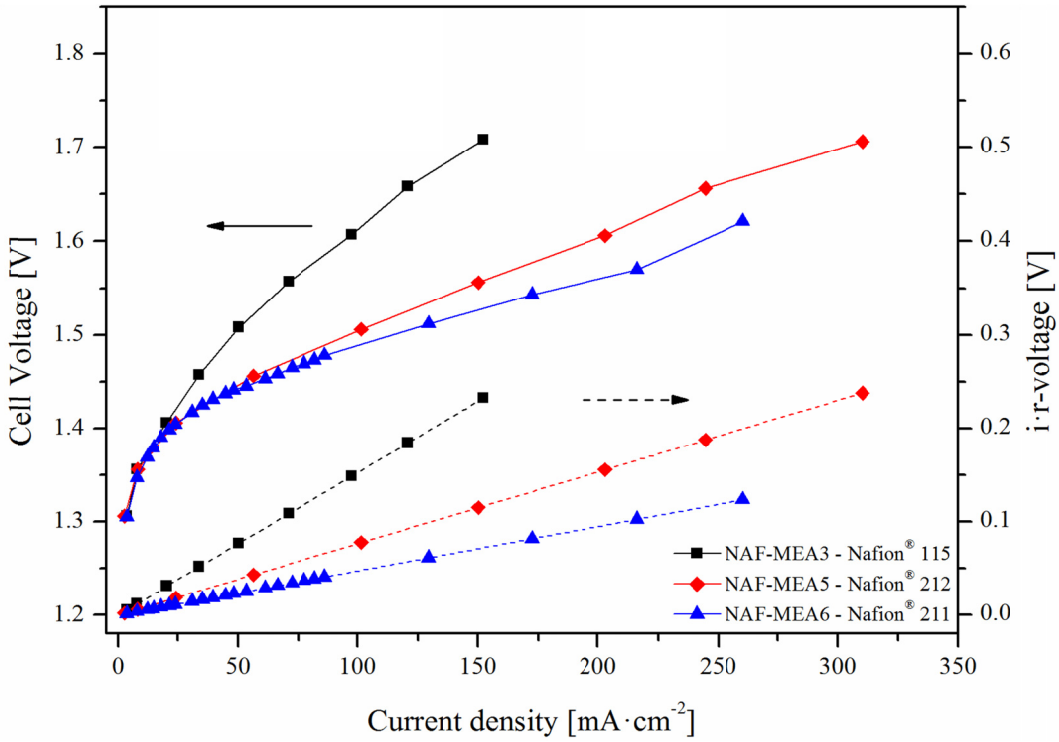


**Figure 6.12: Polarisation curves for the MEAs with PA doped ZrP composite Nafion® membranes (see tables 6.8-6.10), tested at 130 °C and ambient pressure. Dashed lines are calculated i·r-voltages. The arrows indicate the corresponding axis.**

In figure 6.12 the three polarisation curves for the PA doped ZrP composite Nafion® membranes are depicted as solid lines. Furthermore, the three calculated curves for the ohmic resistance contribution to

the voltage in the systems (dashed lines) are also plotted. The data for the ohmic resistance part was found as described in section 2.2.2 by doing regression on the data.

The ohmic resistance voltages from figure 6.12 clearly show that the overall ohmic resistance in the system goes down when the membranes thickness is lowered from 175 μm (NAF-MEA3) to 25 μm (NAF-MEA6). However it does not seem likely that the majority of ohmic resistance comes from the membrane's proton conductivity in these cases. If the ohmic resistance primarily was caused by the area specific resistance of the membrane, the slope of NAF-MEA3 ought to be 7 times greater (from the actual membrane thicknesses measured) than the slope of NAF-MEA6. To visualise the discrepancy between the overall ohmic resistance voltage and the electrolyte thickness, the i·r voltage can be normalised by dividing it with the thickness of the membrane. In figure 6.13 it is clearly illustrated that the ohmic resistance voltage not necessarily is controlled by the ionic conductivity of the membranes. There is no connection between the membrane thickness and the ohmic resistance contribution to the voltage, hence it seems clear that a major part of the resistance contribution must come from something else than the proton conductivity through the membrane.

This lack of connection between membrane conductivity and overall ohmic resistance was the same as was found for the PBI membrane MEAs. In the case of the ternary PA doped Nafion® composite membranes no proton conductivity data were determined. Hence plotting a curve for the estimated i·r-voltage contribution for the membrane is not feasible.

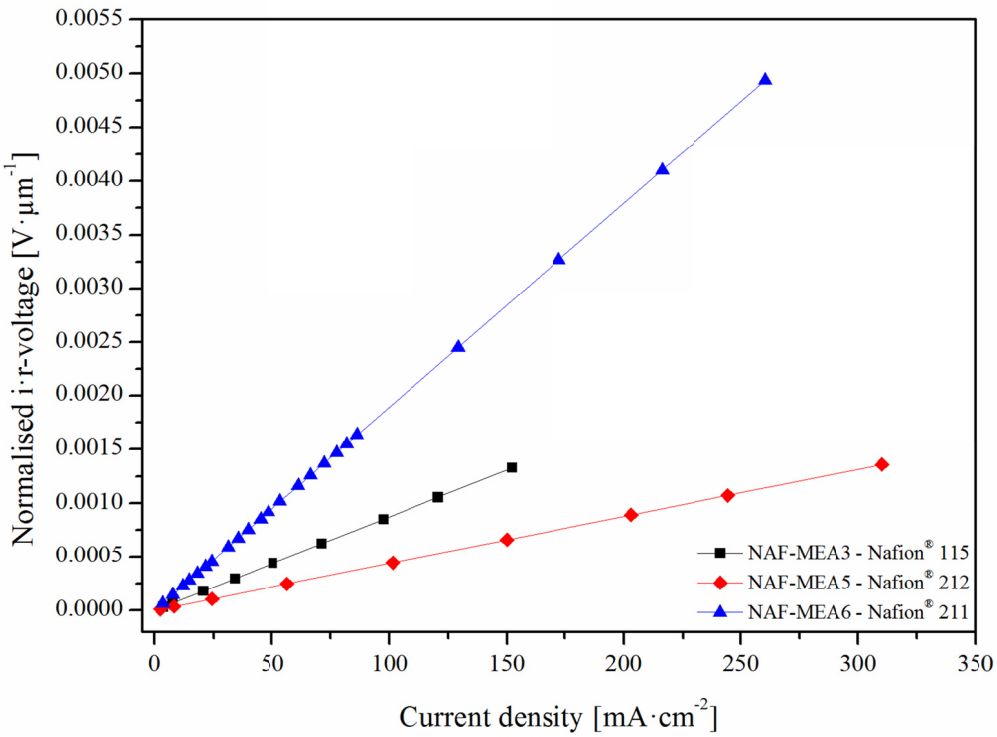


**Figure 6.13: Normalised i·r voltages from calculated data of i·r voltages.**

The reason for much larger normalised ohmic resistance contribution to the voltage for the Nafion® 211 MEA could lie in the fact that the Nafion® 211 membrane is very thin and after doping with PA it gets quite soft. The membrane's loss of dimensional stability can imply that the contact between membrane and electrodes is lost, *i.e.* increasing the interfacial contact resistance between these two. Furthermore, it was quite challenging to work which such thin and soft membranes. Around 85 % of the MEAs tested with this type membrane failed during assembly or shortly after the electrolysis test was started. So even though a gain in performance is achieved by decreasing the membrane thickness, the difficulties in handling these MEAs and the high uniformity requirements to the surface of the gas diffusion electrodes can limit the practical usability of this membrane type. This is especially true since the gain in performance is not proportional to the decrease of thickness due to larger interfacial resistance, as these initial experiments indicate.

**Comparison of commercial and in-house cast ternary PA doped Nafion® composite membranes**

Apart from PA doped Nafion® + ZrP composite membranes from commercial Nafion® membranes similar composite membranes were tested using recast Nafion® membranes cast in-house at DTU. A MEA with a PA doped recast Nafion® ternary composite membrane was prepared (NAF-MEA7). The anode loading of NAF-MEA7 was 3.53 mg·cm$^{-2}$ $IrO_2$ and the Nafion® binder content was 6.2 wt.%. The post doping level of PA on the anode was 0.3 mg·cm$^{-2}$. As earlier tested NAF-MEAs a 0.2 mm thick tantalum coated felt was used as GDL as well as the MEA was assembled directly in the cell and tested with the asymmetric spiral flow pattern. The doped composite membrane had a thickness of approximately 65 μm. In table 6.11 the characteristics for both the anode and electrolyte are summarised. In figure 6.14 the electrolyser performance of NAF-MEA7 is compared to the performance of the commercial ternary Nafion® composite MEAs.

**Table 6.11: Characteristics for MEA with PA doped recast Nafion® composite membrane.**

| MEA # | Anode | | | Electrolyte | |
|---|---|---|---|---|---|
| | $IrO_2$ [mg·cm$^{-2}$] | Binder Nafion® [wt.%] | PA [mg·cm$^{-2}$] | Electrolyte type | Thickness [μm] |
| NAF-MEA7 | 3.53 | 6.2 | 0.3 | Recast Nafion® + PA + ZrP | 65 |

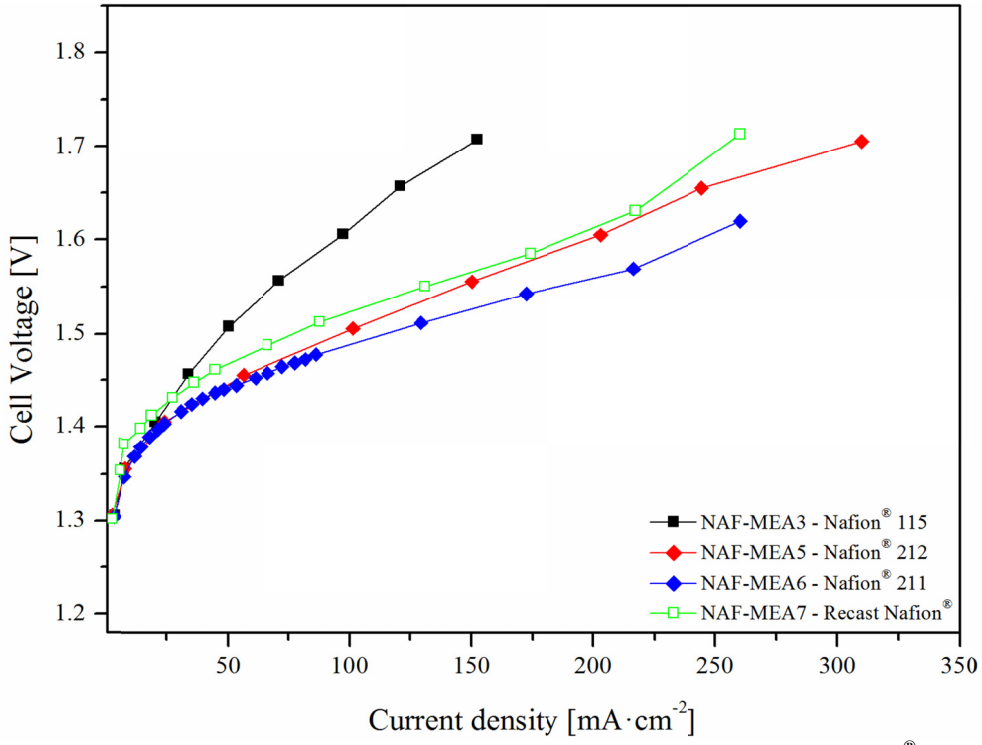


**Figure 6.14: Polarisation curves for PA doped ZrP composite MEAs from commercial Nafion® and recast Nafion® membranes prepared in-house (see tables 6.8-6.11), tested at 130 °C and ambient pressure.**

In figure 6.14 it can be seen that the performance of NAF-MEA5 with a Nafion® 212 membrane (approximately 75 µm) is more or less identical with the performance of NAF-MEA7 which has a thickness of approximately 65 µm. Since the thicknesses of the two MEAs are quite close to each other it is not that surprising that the performance is similar, only indicating that in this experimental setup in-house cast membranes had similar properties. The manufacturing procedure for thin Nafion® 212 and 211 membranes is the same, since they likewise are cast from a Nafion® solution and not extruded as the Nafion® membranes with an EW of 1100 $g \cdot eq^{-1}$.

### Durability of Nafion® membrane

Since it was found that the PA doped PBI membranes were not stable in the steam electrolysis experiments conducted, the durability of PA doped Nafion® composite membranes was examined. NAF-MEA3 tested using the spiral flow pattern showed quite promising durability compared to the PBI MEAs. The durability test, where conducted by keeping a constant voltage of 1.7 V and

monitoring the current density. Figure 6.15 shows the current density and cell voltage as function of time. The data is smoothed by averaging the data over five minutes time intervals (150 data points).

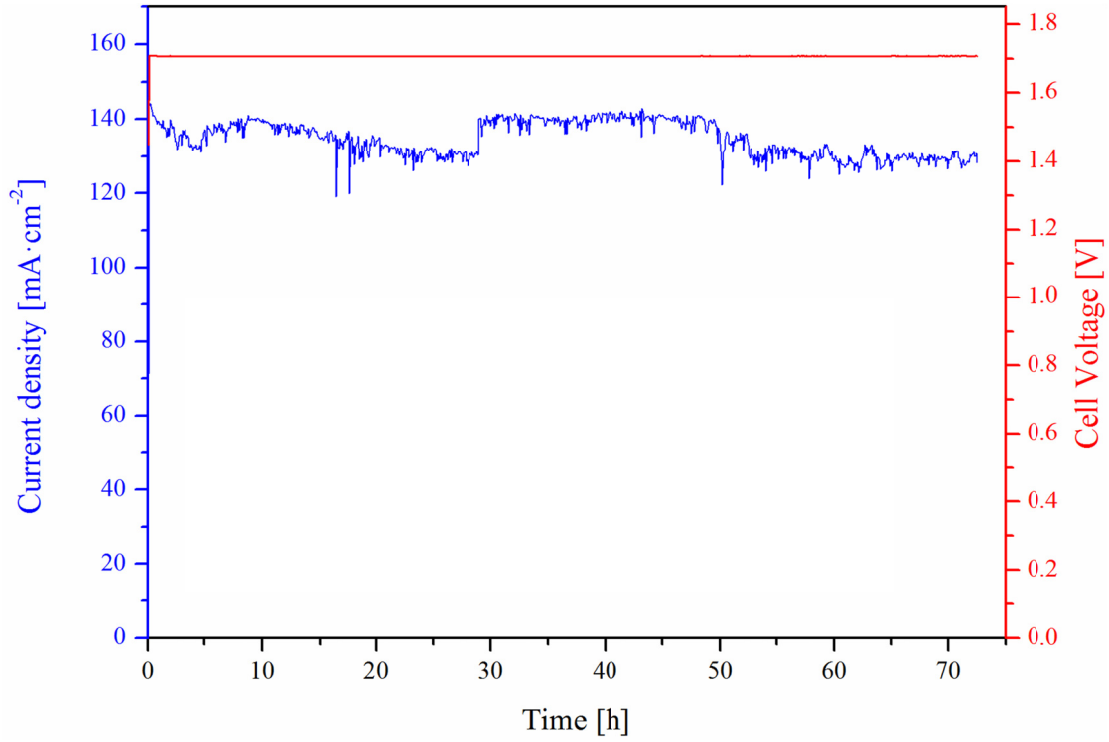


**Figure 6.15: Durability of NAF-MEA3, tested at 130 °C and ambient pressure. Data are averaged over five minutes.**

From figure 6.15 it can be seen that the current density of NAF-MEA3 is not completely constant when the cell voltage is fixed to 1.7 V. With some fluctuation in the current density during the test period, the overall decline in current density is 12 mA over a time period of 72 hours giving *i.e.* a degradation of 0.17 $mA \cdot h^{-1}$. Even though the electrolyser performance do degrade some over time, the PA doped composite Nafion® 115 + ZrP membrane does not fail when tested a 130 °C and atmospheric pressure at a reasonable cell voltage. However the current density at this voltage is low and should be improved considerably, *e.g.* by using thinner Nafion® membranes which has shown approximately double the current density (NAF-MEA5 – 75 µm, see figure 6.14) at similar cell voltage.

## CCM Anodes for PA doped Nafion® 212 membranes

In an attempt to improve the electrolyser performance, effort was once again put into making catalyst coated membrane anodes by the decal method. Four MEAs were prepared using a PA doped Nafion® 212 membrane as electrolyte. The MEAs had the Nafion® binder content varied from approximately 33 to 10 wt.%. The anodes were transferred to the membrane by hot pressing for 10 minutes at 140 °C using a pressure of approximately 10 MPa, furthermore the pressure was maintained while cooling the hot press. In table 6.12 the anode and electrolyte characteristics for the four MEAs are listed.

**Table 6.12: Characteristics for MEAs in decal experiment.**

| MEA # | Anode | | | Electrolyte | |
|---|---|---|---|---|---|
| | $IrO_2$ [mg·cm$^{-2}$] | Binder Nafion® [wt.%] | PA [mg·cm$^{-2}$] | Electrolyte type | Thickness [µm] |
| NAF-MEA8 | 2.5 | 33 | 0.12 | Nafion® 212 + PA | 62 |
| NAF-MEA9 | 2.5 | 27 | 0.14 | Nafion® 212 + PA | 59 |
| NAF-MEA10 | 2.3 | 20 | 0.14 | Nafion® 212 + PA | 62 |
| NAF-MEA11 | 2.0 | 11 | 0.16 | Nafion® 212 + PA | 60 |

**Table 6.13: Transfer of anode from PTFE support to membrane in decal experiments.**

| MEA # | Binder Nafion® [wt.%] | Binder Nafion® [vol.%] | Transfer percentage [%] |
|---|---|---|---|
| NAF-MEA8 | 33 | 75 | 99 |
| NAF-MEA9 | 27 | 68 | 97 |
| NAF-MEA10 | 20 | 59 | 87 |
| NAF-MEA11 | 11 | 43 | 87 |

The transfer percentages for the four decal method PA doped Nafion® 212 MEAs (NAF-MEA8-11) are summarised in table 6.13. It can be seen that the transfer percentage from the PTFE substrate diminish as the binder content of Nafion® is lowered. However a factor which cannot be seen from the percentages in table 6.13 is the uniformity of the anode transfer. As the binder content was lowered it became increasingly hard to get a uniform transfer to the membrane. Especially in the case of NAF-MEA11 the uniformity was quite poor. In figure 6.16 the four polarisation curves for the decal experiments are depicted. From these it is clear that the electrolyser performance is dependent on the binder content in the anode. NAF-MEA8 and 9 with a binder content of 33 and 27 wt.% respectively

have a considerably worse performance than NAF-MEA10 and 11 which had a Nafion® binder content around 20 and 11 wt.% respectively.

The reason that it is not possible to see any significant improvement by going from 20 to 11 wt.% is most likely due to the fact that NAF-MEA11 (11 wt.% binder in anode) had a far less uniform anode transfer. Hence the geometric electrode area was in reality lower than the other 3 MEAs tested in this series, although when calculating the current density for NAF-MEA11 the geometric area of 10 $cm^2$ (actual geometric area of electrode on the PTFE substrate) was used, since a precise determination of the transferred electrode area was impossible to obtain.

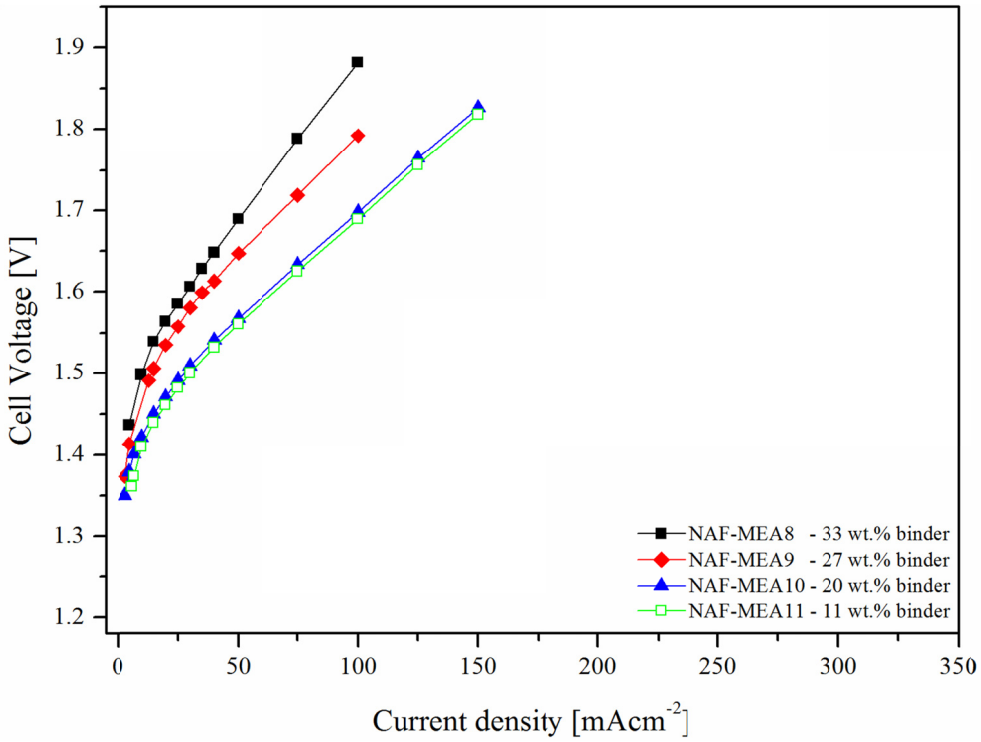


**Figure 6.16: Polarisation curves for decal experiment MEAs (see table 6.12), tested at 130 °C and ambient pressure.**

In figure 6.17 three photographs of PTFE pieces with the catalyst layer sprayed on PTFE before and after being hot pressed to the membrane according to the decal procedure are shown.

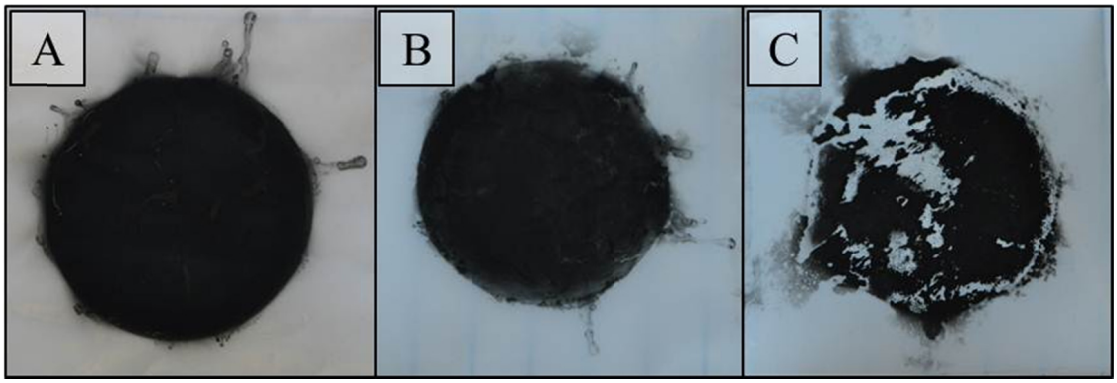


**Figure 6.17: Photographs of PTFE pieces with catalyst layer. A: PTFE before hot press, B: PTFE after hot press and C: PTFE after hot press. The diameters of all the electrodes are 38.5 mm.**

The pictures in figure 6.17 are not from the decal experiments presented above, however they perfectly illustrate what is meant by the concepts of uniform and non-uniform transfer from the PTFE substrate to the membrane. In picture A an electrode before it was hot pressed to the membrane is shown. Picture B shows the PTFE piece after the electrode had been transferred to the membrane. In the case on picture B the transfer percentage was only 52 % (the electrode had a binder content of 15 wt.%), although the transfer percentage was low, the uniformity of transfer was quite good. The electrode transfer from the PTFE piece on picture C was as low as 29 % and it is clear that the catalyst layer had been transferred very unevenly, in certain places the transfer had been almost perfect and in others nothing had been transferred. The catalyst layer on picture C also had a binder content of 15 wt.%, however in picture C it was a cathode with Pt/C as catalyst that was hot pressed to the membrane, where it in picture B was an anode using $IrO_2$ as catalyst.

Using high binder content in the electrode promotes the transferring capability of the electrode layer to the membrane, however as it was seen in figure 6.16 high binder content depresses the electrolyser performance. A binder content of 33 wt.% can be recalculated to a volume percentage of 75 vol.%, assuming that Nafion® has a density of approximately 2 $g \cdot cm^{-3}$ (in literature values of 1.8 $g \cdot cm^{-3}$ [214] and 2 $g \cdot cm^{-3}$ [215] are given) and $IrO_2$ has a density of 11.7 $g \cdot cm^{-3}$ [54]. In table 6.13 are both weight and volume percentages for the four CCM MEAs summarised. With such a high volume percentage of electrical insulating binder material in the anode, it seems very likely that the loss in performance can be attributed to increased resistance. A high volumetric percentage increases the probability of relative

large portions of the catalyst particles being totally enclosed by the binder material, *i.e.* effectively lowering the triple-phase boundary area onto which the electrochemical reaction takes place [216]. The reason why no clear trend in the ohmic resistance part of the polarisation curves could be observed, as would be expected, can be that the actual area of the anodes varied quite a bit. Another factor which should be noted from figure 6.16, is that the cell voltage starts from a considerably higher level for NAF-MEA8 (33 wt.% Nafion® binder), which also indicate that the catalytic available area is smaller.

A possible route to circumvent the issue of mismatch between the binder content necessary to ensure proper anode transfer and an optimum content in the electrode structure, hence avoiding isolating the $IrO_2$ particles, could be applying an extra layer of binder on top of the catalytic layer. This extra binder layer should then enhance the transferability of the electrode without increasing the bulk content of binder in the anode. This concept is much like experiments done by Zhang *et al.* [115] and Wang *et al.* [216] where an extra layer of Nafion® binder is sprayed to the membrane to improve the contact between membrane and electrodes. A preliminary test experimenting with this technique did however not show promising results. An electrode layer was sprayed on top of a PTFE substrate, doped with PA and subsequently sprayed an extra layer of Nafion® binder on top of the doped electrode layer. The nominal binder content in the electrode layer was 4 wt.% and the top layer of binder was 0.25 $mg \cdot cm^{-2}$, the hot pressing procedure was unchanged using 140 °C, 10 minutes and approximately 10 MPa with cooling under pressure. However the transfer percentage was lowered to only 79 %. This could possibly be a result of a non-optimised hot pressing procedure, or that the loading of the Nafion® top coating layer was far from optimal.

### 6.2.4 Summary

It was found that ternary composite membranes of Nafion® and zirconium phosphates doped with phosphoric acid gave a better performance than Nafion® membranes which was doped just with PA. A possible explanation of this phenomenon could be that part of the proton conductivity is handled by the vehicle mechanism, where the water activity in the membrane is crucial for the performance. Another possible reason could be the ZrP as inorganic filler also improves the mechanical properties of the composite membrane. By a better dimensional stability of the membrane a better contact between the

membrane and electrodes can be maintained *i.e.* resulting in lower contact resistance. It was found that thinner composite membranes based on commercial Nafion® membranes improved the electrolyser performance, mainly by lowering the ohmic resistance contribution to cell voltage. In an attempt to check if the lower resistance only was a function of the membrane thickness, the ohmic resistance contribution was normalised with the membrane thickness. It was found that this could not explain the trend. The normalised ohmic resistance voltage contribution was much higher for the thin PA doped Nafion® 211 composite membrane than for the two thicker composite membranes. Hence it was concluded that several other factors than proton conductivity of the membrane contribute to the ohmic resistance of the system. The only approximately 25 μm thin Nafion® 211 membrane was also harder to manage during MEA preparation and had a considerably higher percentage of failure. Due to the higher failure rate of thin Nafion® composite membranes, these were deemed unfit for further testing.

Experiments with the decal method of transferring the electrode from a substrate to the membrane by hot pressing were conducted. It was found that there exist a mismatch between the necessary amount of Nafion® binder content in the anode to ensure proper transfer to the membrane and the optimum for electrolysis performance. High amounts of binder were necessary for good transfer, however good electrolyser performance was favoured by low amounts of binder. Preliminary experiments with applying an extra layer of binder on top of the catalyst layer before hot pressing did not give the expected improvement in electrode transfer. However this result could also be explained by lack of time to optimise the hot pressing conditions and the optimum loading for the extra binder layer. As a consequence of this finding transferring anodes to the membrane by the decal method was abandoned for further experiments with PA doped PFSA membranes.

## 6.3 Aquivion™ + PA

Durability data for PA doped Aquivion™ were obtained in collaboration with guest Ph.D. student Junyuan Xu. The durability data was recorded in the DTU steam electrolysis setup.

Due to the limited success with getting reasonable result using Nafion® membranes as the electrolyte in steam electrolysis mode, a new membrane as electrolyte was a necessity. The lack of success could possibly be explained by the limited dimensional stability of the PA doped Nafion® and composite membranes of Nafion® and ZrP. The softening of the membrane at the operation temperature of 130 °C, would mean high interfacial contact resistance, *i.e.* quite high ohmic resistance contributions to the overall cell voltage. As described in section 2.5 the new class of PFSA membranes with shorter side chains, SSC-PFSA, exhibit greater dimensional stability [33], this and their improved ability to retain water in the higher temperature range [34] makes them an interesting class of membranes for steam electrolysis at elevated temperature.

The membranes tested in this section were commercially available membranes from Solvay Solexis by the trade name Aquivion™. Although Aquivion™ exhibit improved water retention compared to classical PFSA membranes as Nafion® it is not sufficient to have reasonable proton conductivity at 130 °C, hence the Aquivion membranes were doped with PA using the same technique and conditions described in section 6.2.1.

Several different parameters were tested *e.g.* two new flow patterns, variations of anode loading, importance of assembly procedure and the importance of GDL. Several of the results in this section are submitted to International Journal of Hydrogen Energy titled: *PEM steam electrolysis at 130 °C using a phosphoric acid doped short side chain PFSA membrane* the manuscript is attached as paper II in chapter 14.

The proton conductivity and mechanical strength measurements were conducted by David Aili, PhD at Technical University of Denmark.

### 6.3.1 Proton conductivity

The proton conductivity of PA doped membranes is strongly dependent on the doping level of the membrane. It was found that the doping level of melt extruded Aquivion™ (EW 790 $g \cdot eq^{-1}$) had a considerably higher doping level than Nafion® membranes.

**Table 6.14: Phosphoric acid content in different PFSA type membranes. Membranes doped at 150 °C in 85 wt.% for 16 hours [203].**

| # | PFSA membrane type | PA content [wt.%] | Relative PA level |
|---|---|---|---|
| 1 | Nafion® 212 | 19.5 | 5.2 |
| 2 | Nafion® 115 | 25.7 | 3.8 |
| 3 | 50 µm recast Nafion® | 36.6 | 6.5 |
| 4 | Aquivion™ | 43.9 | 6.3 |

In table 6.14 the observed PA content of selected PFSA membranes and the relative PA content per sulfonic acid group are listed. By calculating the relative PA acid content of the membrane, *i.e.* the number of PA per unit of sulfonic acid group, it can be seen that the relative PA doping level is quite constant around 5-6 PA molecules per sulfonic acid group. However, it is clear that Aquivion™ has much higher total PA content than other commercial available PFSA membranes. This should considerably improve the proton conductivity *i.e.* ensuring enhanced electrolyser performance. The reason for the high total PA content in Aquivion™ is most likely due to the considerably lower equivalent weight.

### 6.3.2 Mechanical strength

Mechanical strength tests were performed as described above in section 6.2.2. Measurements were performed on both pristine and PA doped Aquivion™ membranes and recast Nafion® membranes. In figure 6.18 some representative stress-strain curves are shown for PA doped recast Nafion® and Aquivion™ membranes. The doping level of PA was 34 wt.% and 44 wt.% for the recast Nafion® and Aquivion™ respectively [203]. In table 6.15 the mechanical values for both pristine and PA doped recast Nafion® and Aquivion™ are summarised.

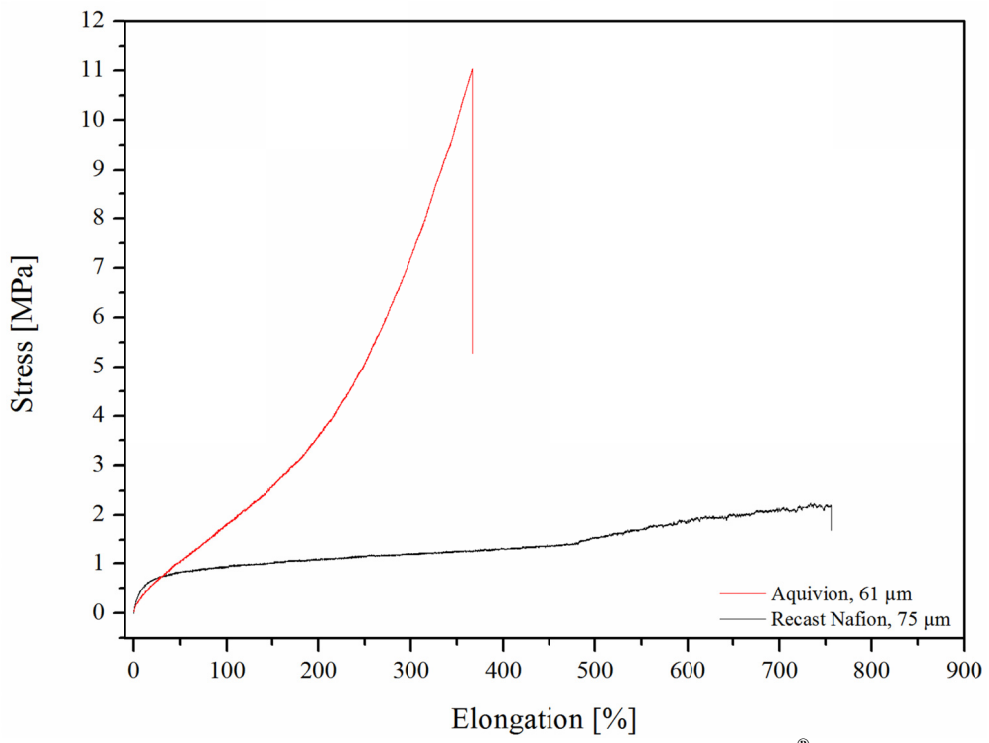


**Figure 6.18: Representative stress-strain curves at 130 °C for PA doped recast Nafion® and Aquivion™ membranes.**

From figure 6.18 it is clear that PA doped Aquivion™ exhibit much greater mechanical strength, *e.g.* the engineering tensile stress at break is approximately 4 times higher for the PA doped Aquivion than for PA doped recast Nafion®. The maximal strain is also lower for Aquivion than for Nafion®.

**Table 6.15: Summary of mechanical data for pristine and PA doped Nafion® and Aquivion™ membranes, tested at 130 °C [203].**

| | Pristine | | PA doped | |
|---|---|---|---|---|
| | Recast Nafion® | Aquivion™ | Recast Nafion® | Aquivion™ |
| Young's modulus [MPa] | 2.9 ± 0.5 | 113.7 ± 24.3 | 5.5 ± 0.8 | 8.8 ± 1.5 |
| Engineering tensile stress at break [MPa] | ≈ 0 | 13.8 ± 2.9 | 2.3 ± 0.2 | 10.0 ± 0.8 |
| Elongation at break [%] | > 800 | 166 ± 14 | 732 ± 49 | 347 ± 13 |

From table 6.15 it can be seen that the Young's modulus for the recast Nafion® is improved by the doping with phosphoric acid. The reason for this could at least partly be due to the fact that during the doping procedure the membrane is heated to 150 °C for an extended period of time. It is known from literature that heat treatment of recast Nafion® membranes can give better mechanical properties to the

membrane [217]. Hence it is possible that something similar can be observed during the doping procedure. The reason for the change in Nafion®'s $T_g$ could also be that the glass transition temperature of the membranes increases with PA doping and this give the PA doped Nafion membrane® its improved Young's modulus, whereas Aquivion™ which already has $T_g$ above 130 °C doesn't benefit from the improved $T_g$, but only experience the plasticising effect of PA.

Aquivion™ on the other hand has considerably less mechanical strength after the PA doping procedure. The Young's modulus of the membrane changes from around 100 MPa as pristine membrane to approximately 10 MPa after the PA doping. As mentioned in section 6.2.2 a possible explanation to this is that PA has a plasticising effect on the membrane much like it is the case for PBI. The plasticising effect of PA is believed to be due the swelling of the membrane, hence lowering the attractive forces between the macromolecules in the membrane [212, 213]. Although the mechanical properties of PA doped Aquivion™ are dramatically worsened compared to the pristine Aquivion™ membrane they are still slightly better than PA doped recast Nafion®, even with slightly thinner membranes.

### 6.3.3 Electrolysis tests

Electrolysis test were performed on 12 different MEAs which are listed in table 6.16. In the table it is possible to see the parameters for each MEA, how they differ in each comparison series and the data which are kept constant for each MEA. In the table the individual comparison series are marked by grey.

Common for all the MEAs are that both the anode and cathode are made as GDE with the catalyst layer sprayed to the GDL. Tantalum coated stainless steel and wet-proofed non-woven carbon cloth with a micro porous support layer for the anode and cathode respectively. The catalyst loading of the cathodes were approximately 0.8 $mg \cdot cm^{-2}$ Pt. In the case of the MEAs which were hot pressed before cell assembly the MEA hot pressing procedure was as follows: 2 minutes at 155 °C with at pressure of approximately 5 MPa. Two different batches of tantalum coated steel felt GDL were tested, one where the felt consisted of two different fibre thickness making a double layer felt (Batch 1) and another felt

which had the same fibre thickness throughout the whole felt making a single layer felt (Batch 2). More information and results were given on the tested anode GDLs in chapter 5 above. As in the earlier described electrolyser tests the cell was tested at 130 °C and atmospheric pressure.

**Table 6.16: Data for tested MEAs with grey indicated the varied component in each series**

| | Anode | | | Testing condition | |
|---|---|---|---|---|---|
| MEA # | $IrO_2$ [mg·cm$^{-2}$] | Binder [wt.%] | GDL Batch # | Flow pattern | Hot pressed |
| AQU-MEA1 | 3.61 | 15 | 1 | B | No |
| AQU-MEA2 | 3.66 | 15 | 1 | C | No |
| AQU-MEA3 | 3.41 | 15 | 1 | D | No |
| AQU-MEA4 | 1.44 | 15 | 1 | D | No |
| AQU-MEA5 | 1.01 | 15 | 1 | D | No |
| AQU-MEA6 | 1.02 | 15 | 1 | D | Yes |
| AQU-MEA7 | 1.05 | 10 | 1 | D | Yes |
| AQU-MEA8 | 1.11 | 20 | 1 | D | Yes |
| AQU-MEA9 | 1.06 | 5 | 1 | D | Yes |
| AQU-MEA10 | 0.98 | 5 | 1 | D | Yes |
| AQU-MEA11 | 0.93 | 5 | 2 | D | Yes |
| AQU-MEA12 | 1.22 | 5 | 2 | D | Yes |
| Constant for all MEAs | | | | | |
| Cathode | Pt loading of 0.8 mg·cm$^{-2}$, Binder loading of 30 wt.% | | | | |
| Membrane | PA doped Aquivion™ Thickness 116pprox.. 60 µm | | | | |

**Variation of flow pattern**

Three different flow patterns were tested *i.e.* an asymmetric spiral pattern, a straight channelled pattern with 2 mm wide flow channels and finally a pattern also with straight channels but with a channel width of 1 mm, see pattern B, C and D respectively in figure 4.4. The polarisation curves for the MEAs tested with the three flow patterns are shown in figure 6.19.

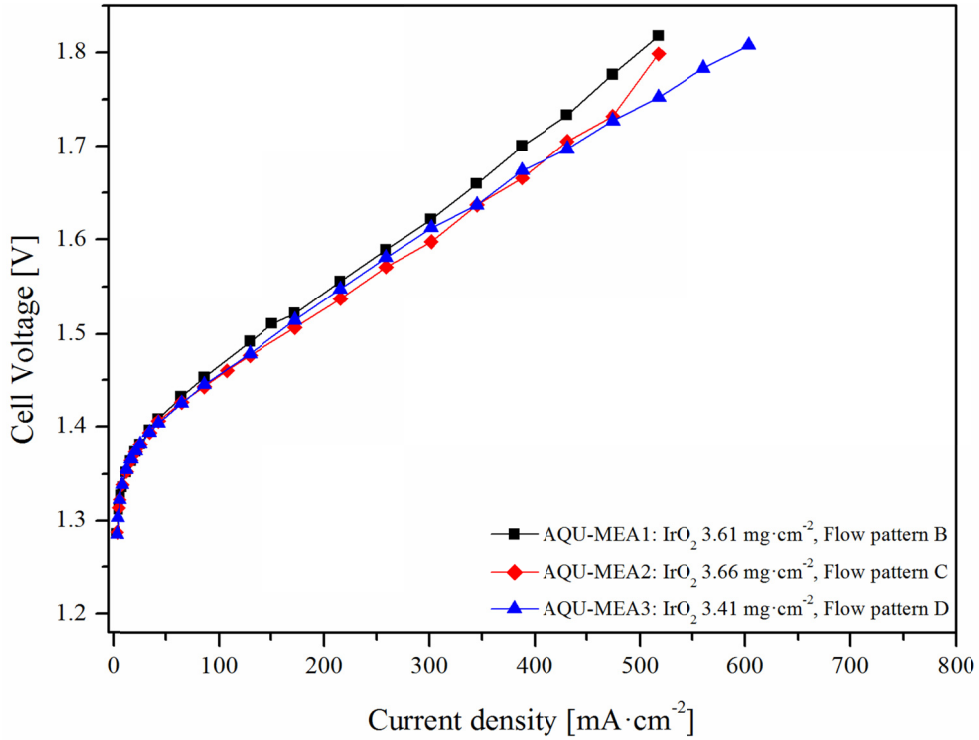


**Figure 6.19: Polarisation curves for three MEAs (see table 6.16). Variation of the flow pattern: Flow pattern B is an asymmetric spiral and flow patterns C and D are both straight channel with different channel widths, see table 4.1 for more information. The polarisation curves were obtained at 130 °C and ambient pressure.**

From figure 6.19 it can be seen that the performance for the MEAs at low current densities to around 100 $mA \cdot cm^{-2}$ is the same for all three flow patterns. However at larger current densities the performance of the two MEAs (AQU-MEA2 and 3) with straight channelled flow patterns show a slightly improved performance. A slightly lower slope on the linear part of the polarisation curves is observed indicating lower resistance in the systems. At 475 $mA \cdot cm^{-2}$ the potential of the MEAs in the straight flow channels experiments is 50 mV lower than the potential for the MEA (AQU-MEA1) tested in the cell using a spiral flow pattern. However above 475 $mA \cdot cm^{-2}$ the voltage in the electrolysis experiment using 2 mm straight channels show signs of mass transportation limitations. This could partly be a consequence of the flow pattern design, another and more likely possibility is that the mass transport limitation is governed by problems in the steam feed due to temperature instability in the evaporator design. The contact resistance between flow plates or in the case of stacks bipolar plates and GDL is dependent on the 'land' or 'ribs' area in the flow pattern. In literature ratios between channel and land in flow patterns are reported to be between 1 and 3 [218]. Based on the

hypothesis that an increased 'land' area, *i.e.* lower channel/land ratio, lowers the contact resistance between the flow plate and GDL the results in figure 6.19 can be evaluated. The channel to land ratios for the three flow patterns are: 1.569 (B), 1.479 (C) and 1.474 (D). Hence it makes sense that the best preforming MEA in this test series was AQU-MEA3 tested with pattern D. The improved performance with flow pattern D probably comes from shorter channel lengths than in pattern B and having a slightly improved electrical contact and flow distribution compared to both the B and C pattern, due to the narrower land width.

It is clear from figure 6.19 the difference in electrolyser performance under testing conditions are very minute, thus making it hard to make a firm conclusion whether one flow pattern is significantly better than the rest. The three tested flow patterns performed reasonable well under the tested conditions, however since the narrower channelled straight flow pattern (D) did perform marginally better and since this improvement makes sense from a theoretically point of view, it was chosen to continue experiments with this flow pattern.

**Variation of anode loading**

Using flow pattern D the importance of the anode catalyst loading was examined. Three MEAs with different anode loading varying from approximately 3.5 to 1 $mg \cdot cm^{-2}$ $IrO_2$ were tested. In figure 6.20 the polarisation data for the three tested MEAs is plotted.

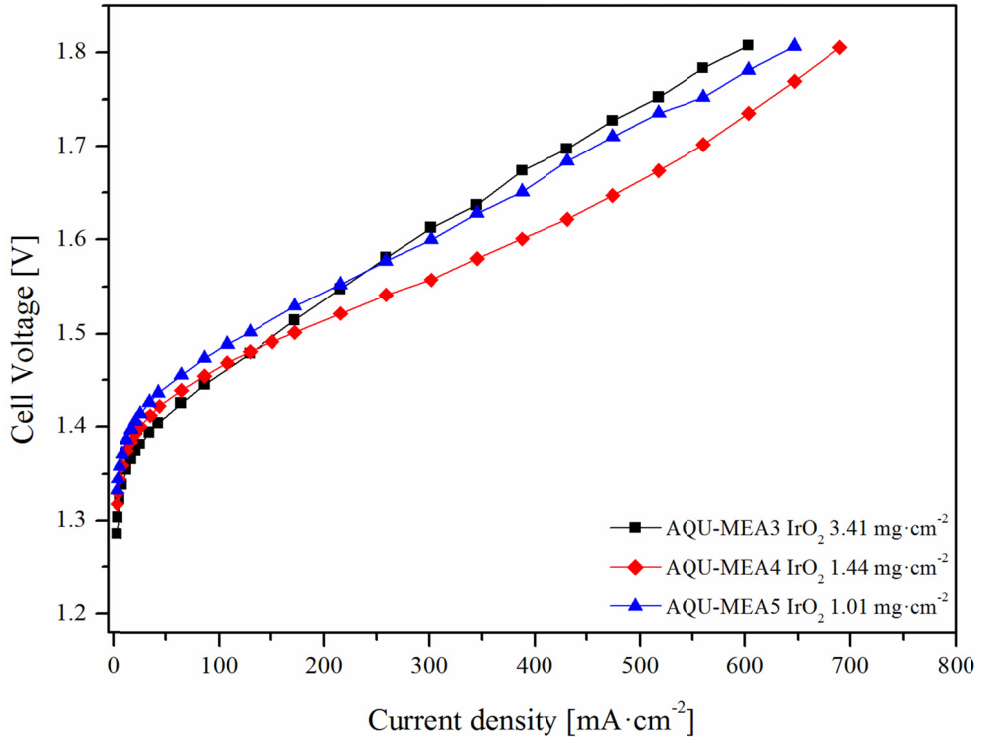


**Figure 6.20: Polarisation curves for AQU-MEA3-5 (see table 6.16). The $IrO_2$ loading was varied from 1 mg·cm$^{-2}$ to 3.4 mg·cm$^{-2}$, tested at 130 °C and ambient pressure.**

The polarisation curves in figure 6.20 for the variation of anode loading test series shows that high anode loadings will not automatically be beneficial for the performance. The data suggest that the optimum anode loading is around 1.5 mg·cm$^{-2}$ $IrO_2$, although further investigations should be carried out to verify this result. It can be seen that at higher current densities (> 475 mA·cm$^{-2}$) AQU-MEA4 experience mass transport limitations. This was most likely due to temperature instabilities in the evaporator. Fluctuations in the evaporator temperature and droplets of condensed water bursting out from the outlet gas tubing were observed to correspond with the fluctuations in the cell voltage.

Similar results for anode loadings have been reported for PEM liquid water electrolysis where Ma *et al.* [126] found that the optimal anode loading was around 2.0 – 2.5 mg Ir per cm$^2$ for a cell tested at 30 °C and ambient pressures with a binder content of 30 wt.% Nafion®. The loadings examined were between 1 and 3.5 mg Ir per cm$^2$. Hence the finding from this work is in correlation with the conclusion from Ma *et al.* [126] and subsequently MEAs were tested with a low iridium oxide loading on the anode.

**Variation of MEA assembling procedure**

Another parameter which has been proposed having a substantial influence on the electrolysis performance is the assembly of the MEA, hence the importance of hot pressing the MEA before electrolysis test was studied. Two different ways of assembling the MEA were investigated, direct assembly of the MEA in the cell without prior hot pressing and hot pressing the MEA before cell assembly.

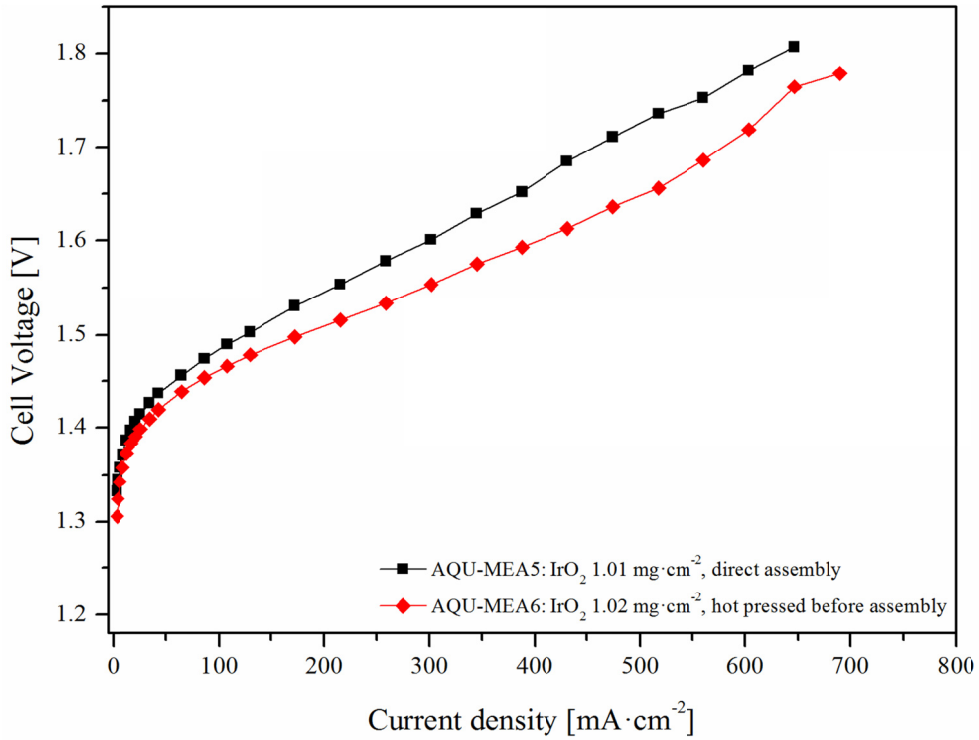


**Figure 6.21: Polarisation curves for AQU-MEA5 and 6 (see table 6.16). AQU-MEA6 was hot pressed before cell assembly whereas AQU-MEA5 was assembled directly in the cell without any prior hot press procedure. The polarisation data recorded at 130 °C and ambient pressure.**

From figure 6.21 it can be seen that hot pressing the MEA before the cell assembly gave a better performance. Throughout the whole current density range the hot pressed MEA (AQU-MEA6) showed lower voltages than the MEA that had been assembled directly in the cell (AQU-MEA5). This was most likely due to lower contact resistance between the electrodes and the membrane and better utilisation of the catalyst. The increase in the voltage at current densities above 520 $mA \cdot cm^{-2}$ for AQU-

MEA6 is more likely to be due to problems with the temperature stability of the evaporator used to feed the steam to the cell and condensation of water in the gas outlet tubing on the anode side, than an actual effect of mass transport limitations at the electrodes. Same fluctuations in evaporator temperature as earlier described were observed.

Hot pressing the MEA before cell assembly convincingly improved performance and all the next tested MEAs went through the hot pressing procedure before cell assembly even though it added an extra step to the testing procedure.

**Variation of anodic binder content**

Next a variation of the binder content was done, to examine if an optimum in binder content could be found for steam electrolysis.

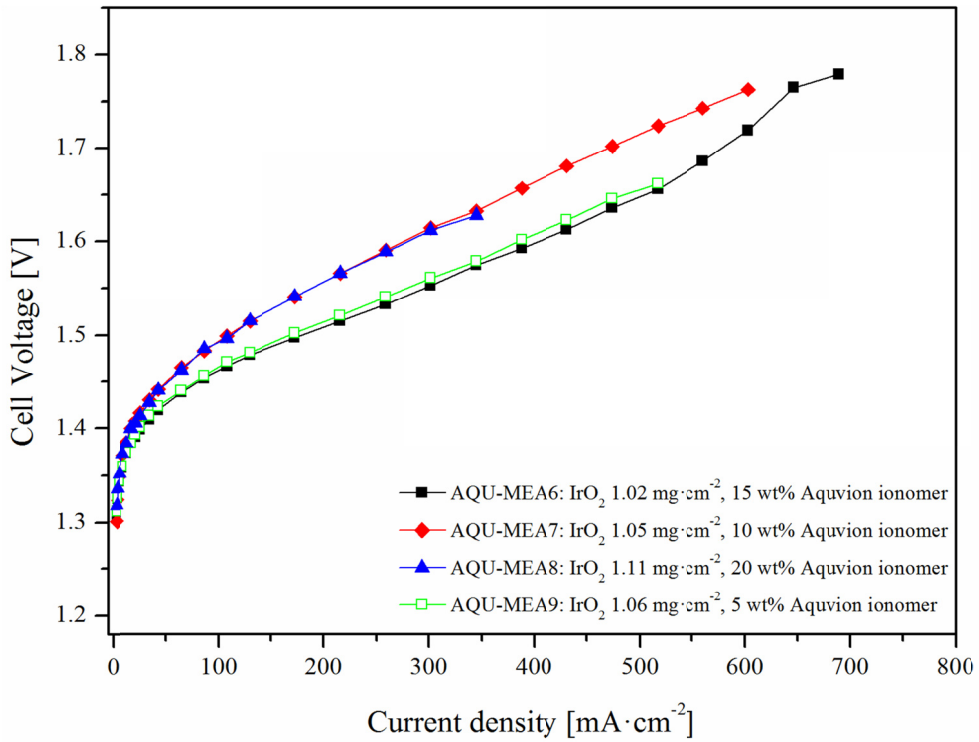


**Figure 6.22: Polarisation curves for AQU-MEA6-9 (see table 6.16). Variation of the binder content on the anode side from approximately 5 wt.% to approximately 20 wt.% in steps of 5 wt.% Aquivion ionomer. Tested at 130 °C and ambient pressure.**

The experiments with the binder loading in the anode catalyst layer showed, as it can be observed in figure 6.22 no clear trend between the performance and the binder content. The MEAs were divided into two groups. AQU-MEA6 and 9 with a binder content of 15 and 5 wt.% respectively showed much lower resistance than AQU-MEA7 and 8 which had a binder content of 10 and 20 wt.% respectively. The reason for this is not fully understood, and further experiments should be undertaken to find the optimal binder content in the anode. Prior experiments done by Ma *et al.* [126] showed a clear trend for liquid water electrolysis at 30 °C, ambient pressure and an Ir loading of 1.5 $mg \cdot cm^{-2}$ with a binder content varied from 10 wt.% to 40 wt.% in intervals of 10 wt.%. Ma *et al.* [126] showed that the resistance in the system decreased with lower binder contents, *i.e.* the MEA with a binder content of 10 wt.% Nafion® ionomer showed the best electrolysis performance. A possible reason for it not being evident in this work could be uneven distribution of the binder in the catalyst layer or that another and more uniform procedure for doping of the anode with phosphoric acid before assembly should be developed. It could for instance be by making a more diluted PA in acetic acid mixture, or PA could be added directly into the ink. However, PA in the ink could possibly make the ink more unstable, but it ought to be tested.

Even though no firm conclusion about the binder content in the anode could be drawn from the above mentioned test series, the low binder loading of 5 wt.% Aquivion ionomer showed good performance and literature supports low binder loadings in the anode, hence the succeeding MEAs were made with 5 wt.% binder in the anode.

**Variation of type of anodic GDL**

Next tests with different types of GDL were performed, to investigate the importance of the porosity and topology of the GDL and the tantalum coating of this.

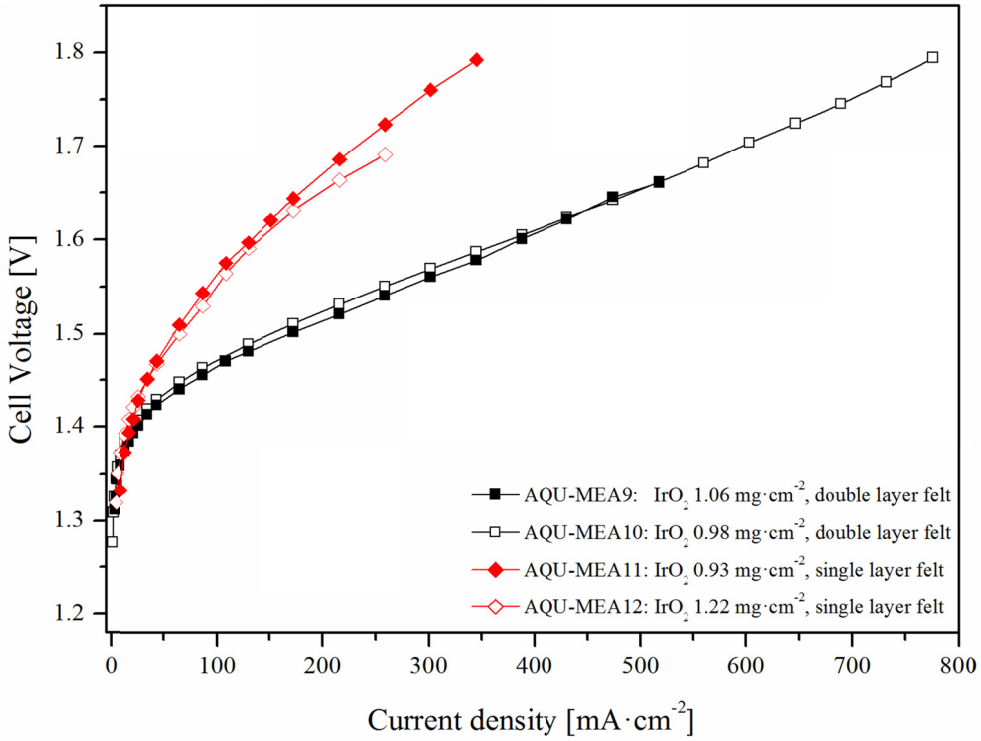


**Figure 6.23: Polarisation curves for AQU-MEA9-12 (see table 6.16). Variation of the anode GDLs, AQU-MEA9 and 10 used double layer felt (Batch 1) as GDL whereas AQU-MEA11 and 12 used single layer felt (Batch 2) as GDL. Tested at 130 °C and ambient pressure.**

From figure 6.23 it is clear that the topology and porosity of the GDL plays a tremendous role for the performance of the MEA. In figure 5.2 SEM images for the both single layer felt and double layer felt are shown. In figure 6.23 it can be seen that the performance differs in both the catalytically controlled range and in the resistance range of current densities. As previously mentioned it has been established in literature, that polarisation curves can be divided into different contribution regions a catalytically governed region at low current densities, an ohmic governed region at intermediate current densities and a mass transport governed region at high current densities. In the case of the polarisation curves in figure 6.23 there is not yet any significant contribution from mass transport limitations and the voltage can be described from equation (6-1).

On figure 6.24 the ohmic resistance contributing voltage and the activation voltage or ohmic resistance compensated voltage is plotted.

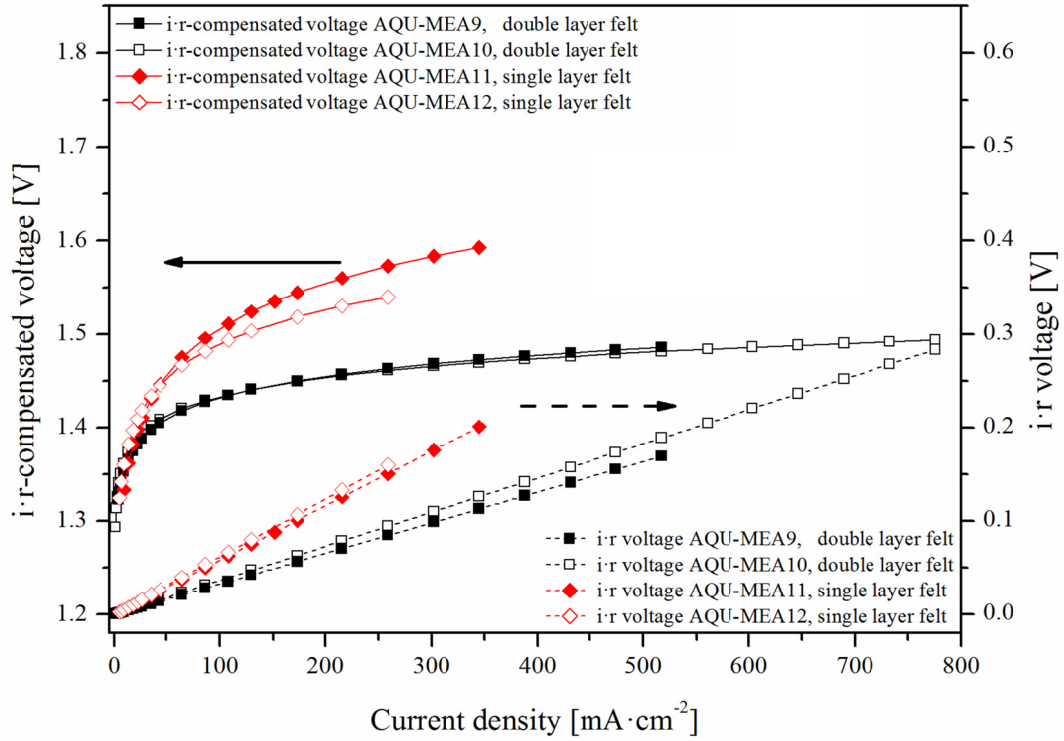


**Figure 6.24: Treated data from figure 6.23 made from equation (6-1). The arrows indicate to which axis the curves belong.**

It can be seen from figure 6.24, that AQU-MEA11 and 12 using single layer felt clearly have worse properties both in the catalytic activity and in the ohmic resistance compared to AQU-MEA9 and 10 which both use double layer felt.

Since all four MEAs had been hot pressed under the same conditions they should have similar interfacial contact resistance between the membrane and the electrode. However, since the topology of the tantalum coating was strikingly different between the two batches of felt (see figure 5.2) there was an obvious difference in the interfacial contact resistance between the membrane and the electrode. For the difference in the activation overvoltage range there are two obvious explanations. Firstly, due to the more open structure of the single layer felt with smoother Ta coating, the catalytic ink penetrates deeper into the felt which limits the catalyst utilisation. Another reason for the better catalytic performance of double layer felt could be better dispersion of the $IrO_2$ particles on the rougher surface of the fibres. The better dispersion gives rise to a higher active catalytic area and thus a higher catalytic performance, much like the strategy of using supported catalyst to increase the catalytic active area as

discussed by Nikiforov *et al.* [219]. The lower resistance in the system can also be explained as a combination of the rougher topology of the tantalum coating of the double layer felt and the fact that the fibres of the double layer felt facing the membrane is closer together, which gives shorter distance between the contact points. A rougher surface on the GDL will give rise to a larger total surface area and thus more contact points between the membrane and gas diffusion layer leading to a lower total resistance [9, 40].

**Durability of PA doped Aquivion™ membranes**

A durability test was performed on an Aquivion™ MEA based on the thicker membrane E79-12s, which had the same EW weight of 790 $g \cdot eq^{-1}$, only differing in terms of thickness, nominally 120 μm compared to 50 μm. Furthermore there was a difference in the anode catalyst. A 1:1 mixture of $IrO_2$ and tin pyrophosphate (SnP) doped antimony doped tin oxide (ATO) was used, the SnP doped ATO was used as support material for the $IrO_2$. The catalyst was prepared using a modified Adam's Fusion method, where the support was added to the iridium chloride solution before evaporation of the 2-propanol. As anode GDL a single layer felt of batch 2 with an approximately thickness of 0.5 mm was used.

**Table 6.17: Anode characteristics for durability MEA, tested at 130 °C and 1 atm.**

| MEA# | $IrO_2$ [$mg \cdot cm^{-2}$] | Binder [wt.%] | PA [$mg \cdot cm^{-2}$] |
|---|---|---|---|
| AQU-MEA13 | 0.7 | 9.1 | 0.43 |

In table 6.17 the characteristics for AQU-MEA13 are listed. The duration of the durability test was approximately 760 hours using a constant current density of 400 $mA \cdot cm^{-2}$ at 130 °C and atmospheric pressure. In figure 6.25 the cell voltage behaviour over time is shown.

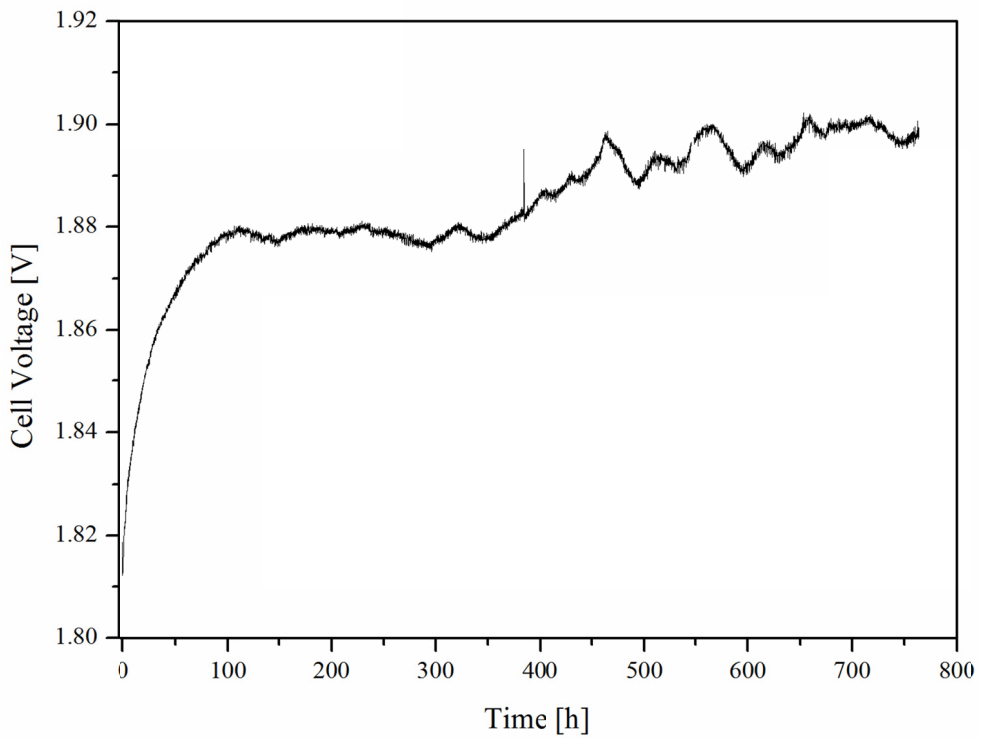


**Figure 6.25: Durability of AQU-MEA13 at constant current density of 400 mA·cm$^{-2}$, tested at 130 °C and ambient pressure.**

From the durability data in figure 6.25 it is clear that the first 100 hours, some kind of degradation takes place, since the cell voltage abruptly increases from approximately 1.82 V to 1.88 V, which corresponds to a voltage increase of 0.6 mV·h$^{-1}$. However, the next 660 hours the voltage was considerably more stable, actually the voltage increase during the next 300 hours (from 100-400 hours) was only 0.023 mV·h$^{-1}$, while it the last 360 hours (400-760 hours) had increased to 0.04 mV·h$^{-1}$.

After disassembly of the cell, it could be seen that there, in the membrane and around the edge of the anode, had precipitated some green substance, most likely nickel phosphate. The nickel probably originated from the stainless steel in the anode gas diffusion layer. The steel in the tantalum coated felt gets in contact with the acidic environment in the cell from the edges of the GDL, which are exposed when the discs are stamped out. The observed degradation over time could hence be an effect of the nickel affecting the conductivity of the membrane. However no polarisation data was collected during the durability test, so it is unknown if the loss of performance is from loss of conductivity or from loss

of catalytic performance. A way to avoid contaminating the MEA with nickel over time is to simply boil the felt discs in concentrated HCl acid overnight to remove the easily accessible nickel in the steel.

### 6.3.4 Summary

The steam electrolysis experiments using PA doped Aquivion™ membrane as electrolyte showed quite good performances probably due to the slightly improved mechanical stability for the PA doped Aquivion™ membrane compared to PA recast Nafion® membranes. It was found that even though all the tested flow patterns in this section gave reasonable electrolyser performance, pattern D with the narrower straight channels had a slightly better performance indicated by lower overall ohmic resistance in the system. Furthermore it was found that lowering the $IrO_2$ loading in the anode and hot pressing the MEAs before cell assembly both gave better performance. However no clear trend could be observed when varying the binder content in the anode from 20 to 5 wt.%. It was found, as seen in literature, that a low binder content gave good performance. The topology of the anode GDL was found to play a crucial role for how well the electrolyser cell performed. It was found that a double layer felt with the more dense side towards the membrane gave both a better catalyst utilisation and lower overall ohmic resistance in the electrolyser. Finally durability test of a thicker Aquivion™ membrane in the MEA gave quite promising results, after an initial fast degradation of 0.6 $mV \cdot h^{-1}$ the degradation slowed considerably down, and the performance stabilized with less than a tenth of the initial degradation rate.

## 6.4 Summary steam electrolysis

Three different membrane and composite membrane systems have been tested for their performance as electrolyte in steam electrolysis at 130 °C and atmospheric pressure. In all three cases the anode catalyst has been $IrO_2$. In figure 6.26 the polarisation curves for the best performing MEA in the three different electrolyte cases are plotted.

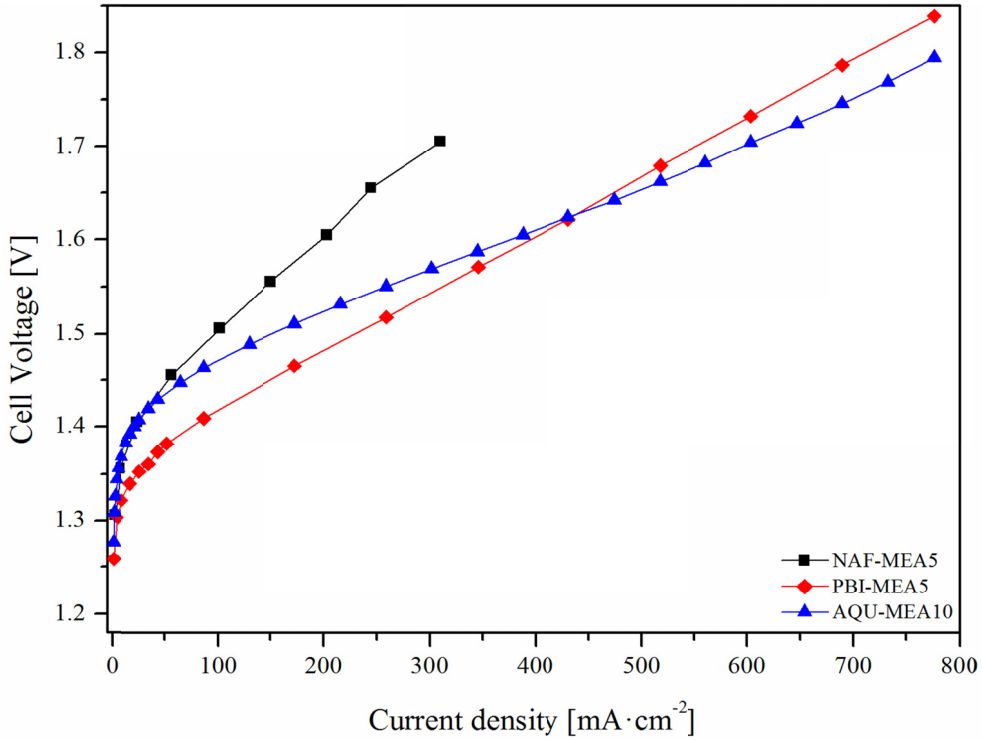


**Figure 6.26: Polarisation curves for the best performing MEAs using either: PA doped PBI (see table 6.4), PA doped ternary ZrP Nafion® 212 composite (see table 6.9) or PA doped Aquivion™ (see table 6.16) as electrolyte. Tested at 130 °C and ambient pressure.**

In figure 6.26 it can be seen that the two phosphoric acid doped PFSA electrolytes have approximately the same voltages in the activation governed region of the current density whereas the PA doped PBI electrolyte shows considerably lower voltages in the same region. However, the anode catalyst loading is much higher for the PBI-MEA, as can be seen in table 6.18, the loading was 10 mg·cm$^{-2}$ $IrO_2$ compared to 3 and 1 mg·cm$^{-2}$ respectively for the Nafion® and Aquivion™ based MEAs. Though it is not fair to compare the performance of these MEAs since so many parameters were changed during the progress of this study. For instance were the flow pattern, GDL and assembly procedure different for them, factors which all have been proved to have an effect on the electrolyser performance. Also for the Aquivion™ and Nafion® MEAs there were no discrepancy between membrane and anode binder material as was the case for the PBI based MEAs. It is positive though, that during this study it has been possible to reduce the total ohmic resistance in the system so the cell voltage at high current densities is lower for a PA doped Aquivion™ membrane than for a corresponding PBI/PA membrane.

**Table 6.18: Current densities at standard thermoneutral voltage (1.48 V) and 1.7 V for the three best performing MEAs in the different electrolyte series. Tested at 130 °C and ambient pressure.**

| # | Electrolyte | Anode loading [mg·cm$^{-2}$] $IrO_2$ | Flow pattern | $i_{TN}$ [mA·cm$^{-2}$] | $i_{1.7\ V}$ [mA·cm$^{-2}$] |
|---|---|---|---|---|---|
| 1 | PBI + PA | 10 | A | 215 | 538 |
| 2 | Nafion® 212 + ZrP + PA | 3 | B | 86 | 310 |
| 3 | Aquivion™ + PA | 1 | D | 129 | 602 |

The result for PA doped Aquivion™ is quite promising compared to the relatively few previous published steam electrolysis studies at elevated temperatures and ambient pressures. For example, Antonucci *et al.* [29] used a Nafion®-$SiO_2$ composite membrane based system and operated the cell in steam electrolysis mode at 120 °C and ambient pressures. The best performance for this system was 450 mA·cm$^{-2}$ at 1.8 V [29]. Furthermore, also at 120 °C and at ambient pressures, Baglio *et al.* [30] used a Nafion®-$TiO_2$ composite membrane based system, and obtained a current density of 700 mA·cm$^{-2}$ at 1.8 V [30]. Both inorganic filler composite systems had an anode catalyst loading of 5 mg·cm$^{-2}$. The best result obtained in the present work with steam electrolysis was 775 mA·cm$^{-2}$ at 1.8 V and 130 °C, using a PA doped Aquivion membrane and with an anode loading of 1 mg·cm$^{-2}$ $IrO_2$, see table 6.19. However, the performance is still considerably lower than that of the state-of-the-art low temperature PEM electrolysers. Nevertheless, it is encouraging with these improvements in performance for high temperature PEM electrolysers with respect to future work. The result demonstrates proof of concept of using PA instead of water as proton conducting phase in steam electrolysis.

A good fix point to compare electrolysis performances from different systems is the thermoneutral voltage (1.48 V at standard conditions). This is the voltage where the cell neither is consuming heat from nor emitting heat to the surroundings. Hence at current densities corresponding to voltages above this value heat will be released to the surroundings. Compared to other PFSA composite MEAs at comparable voltages, the best performing MEA in this work had a current density of 75 mA·cm$^{-2}$ higher than a Nafion®-$TiO_2$ composite system [30], and 225 mA·cm$^{-2}$ higher than a Nafion®-$SiO_2$ composite MEA [29] at 1.8 V, even though the operating temperature was higher and the anode catalyst loading in the present work was considerably lower.

**Table 6.19: Comparison of current densities with literature values at the standard thermoneutral voltage (1.48 V) and at 1.8 V.**

| | Electrolyte | Anode loading [mg·cm$^{-2}$] $IrO_2$ | Temperature [°C] | $i_{TN}$ [mA·cm$^{-2}$] | $i_{1.8\,V}$ [mA·cm$^{-2}$] |
|---|---|---|---|---|---|
| Antonucci *et al.* [29] | Nafion®-$SiO_2$ | 5 | 120 | 250 | 450 |
| Baglio *et al.* [30] | Nafion®-$TiO_2$ | 5 | 120 | 350 | 700 |
| Present work (AQU-MEA10) | Aquivion™+PA | 1 | 130 | 129 | 775 |

As it can be seen from table 6.19, both the inorganic filler systems [29, 30] have considerably better performance at the thermoneutral voltage. This could eventually be explained by the considerably larger $IrO_2$ loading on the anode, which would give a much larger active catalytic area. And the fact that the catalyst layer is deposited directly to the membrane and not on the GDL like in the present work. Furthermore it is known that PA is inhibiting the catalytic performance of $IrO_2$ in the oxygen evolution reaction [220]. However, these experiments were done in a liquid electrolyte where the influence of the phosphate anion is believed to be much larger than for PA in a PFSA matrix. Finally it can be seen from table 6.19 that the current density for AQU-MEA10 at 1.8 V is higher than the two inorganic filler composite systems [29, 30], hence it is very clear that the ohmic resistance (most likely due to enhanced proton conductivity and mechanical stability) of the PA doped system is much lower than in the $TiO_2$ and $SiO_2$ systems.

The durability of PBI-MEAs in this work was very poor with life times before membrane failure in the range of few hours. The durability of Nafion® based PA doped ZrP composite membranes (thickness of around 175 μm) was much better, here a degradation rate of 0.21 mA·h$^{-1}$ for a 72 hour time period was observed (voltage was kept constant at 1.7 V). The best durability was achieved for an Aquivion™ based MEA, it lasted for around 760 hours without major loss of performance after an initial degradation rate (first 100 hours) of 0.6 mV·h$^{-1}$, the degradation rate went substantial down to 0.023 mV·h$^{-1}$ for the next 300 hours and 0.04 mV·h$^{-1}$ for the last 360 hours (constant current density of 400 mA·cm$^{-2}$ for all 760 hours).

The performance and durability of PA doped Aquivion™ is promising for future use of this type of membrane in PEM water electrolysis at elevated temperatures.

# 7 Pressurised electrolysis. Results and discussion

As mentioned in chapter 4 most of the pressurised water electrolysis at elevated temperature experiments were conducted at ICTP in Prague. All the results presented in this work were done at ICTP and the electrolysis tests were done in collaboration with Dr. Martin Paidar and Ph.D. student Petr Mazur. The tests were, unless otherwise mentioned, performed using an electrolysis cell constructed at DTU with two different flow patterns: An asymmetric spiral flow pattern or a pattern constructed of commercially available topped sheets of stainless steel. The pressurised setup used was constructed at ICTP see figure 4.9 in section 4.2.

In table 13.1 (Appendix 3) an overview of all the presented MEAs is given to aid the reader.

## 7.1 Aquivion™

As in the steam electrolysis tests the membrane used was a commercially available Aquivion E79-05S from Solvay Solexis with an approximate thickness of 60 μm. The membrane was pre-treated as described in section 6.2.1. Since the tests were performed in a pressurised liquid setup the membranes were not doped with phosphoric acid. The MEAs were assembled directly in the electrolysis cell without any prior hot pressing. All the electrodes, anodes as well as cathodes, were of the GDE type. The anodes consisted of $IrO_2$ and Aquivion™ binder sprayed directly onto two different types of tantalum coated stainless steel felt as described in section 3.7. The two types of felt were a 0.2 mm thick single layer felt and a 0.5 mm thick double layer felt as described in chapter 5. The dense side (8 μm fibre) of the felt was facing towards the membrane. The anodes were not post doped with PA since they were used in liquid electrolysis mode. The cathodes were of the usual type with a 0.8 $mg \cdot cm^{-2}$ Pt loading (40 wt.% Pt/C) and 0.3 $mg \cdot cm^{-2}$ Nafion® binder on non-woven carbon cloth. All the electrolysis tests were performed at 120 °C using a total pressure of 3 bar to keep water in the liquid phase.

Two different flow patterns were used, the asymmetric spiral pattern which was described in detail in section 4.1 and a topped pattern which was constructed from commercially available stainless steel topped plates see figure 7.1 A. From the topped sheet a circular disc with an area of 10 $cm^2$ was cut. The disc had in- and outlet holes made in the top and bottom of the disc perimeter. It was fixed in the electrolysis cell using a PTFE ring having holes to let the cell assembly bolts going through. This way the topped flow pattern was aligned correctly with the in- and outlet holes in the end plates, see figure 7.1 B. As can be seen from figure 7.1 each top was flattened to ensure a more uniform pressure to the GDL. The height of the tops was approximately 0.9 mm. The backside of the topped disc flow pattern was kept in electrical contact with the existing flow plate by Papyex® flexible graphite paper. The Papyex® also prevented water running from the inlet to the outlet on the backside of the topped sheet dics.

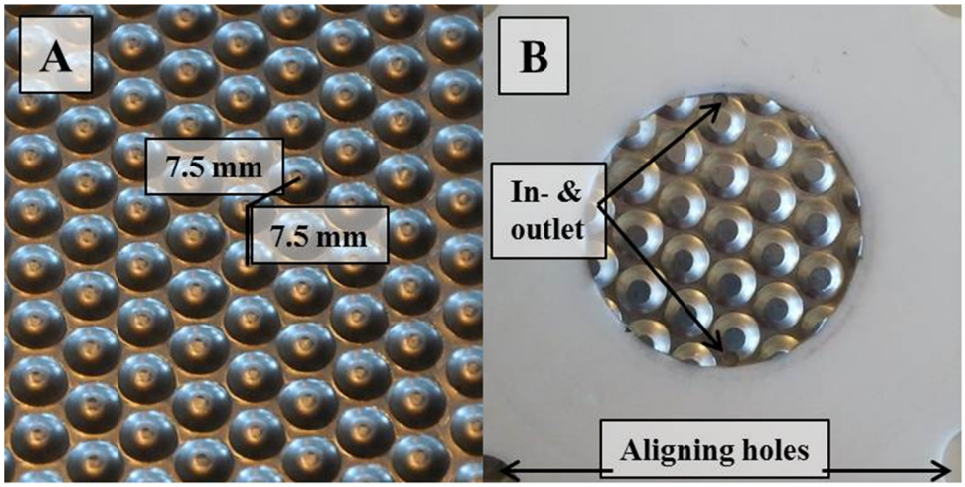


**Figure 7.1: Photograph of: A: Topped sheet plate, B: Flow pattern fixed in PTFE ring, used in pressurised water electrolysis setup. In picture B the diameter of the steel disc is 35.7 mm.**

The topped sheet pattern was tested to see if a commercially available product, produced as cheap sheet material, could substitute the specially constructed flow patterns which are made by machining.

Finally, also a test was performed using the ICTP cell to compare with the DTU electrolysis cell. The ICTP cell had a conventional square serpentine flow pattern with a channel width and depth of 1 mm.

Table 7.1 summarise the flow pattern and anode characteristics *i.e.* loading, binder content and GDL.

**Table 7.1: Characteristics for Aquivion MEAs tested at 120 °C and 3 bar absolute pressure.**

| MEA # | $IrO_2$ [mg·cm$^{-2}$] | Anode Binder Aquivion™ [wt.%] | GDL [mm] / type | Flow pattern |
|---|---|---|---|---|
| LIQ-MEA1 | 3.49 | 15 | 0.2 / single | Spiral |
| LIQ-MEA2 | 3.54 | 15 | 0.5 / double | Spiral |
| LIQ-MEA3 | 3.40 | 15 | 0.2 / single | Topped |
| LIQ-MEA4 | 3.77 | 15 | 0.5 / double | Topped |
| LIQ-MEA5 | 1.72 | 15 | 0.2 / single | Serpentine* |

* Parallel serpentine channels in ICTP cell

First the influence of GDL type and thickness was tested. In figure 7.2 the polarisation curves for LIQ-MEA1 and 2 are plotted. The electrolysis tests were done with the DTU cell using the spiral flow pattern.

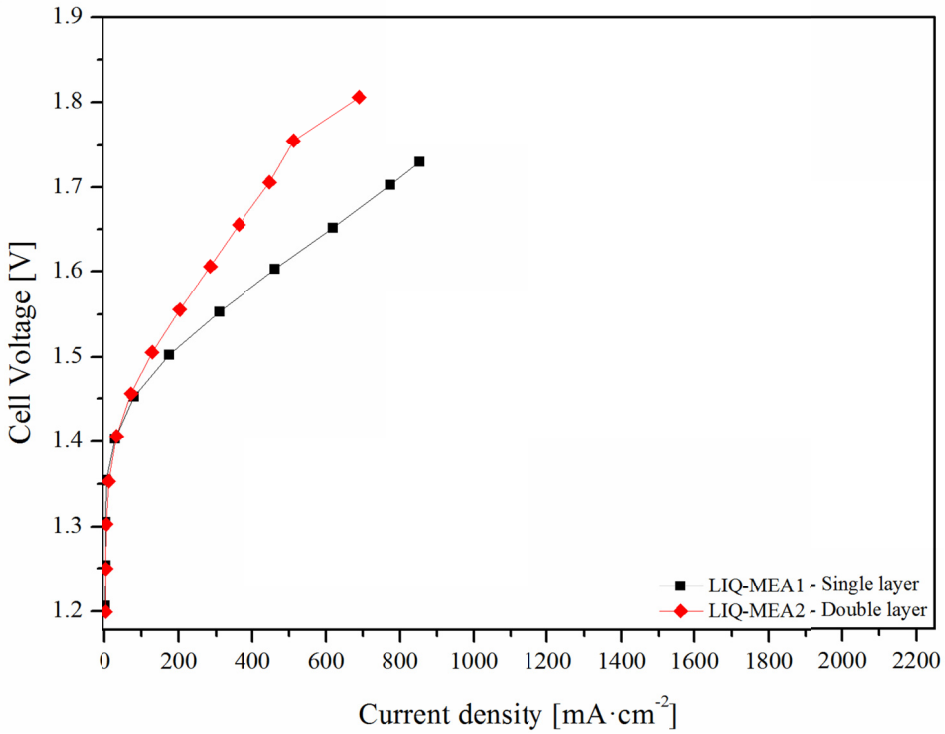


**Figure 7.2: Polarisation curves for LIQ-MEAs with different GDLs (see table 7.1) tested in DTU Cell with spiral flow pattern at 120 °C and 3 bar absolute pressure.**

From figure 7.2 it can be seen that LIQ-MEA2 with the double layer felt has considerably higher ohmic resistance than LIQ-MEA1 which used a single layer felt. The fibre thickness of the felts was the same

on the side facing towards the membrane. However the thickness of the double layer felt was considerably larger with approximately 0.5 mm compared to only 0.2 mm for the single layer felt. Given that the surface of the felts onto which the catalyst was sprayed was equal, which it ought to be, since the fibre thickness were the same and they were coated with tantalum in the same batch, the extra ohmic resistance in the system could be explained by the increase in overall thickness of the felt. Similar observation was done by Ma *et al.* [126] who found that increasing the anode GDL from 200 µm to 380 µm gave a decrease in current density of approximately 100 $mA \cdot cm^{-2}$ at a cell voltage of 2 V.

The influence of thickness and type of GDLs was also tested in the DTU cell with the topped sheet flow pattern. In figure 7.3 the polarisation curves for LIQ-MEA3 and 4 can be seen.

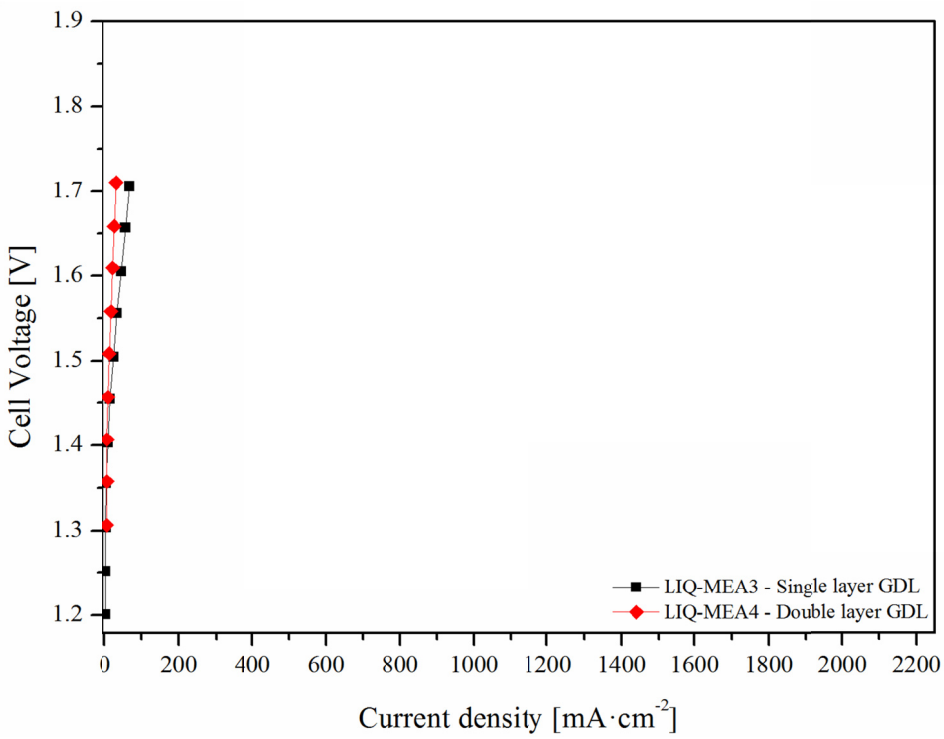


**Figure 7.3: Polarisation curves for LIQ-MEAs with different GDLs (see table 7.1) tested in DTU Cell with topped sheet flow pattern at 120 °C and 3 bar absolute.**

Using the topped sheet flow pattern (see figure 7.3) the same trend as with the spiral flow pattern was found, *i.e.* the double layer also in this flow configuration performed worse. Moreover it was clear from

the electrolysis test using the topped sheet flow pattern that it was not providing sufficient support and distribution of the flow to give reasonable performance. At a cell voltage of 1.7 V the current density was in both cases well below 100 $mA \cdot cm^{-2}$ (68 and 33 $mA \cdot cm^{-2}$ for LIQ-MEA3 and 4 respectively). The hypothesis was that using a thicker GDL could provide the extra stiffness in the GDL to apply the force between GDL and membrane evenly. Assuming this hypothesis is true, the main reason for the considerably lower electrolysis performance should be found in poor flow distribution. After disassembly of a LIQ-MEA3 it was clear that the force was concentrated on the tops, hence the contact between the GDE and membrane was limited and gave rise to a larger ohmic resistance in the system. In figure 7.4 the membrane from LIQ-MEA3 after disassembly of cell and removal of electrodes is shown. Only at the tops the force from the flow plate was high enough to make the catalyst stick to the membrane.

**Figure 7.4: LIQ-MEA3 disassembled after electrolysis test. The electrode diameter was 38.5 mm.**

The importance of the flow pattern is further shown when a comparison of the DTU spiral and topped sheet patterns are compared with the serpentine pattern used at ICTP. In figure 7.5 the three polarisation curves for the test using different flow patterns are shown. All the MEAs used the 0.2 mm thick single layer felt.

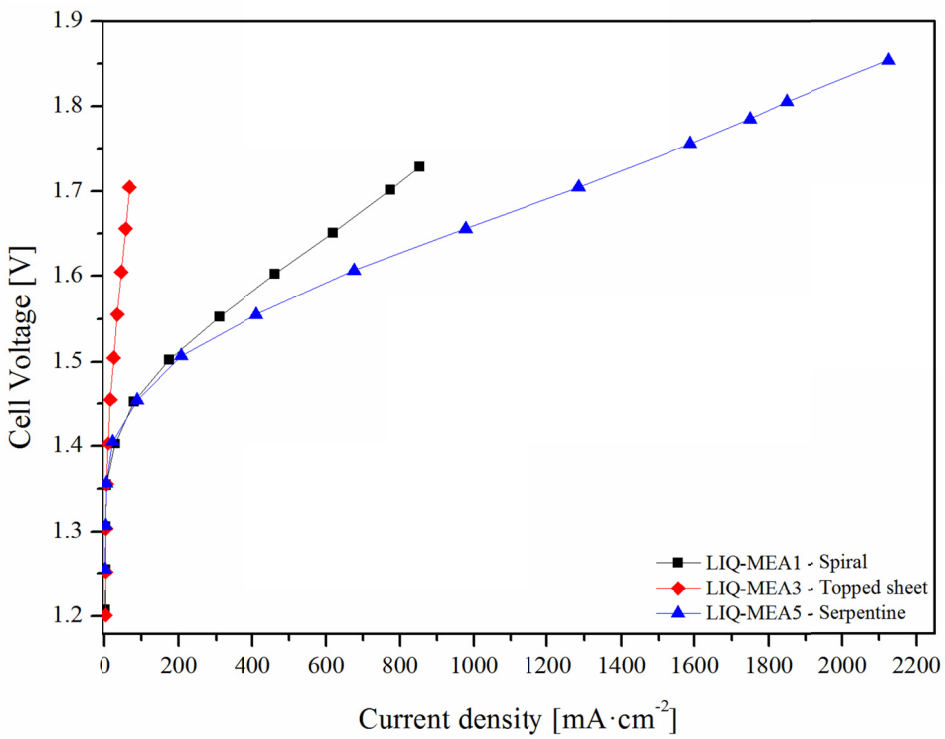


**Figure 7.5: Polarisation curves for LIQ-MEAs with different flow patterns (see table 7.1) tested using 0.2 mm single layer anode GDL at 120 °C and 3 bar absolute pressure.**

From figure 7.5 it is obvious that the flow pattern plays a crucial role for the electrolyser performance. Using a novel flow design chosen from the availability of commercial sheet material clearly shows lack of ability to provide a sufficient support to the GDL and hence enabling a good contact between the GDE and the membrane. Furthermore, it is doubtful whether the topped sheet pattern distributes the flows over the total electrode area.

The two machined flow patterns show considerably better performance with approximately 775 and 1300 $mA \cdot cm^{-2}$ at 1.7 V respectively for the spiral and serpentine patterns, compared to the approximately 68 $mA \cdot cm^{-2}$ for the topped sheet pattern. However the contact area between the topped sheet flow pattern and GDL is only approximately 135 $mm^2$ (divided between 19 points) compared to 387 $mm^2$ for the spiral pattern (both having a total area of 1000 $mm^2$). Clearly the lower contact area and having individual points create a less uniform press from the backside of the GDL to the membrane. The serpentine pattern used at ICTP has a narrower channel width than the DTU spiral pattern, hence it also has a better force distribution to the GDL *i.e.* giving better contact between GDL

and membrane. Furthermore it is likely that the current and flow distribution in the GDL are better when the channels are closer together.

### 7.1.1 Summary Aquivion™ pressurised electrolysis

Three different flow pattern and two different types and thicknesses of anode GDL was tested using a Aquivion™ membrane in a pressurised setup operated at 120 °C and 3 bar pressure. It was found that the thin (0.2 mm) single layer felt gave a better performance compared to a thicker (0.5 mm) double layer felt although the fibre thickness was the same on the side of the felts facing towards the membrane. It was believed that difference in performance was a result of the thickness simply having less GDL material to provide ohmic resistance.

Of the three tested flow patterns the square serpentine flow pattern used at ITCP clearly had a better performance than both the circular spiral pattern and in particular the circular topped sheet pattern. The reduction of ohmic resistance in the serpentine flow pattern was believed to be caused by the larger contact area and better current and flow distribution from the flow pattern to the GDL.

## 7.2 Nafion® + $BPO_4$

As electrolyte was also tested a recast Nafion® composite membrane with boron phosphate. The composite membranes were cast by David Aili at the Technical University of Denmark using the following procedure [203] inspired by preparation of boron phosphate by Moffat *et al.* [221] and SPEEK + $BPO_4$ composite membranes by Krishnan *et al.* [222] .

5 wt.% Nafion® ionomer (on $NH_4$-form) in DMAc solution was mixed with $B(Oet)_3$ and $H_3PO_4$ (100 wt.%) at room temperature. The mixture was magnetically stirred until a homogenous, colourless and transparent solution was obtained. The membranes were solution cast to a size of 95 $cm^2$. The membranes were treated in 1 $mol \cdot L^{-1}$ $H_2SO_4$ at 80 °C for 1 hour to protonate them and were subsequently treated in 90 °C demineralised water for 2 hours before being stored in demineralised water.

A MEA with a Nafion® + $BPO_4$ composite membrane with a $BPO_4$ content of 5 wt.% (LIQ-MEA6) was tested in the pressurised electrolysis setup at 120 °C and 3 bar pressure using the DTU cell with spiral flow pattern. The Nafion® + $BPO_4$ composite membrane had a thickness of approximately 90 µm. The anode and cathode was of the GDE type with a cathode loading of 0.8 $mg \cdot cm^{-2}$ Pt (40 wt.% Pt/C on non-woven carbon cloth, and 0.3 $mg \cdot cm^{-2}$ Nafion as binder) and a anode loading of 3.31 $mg \cdot cm^{-2}$ $IrO_2$ with a binder content of approximately 17.5 wt.%. As anode GDL a 0.2 mm tantalum coated single layer stainless steel felt was used. The MEA was assembled directly in the cell without prior hot pressing. As a reference MEA an earlier tested Nafion® 112 membrane (LIQ-MEA7) with approximately 5.7 $mg \cdot cm^{-2}$ $IrO_2$ and a Nafion® binder content of 5 wt.% was used. The cathode had a Pt loading of 1 $mg \cdot cm^{-2}$ (30 wt.% Pt/C) using 30 wt.% Nafion® as binder. The reference MEA was tested at 120 °C and 3 bar in the ICTP cell using a serpentine flow pattern. In table 7.2 the anode characteristics, the flow pattern and electrolyte used for electrolysis tests are listed.

**Table 7.2: Characteristics for LIQ-MEAs using Nafion® based electrolytes, tested at 120 °C and 3 bar absolute pressure.**

| MEA # | Anode $IrO_2$ [$mg \cdot cm^{-2}$] | Anode Binder Aquivion™ [wt.%] | GDL [mm] / type | Electrolyte Type | Electrolyte [µm] | Flow pattern |
|---|---|---|---|---|---|---|
| LIQ-MEA6 | 3.31 | 17.5 | 0.2 / single | Recast Nafion® 5 wt.% $BPO_4$ | ~90 | Spiral |
| LIQ-MEA7 | 5.7 | 5 | 0.2 / single | Nafion® 112 | ~50 | Serpentine |

In figure 7.6 the polarisation curves for LIQ-MEA6 and 7 are plotted.

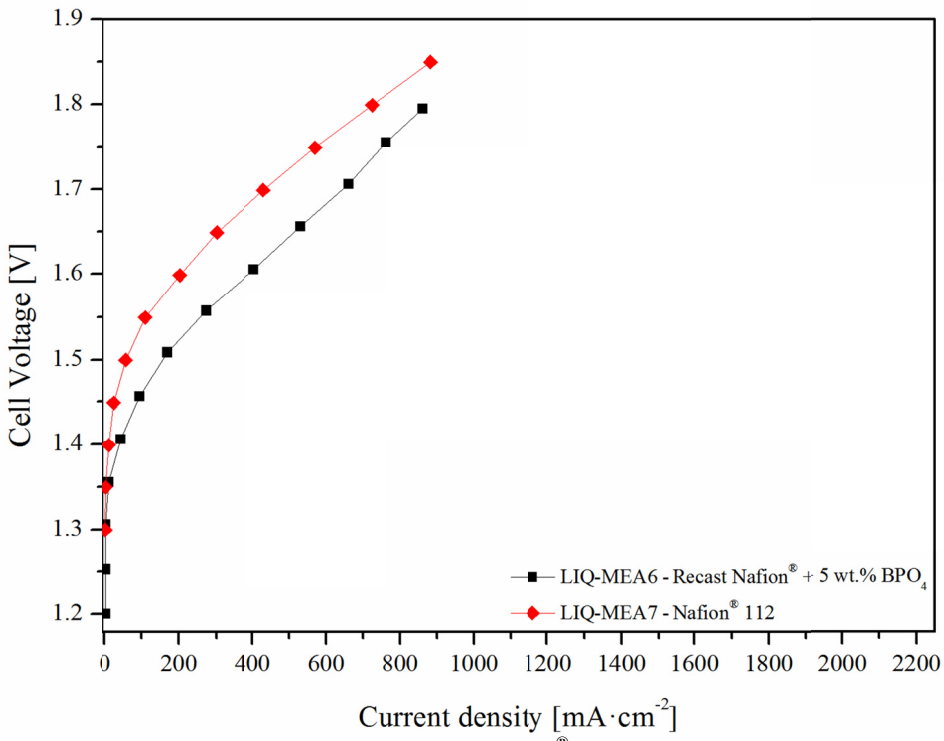


**Figure 7.6: Polarisation curves for LIQ-MEA6 and 7 using Nafion® based membranes (see table 7.2), tested at 120 °C and 3 bar absolute pressure.**

It can be seen from figure 7.6 that using a Nafion® + $BPO_4$ composite membrane gives reasonable performance in the electrolysis setup at 120 °C and 3 bar pressure compared to a considerably thinner commercially available Nafion® 112 tested under similar conditions. The area specific resistance in the ohmic resistance dominated region (between 200 and 700 $mA \cdot cm^{-2}$] of the two polarisation curves in figure 7.6 are fairly similar with 416 $m\Omega \cdot cm^2$ and 367 $m\Omega \cdot cm^2$ for LIQ-MEA6 and 7 respectively. Assuming that all the resistance in this current density range is controlled by the proton conductivity in the membranes the conductivity of the membranes can be estimated by dividing by their thickness. The conductivities of LIQ-MEA6 and 7 are in this case 0.022 and 0.014 $S \cdot cm^{-1}$ respectively. Hence it seems plausible that the 5 wt.% $BPO_4$ in the membrane significantly improves the conductivity of the membrane. However the improvement can also be caused by the greater dimensional stability of the composite membrane. Another remarkable feature is that even though the Nafion® + $BPO_4$ composite membrane was tested using the DTU spiral pattern, the overall resistance in the system is only slightly higher, although a considerably different effect was observed using Aquivion™ membranes. This

further strengthens the hypothesis that the $BPO_4$ gives improved mechanical stability to the Nafion® membrane.

The overall improvement of the electrolyser performance comes from activation voltage domain, it is most likely due to a better utilisation of the catalyst in LIQ-MEA6 even though the loading of $IrO_2$ is considerably lower. A possible explanation could be differences in the spraying procedures at ICTP and DTU *i.e.* the penetration depth of the catalyst into the GDL.

### 7.2.1 Summary Nafion® + $BPO_4$ pressurised electrolysis

It was found that pressurised liquid water electrolysis (120 °C and 3 bar) using a composite membrane of Nafion® and $BPO_4$ gave reasonable electrolyser result compared to traditional Nafion® 112 membrane. At a cell voltage of approximately 1.75V the current density of the Nafion® + $BPO_4$ composite was 750 $mA \cdot cm^{-2}$ approximately 180 $mA \cdot cm^{-2}$ higher than the Nafion® 112 MEA. The conductivity of the composite membrane was 0.008 $S \cdot cm^{-1}$ (equal to 36 % of its own conductivity) higher than that of the traditional Nafion® membrane when assumed that the entire ohmic resistance was due to membrane conductivity. This assumption seems unlikely, some of the improvement is most likely due to improved mechanical stability of the composite membrane.

## 7.3 Comparison of pressurised PFSA membranes and PFSA composite membranes

A comparison between the short side chained Aquivion™ with its improved water retention and mechanical properties and an inorganic composite membrane of recast Nafion® and $BPO_4$ can be made. In figure 7.7 the polarisation curves and calculated i·r-voltages (equation (6-1), data found by regression) for LIQ-MEA1 and 6 are shown. Both MEAs use the same type of cathode and anodes with similar anode loadings. The Nafion® + $BPO_4$ composite membrane in LIQ-MEA6 is considerably thicker with 90 µm compared to 60 µm for the Aquivion™ in LIQ-MEA1.

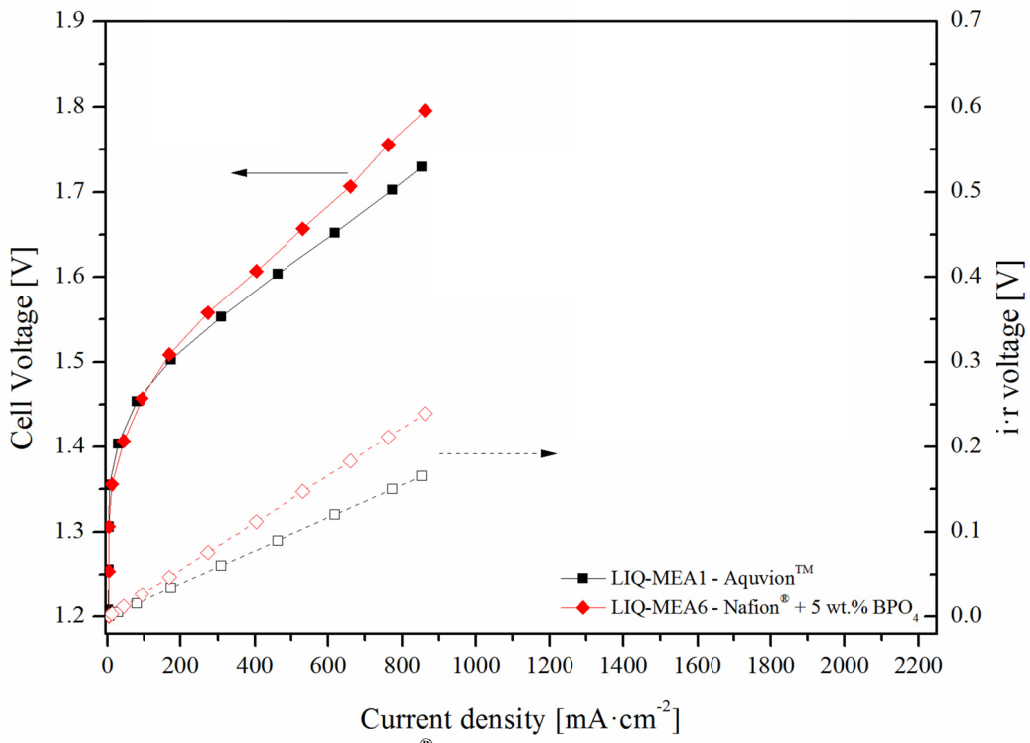


**Figure 7.7: Comparison of Aquivion and Nafion® + 5 wt.% $BPO_4$, tested in DTU spiral cell at 120 °C and 3 bar absolute pressure.**

From the polarisation data for LIQ-MEA1 and 6 it can be seen that at a current density of approximately 850 mA·cm$^{-2}$ the voltage is 70 mV lower for LIQ-MEA1, however at low current densities, in the activation voltage range, the MEAs are behaving very similar. This corresponds well with the fact that the electrodes are almost identical. Therefore the observed polarisation difference comes from the ohmic resistance in the cell, which is also clear from the i·r-voltage curves in figure 7.7.

The area specific resistance of LIQ-MEA1 and 6 in figure 7.7 are 194 and 278 mΩ·cm$^2$ respectively. Using the same assumption as above that all the ohmic resistance comes from the conductivity of the respective membranes and divide by the membrane thickness the proton conductivity can be found. The conductivities are then approximately equal to 0.031 S·cm$^{-1}$ for LIQ-MEA1 and 0.032 S·cm$^{-1}$ for LIQ-MEA6, hence showing that the $BPO_4$ composite Nafion® membrane had approximately the same conductivity as the Aquivion™ membrane.

Mechanical strength data for Aquivion™ and 5 wt.% $BPO_4$ Nafion composite membranes obtained at 130 °C are summarised in table 7.3.

**Table 7.3: Mechanical strength data for Aquivion™, Recast Nafion® and 5 wt.% $BPO_4$ Nafion® composite tested at 130 °C at ambient pressure.**

| | Recast Nafion® | Aquivion™ | Recast Nafion® 5 wt.% $BPO_4$ |
|---|---|---|---|
| Young's modulus [MPa] | 2.9 ± 0.5 | 113.7 ± 24.3 | 15.8 ± 3.7 |
| Engineering tensile stress at break [MPa] | ≈ 0 | 13.8 ± 2.9 | 1.9 ± 0.9 |
| Elongation at break [%] | > 800 | 166 ± 14 | 631 ± 103 |

Judging from the mechanical strength data for both it seems unlikely that the mechanical strength and hence the dimensional stability *i.e.* contact resistance between the electrodes and membrane should be the same. However the mechanical strength tests are done at 10 °C higher than the electrolysis tests, and it is just in the range of the softening temperature of Nafion®. So the dimensional stability of the two different electrolytes could be similar, otherwise it could be argued that the conductivity of the composite membrane was considerably improved compared to the Aquivion™ membranes, since it should compensate for the lack in dimensional stability to reach equal conductivity.

# 8 Further discussions

## 8.1 Correct geometric anode area

The size of the 'active' or utilised geometric area of the electrodes is a matter which could and rightly should be discussed. In this thesis electrodes with a geometric area of approximately 11.6 $cm^2$ (38.5 mm in diameter) were used. This area was hence used for calculating the current densities, however the area of the flow pattern was only 10 $cm^2$ (35.8 mm in diameter). The reason for having the discrepancy between the flow area and the electrodes was, as mentioned in section 3.7, that placing a MEA with the same electrodes size as the flow area was extremely difficult and that having the same size electrodes and flow area often resulted in breaking of the membrane due to mechanical stress coming from the reactant flow if the MEA was not exactly aligned.

Assuming that all of the electrode area outside the flow area participates in the electrode reaction is not necessarily correct, however assuming that only the electrode area inside the flow area is active can be equally wrong. During the electrolysis tests two straight channelled flow patterns with equal channel length were tested. The difference between these two patterns lied in the width of the channels and land (rib) areas, one of having 1 mm wide channels and ribs whereas the other flow pattern had 2 mm. Electrolysis tests showed that, although to a very limited extent, the 1 mm channelled flow pattern performed best. This could indicate that 2 mm wide land area is a bit too wide to get proper distribution of steam into the active areas. 2 mm wide land areas corresponds to 1 mm from each side of the ribs. If placed precisely in the middle of the flow area, the electrodes would have a 1.35 mm wide ring extending outside the flow area, hence having distances up to 35 % larger than the distance (1 mm) which already to some extent had shown problematic. All these speculations however are very much dependent on the properties of the GDL which already have been mentioned in chapter 5 but will be further discussed below.

Going to the other extreme and assuming that there are such restrictions in the flow of reactant to the anode that only the area of the flow pattern area can be utilised, the assumed area (11.6 $cm^2$) used for calculating current densities is 16 % too large, hence the possibility of underestimating the current

densities with up to 16 % exists. The utilised geometric area of the electrode lies somewhere between these two extremities. In an attempt to clarify this, two more experiments were carried out using PA doped Aquivion™ membrane as electrolyte. In the first MEA the catalyst layer was sprayed onto the whole area of the GDL disc (11.6 $cm^2$), in the second MEA the catalyst layer was only sprayed onto 10 $cm^2$ of the GDL disc area. This was done by using a 10 $cm^2$ template placed on top of the GDL so the size of the catalyst layer was kept to the desired area. The usual Pt/C cathode was used, and for anode GDL was used a nominal 0.5 mm single layer felt coated with tantalum. The membrane was the previously seen PA doped Aquivion™ with a thickness of approximately 60 μm. The anode characteristics for both MEAs are listed in table 8.1.

**Table 8.1: Anode characteristics for MEAs used for determination of electrode size.**

| | Anode | | | | |
|---|---|---|---|---|---|
| MEA# | $IrO_2$ [$mg \cdot cm^{-2}$] | Binder [wt.%] | PA [$mg \cdot cm^{-2}$] | Felt thickness [mm] | Catalyst area [$cm^2$] |
| AQU-MEA14 | 1.01 | 5.2 | 0.22 | 0.6 | 11.6 |
| AQU-MEA15 | 1.11 | 5.7 | 0.16 | 0.6 | 10 |

The MEAs were both tested at 130 °C and atmospheric pressure, the currents were chosen to be the same for both MEAs obtaining data for the polarisation curves. In figure 8.1 the polarisation data are plotted for AQU-MEA14 and 15. AQU-MEA14 are plotted calculating the current density using electrode areas of both 10 and 11.6 $cm^2$.

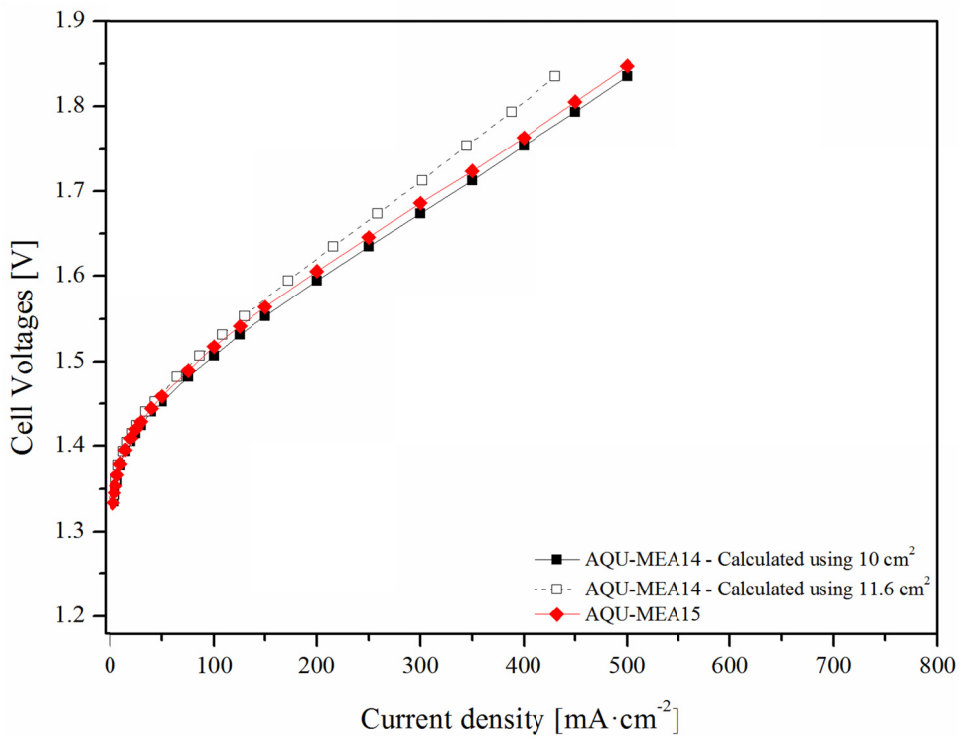


**Figure 8.1: Polarisation curves for AQU-MEAs difference in catalyst geometric area of anode. Tested at 130 °C and 1 ambient pressure.**

In figure 8.1 it is indicated by the polarisation curves for AQU-MEA14, that assuming that the geometric area of the electrodes are equal to the flow area (the solid black line), in this case, is not far from the truth. The red polarisation curve, having an actual anodic geometric area of 10 cm$^2$, was used as the reference curve. Hence it can be seen that the dashed black polarisation curve where the current densities were calculated using the full geometric area of 11.6 cm$^2$ is further from the reference curve.

The areas used for calculating the current densities throughout this work were however still calculated using the full geometric area of 11.6 cm$^2$ (when this was used), getting somewhat perhaps conservative results. The reason for this is, that many factors influence the polarisation behaviour of the MEAs, *e.g.* the topology and porosity of the GDL being some of the most important. It is known that the porosity of the GDL can vary with several percentage points, also the topology of the tantalum coating is very dependent on the placement in the CVD reactor and the gas flow rates. The porosity of the anode GDLs for AQU-MEA14 and 15 was in the lower range, hence potentially having worse reactant and product

flow distribution than MEAs tested in this study. Making the conservative choice of electrode area (the full geometric area) the perhaps more correct area.

## 8.2 Importance of flow area

Five different flow patterns were tested. Four CNC machined ones and one adapted from commercially available stainless steel topped sheets (see figure 4.4, figure 4.5 and figure 7.1). It can be hard to make a fair comparison between the four machined flow patterns since, many changes in: GDL, electrolyte, anode loading and anode ionomer binder content, were carried out between the applications of these four patterns. During the initial experiments with PA doped PBI membranes reasonably good electrolysis results were obtained using the first designed waffle-like flow pattern. Using the same pattern for PA doped Nafion® membranes and ternary ZrP composite Nafion® membranes and comparing it with the next designed flow pattern – the asymmetrical spiral pattern, did not reveal any major differences in electrolysers performances. What was revealed was that the stress from the spiral pattern to the GDEs and hence the membrane was less with the spiral pattern. Thus a change from this initial flow design to the spiral pattern was chosen.

Experiments at ICTP in Prague made clear however that the spiral flow pattern was not the optimal design either. This was found by conducting experiments under liquid water conditions using the DTU spiral flow pattern cell and comparing it with the more traditional square serpentine flow pattern used at ICTP. The findings from water electrolysis experiments at elevated temperature done at ICTP led to the development of two straight channelled circular flow patterns. Testing these new flow patterns with PA doped Aquivion™ membrane did however only show minute differences in electrolysers performance, although with a small tendency to that the pattern which was expected to be the best also showed the best performance. This finding clearly supported our belief that other factors than the flow pattern itself were influencing the results. Possible factors could very well be the catalyst loading, post doping procedure of the electrodes, assembly procedure and the properties of the GDL.

The tests of the different flow patterns did however reveal one thing clearly. The flow pattern based on the topped commercial stainless steel sheet, showed very clearly a lower performance than both the

spiral pattern and the square serpentine flow pattern from ICTP. Disassembling the MEAs with the topped pattern after electrolysis tests showed that the contact between the membrane and electrodes was quite poor. The rigidity of the GDE was not sufficient to ensure a uniform contact, and only at the areas of the tops had the electrodes touched the membrane with enough force to actually transfer part of the catalyst to the membrane (see figure 7.4). This fact and the limited probability of proper distribution of flows was assumed to be the reason to the very poor performance, hence this approach to make cheap flow patterns for commercialising of electrolysers seems stillborn without at least serious alterations to the GDL material.

## 8.3 Importance of GDL

As mentioned above the properties of the GDL have a significant influence on the electrolyser performance especially when the electrodes are GDEs. The properties of the GDL used in this work however have shown to be difficult to sufficiently characterise, since each time a new batch of tantalum coated felt was received the coating was different. In chapter 5 results for the different characterisation done on the GDL are presented. It was found that pristine felt was quite homogenous when it came to the weight of discs stamped out from sheet with standard deviation in weight only 0.1 %. However after the tantalum coating of the felt the mass variation and porosity variation is quite large with between 2 and 7 % for mass and around 5 % for porosity. These variations alone makes it quite hard to predict the properties of the GDL/GDE and hence performance of the electrolyser. Furthermore, the surface topology of the tantalum coating on the felt fibres is also quite different. It has been seen going from a fairly smooth coating to very rough coating with dendrites on the fibre surface. Obviously the porosity has great influence on the flow properties of reactants and products and in most cases the porosity of the GDL used in this work was also in the range of the optimum proposed by Grigoriev *et al.* [9]. A more open, hence more porous GDL will favour the distribution of flows and render probable that the full geometric area of the GDE is available for the gases. However, it was found that to achieve good electrolysis performance the porosity of the GDL should be in the lower end of the porosity window *i.e.* around 30-40 %.

The proposed explanation for this fact was supported by the acquired SEM images. As seen on the SEM images in figure 5.2 the felt from batch 1 had, as mentioned above, a rough surface of tantalum dendrites on the stainless steel fibres. MEAs using felt from this batch in general showed improved electrolysis performance, hence it was proposed that this improvement could be attributed two causes. The dendrite structure of the surface topology of the fibres in the GDL greatly improves the number of contact points between then membrane and the electrode, hence increasing the surface area in contact. The increased contact area will then lead to a decrease in the overall ohmic resistance, this phenomenon can be seen in the electrolyser experiments with a PA doped Aquivion™ membrane as electrolyte and using the two different batches of tantalum coated GDL (Batch 1, with a low porosity and rough dendrite like tantalum coating and batch 2, with high porosity and fairly smooth tantalum coating). The GDLs further had the difference that the ones from batch 1 were of the double layer type and those from batch 2 were of the single layer type. This meant that the individual fibres in the pristine double layer felt were closer together than in the single layer felt type of similar overall thickness. So these two facts together improved the contact between the GDE and membrane which can also be seen from the calculated i·r-voltages in figure 6.24. The calculated i·r-voltages for the MEAs using GDL from batch 1 are considerably lower even though the overall thickness is the same. In section 5.2 it was found that the sum of bulk- and interfacial resistances was a function of the porosity of the GDL, *i.e.* the amount of tantalum coating on the fibres, showing that lower porosity led to less resistance at lower compression force (see figure 5.1). The reason, that the same trend is not observed in the real electrolysis application, is most likely that the interface between the GDE and the flow plate are of less importance compared to the interface between GDE and membrane. The membrane is soft and flexible and can be curved to the overall roughness of the GDE surface and hence be in close proximity to all the surface fibres of the GDE, *i.e.* the surface topology of the tantalum coating on the individual fibres play an important role.

Moreover it was proposed that the roughness of the coating was helping to a better distribution of catalyst when spraying the electrode to the GDL. The better distribution of catalyst makes a larger catalytic area of the electrode which can be compared to the effect obtained by using supported catalysts. Furthermore, lower porosity also means that less catalyst penetrates so deeply into the GDL that it is out of range of the three phase boundary area and therefore useless. In figure 6.24 these

suggested explanations were supported by the fact that not only did MEAs using felt from batch 1 have lower ohmic resistance contribution to the voltage it also showed lower voltage in the activation governed current density range, although the nominal loading of the MEAs were almost equal.

The properties of the GDL seem to be of the utmost importance to make high performing and reproducible anodes. However as mentioned above the CVD process of coating the stainless steel felt with tantalum leaves the GDL inhomogeneous. To counteract this issue an obvious method would be to be inspired of the cathode and fuel cell technology where the carbon GDLs have been coated with a micro porous layer to create a uniform porous layer onto which the catalyst layer can be sprayed. However making such kinds of porous supporting layers on top of the anode GDL felt is not a trivial task. Corrosion resistant and conducting materials have to be identified, after which a suitable and stable slurry or ink recipe should be found before the optimal method for applying the slurry or ink to the GDL can be determined. Initial work at DTU has been carried out and as a suggested material a combination of tungsten carbide (WC) and PTFE possibly with some suspension agent(s) to achieve the desired properties was tried. The work is still very much in its initial phase and no conclusions about the ratio between WC and PTFE has been found as with the optimum conditions for applying it to the GDL that still need fine tuning.

## 8.4 Importance of anode type – CCM or GDE

It was found that in both the cases for MEAs based on PA doped PBI and PA doped Nafion® that transferring the electrode to the membrane by the decal method can improve the contact between electrode and membrane. In figure 6.2 it could be seen from electrolysis tests with PA doped PBI that having the anode coated to the membrane from the decal method improved the overall performance, mainly by lowering the overall ohmic resistance in the system. However it was, as described earlier, more difficult to get uniform electrodes from the decal transferring method. In figure 6.17 the difficulties about complete and uniform transfer are illustrated. Often it was the case that the transferring percentage was quite low, and also that the transfer was non-uniform. Meaning that in certain areas there were a complete transfer of electrode from the substrate to the membrane, while in other areas no transfer of the electrode was taking place. This made it very difficult to determine the

actual geometric area of the electrode on the membrane, hence making the current density calculations very unreliable.

The initial experiments with transferring the anode to the membrane also revealed that the optimal ionomer binder content in the anode to ensure good and uniform transfer was in conflict with achieving proper electrolyser results. By calculating the approximate volume percentage of binder in the anode it could be explained by a very large volume percentage around 70 vol.%. With such a high volume percentage it is likely that a substantial part of the catalytic active $IrO_2$ is electrically insulated from the GDL and hence not part of the active three phase boundary area. It was proposed that a way to keep the nominal binder amount in the electrode down and still achieving reasonable transfer rate, could be achieved by using a catalyst ink with a lower and more optimal binder content. This ink should then be sprayed to the substrate and first afterwards should an extra layer of binder be applied on top of the catalyst layer. This approach should ensure a sufficient amount of binder to make the catalyst bind better to the membrane than the PTFE substrate and at the same time not mix with the rest of the electrode keeping the nominal binder content in the actual electrode. However during the first initial experiment the problem of complete and uniform transfer still persisted and the greater reproducibility of GDEs made them the preferred electrodes for both the anodes and cathode. This does not mean that it is not possible with sufficient effort and time to optimise the transferring conditions and gain the benefits of a CCM electrode.

## 8.5 Importance of electrode doping

It was, from early on in the electrolysis tests, clear that having sufficient ionic conductivity in the electrodes was crucial to achieve reasonable electrolysis performance. Since the ionic conductivity in the membrane in the case of steam electrolysis was reliant on the PA content of the membrane it was natural to also dope the anode with PA. It was chosen to use a post doping procedure to dope the anodes. First a rather concentrated mixture of PA and acetic acid was used, however this made the total amount of the mixture very small and this limited the coverage of the electrode with PA and also gave rise to issue concerning reproducibility. Hence a more diluted mixture of the acids were used which gave both better coverage and reproducibility. Another possibility of doping the anodes, which was not

pursued in this study, could be mixing the PA in the catalyst ink, this is likely to further improve the distribution of PA over the electrode area.

During the electrolysis experiments only the anode was doped with PA, it was assumed that the cathode was sufficiently doped by residual PA on the surface of the membrane. Further doping of PA of the cathode was avoided since studies from fuel cell literature shows that too high PA levels inhibit the fuel cell performance [223, 224]. The performance is believed to be especially affected by the cathode reaction *i.e.* the oxygen reduction reaction, since PA strongly binds to Pt through the P-O-Pt bond [225, 226] and hence can block oxygen reaction sites [227]. In other fuel cell studies high coverages of PA on the platinum have also been reported [228]. However Oono *et al.* [223] also reported that when the doping level in the electrodes was insufficient then a loss of fuel cell performance was observed. The proposed explanation is that parts of the catalyst in the electrode are not in ionic contact *i.e.* not part of the three phase boundary and hence not catalytic active. The task is then to reach the optimum amount of PA doping where all the electrode area can take part of the catalytic reaction, however still avoiding so much that the catalytic active sites are totally covered by PA. The optimum amount of doping of the PBI membrane in Oono *et al.*'s [223] experiments was 75 wt.% PA this corresponded to a PA amount in the electrodes of 10 $mg \cdot cm^{-2}$ coming from acid migration from the membrane to the electrodes. As mentioned in section 6.3.1 was the PA level in Aquivion™ considerably lower with just approximately 44 wt.%, hence it possible that the level of free PA is not sufficient to migrate in the electrolyse cathode (hydrogen reduction reaction) and ensure adequate ionic conductivity.

It is hard to say if the PA doping of the cathode plays any significant role. When comparing the best obtained steam electrolysis results (see figure 6.26) using different electrolytes the best performing PA doped Aquivion™ MEA show lower overall ohmic resistance than the PA doped PBI MEA. Although the cathode in this case was made with a PA content of approximately 1 $mg \cdot cm^{-2}$ before the MEA assembly, whereas the cathode in the Aquivion™ MEA did not have any pre-doping with PA and thus solely relied on PA migration from the membrane. However many other improvements have been made in the electrolysis setup since the PBI tests *e.g.* new flow pattern and better GDL. It is thus likely that the cathode has not yet become the rate determining step. However in the future it could be the

case, with the further improvements in the anode that the cathode activity becomes a limiting factor and the question about optimal PA content should be addressed.

## 8.6 Stability of PA doped PBI under electrolysis conditions

Another thing that should be addressed in future work is the degradation mechanism of the PA doped PBI membrane. It should be determined whether, as discussed earlier in section 6.1.2, PBI lacks chemical stability under the harsh oxidative and highly humidified conditions and is thermohydrolytically degraded or if it a case of mechanical factors from the materials used. Moreover the failures could also be caused by poor distribution of post-doped PA on the anodes which led to local hot spots in the membrane that hence burned through and made it fail. Until this has been determined PA doped PBI as electrolyte in water electrolysis at elevated temperatures should not be completely ruled out.

## 8.7 Conductivity of electrolytes

When it came to the proton conductivity of the different membranes it was found that at 130 °C and a RH of 16-18 % that PA doped PBI (78 wt.% PA) had a proton conductivity of $9 \cdot 10^{-2}$ $S \cdot cm^{-1}$ while PA doped Nafion which had a considerably lower PA content (34 wt.%) had a conductivity of $3 \cdot 10^{-2}$ $S \cdot cm^{-1}$. The proton conductivity of the PA doped membrane are under these conditions mainly dependent on the PA content, hence it is likely that the proton conductivity of PA doped Aquivion™, which has a PA content of 44 wt.%, lies somewhere between these values. Since PBI was found unsuitable in the tested setup the effort was directed to test PA doped PFSA membranes or ternary composite membranes. The proton conductivities were roughly the same, at least in the same order of magnitude hence it was natural to ascribe the difference in electrolysis performance to mechanical strength. The improvement in electrolyser performance going from Nafion® to Aquivion™ based MEAs fits the found improvement in mechanical strength. This explanation has also been proposed in literature as discussed in section 6.3.

During the experiments it was found that the electrolyser performance was significantly improved by conducting the experiments at elevated pressure in order to keep water in the liquid phase even at elevated temperatures. One reason for this is that the proton conductivity of fully humidified PFSA membranes are in the order of one magnitude higher compared to PA doped PFSA membranes, *e.g.* David Aili reports in his doctoral thesis [203] that the proton conductivity of pure recast Nafion® was $35 \cdot 10^{-2}$ S·cm$^{-1}$ (liquid water, 150 °C and 6 bar) compared to $3 \cdot 10^{-2}$ S·cm$^{-1}$ for PA doped recast Nafion® (34 wt.% PA) (RH 16-18 %, 130 °C and atmospheric pressure). However the improvement in performance could also be from the fact that ionomer binder in both electrodes get fully wetted and hence have circumvented the problem about optimal PA doping of the electrodes, especially the anode.

# 9 Conclusions and outlook

## 9.1 Gas diffusion layers

It was found that even though the variation of the mass of discs punched out from the same sheet of pristine felt was negligible (0.1 %) the variation for tantalum coated felt was considerable in the range between 2 and 7 %. Beside the variation of mass on the same sheet of felt there was also a considerable variation between sheets of felt, where the percentage-wise difference in average mass between discs from different sheets of felt could be up to 10 %. As with the variation of mass a considerable variation of porosity was also observed. The standard deviation between felts of same type and batch tantalum coating was around 5 %, meaning that the porosity in some cases were 10 percentage points different.

Furthermore a marked difference in the appearance of the tantalum coating was also seen between different batches. It was seen that it could vary from quite smooth on the surface of the felt fibres to very rough with dendrites on the fibre surface. There was a correlation between the porosity and the topology of the tantalum coating on the fibres. High porosity gave thinner and smoother coating whereas lower porosity gave coatings with surface dendrites. All this comes down to the CVD process and should of course be optimised.

## 9.2 Steam electrolysis

The electrolysis testing of MEAs with PBI membranes showed that it was possible to achieve reasonably short term electrolysis performance of PBI-MEAs with high anode catalyst loading. The best performance of a PBI-MEA with an anode loading of approximately 10 $mg \cdot cm^{-2}$ $IrO_2$, had a current density of 538 $mA \cdot cm^{-2}$ at a cell voltage of 1.7 V. The durability of MEAs using PBI as membrane however is very poor with an expected life time in this system of few hours.

Concerning MEAs based on Nafion® membranes it was found that ternary composite membranes of ZrP and PA gave better performance than Nafion® membranes only doped with PA. For the best

performing MEA using a Nafion® 212 + ZrP + PA membrane and an anode loading of approximately 3 $mg \cdot cm^{-2}$ $IrO_2$, a current density of 310 $mA \cdot cm^{-2}$ at 1.7 V was achieved. Durability test with a Nafion® 115 + ZrP + PA ternary composite membrane showed that the MEA could be run for at least 72 hours without membrane failure, which was a considerable improvement compared to the PBI MEAs. However, the performance was not very stable and the current density decayed with around 0.17 $mA \cdot h^{-1}$, with the voltage kept constant at 1.7 V.

The steam electrolysis experiments using PA doped Aquivion™ membrane as electrolyte showed quite good performance probably due to the slightly improved mechanical stability for the PA doped Aquivion™ membrane compared to PA recast Nafion® membranes. The best performing PA doped Aquivion™ MEA had a current density of 602 $mA \cdot cm^{-2}$ at a cell voltage of 1.7 V, with an $IrO_2$ loading of approximately 1 $mg \cdot cm^{-2}$. The durability of PA doped Aquivion™ also showed quite promising results, with a thicker Aquivion™ membrane a life time of at least 760 hours was achieved, after a fast degradation of the first 100 hours the increase in voltage over the next 660 hours was between 0.023 and 0.04 $mV \cdot h^{-1}$ at a constant current density of 400 $mA \cdot cm^{-2}$.

It was found that even with a factor of ten decreased anode loading, the electrolyser performance was improved by approximately 64 $mA \cdot cm^{-2}$ (at 1.7 V) using a PA doped Aquivion membrane compared to a PA doped PBI membrane. The increase in performance came from a lower ohmic resistance in the system. However many improvements were done in the surrounding parameters since the first experiments with the PBI systems, *e.g.* better flow pattern, GDL etc.

## 9.3 Pressurised liquid electrolysis

Three different flow patterns and two different types and thicknesses of anode GDL were tested using an Aquivion™ membrane in a pressurised setup operated at 120 °C and 3 bar pressure. It was found that the thin (0.2 mm) single layer felt gave a better performance compared to a thicker (0.5 mm) double layer felt although the fibre thickness was the same on the side of the felts facing towards the membrane. Of the three tested flow patterns the square serpentine flow pattern used at ITCP clearly had

the best performance reaching current densities of approximately 1300 $mA \cdot cm^{-2}$ at 1.7 V using an anode loading of approximately 3 $mg \cdot cm^{-2}$ $IrO_2$. The reduction of ohmic resistance in the serpentine flow pattern was believed to be caused by the larger contact area and better current and flow distribution from the flow pattern to the GDL.

It was found that pressurised liquid water electrolysis (120 °C and 3 bar) using a composite membrane of Nafion® and $BPO_4$ gave reasonable electrolyser result compared to traditional Nafion® 112 membrane. At a cell voltage of approximately 1.75 V the Nafion® + $BPO_4$ composite had a current density of 180 $mA \cdot cm^{-2}$ (750 $mA \cdot cm^{-2}$) higher than a comparable Nafion® 112 MEA.

## 9.4 Outlook

For future water electrolysis at elevated temperatures, it seems obvious that pressurised systems give much better performance than steam electrolysis. However further improvements to be carried out for both steam and liquid water electrolysis at elevated temperatures in order to get improved performance are *e.g.* an optimisation of the electrode structure especially for the anodes. For commercial PEM electrolysers GDEs seem to be the way to go, since they are easier to manufacture in a reproducible way. However many factors concerning the GDL onto which the electrode layer is sprayed can be greatly optimised, *e.g.* the porosity and the topology of the fibres in the felt. Optimising the process parameters for the tantalum CVD coating of porous felt is of the utmost importance, since without proper and reproducible GDLs further water electrolysis tests at elevated temperature will be severely hampered. Concerning the electrolyte, in the case of PFSA based membranes, some kind of inorganic filler (*e.g.* ZrP or $BPO_4$) should be incorporated in the membrane mainly to increase the mechanical strength of the membrane, but also to improve the water retention, i.e. the proton conductivity. Another way to strengthen the membrane and hence enabling it to withhold sufficient structural integrity, could be to make a composite membrane with another kind of reinforcement, *e.g.* a porous PTFE mesh.

# 10 References


[1] Mann, Bradley, Hughes. *Northern hemisphere temperatures during the past millennium: inferences, uncertainties, and limitations*. Geophys. Res. Lett. **1999**;26:759-62.

[2] Cao L, Bala G, Caldeira K, Nemani R, Ban-Weiss G. *Importance of carbon dioxide physiological forcing to future climate change*. Proc. Natl. Acad. Sci. U. S. A. **2010**;107:9513-8.

[3] Princiotta F. *Global climate change and the mitigation challenge*. Journal of the Air and Waste Management Association **2009**;59:1194-211.

[4] Dufresne JL, Friedlingstein P, Berthelot M, Bopp L, Ciais P, Fairhead L, et al. *On the magnitude of positive feedback between future climate change and the carbon cycle*. Geophys. Res. Lett. **2002**;29:43-1-4.

[5] Siegenthaler U, Stocker TF, Monnin E, Luthi D, Schwander J, Stauffer B, et al. *Stable carbon cycle-climate relationship during the late Pleistocene*. Science (Washington D C) **2005**;310:1313-7.

[6] Harris DC. *Charles David Keeling and the Story of Atmospheric $CO_2$ Measurements*. Anal. Chem. **2010**;82:7865-70.

[7] Jensen JO, Bandur V, Bjerrum NJ, Jensen SH, Ebbesen S, Mogensen M, et al., *Pre-investigation of water electrolysis*. **2008**: Lyngby. p. 195.

[8] Millet P, Andolfatto F, Durand R. *Design and performance of a solid polymer electrolyte water electrolyzer*. Int. J. Hydrogen Energy **1996**;21:87-93.

[9] Grigoriev SA, Millet P, Volobuev SA, Fateev VN. *Optimization of porous current collectors for PEM water electrolysers*. Int. J. Hydrogen Energy **2009**;34:4968-73.

[10] Rasten E, Hagen G, Tunold R. *Electrocatalysis in water electrolysis with solid polymer electrolyte*. Electrochim. Acta **2003**;48:3945-52.

[11] Grigoriev SA, Millet P, Korobtsev SV, Porembskiy VI, Pepic M, Etievant C, et al. *Hydrogen safety aspects related to high-pressure polymer electrolyte membrane water electrolysis*. Int. J. Hydrogen Energy **2009**;34:5986-91.

[12] Grigoriev SA, Porembskiy VI, Korobtsev SV, Fateev VN, Auprêtre F, Millet P. *High-pressure PEM water electrolysis and corresponding safety issues*. Int. J. Hydrogen Energy **2011**;36:2721-8.

[13] Narayanan SR, Kindler A, Kisor A, Valdez T, Roy RJ, Eldridge C, et al. *Dual-feed balanced high-pressure electrolysis of water in a lightweight polymer electrolyte membrane stack*. J. Electrochem. Soc. **2011**;158:B1348-B57.

[14] Hamdan M, Norman T. *2010 Annual Progress Report - DOE Hydrogen Program*. Section II.E.2 - PEM Electrolyzer Incorporating an Advanced Low-Cost Membrane, U.S. Department of Energy; **2010**

[15] Marangio F, Pagani M, Santarelli M, Calì M. *Concept of a high pressure PEM electrolyser prototype*. Int. J. Hydrogen Energy **2011**;36:7807-15.

[16] Ni M, Leung MKH, Leung DYC. *Technological development of hydrogen production by solid oxide electrolyzer cell (SOEC)*. Int. J. Hydrogen Energy **2008**;33:2337-54.

[17] Ebbesen SD, Graves C, Hauch A, Jensen SH, Mogensen M. *Poisoning of solid oxide electrolysis cells by impurities*. J. Electrochem. Soc. **2010**;157:B1419-B29.

[18] Knibbe R, Traulsen ML, Hauch A, Ebbesen SD, Mogensen M. *Solid oxide electrolysis cells: Degradation at high current densities*. J. Electrochem. Soc. **2010**;157:B1209-B17.

[19] Schefold, Brisse, Zahid. *Electronic Conduction of Yttria-Stabilized Zirconia Electrolyte in Solid Oxide Cells Operated in High Temperature Water Electrolysis*. J. Electrochem. Soc. **2009**;156:897-904.

[20] Brisse A, Schefold J, Zahid M. *High temperature water electrolysis in solid oxide cells*. Int. J. Hydrogen Energy **2008**;33:5375-82.

[21] Schiller G, Ansar A, Lang M, Patz O. *High temperature water electrolysis using metal supported solid oxide electrolyser cells (SOEC)*. J. Appl. Electrochem. **2009**;39:293-301.

[22] Laguna-Bercero MA, Kilner JA, Skinner SJ. *Performance and Characterization of (La, Sr)$MnO_3$/YSZ and $La_{0.6}Sr_{0.4}Co_{0.2}Fe_{0.8}O_3$ Electrodes for Solid Oxide Electrolysis Cells*. Chem. Mater. **2010**;22:1134-41.

[23] Linkous CA, Anderson HR, Kopitzke RW, Nelson GL. *Development of new proton exchange membrane electrolytes for water electrolysis at higher temperatures*. Int. J. Hydrogen Energy **1998**;23:525-9.

[24] Li Q, He R, Jensen JO, Bjerrum NJ. *Approaches and Recent Development of Polymer Electrolyte Membranes for Fuel Cells Operating above 100 °C*. Chem. Mater. **2003**;15:4896-915.

[25] Macdonald DI, Boyack JR. *Density, Electrical Conductivity, and Vapor Pressure of Concentrated Phosphoric Acid*. J Chem & Eng Data **1969**;14:380-4.

[26] Wainright JS, Wang JT, Weng D, Savinell RF, Litt M. *Acid-doped polybenzimidazoles: A new polymer electrolyte*. J. Electrochem. Soc. **1995**;142:L121-3.

[27] Li Q, Jensen JO, Savinell RF, Bjerrum NJ. *High temperature proton exchange membranes based on polybenzimidazoles for fuel cells*. Prog. Polym. Sci. **2009**;34:449-77.

[28] Xu W, Scott K, Basu S. *Performance of a high temperature polymer electrolyte membrane water electrolyser*. J. Power Sources **2011**;196:8918-24.

[29] Antonucci V, Di Blasi A, Baglio V, Ornelas R, Matteucci F, Ledesma-Garcia J, et al. *High temperature operation of a composite membrane-based solid polymer electrolyte water electrolyser*. Electrochim. Acta **2008**;53:7350-6.

[30] Baglio V, Ornelas R, Matteucci F, Martina F, Ciccarella G, Zama I, et al. *Solid Polymer Electrolyte Water Electrolyser Based on Nafion-$TiO_2$ Composite Membrane for High Temperature Operation*. Fuel Cells **2009**;9:247-52.

[31] Millet P, Dragoe D, Grigoriev S, Fateev V, Etievant C. *GenHyPEM: A research program on PEM water electrolysis supported by the European Commission*. Int. J. Hydrogen Energy **2009**;34:4974-82.

[32] Ghielmi A, Vaccarono P, Troglia C, Arcella V. *Proton exchange membranes based on the short-side-chain perfluorinated ionomer*. J. Power Sources **2005**;145:108-15.

[33] Kreuer KD, Schuster M, Obliers B, Diat O, Traub U, Fuchs A, et al. *Short-side-chain proton conducting perfluorosulfonic acid ionomers: Why they perform better in PEM fuel cells*. J. Power Sources **2008**;178:499-509.

[34] Aricò AS, Di Blasi A, Brunaccini G, Sergi F, Dispenza G, Andaloro L, et al. *High Temperature Operation of a Solid Polymer Electrolyte Fuel Cell Stack Based on a New Ionomer Membrane*. Fuel Cells **2010**;10:1013-23.

[35] Hwang CM, Ishida M, Ito H, Maeda T, Nakano A, Hasegawa Y, et al. *Influence of properties of gas diffusion layers on the performance of polymer electrolyte-based unitized reversible fuel cells*. Int. J. Hydrogen Energy **2011**;36:1740-53.

[36] Nikiforov AV, Petrushina IM, Christensen E, Tomás-García AL, Bjerrum NJ. *Corrosion behaviour of construction materials for high temperature steam electrolysers*. Int. J. Hydrogen Energy **2011**;36:111-9.

[37] Kouřil M, Christensen E, Eriksen S, Gillesberg B *Corrosion rate of construction materials in hot phosphoric acid with the contribution of anodic polarization*. Mater. Corros. **2011** DOI: 10.1002/maco.201006021.

[38] Lecuyer, Quemerais, Jezequel. *Composition of natural oxide films on polycrystalline tantalum using XPS electron take-off angle experiments*. Surf. Interface Anal. **1992**;18:257-61.

[39] Zhang L, Liu Y, Song H, Wang S, Zhou Y, Hu SJ. *Estimation of contact resistance in proton exchange membrane fuel cells*. J. Power Sources **2006**;162:1165-71.

[40] Zhou Y, Lin G, Shih AJ, Hu SJ. *A micro-scale model for predicting contact resistance between bipolar plate and gas diffusion layer in PEM fuel cells*. J. Power Sources **2007**;163:777-83.

[41] de Levie R. *The electrolysis of water*. J. Electroanal. Chem. **1999**;476:92-3.

[42] Trasatti S. *Water electrolysis: who first?* J. Electroanal. Chem. **1999**;476:90-1.

[43] Cavendish H. *Experiments on Air*. Philosophical Transactions of the Royal Society of London **1784**;74:119-53.

[44] Trasatti S. *1799-1999: Alessandro Volta's "Electric Pile": Two hundred years, but it doesn't seem like it*. J. Electroanal. Chem. **1999**;460:1-4.

[45] Volta A. *On the Electricity Excited by the Mere Contact of Conducting Substances of Different Kinds*. Philosophical Transactions of the Royal Society of London **1800**;90:403-31.

[46] Nicholson W. *BESCHREIBUNG des neuen electrischen oder galvanischen Apparats ALEXANDER VOLTA'S, und einiger wichtigen damit angestellten Versuche*. Annalen der Physik **1800**;6:340-59.

[47] Kreuter W, Hofmann H. *Electrolysis: the important energy transformer in a world of sustainable energy*. Int. J. Hydrogen Energy **1998**;23:661-6.

[48] Millet P, Alleau T, Durand R. *Characterization of membrane-electrode assemblies for solid polymer electrolyte water electrolysis*. J. Appl. Electrochem. **1993**;23:322-31.

[49] Takenaka H, Torikai E, Kawami Y, Wakabayashi N. *Solid polymer electrolyte water electrolysis*. Int. J. Hydrogen Energy **1982**;7:397-403.

[50] Yamaguchi M, Okisawa K, Nakanori T. *Development of high performance solid polymer electrolyte water electrolyzer in WE-NET*. Proc. Intersoc. Energy Convers. Eng. Conf. **1997**;3-4:1958-61.

[51] Bard AJ, Faulkner LR, Zoski CG, Leddy J. *Electrochemical methods ; fundamentals and applications ; Allen J. Bard, Larry R. Faulkner*. 2nd ed. New York: John Wiley **2001**.

[52] Millet P, Ngameni R, Grigoriev SA, Mbemba N, Brisset F, Ranjbari A, et al. *PEM water electrolyzers: From electrocatalysis to stack development*. Int. J. Hydrogen Energy **2010**;35:5043-52.

[53] Zeng K, Zhang D. *Recent progress in alkaline water electrolysis for hydrogen production and applications*. Progr. Energy Combust. Sci. **2010**;36:307-26.

[54] Haynes WM, Lide DR. *CRC handbook of chemistry and physics 91st Ed.* Boca Raton, Fla.: CRC **2010**.

[55] Slavcheva E, Schnakenberg U, Mokwa W. *Deposition of sputtered iridium oxide - Influence of oxygen flow in the reactor on the film properties*. Appl. Surf. Sci. **2006**;253:1964-9.
[56] Da Silva LM, Franco DV, De Faria LA, Boodts JFC. *Surface, kinetics and electrocatalytic properties of Ti/($IrO_2$ + $Ta_2O_5$) electrodes, prepared using controlled cooling rate, for ozone production*. Electrochim. Acta **2004**;49:3977-88.
[57] Hanslmeier A. *Water in the universe*. Dordrecht: Springer; **2011**. p. 1-24.
[58] Elshout R. *Hydrogen Production By Steam Reforming*. Chem. Eng. (N.Y.) **2010**;117:34-8.
[59] Balat M. *Possible Methods for Hydrogen Production*. Energy Sources Part A **2009**;31:39-50.
[60] Momirlan M, Veziroglu TN. *Current status of hydrogen energy*. Renewable and Sustainable Energy Reviews **2002**;6:141-79.
[61] Hulteberg C. *Sulphur-tolerant catalysts in small-scale hydrogen production, a review*. Int. J. Hydrogen Energy **2012**;37:3978-92.
[62] Kogan A. *Direct solar thermal splitting of water and on-site separation of the products - II. Experimental feasibility study*. Int. J. Hydrogen Energy **1998**;23:89-98.
[63] Perkins C, Weimer AW. *Likely near-term solar-thermal water splitting technologies*. Int. J. Hydrogen Energy **2004**;29:1587-99.
[64] Ahmed I, Jangsawang W, Gupta AK. *Energy recovery from pyrolysis and gasification of mangrove*. Appl. Energy **2012**;91:173-9.
[65] Guo H, Zhang P, Chen S, Wang L, Xu J. *Review of thermodynamic properties of the components in HI decomposition section of the iodine-sulfur process*. Int. J. Hydrogen Energy **2011**;36:9505-13.
[66] Giaconia A, Grena R, Lanchi M, Liberatore R, Tarquini P. *Hydrogen/methanol production by sulfur-iodine thermochemical cycle powered by combined solar/fossil energy*. Int. J. Hydrogen Energy **2007**;32:469-81.
[67] Bulushev DA, Ross JRH. *Catalysis for conversion of biomass to fuels via pyrolysis and gasification: A review*. Catal. Today **2011**;171:1-13.
[68] Sayama K, Abe R, Arakawa H, Sugihara H. *Decomposition of water into $H_2$ and $O_2$ by a two-step photoexcitation reaction over a Pt-$TiO_2$ photocatalyst in $NaNO_2$ and $Na_2CO_3$ aqueous solution*. Catal. Commun. **2006**;7:96-9.
[69] Simarro R, Cervera-March S, Esplugas S. *Hydrogen photoproduction in a continuous flow system with u.v.-light and aqueous suspensions of $RuO_x$/Pt/$TiO_2$*. Int. J. Hydrogen Energy **1985**;10:221-6.
[70] Levin DB, Pitt L, Love M. *Biohydrogen production: prospects and limitations to practical application*. Int. J. Hydrogen Energy **2004**;29:173-85.
[71] Zhang YHP. *A sweet out-of-the-box solution to the hydrogen economy: is the sugar-powered car science fiction?* Energy & Environmental Science **2009**;2:272-82.
[72] Ye X, Wang Y, Hopkins RC, Adams MWW, Evans BR, Mielenz JR, et al. *Spontaneous High-Yield Production of Hydrogen from Cellulosic Materials and Water Catalyzed by Enzyme Cocktails*. CHEMSUSCHEM **2009**;2:149-52.
[73] Ho GW, Chua KJ, Siow DR. *Metal loaded $WO_3$ particles for comparative studies of photocatalysis and electrolysis solar hydrogen production*. Chem. Eng. J. (Lausanne) **2012**;181-182:661-6.
[74] Zhong M, Shi J, Xiong F, Zhang W, Li C. *Enhancement of photoelectrochemical activity of nanocrystalline CdS photoanode by surface modification with $TiO_2$ for hydrogen production and electricity generation*. Solar Energy **2012**;86:756-63.

[75] Wang L, Chen Y, Ye Y, Lu B, Zhu S, Shen S. *Evaluation of low-cost cathode catalysts for high yield biohydrogen production in microbial electrolysis cell*. Water Sci. Technol. **2011**;63:440-8.
[76] Liu H, Grot S, Logan BE. *Electrochemically Assisted Microbial Production of Hydrogen from Acetate*. Environ. Sci. Technol. **2005**;39:4317-20.
[77] Stiegel GJ, Ramezan M. *Hydrogen from coal gasification: An economical pathway to a sustainable energy future*. Int. J. Coal Geol. **2006**;65:173-90.
[78] Rostrup-Nielsen JR, Sehested J, Nørskov JK. *Hydrogen and synthesis gas by steam- and $CO_2$ reforming*. Adv. Catal.: Academic Press; **2002**. p. 65-139.
[79] Rostrup-Nielsen JR. *Production of synthesis gas*. Catal. Today **1993**;18:305-24.
[80] Sehested J. *Four challenges for nickel steam-reforming catalysts*. Catal. Today **2006**;111:103-10.
[81] Sehested J, Gelten JAP, Helveg S. *Sintering of nickel catalysts: Effects of time, atmosphere, temperature, nickel-carrier interactions, and dopants*. Applied Catalysis A, General **2006**;309:237-46.
[82] Sircar S, Waldron WE, Rao MB, Anand M. *Hydrogen production by hybrid SMR-PSA-SSF membrane system*. Sep. Purif. Technol. **1999**;17:11-20.
[83] Oetjen, Schmidt, Stimming, Trila. *Performance data of a proton exchange membrane fuel cell using $H_2$/CO as fuel gas*. J. Electrochem. Soc. **1996**;143:3838-42.
[84] Li Q, He R, Gao J-A, Jensen JO, Bjerrum NJ. *The CO poisoning effect in PEMFCs operational at temperatures up to 200 °C*. J. Electrochem. Soc. **2003**;150:A1599-A605.
[85] Wannek C, Kohnen B, Oetjen HF, Lippert H, Mergel J. *Durability of ABPBI-based MEAs for High Temperature PEMFCs at Different Operating Conditions*. Fuel Cells **2008**;8:87-95.
[86] Schmidt TJ, Baurmeister J. *Properties of high-temperature PEFC Celtec®-P 1000 MEAs in start/stop operation mode*. J. Power Sources **2008**;176:428-34.
[87] Lopes FVS, Grande CA, Rodrigues AE. *Activated carbon for hydrogen purification by pressure swing adsorption: Multicomponent breakthrough curves and PSA performance*. Chem. Eng. Sci. **2011**;66:303-17.
[88] Bastos-Neto M, Moeller A, Staudt R, Böhm J, Gläser R. *Dynamic bed measurements of CO adsorption on microporous adsorbents at high pressures for hydrogen purification processes*. Sep. Purif. Technol. **2011**;77:251-60.
[89] Sircar S, Golden TC. *Purification of hydrogen by pressure swing adsorption*. Sep. Sci. Technol. **2000**;35:667-87.
[90] Ryland, Li, Sadhankar. *Electrolytic hydrogen generation using CANDU nuclear reactors*. International Journal of Energy Research **2007**;31:1142-55.
[91] Trasatti S. *Electrocatalysis in the anodic evolution of oxygen and chlorine*. Electrochim. Acta **1984**;29:1503-12.
[92] Vayenas CG. *Electrochemical activation of catalysis*. Norwich, NY: Knovel **2005**.
[93] Parsons R. *The kinetics of electrode reactions and the electrode material*. Surf. Sci. **1964**;2:418-35.
[94] Kinoshita K. *Electrochemical oxygen technology*. New York,N.Y.: Wiley **1992**.
[95] Guanti, Moran. *Measurement of electrolyte conductivity in highly conducting solutions*. J. Appl. Electrochem. **1986**;16:678-82.
[96] Shcherbakov VV. *Regularity of conductivity of concentrated aqueous solutions of strong electrolytes*. Russ. J. Electrochem. **2009**;45:1292-5.

[97] Rosa VM, Santos MBF, Da Silva EP. *New materials for water electrolysis diaphragms*. Int. J. Hydrogen Energy **1995**;20:697-700.
[98] Smith AH, Wright CC. *Chrysotile asbestos is the main cause of pleural mesothelioma*. American Journal of Industrial Medicine **1996**;30:252-66.
[99] Appleby AJ, Crepy G, Jacquelin J. *High efficiency water electrolysis in alkaline solution*. Int. J. Hydrogen Energy **1978**;3:21-37.
[100] Pletcher D, Li X. *Prospects for alkaline zero gap water electrolysers for hydrogen production*. Int. J. Hydrogen Energy **2011**;36:15089-104.
[101] Li X, Walsh FC, Pletcher D. *Nickel based electrocatalysts for oxygen evolution in high current density, alkaline water electrolysers*. Physical chemistry chemical physics. **2011**;13:1162-7.
[102] Bocca C, Barbucci A, Cerisola G. *The influence of surface finishing on the electrocatalytic properties of nickel for the oxygen evolution reaction (OER) in alkaline solution*. Int. J. Hydrogen Energy **1998**;23:247-52.
[103] Bocca C, Barbucci A, Delucchi M, Cerisola G. *NICKEL-COBALT oxide-coated electrodes: influence of the preparation technique on oxygen evolution reaction (OER) in an alkaline solution*. Int. J. Hydrogen Energy **1999**;24:21-5.
[104] Mauer AE, Kirk DW, Thorpe SJ. *The role of iron in the prevention of nickel electrode deactivation in alkaline electrolysis*. Electrochim. Acta **2007**;52:3505-9.
[105] Abouatallah RM, Kirk DW, Thorpe SJ, Graydon JW. *Reactivation of nickel cathodes by dissolved vanadium species during hydrogen evolution in alkaline media*. Electrochim. Acta **2001**;47:613-21.
[106] Ishihara T, Kanno T. *Steam electrolysis using $LaGaO_3$ based perovskite electrolyte for recovery of unused heat energy*. ISIJ Int. **2010**;50:1291-5.
[107] Liu Q, Yang C, Dong X, Chen F. *Perovskite $Sr_2Fe_{1.5}Mo_{0.5}O_{6-\delta}$ as electrode materials for symmetrical solid oxide electrolysis cells*. Int. J. Hydrogen Energy **2010**;35:10039-44.
[108] Jin C, Yang C, Zhao F, Cui D, Chen F. *$La_{0.75}Sr_{0.25}Cr_{0.5}Mn_{0.5}O_3$ as hydrogen electrode for solid oxide electrolysis cells*. Int. J. Hydrogen Energy **2011**;36:3340-6.
[109] Hauch A, Ebbesen SD, Jensen SH, Mogensen M. *Highly efficient high temperature electrolysis*. J. Mater. Chem. **2008**;18:2331-40.
[110] Huang KQ, Goodenough JB. *A solid oxide fuel cell based on Sr- and Mg-doped LaGaO3 electrolyte: the role of a rare-earth oxide buffer*. J. Alloys Compd. **2000**;303:454-64.
[111] Kreuer K-D, Schuster M, Paddison SJ, Spohr E. *Transport in proton conductors for fuel-cell applications: Simulations, elementary reactions, and phenomenology*. Chem. Rev. (Washington, DC, U. S.) **2004**;104:4637-78.
[112] Page KA, Cable KM, Moore RB. *Molecular origins of the thermal transitions and dynamic mechanical relaxations in perfluorosulfonate ionomers*. Macromolecules **2005**;38:6472-84.
[113] Mayousse E, Maillard F, Fouda-Onana F, Sicardy O, Guillet N. *Synthesis and characterization of electrocatalysts for the oxygen evolution in PEM water electrolysis*. Int. J. Hydrogen Energy **2011**;36:10474-81.
[114] Zhang L, Jie X, Shao Z-G, Zhou Z-M, Xiao G, Yi B. *The influence of sodium ion on the solid polymer electrolyte water electrolysis*. Int. J. Hydrogen Energy **2011**:In press.
[115] Zhang Y, Wang C, Wan N, Liu Z, Mao Z. *Study on a novel manufacturing process of membrane electrode assemblies for solid polymer electrolyte water electrolysis*. Electrochem. Commun. **2007**;9:667-70.

[116] Marshall A, Børresen B, Hagen G, Tsypkin M, Tunold R. *Hydrogen production by advanced proton exchange membrane (PEM) water electrolysers - Reduced energy consumption by improved electrocatalysis*. Energy **2007**;32:431-6.
[117] Giddey S, Ciacchi FT, Badwal SPS. *High purity oxygen production with a polymer electrolyte membrane electrolyser*. J. Membr. Sci. **2010**;346:227-32.
[118] Grigoriev SA, Millet P, Fateev VN. *Evaluation of carbon-supported Pt and Pd nanoparticles for the hydrogen evolution reaction in PEM water electrolysers*. J. Power Sources **2008**;177:281-5.
[119] Siracusano S, Baglio V, Di Blasi A, Briguglio N, Stassi A, Ornelas R, et al. *Electrochemical characterization of single cell and short stack PEM electrolyzers based on a nanosized $IrO_2$ anode electrocatalyst*. Int. J. Hydrogen Energy **2010**;35:5558-68.
[120] Siracusano S, Baglio V, Stassi A, Ornelas R, Antonucci V, Aricò AS. *Investigation of $IrO_2$ electrocatalysts prepared by a sulfite-couplex route for the $O_2$ evolution reaction in solid polymer electrolyte water electrolyzers*. Int. J. Hydrogen Energy **2011**;36:7822-31.
[121] Siracusano S, Di Blasi A, Baglio V, Brunaccini G, Briguglio N, Stassi A, et al. *Optimization of components and assembling in a PEM electrolyzer stack*. Int. J. Hydrogen Energy **2011**;36:3333-9.
[122] Cruz JC, Baglio V, Siracusano S, Ornelas R, Ortiz-Frade L, Arriaga LG, et al. *Nanosized $IrO_2$ electrocatalysts for oxygen evolution reaction in an SPE electrolyzer*. Journal of Nanoparticle Research **2011**;13:1639-46.
[123] Marshall A, Børresen B, Hagen G, Tsypkin M, Tunold R. *Electrochemical characterisation of $Ir_xSn_{1-x}O_2$ powders as oxygen evolution electrocatalysts*. Electrochim. Acta **2006**;51:3161-7.
[124] Ito H, Maeda T, Nakano A, Hasegawa Y, Yokoi N, Hwang CM, et al. *Effect of flow regime of circulating water on a proton exchange membrane electrolyzer*. Int. J. Hydrogen Energy **2010**;35:9550-60.
[125] Fuentes RE, Weidner JW, Rau S, Smolinka T. *Bimetallic electrocatalysts supported on $TiO_2$ for PEM water electrolyzer*. ECS Trans. **2010**;28:23-35.
[126] Ma L, Sui S, Zhai Y. *Investigations on high performance proton exchange membrane water electrolyzer*. Int. J. Hydrogen Energy **2009**;34:678-84.
[127] Shao ZG, Yi BL, Han M. *The membrane electrodes assembly for SPE water electrolysis*. HYDROGEN ENERGY PROGRESS XIII, VOLS 1 AND 2, PROCEEDINGS **2000**:269-73.
[128] Marshall AT, Sunde S, Tsypkin M, Tunold R. *Performance of a PEM water electrolysis cell using $Ir_xRu_yTa_zO_2$ electrocatalysts for the oxygen evolution electrode*. Int. J. Hydrogen Energy **2007**;32:2320-4.
[129] Labou D, Slavcheva E, Schnakenberg U, Neophytides S. *Performance of laboratory polymer electrolyte membrane hydrogen generator with sputtered iridium oxide anode*. J. Power Sources **2008**;185:1073-8.
[130] Siracusano S, Baglio V, D´Urso C, Antonucci V, Aricò AS. *Preparation and characterization of titanium suboxides as conductive supports of $IrO_2$ electrocatalysts for application in SPE electrolysers*. Electrochim. Acta **2009**;54:6292-9.
[131] Grigoriev SA, Mamat MS, Dzhus KA, Walker GS, Millet P. *Platinum and palladium nano-particles supported by graphitic nano-fibers as catalysts for PEM water electrolysis*. Int. J. Hydrogen Energy **2011**;36:4143-7.
[132] Naga Mahesh K, Sarada Prasad J, Venkateswer Rao M, Himabindu V, Yerramilli A, Raghunathan Rao P. *Performance of Pd on activated carbon as hydrogen electrode with respect*

*to hydrogen yield in a single cell proton exchange membrane (PEM) water electrolyser*. Int. J. Hydrogen Energy **2009**;34:6085-8.

[133] Holze R, Ahn JC. *Advances in the use of perfluorinated cation-exchange membranes in integrated water electrolysis and hydrogen oxygen fuel-cell systems*. J. Membr. Sci. **1992**;73:87-97.

[134] Slavcheva E, Radev I, Bliznakov S, Topalov G, Andreev P, Budevski E. *Sputtered iridium oxide films as electrocatalysts for water splitting via PEM electrolysis*. Electrochim. Acta **2007**;52:3889-94.

[135] Millet P, Durand R, Pineri M. *Preparation of new solid polymer electrolyte composites for water electrolysis*. Int. J. Hydrogen Energy **1990**;15:245-53.

[136] Di Blasi A, D'Urso C, Baglio V, Antonucci V, Arico' AS, Ornelas R, et al. *Preparation and evaluation of $RuO_2$-$IrO_2$, $IrO_2$-Pt and $IrO_2$-$Ta_2O_5$ catalysts for the oxygen evolution reaction in an SPE electrolyzer*. J. Appl. Electrochem. **2009**;39:191-6.

[137] Onda, Murakami, Hikosaka, Kobayashi, Notu, Ito. *Performance analysis of polymer-electrolyte water electrolysis cell at a small-unit test cell and performance prediction of large stacked cell*. J. Electrochem. Soc. **2002**;149:A1069-78.

[138] Paunovic P, Gogovska DS, Popovski O, Stoyanova A, Slavcheva E, Lefterova E, et al. *Preparation and characterization of Co-Ru/$TiO_2$/MWCNTs electrocatalysts in PEM hydrogen electrolyzer*. Int. J. Hydrogen Energy **2011**;36:9405-14.

[139] Slavcheva EP. *Magnetron sputtered iridium oxide as anode catalyst for pem hydrogen generation*. Macedonian Journal of Chemistry and Chemical Engineering **2011**;30:45-54.

[140] Aldebert P, Novel-Cattin F, Pineri M, Millet P, Doumain C, Durand R. *Preparation and characterization of SPE composites for electrolyzers and fuel cells*. Solid State Ionics **1989**;35:3-9.

[141] Tanaka Y, Uchinashi S, Saihara Y, Kikuchi K, Okaya T, Ogumi Z. *Dissolution of hydrogen and the ratio of the dissolved hydrogen content to the produced hydrogen in electrolyzed water using SPE water electrolyzer*. Electrochim. Acta **2003**;48:4013-9.

[142] Balaji R, Senthil N, Vasudevan S, Ravichandran S, Mohan S, Sozhan G, et al. *Development and performance evaluation of Proton Exchange Membrane (PEM) based hydrogen generator for portable applications*. Int. J. Hydrogen Energy **2011**;36:1399-403.

[143] Millet P, Pineri M, Durand R. *New solid polymer electrolyte composites for water electrolysis*. J. Appl. Electrochem. **1989**;19:162-6.

[144] Sapountzi FM, Divane SC, Papaioannou EI, Souentie S, Vayenas CG. *The role of Nafion content in sputtered $IrO_2$ based anodes for low temperature PEM water electrolysis*. J. Electroanal. Chem. **2011**;662:116-22.

[145] Sakai T, Kawami Y, Takenaka H, Torikai E. *Effects of surface roughening of Nafion$^{(R)}$ on electrode plating, mechanical strength, and cell performances for SPE water electrolysis*. J. Electrochem. Soc. **1990**;137:3777-83.

[146] Scherer GG, Killer E, Grman D. *Radiation grafted membranes: Some structural investigations in relation to their behavior in ion-exchange-membrane water electrolysis cells*. Int. J. Hydrogen Energy **1992**;17:115-23.

[147] Lee K-M, Woo J-Y, Jee B-C, Hwang Y-K, Yun C-h, Moon S-B, et al. *Effect of cross-linking agent and heteropolyacid (HPA) contents on physicochemical characteristics of covalently cross-linked sulfonated poly(ether ether ketone)/HPAs composite membranes for water electrolysis*. Journal of Industrial and Engineering Chemistry **2011**;17:657-66.

[148] Jang I-Y, Kweon O-H, Kim K-E, Hwang G-J, Moon S-B, Kang A-S. *Covalently cross-linked sulfonated poly(ether ether ketone)/tungstophosphoric acid composite membranes for water electrolysis application*. J. Power Sources **2008**;181:127-34.

[149] Jang I-Y, Kweon O-H, Kim K-E, Hwang G-J, Moon S-B, Kang A-S. *Application of polysulfone (PSf) and polyether ether ketone (PEEK) tungstophosphoric acid (TPA) composite membranes for water electrolysis*. J. Membr. Sci. **2008**;322:154-61.

[150] Cheng J, Zhang H, Ma H, Zhong H, Zou Y. *Study of carbon-supported $IrO_2$ and $RuO_2$ for use in the hydrogen evolution reaction in a solid polymer electrolyte electrolyzer*. Electrochim. Acta **2010**;55:1855-61.

[151] Cheng J, Zhang H, Ma H, Zhong H, Zou Y. *Preparation of $Ir_{0.4}Ru_{0.6}Mo_xO_y$ for oxygen evolution by modified Adams' fusion method*. Int. J. Hydrogen Energy **2009**;34:6609-13.

[152] Cheng J, Zhang H, Chen G, Zhang Y. *Study of IrxRu1-xO2 oxides as anodic electrocatalysts for solid polymer electrolyte water electrolysis*. Electrochim. Acta **2009**;54:6250-6.

[153] Wei G, Wang Y, Huang C, Gao Q, Wang Z, Xu L. *The stability of MEA in SPE water electrolysis for hydrogen production*. Int. J. Hydrogen Energy **2010**;35:3951-7.

[154] Song S, Zhang H, Ma X, Shao Z, Baker RT, Yi B. *Electrochemical investigation of electrocatalysts for the oxygen evolution reaction in PEM water electrolyzers*. Int. J. Hydrogen Energy **2008**;33:4955-61.

[155] Sui S, Ma L, Zhai Y. *Investigation on the proton exchange membrane water electrolyzer using supported anode catalyst*. Asia-Pac. J. Chem. Eng. **2009**;4:8-11.

[156] Grigoriev SA, Millet P, Porembsky VI, Fateev VN. *Development and preliminary testing of a unitized regenerative fuel cell based on PEM technology*. Int. J. Hydrogen Energy **2011**;36:4164-8.

[157] Xu J, Miao R, Zhao T, Wu J, Wang X. *A novel catalyst layer with hydrophilic-hydrophobic meshwork and pore structure for solid polymer electrolyte water electrolysis*. Electrochem. Commun. **2011**;13:437-9.

[158] Wu X, Scott K. *$RuO_2$ supported on Sb-doped $SnO_2$ nanoparticles for polymer electrolyte membrane water electrolysers*. Int. J. Hydrogen Energy **2011**;36:5806-10.

[159] Xu J, Wang M, Liu G, Li J, Wang X. *The physical-chemical properties and electrocatalytic performance of iridium oxide in oxygen evolution*. Electrochim. Acta **2011**;56:10223-30.

[160] Su H, Bladergroen BJ, Linkov V, Pasupathi S, Ji S. *Study of catalyst sprayed membrane under irradiation method to prepare high performance membrane electrode assemblies for solid polymer electrolyte water electrolysis*. Int. J. Hydrogen Energy **2011**;36:15081-8.

[161] Wei G, Xu L, Huang C, Wang Y. *SPE water electrolysis with SPEEK/PES blend membrane*. Int. J. Hydrogen Energy **2010**;35:7778-83.

[162] Woo J-Y, Lee K-M, Jee B-C, Ryu C-H, Yoon C-H, Chung J-H, et al. *Electrocatalytic characteristics of Pt-Ru-Co and Pt-Ru-Ni based on covalently cross-linked sulfonated poly(ether ether ketone)/heteropolyacids composite membranes for water electrolysis*. Journal of Industrial and Engineering Chemistry **2010**;16:688-97.

[163] Kreuer KD. *On the development of proton conducting polymer membranes for hydrogen and methanol fuel cells*. J. Membr. Sci. **2001**;185:29-39.

[164] Goñi-Urtiaga A, Presvytes D, Scott K. *Solid acids as electrolyte materials for proton exchange membrane (PEM) electrolysis: Review*. Int. J. Hydrogen Energy **2012**;37:3358-72.

[165] Bouchet R, Miller S, Duclot M, Souquet JL. *A thermodynamic approach to proton conductivity in acid-doped polybenzimidazole*. Solid State Ionics **2001**;145:69-78.

[166] Ludueña GA, Kühne TD, Sebastiani D. *Mixed Grotthuss and Vehicle Transport Mechanism in Proton Conducting Polymers from Ab initio Molecular Dynamics Simulations*. Chem. Mater. **2011**;23:1424-9.
[167] Agmon N. *The Grotthuss mechanism*. Chem. Phys. Lett. **1995**;244:456-62.
[168] He R, Li Q, Jensen JO, Bjerrum NJ. *Doping phosphoric acid in polybenzimidazole membranes for high temperature proton exchange membrane fuel cells*. Journal of Polymer Science Part A: Polymer Chemistry **2007**;45:2989-97.
[169] Jayakody JRP, Chung SH, Durantino L, Zhang H, Xiao L, Benicewicz BC, et al. *NMR studies of mass transport in high-acid-content fuel cell membranes based on phosphoric acid and polybenzimidazole*. J. Electrochem. Soc. **2007**;154:B242-6.
[170] Ma YL, Wainright JS, Litt MH, Savinell RF. *Conductivity of PBI membranes for high-temperature polymer electrolyte fuel cells*. J. Electrochem. Soc. **2004**;151:A8-A16.
[171] Hughes CE, Haufe S, Angerstein B, Kalim R, Mähr U, Reiche A, et al. *Probing structure and dynamics in poly[2,2'-(m-phenylene)-5,5'-bibenzimidazole] fuel cells with magic-angle spinning NMR*. J. Phys. Chem. B **2004**;108:13626-31.
[172] Bouchet R, Siebert E. *Proton conduction in acid doped polybenzimidazole*. Solid State Ionics **1999**;118:287-99.
[173] Kötz R, Stucki S. *Stabilization of $RuO_2$ by $IrO_2$ for anodic oxygen evolution in acid media*. Electrochim. Acta **1986**;31:1311-6.
[174] Koda Y. *Boiling points and ideal solutions of ruthenium and osmium tetraoxides*. J. Chem. Soc., Chem. Commun. **1986**; :1347-8.
[175] Gatineau J, Yanagita K, Dussarrat C. *A new $RuO_4$ solvent solution for pure ruthenium film depositions*. Microelectron. Eng. **2006**;83:2248-52.
[176] Ma H, Liu C, Liao J, Su Y, Xue X, Xing W. *Study of ruthenium oxide catalyst for electrocatalytic performance in oxygen evolution*. Journal of Molecular Catalysis. A, Chemical **2006**;247:7-13.
[177] Baglio V, Di Blasi A, Denaro T, Antonucci V, Arico AS, Ornelas R, et al. *Synthesis, characterization and evaluation of $IrO_2$-$RuO_2$ electrocatalytic powders for oxygen evolution reaction*. Journal of New Materials for Electrochemical Systems **2008**;11:105-8.
[178] Grigor'ev SA, Khaliullin MM, Kuleshov NV, Fateev VN. *Electrolysis of Water in a System with a Solid Polymer Electrolyte at Elevated Pressure*. Russ. J. Electrochem. **2001**;37:819-22.
[179] Sawada S, Yamaki T, Maeno T, Asano M, Suzuki A, Terai T, et al. *Solid polymer electrolyte water electrolysis systems for hydrogen production based on our newly developed membranes, Part I: Analysis of voltage-current characteristics*. Prog. Nucl. Energy **2008**;50:443-8.
[180] Matsuzawa K, Igarashi C, Mitsushima S, Ota K. *Non-precious metal electrocatalyst for oxygen evolution in polymer electrolyte water electrolysis*. ECS Trans. **2010**;25:119-24.
[181] Adams R, Shriner RL. *Platinum oxide as a catalyst in the reduction of organic compounds III Preparation and properties of the oxide of platinum obtained by the fusion of ceiloroplatinic acid with sodium nitrate*. J. Am. Chem. Soc. **1923**;45:2171-9.
[182] Marshall A, Børresen B, Hagen G, Tsypkin M, Tunold R. *Preparation and characterisation of nanocrystalline $Ir_xSn_{1-x}O_2$ electrocatalytic powders*. Mater. Chem. Phys. **2005**;94:226-32.
[183] Cloutier CR, Wilkinson DP. *Electrolytic production of hydrogen from aqueous acidic methanol solutions*. Int. J. Hydrogen Energy **2010**;35:3967-84.
[184] Wilson MS, Gottesfeld S. *Thin-film catalyst layers for polymer electrolyte fuel cell electrodes*. J. Appl. Electrochem. **1992**;22:1-7.

[185] Patterson AL. *The Scherrer formula for x-ray particle size determination*. PHYSICAL REVIEW **1939**;56:978-82.
[186] Smart LE, Moore EA. *Solid state chemistry: An introduction*. 3rd ed. Boca Raton: CRC Press **2005**.
[187] Chorkendorff I, Niemantsverdriet JW. *Concepts of modern catalysis and kinetics*. Weinheim: Wiley-VCH **2003**.
[188] Thomas JM, Thomas WJ. *Principles and practice of heterogeneous catalysis*. Weinheim: Wiley **1997**.
[189] Brunauer, Emmett, Teller. *Adsorption of gases in multimolecular layers*. J. Am. Chem. Soc. **1938**;60:309-19.
[190] Goodhew PJ, Humphreys J, Beanland R. *Electron microscopy and analysis*. New York: Taylor & Francis **2001**.
[191] *Hydrogen, Fuels Cells and Infrastucture Technologies - Program Multi-Year Research, Development and Demonstration Plan - Planned program activities for 2005-2015*. Section 3.4, U.S. Department of Energy; **2007** [DOE/GO-102007-2430]
[192] Callister WD. *Materials science and engineering - an introduction*. New York: Wiley **2003**.
[193] Yaws CL, ed. *Chemical Properties Handbook*. **1999**, McGraw-Hill. 159-84.
[194] Pierson HO. *Handbook of chemical vapor depostion*. Norwich, N.Y.: Noyes Publications/William Andrew Pub. **1999**.
[195] Eriksen S, *Chemical vapour deposition of tantalum - and experiments on niobium, tungsten and platinum CVD*, in *Department of Chemistry*. **1999**, Technical University of Denmark: Kgs. Lyngby.
[196] Kodas TT, Hampden-Smith MJ. *The Chemistry of Metal CVD*: VCH, Weinheim **1994**.
[197] Kraytsberg A, Auinat M, Ein-Eli Y. *Reduced contact resistance of PEM fuel cell's bipolar plates via surface texturing*. J. Power Sources **2007**;164:697-703.
[198] Pan C, Li Q, Jensen JO, He R, Cleemann LN, Nilsson MS, et al. *Preparation and operation of gas diffusion electrodes for high-temperature proton exchange membrane fuel cells*. J. Power Sources **2007**;172:278-86.
[199] Aili D, Hansen MK, Pan C, Li Q, Christensen E, Jensen JO, et al. *Phosphoric acid doped membranes based on Nafion®, PBI and their blends - Membrane preparation, characterization and steam electrolysis testing*. Int. J. Hydrogen Energy **2011**;36:6985-93.
[200] Linkous CA. *Development of solid polymer electrolytes for water electrolysis at intermediate temperatures*. Int. J. Hydrogen Energy **1993**;18:641-6.
[201] Savinell R, Yeager E, Tryk D, Landau U, Wainright J, Weng D, et al. *A Polymer Electrolyte For Operation at Temperatures up to 200 °C*. J. Electrochem. Soc. **1994**;141:L46-8.
[202] Bauer F, Willert-Porada M. *Zirconium phosphate Nafion® composites - a microstructure-based explanation of mechanical and conductivity properties*. Solid State Ionics **2006**;177.
[203] Aili D, *Proton Conducting Polymeric Materials for Hydrogen Based Electrochemical Energy Conversion Technologies*, in *Department of Chemistry*. **2011**, Technical University of Denmark: Kgs. Lyngby.
[204] Clearfield A, Thomas JR. *The solubility of α-zirconium phosphate and hafnium phosphate in strong phosphoric acid*. Inorganic and Nuclear Chemistry Letters **1969**;5:775-9.
[205] Fujimoto CH, Hickner MA, Cornelius CJ, Loy DA. *Ionomeric poly(phenylene) prepared by Diels-Alder polymerization: Synthesis and physical properties of a novel polyelectrolyte*. Macromolecules **2005**;38:5010-6.

[206] Tang Y, Karlsson AM, Santare MH, Gilbert M, Cleghorn S, Johnson WB. *An experimental investigation of humidity and temperature effects on the mechanical properties of perfluorosulfonic acid membrane*. Materials Science & Engineering A **2006**;425:297-304.

[207] Werner S, Jörissen L, Heider U. *Conductivity and mechanical properties of recast nafion films*. Ionics **1996**;2:19-23.

[208] Liu, Kyriakides, Case, Lesko, Yanxiang L, McGrath. *Tensile behavior of Nafion and sulfonated poly(arylene ether sulfone) copolymer membranes and its morphological correlations*. Journal of Polymer Science, Part B (Polymer Physics) **2006**;44:1453-65.

[209] Kundu S, Simon LC, Fowler M, Grot S. *Mechanical properties of Nafion$^{TM}$ electrolyte membranes under hydrated conditions*. Polymer **2005**;46:11707-15.

[210] Osborn SJ, Hassan MK, Divoux GM, Rhoades DW, Mauritz KA, Moore RB. *Glass transition temperature of perfluorosulfonic acid ionomers*. Macromolecules **2007**;40:3886-90.

[211] Li Q, Li W, Zhang H, Pan M. *Immobilization of imidazole in polymer electrolyte membranes for elevated temperature anhydrous applications*. J. Appl. Polym. Sci. **2012**;123:382-7.

[212] He R, Li Q, Bach A, Jensen JO, Bjerrum NJ. *Physicochemical properties of phosphoric acid doped polybenzimidazole membranes for fuel cells*. J. Membr. Sci. **2006**;277:38-45.

[213] Li Q, Jensen JO, Pan C, Bandur V, Nilsson MS, Schoenberger F, et al. *Partially fluorinated aarylene polyethers and their ternary blends with PBI and $H_3PO_4$*. Fuel Cells **2008**;8:188-99.

[214] Thomas SC, Ren X, Gottesfeld S. *Batteries and Energy Conversion - Influence of lonomer Content in Catalyst Layers on Direct Methanol Fuel Cell Performance*. J. Electrochem. Soc. **1999**;146.

[215] Yang C, Srinivasan S, Bocarsly AB, Tulyani S, Benziger JB. *A comparison of physical properties and fuel cell performance of Nafion and zirconium phosphate/Nafion composite membranes*. J. Membr. Sci. **2004**;237:145-61.

[216] Wang S, Sun G, Wang G, Zhou Z, Zhao X, Sun H, et al. *Improvement of direct methanol fuel cell performance by modifying catalyst coated membrane structure*. Electrochem. Commun. **2005**;7:1007-12.

[217] Gebel G, Aldebert P, Pineri M. *STRUCTURE AND RELATED PROPERTIES OF SOLUTION-CAST PERFLUOROSULFONATED IONOMER FILMS*. Macromolecules **1987**;20:1425-8.

[218] Iranzo A, Muñoz M, López E, Pino J, Rosa F. *Experimental fuel cell performance analysis under different operating conditions and bipolar plate designs*. Int. J. Hydrogen Energy **2010**;35:11437-47.

[219] Nikiforov AV, Tomás García AL, Petrushina IM, Christensen E, Bjerrum NJ. *Preparation and study of $IrO_2$/SiC-Si supported anode catalyst for high temperature PEM steam electrolysers*. Int. J. Hydrogen Energy **2011**;36:5797-805.

[220] Owe L-E, Tsypkin M, Sunde S. *The effect of phosphate on iridium oxide electrochemistry*. Electrochim. Acta **2011**;58:231-7.

[221] Moffat JB, Neeleman JF. *The preparation and some properties of high-surface-area boron phosphate*. J. Catal. **1973**;31:274-7.

[222] Krishnan P, Park J-S, Kim C-S. *Preparation of proton-conducting sulfonated poly(ether ether ketone)/boron phosphate composite membranes by an in situ sol-gel process*. J. Membr. Sci. **2006**;279:220-9.

[223] Oono Y, Sounai A, Hori M. *Influence of the phosphoric acid-doping level in a polybenzimidazole membrane on the cell performance of high-temperature proton exchange membrane fuel cells*. J. Power Sources **2009**;189:943-9.

[224] Mamlouk M, Scott K. *Phosphoric acid-doped electrodes for a PBI polymer membrane fuel cell*. International Journal of Energy Research **2011**;35:507-19.
[225] Habib, Bockris. *Adsorption at the solid/solution interface. An FTIR study of phosphoric acid on platinum and gold*. J. Electrochem. Soc. **1985**;132:108-14.
[226] Nart FC, Iwasita T. *On the adsorption of $H_2PO_4^-$ and $H_3PO_4$ on platinum: an in situ FT-ir study*. Electrochim. Acta **1992**;37:385-91.
[227] Liu Z, Wainright JS, Litt MH, Savinell RF. *Study of the oxygen reduction reaction (ORR) at Pt interfaced with phosphoric acid doped polybenzimidazole at elevated temperature and low relative humidity*. Electrochim. Acta **2006**;51:3914-23.
[228] Kamat A, Herrmann M, Ternes D, Klein O, Krewer U, Scholl S. *Experimental Investigations into Phosphoric Acid Adsorption on Platinum Catalysts in a High Temperature PEM Fuel Cell*. Fuel Cells **2011**;11:511-7.

# 11 Appendix 1 – Thermodynamic calculations

All the values in table 11.1 and table 11.2 are from the online version of CRC Handbook of Chemistry and Physics 91st edition 2010-2011 [54].

**Table 11.1: Standard thermodynamic values (298.15K and 1 bar)**

| Species | Enthalpy $kJ \cdot mol^{-1}$ | Entropy $J\ mol^{-1} \cdot K^{-1}$ | $C_p$ $J\ mol^{-1} \cdot K^{-1}$ | Gibbs $kJ \cdot mol^{-1}$ |
|---|---|---|---|---|
| $H_2(g)$ | 0 | 130.7 | 28.8 | 0 |
| $O_2(g)$ | 0 | 205.2 | 29.4 | 0 |
| $H_2O(l)$ | -285.8 | 70 | 75.3 | -237.1 |
| $H_2O(g)$ | -241.8 | 188.8 | 33.6 | -228.6 |

**Table 11.2: Constants**

| Quantity | Symbol | Value* | Unit |
|---|---|---|---|
| Gas constant | R | 8.3145 | $J \cdot mol^{-1} \cdot K^{-1}$ |
| Faradays number | F | 96485.3399 | $C \cdot mol^{-1}$ |

*Values are rounded to four decimals

**Table 11.3: Calculated thermodynamic values at 130 °C and 1 bar**

| Species | Enthalpy $kJ \cdot mol^{-1}$ | Entropy $J\ mol^{-1} \cdot K^{-1}$ | Gibbs $kJ \cdot mol^{-1}$ |
|---|---|---|---|
| $H_2(g)$ | 3.02 | 139.39 | -53.17 |
| $O_2(g)$ | 3.09 | 214.07 | -83.22 |
| $H_2O(g)$ | -238.27 | 198.94 | -318.47 |

The values in table 11.3 are calculated from equation (2-4) and (2-5)

The tabulated values below (see table 11.4) give the thermodynamic and electrochemical values for the electrolysis reaction at 130 °C and 1 bar. Calculated using equation (2-1).

**Table 11.4: Electrolysis reaction data at 130 °C and 1 bar**

| | $\Delta_r H$ $kJ \cdot mol^{-1}$ | $\Delta_r S$ $J\ mol^{-1} \cdot K^{-1}$ | $\Delta_r G$ $kJ \cdot mol^{-1}$ | $E_{rev}$ V | $E_{EMF}$ V |
|---|---|---|---|---|---|
| $H_2O \rightarrow H_2 + ½O_2$ | 242.84 | 47.49 | 223.70 | 1.16 | -1.16 |

If the reversible voltage should be calculated from equation (2-2) then the activities or with good approximation partial pressures of all the species should be known, and it would be quite dependent on these. In table 11.5 the variation in the reversible potential for different partial pressures at 130 °C can be seen.

Anode: $aH_2O \rightarrow ½O_2 + 2H^+ + 2e^- + bH_2O$ (R- 11-1)

**Table 11.5: Reversible voltages at different partial pressures at 130 °C**

| $P_{H_2O}$ bar | $P_{O_2}$ bar | $P_{H_2}$ bar | $E_{rev}$ V |
|---|---|---|---|
| 0.999 | 0.001 | 1 | 1.099 |
| 0.900 | 0.100 | 1 | 1.141 |
| 0.800 | 0.200 | 1 | 1.149 |
| 0.700 | 0.300 | 1 | 1.155 |
| 0.600 | 0.400 | 1 | 1.160 |
| 0.500 | 0.500 | 1 | 1.165 |
| 0.400 | 0.600 | 1 | 1.171 |
| 0.300 | 0.700 | 1 | 1.177 |
| 0.200 | 0.800 | 1 | 1.185 |
| 0.100 | 0.900 | 1 | 1.198 |
| 0.010 | 0.990 | 1 | 1.239 |
| 0.001 | 0.999 | 1 | 1.279 |
| 1.000 | 1.000 | 1 | 1.159 |

# 12 Appendix 2 – Saturated vapour pressure of water

To calculate the saturated vapour pressure of water the Antoine equation [193] is used, see equation (12-1).

$$\log_{10}(p) = A + \frac{B}{T} + C \cdot \log(T) + D \cdot T + E \cdot T^2 \qquad (12\text{-}1)$$

In equation (12-1), p is the pressure in mmHg, A, B, C, D and E are regression coefficients and T is the temperature in K. The regression coefficients for the Antoine equation are summarised in table 12.1, they are not valid in the entire temperature range, only valid from 0 to 374 °C.

**Table 12.1: Regression coefficients for the Antoine equation, valid between 0 and 374 °C [193].**

| Constant | Value |
|---|---|
| A | 29.8605 |
| B | -3152.2 |
| C | -7.3037 |
| D | $2.42 \cdot 10^{-9}$ |
| E | $1.81 \cdot 10^{-6}$ |

To calculate between mmHg and bar are the conversion factor from the online version of CRC Handbook of Chemistry and Physics 91st edition 2010-2011 [54] used, the value can be seen in table 12.2

**Table 12.2: Conversion factor between mmHg and bar [54].**

| mmHg | Bar |
|---|---|
| 1 | $133.322 \cdot 10^{-6}$ |

# 13 Appendix 3 - Overview table of the presented MEAs

**Table 13.1: Overview of the presented MEAs.**

| MEA# | Electrolyte | | Electrode loading [mA·cm$^{-2}$] | | | | | | |
|---|---|---|---|---|---|---|---|---|---|
| | Type | Thickness [µm] | Anode $IrO_2$ | Cathode Pt | Flow pattern | Temp. [°C] | Pressure [bar] | $i_{TN}$ [mA·cm$^{-2}$] | $i_{1.7\,V}$ [mA·cm$^{-2}$] |
| PBI-MEA1 | PBI + PA | 80 | 1.28 | 0.7 | A | 130 | Ambient | ~10 | ~70 |
| PBI-MEA2 | PBI + PA | 80 | 4.13 | 0.7 | A | 130 | Ambient | ~50 | ~280 |
| PBI-MEA3 | PBI + PA | 80 | 1.14 | 0.7 | D | 130 | Ambient | ~32 | ~130 |
| PBI-MEA4 | PBI + PA | 80 | 1.01 | 0.7 | D | 130 | Ambient | ~43 | ~245 |
| PBI-MEA5 | PBI + PA | 80 | 3.08 | 0.7 | A | 130 | Ambient | ~52 | ~210 |
| PBI-MEA6 | PBI + PA | 80 | 3.71[a] | 0.7 | A | 130 | Ambient | ~125 | ~400 |
| PBI-MEA7 | PBI + PA | 80 | 9.97 | 0.7 | A | 130 | Ambient | ~215 | ~538 |
| PBI-MEA8 | PBI + PA | 180 | 2.79 | 0.7 | A | 130 | Ambient | -[b] | -[b] |
| NAF-MEA1 | Nafion® 115 + ZrP | 225 | 3.10 | 0.7 | B | 130 | Ambient | ~10 | ~28 |
| NAF-MEA2 | Nafion® 115 + PA | 165 | 3.03 | 0.7 | A | 130 | Ambient | ~25 | ~113 |
| NAF-MEA3 | Nafion® 115 + ZrP + PA | 175 | 3.35 | 0.7 | A | 130 | Ambient | ~45 | ~152 |
| NAF-MEA3 | Nafion® 115 + ZrP + PA | 175 | 3.35 | 0.7 | B | 130 | Ambient | -[c] | -[c] |
| NAF-MEA4 | Nafion® 212 + PA | 75 | 3.39 | 0.7 | B | 130 | Ambient | ~65 | ~227 |
| NAF-MEA5 | Nafion® 212 + ZrP + PA | 75 | 3.05 | 0.7 | B | 130 | Ambient | ~86 | ~310 |
| NAF-MEA6 | Nafion® 211 + ZrP + PA | 25 | 3.22 | 0.7 | B | 130 | Ambient | ~86 | -[d] |
| NAF-MEA7 | Recast Nafion® + ZrP + PA | 65 | 3.53 | 0.7 | B | 130 | Ambient | ~75 | ~300 |
| NAF-MEA8 | Nafion® 212 + PA | 62 | 2.5 | 0.7 | B | 130 | Ambient | ~8 | ~50 |
| NAF-MEA9 | Nafion® 212 + PA | 59 | 2.5 | 0.7 | B | 130 | Ambient | ~11 | ~70 |
| NAF-MEA10 | Nafion® 212 + PA | 62 | 2.3 | 0.7 | B | 130 | Ambient | ~21 | ~100 |
| NAF-MEA11 | Nafion® 212 + PA | 60 | 2.0 | 0.7 | B | 130 | Ambient | ~25 | ~100 |
| AQU-MEA1 | Aquivion™ + PA | 60 | 3.61 | 0.8 | B | 130 | Ambient | ~125 | ~388 |
| AQU-MEA2 | Aquivion™ + PA | 60 | 3.66 | 0.8 | C | 130 | Ambient | ~130 | ~431 |
| AQU-MEA3 | Aquivion™ + PA | 60 | 3.41 | 0.8 | D | 130 | Ambient | ~130 | ~431 |
| AQU-MEA4 | Aquivion™ + PA | 60 | 1.44 | 0.8 | D | 130 | Ambient | ~129 | ~560 |
| AQU-MEA5 | Aquivion™ + PA | 60 | 1.01 | 0.8 | D | 130 | Ambient | ~95 | ~470 |
| AQU-MEA6 | Aquivion™ + PA | 60 | 1.02 | 0.8 | D | 130 | Ambient | ~129 | ~580 |

**Table continues on next side**

**Table 13.1 continued**

| MEA# | Electrolyte | | Electrode loading [mA·cm$^{-2}$] | | | | | | |
|---|---|---|---|---|---|---|---|---|---|
| | Type | Thickness [μm] | Anode $IrO_2$ | Cathode Pt | Flow pattern | Temp. [°C] | Pressure [bar] | $i_{TN}$ [mA·cm$^{-2}$] | $i_{1.7\ V}$ [mA·cm$^{-2}$] |
| AQU-MEA7 | Aquivion™ + PA | 60 | 1.05 | 0.8 | D | 130 | Ambient | 86 | 474 |
| AQU-MEA8 | Aquivion™ + PA | 60 | 1.11 | 0.8 | D | 130 | Ambient | 80 | -[d] |
| AQU-MEA9 | Aquivion™ + PA | 60 | 1.06 | 0.8 | D | 130 | Ambient | 129 | -[d] |
| AQU-MEA10 | Aquivion™ + PA | 60 | 0.98 | 0.8 | D | 130 | Ambient | 129 | 602 |
| AQU-MEA11 | Aquivion™ + PA | 60 | 0.93 | 0.8 | D | 130 | Ambient | 45 | 230 |
| AQU-MEA12 | Aquivion™ + PA | 60 | 1.22 | 0.8 | D | 130 | Ambient | 50 | 260 |
| AQU-MEA13 | Aquivion™ + PA | 120 | 0.7 | 0.8 | D | 130 | Ambient | -[e] | -[e] |
| AQU-MEA14 | Aquivion™ + PA | 60 | 1.01 | 0.8 | D | 130 | Ambient | 76/65[f] | 330/270[f] |
| AQU-MEA15 | Aquivion™ + PA | 60 | 1.11 | 0.8 | D | 130 | Ambient | 70 | 315 |
| LIQ-MEA1 | Aquivion™ | 60 | 3.49 | 0.8 | B | 120 | 3 | 150 | 775 |
| LIQ-MEA2 | Aquivion™ | 60 | 3.54 | 0.8 | B | 120 | 3 | 100 | 447 |
| LIQ-MEA3 | Aquivion™ | 60 | 3.40 | 0.8 | Topped | 120 | 3 | 21 | 68 |
| LIQ-MEA4 | Aquivion™ | 60 | 3.77 | 0.8 | Topped | 120 | 3 | 12 | 32 |
| LIQ-MEA5 | Aquivion™ | 60 | 1.72 | 0.8 | ICTP[g] | 120 | 3 | 150 | 1285 |
| LIQ-MEA6 | Nafion® + 5 wt.% $BPO_4$ | 90 | 3.31 | 0.8 | B | 120 | 3 | 120 | 660 |
| LIQ-MEA7 | Nafion® 112 | 50 | 5.7 | 1.0 | ICTP[g] | 120 | 3 | 45 | 430 |

[a]Had PBI as ionomer in anode, the rest of the PBI-MEAs had Nafion® as ionomer in anode. In the rest of the MEAs the membrane and ionomer in the electrodes are of the same type.
[b]Durability measurement, lasted only for few hours before membrane failure.
[c]Durability measurement, ran for 72 hours before being shut off. Degradation 0.17 mA·h$^{-1}$at a constant voltage of 1.7 V
[d]MEA broke before reaching 1.7 V
[e]Durability measurement, ran for 760 hours before being shut off. Degradation between 0.023 and 0.04 mV·h$^{-1}$ the last 660 hours at a constant current density of 400 mA·cm$^{-2}$.
[f]Current densities for 10/11.6 cm$^2$ respectively.
[g]Serpentine pattern from ICTP, flow area 4 cm$^2$.

# 14 Publications

I. **Phosphoric acid doped membranes based on Nafion®, PBI and their blends – Membrane preparation, characterization and steam electrolysis test**

D. Aili, M.K. Hansen, C. Pan, Q. Li, E. Christensen, J.O. Jensen and N.J. Bjerrum
*Int. J. Hydrogen Energy* **2011**, 36, 6985-6993


II. **PEM Steam electrolysis at 130 °C using a phosphoric acid doped short side chain PFSA membrane**

M.K. Hansen, D. Aili, E. Christensen, C. Pan, S. Eriksen, J.O. Jensen, J. von Barner, Q. Li and N.J. Bjerrum
Accepted in *Int. J. Hydrogen Energy* the 25th of April 2012.

I

INTERNATIONAL JOURNAL OF HYDROGEN ENERGY 36 (2011) 6985–6993

Available at www.sciencedirect.com

ScienceDirect

journal homepage: www.elsevier.com/locate/he

# Phosphoric acid doped membranes based on Nafion®, PBI and their blends – Membrane preparation, characterization and steam electrolysis testing

*David Aili, Martin Kalmar Hansen, Chao Pan, Qingfeng Li*, Erik Christensen, Jens Oluf Jensen, Niels J. Bjerrum*

*Department of Chemistry, Kemitorvet 207, Technical University of Denmark, DK-2800 Lyngby, Denmark*

ARTICLE INFO

*Article history:*
Received 9 January 2011
Received in revised form
7 March 2011
Accepted 10 March 2011
Available online 20 April 2011

*Keywords:*
Proton exchange membranes
Nafion®
Polybenzimidazole
Phosphoric acid
Steam electrolysis

ABSTRACT

Proton exchange membrane steam electrolysis at temperatures above 100 °C has several advantages from thermodynamic, kinetic and engineering points of view. A key material for this technology is the high temperature proton exchange membrane. In this work a novel procedure for preparation of Nafion® and polybenzimidazole blend membranes was developed. Homogeneous binary membranes covering the whole composition range were prepared and characterized with respect to chemical and physiochemical properties such as water uptake, phosphoric acid doping, oxidative stability, mechanical strength and proton conductivity. An MEA based on phosphoric acid doped Nafion® was operated at 130 °C at ambient pressure with a current density of 300 mA $cm^{-2}$ at 1.75 V, with no membrane degradation observed during a test of 90 h. The PBI based MEAs showed better polarization curves (500 mA $cm^{-2}$ at 1.75 V) but poor durability.


## 1. Introduction

Membranes of perfluorosulfonic acid (PFSA) have emerged as the state-of-the-art proton exchange membrane (PEM) material for fuel cells [1] as well as water electrolyzers [2] operating up to about 80 °C. Nafion® was developed in 1960s and is the most well known of this class of materials, consisting of a perfluorinated polymer backbone and branches with sulfonic acid terminal groups.

Nafion® has been extensively characterized with respect to its structure, properties and mechanism of proton conduction [3,4]. The proton conductivity of this material is strongly dependent on the presence of water and can reach above 0.1 S $cm^{-1}$ under fully hydrous conditions. However, at ambient pressure the membrane dehydrates at temperatures above 80 °C, resulting in dramatic proton conductivity decay. In order to meet several technical challenges for both water electrolysers [5] and fuel cells [6], an operating temperature above 100 °C has been recognized as an attractive objective. This has resulted in an increasing demand for new PEM materials.

For PEM water electrolyzers, an elevated operating temperature offers several advantages from thermodynamic, kinetic and engineering points of view. At elevated temperatures, the electrode kinetics will be enhanced and therefore the overpotentials at both electrodes will be reduced Above 100 °C water is in the gaseous form and the electrolysis process is thermodynamically less energy demanding [7]. The reversible voltage of the water electrolysis cell is 1.23 V at room temperature (liquid) but only 1.14 V at 200 °C (steam). Of

* *Corresponding author*. Tel.: +45 45 25 23 18; fax: +45 45 88 31 36.
E-mail address: lqf@kemi.dtu.dk (Q. Li).
0360-3199/$ – see front matter 
doi:10.1016/j.ijhydene.2011.03.058

course this part of the energy saving should be compensated by heat supply, which is expected to be covered by the waste heat from the cell Ohmic loss by means of e.g. evaporation and preheating of the feed water. From an engineering point of view this may further simplify the intensive cooling of the electrolyzer stacks especially when operating at higher current densities. Pressurized operation of PFSA based PEM water electrolysis systems, on the other hand, has been identified as a potential solution to improve the membrane hydration characteristics and thus the proton conductivity of the electrolyte [8,9], however at the expense of the enhance complexity of the balance of plant components [10]. The higher operational temperatures will additionally benefit the system pressurization and the subsequent gas compression.

An effective approach to improve the conductivity and the hydration characteristics of PFSA membranes at temperatures above 100 °C is to prepare composite membranes with inorganic fillers such as hygroscopic oxides (e.g. $SiO_2$ and $TiO_2$) [9,11–13], zirconium phosphates ($Zr(HPO_4)_2 \cdot nH_2O$, ZrP) [13,14], zirconium sulphophenylphosphates [15] and heteropolyacids [13]. It has also been demonstrated that the high ionic conductivity of Nafion® membranes can be maintained under dehydrating conditions if water is replaced by a less volatile proton solvent, such as ionic liquids [16] or phosphoric acid (PA) [17]. It has been shown that a PA doped Nafion® membrane exhibit proton conductivity of around $10^{-2}$ S $cm^{-1}$ at 120–175 °C [17] as well as improved kinetics for the oxygen reduction reaction (ORR) in the fuel cell mode [18]. However, no successful PEM fuel cell or water electrolysis tests based on PA doped PFSA membranes have to our knowledge yet been demonstrated.

During the last 15 years, on the other hand, PA doped poly [*m*-phenylene-bis(5,5′-benzimidazole)] (PBI) has evolved as a promising PEM material for applications in fuel cells operating at temperatures of up to 200 °C [19,20]. PBI is a basic polymer with good chemical as well as thermal stability due to its rigid aromatic backbone. In PBI/PA systems the proton conductivity is strongly dependent on the acid doping level [21,22], which is defined as the number of PA molecules per repeating unit of the polymer.

Several approaches have been investigated aiming at improving the properties of PBI/PA membranes, including synthesis of PBI structure analogues [23], preparation of PBI composites [24] or covalently cross-linked structures [25,26]. Another approach is to prepare ionically cross-linked membranes from mixtures of PBI and acidic polymers like sulfonated poly(etheretherketone) [27], sulfonated polysulfone [28,29] or sulfonated partially fluorinated arylene polyethers [30,31]. Such blend membranes exhibits improved mechanical strength and chemical stability, allowing for higher acid doping levels and therefore high conductivity and better fuel cell performance. Coating of Nafion® membranes with PBI has been demonstrated as a successful approach in order to decrease the methanol permeability in Nafion® [32,33]. Wycisk et al. used the partially $Na^+$ cation exchanged Nafion® ionomer to prepare Nafion®/PBI blend membranes with PBI contents of up to 8 wt.% [34]. Furthermore, Zhai et al. obtained a transparent and strong film when the neutral $Na^+$ ionomer of Nafion® was employed for casting a Nafion®/PBI blend membrane with 80 wt.% Nafion® and 20 wt.% PBI [35]. The membrane was subsequently doped with PA and evaluated in fuel cell tests at 150 °C, showing improved durability compared with PA doped PBI membranes. However, the reported procedures for Nafion®/PBI blend membrane preparation are rather limited in terms of composition range – most likely due to miscibility problems between the two polymers.

In the present paper the miscibility of Nafion® and PBI was first investigated by using different salt forms of the Nafion® ionomer. Membranes covering the whole composition range were prepared based on the $NH_4^+$ cation exchanged Nafion® ionomer and characterized with respect to chemical and physiochemical properties including water uptake, PA doping, proton conductivity and thermal, mechanical and chemical stability. Based on the membranes exhibiting sufficient proton conductivity, membrane electrode assemblies (MEAs) were prepared and single cell steam electrolysis tests were conducted at 130 °C at ambient pressure.

## 2. Experimental

### 2.1. Membrane preparation

The Nafion® ionomers of $Li^+$, $Na^+$, $K^+$, $NH_4^+$, $N(CH_3)_4^+$, $Rb^+$ and $Cs^+$ were prepared by neutralization of the as received Nafion® dispersion (DuPont) with aqueous solutions of the corresponding hydroxides. After solvent evaporation at 90 °C *in vacuo*, the solid residues were collected and dissolved in dimethylacetamide (DMAc, Merck) to give a 5 wt.% solution. PBI with a number average molecular weight of 66 kDa was supplied by Danish Power Systems ApS and dissolved in DMAc to obtain a 5 wt.% solution after filtration.

The cation exchanged Nafion® ionomer solution was mixed with the PBI/DMAc solution to give polymer blends of Nafion®/PBI with weight ratios of 97/3, 94/6, 88/12, 82/18, 70/30, 40/60, 5/95. The polymer blend solutions were sonicated for 1 h, followed by casting on pre-heated Petri-dishes (95 $cm^2$) and drying in a pre-heated furnace at 120 °C. Pure Nafion® and PBI membranes were prepared according to the same procedure. The membranes were subsequently boiled in 0.1 M $H_2SO_4$ for 1 h in order to restore the $H^+$ form of Nafion® and finally boiled in demineralized water for 4 h. The obtained blend membranes are referred to as Mxxx according to their Nafion® content in wt.%, i.e. M088 for a blend membrane containing 88 wt.% Nafion® and 12 wt.% PBI. The pure Nafion® and PBI membranes are referred to as M100 and M000, respectively.

PA doping was achieved by soaking the membranes in 85% PA at temperatures ranging from 50 to 150 °C for at least 16 h in an open flask covered with a glass plate. The membranes were dried until a constant weight was reached at 100 °C *in vacuo* before and after acid doping. The amount of absorbed PA was calculated based on the weight gains.

### 2.2. Membrane characterization

Fourier Transform InfraRed (FTIR) spectra were recorded on a Perkin–Elmer 1710 Infrared Fourier Transform spectrometer under ambient atmosphere on 5–10 μm thick membrane

samples. The spectra were integrated using Spectrum 2.0 software.

Thermogravimetric analysis (TGA) was performed on a Netzsch STA 409 PC equipped with a Netzsch QMS 403 C mass spectrometer. Synthetic air was used as purge gas and the samples were heated from room temperature to 1000 °C at a rate of 10 °C $min^{-1}$.

For evaluation of the relative chemical stability, membrane samples (approximately 1 g) were immersed in 100 mL 3% $H_2O_2$ (Merck) aqueous solutions containing 4 ppm Fe(II) (added as $(NH_4)_2Fe(SO_4)_2 \cdot 6H_2O$) at 68 °C. After a certain period of time (maximum 20 h), the membrane samples were collected, rinsed with demineralized water and dried at 110 °C for at least 5 h. The dry weight was measured and the membrane samples were immersed in freshly prepared solution for continuation of the experiment. The reported results are the average numbers from two parallel measurements.

Stress-strain curves were recorded at 130 °C under ambient humidity, i.e. without humidity control at a rate of 10.00 mm $min^{-1}$. The equipment used was a modified universal materials testing machine (Testometric Micro 350). The membrane sample, together with grips, was contained in a metallic chamber equipped with heating elements.

Through-plane conductivity was measured by sandwiching the membrane between two gas diffusion electrodes, consisting of a layer of Pt/C catalyst and a porous carbon substrate, as described elsewhere [24]. The relative humidity was controlled by pumping water into a steam generator by means of an infusion pump and converged with an airflow into the conductivity cell. The symmetric square wave current was supplied with a frequency ranging from 6 to 7 kHz.

### 2.3. Electrolysis tests

The anode catalyst ($IrO_2$) was prepared by the Adam fusions method, as described by Marshall et al. [36] but scaled up to 10 times the amount of the precursor salt ($H_2IrCl_6 \cdot 4H_2O$). The calcination time for the salt-oxide mixture was extended to 5 h at 500 °C. The cathode catalyst (Pt/C) was prepared by chemical reduction of $H_2PtCl_6$ by formic acid in the presence of Vulcan XC-72R powder (Cabot) [18]. The final composition of the catalyst was 40 wt.% Pt on carbon.

The anodes were prepared for each MEA by spraying a catalyst ink directly to the gas diffusion layer (GDL). The GDL was made of a tantalum coated (Tantaline®) stainless steel felt (Swiit Metallic Fiber Co. Ltd). The catalyst was sprayed onto the substrate manually at 130 °C from an ink consisting of $IrO_2$, Nafion® dispersion (DuPont) and ethanol. The $IrO_2$ loading was around 4 mg $cm^{-2}$. For the cathode, a 600 $cm^2$ sheet was prepared by spraying the catalyst ink (Pt/C, PBI, PA and formic acid) onto a non-woven carbon cloth GDL (Freudenberg). The catalyst loading was 0.7 mg Pt $cm^{-2}$.

The tests were performed in a round single cell with an active electrode area of 10 $cm^2$. The flow pattern was an asymmetric spiral with inlet and outlet in the outer perimeter. The flow plates were made of tantalum coated stainless steel (Tantaline®) and fixed to aluminum end plates containing heating elements.

The electrolysis tests were performed at a typical cell temperature of 130 °C at ambient pressure. The steam was fed through an evaporator at 180 °C. The cell was first heated to the operating temperature before steam was supplied to the cell in order to avoid condensation of water in the cell. Current step potentiometry was performed and the steady-state potential was recorded 10 min after each current was set.

## 3. Results and discussion

### 3.1. Membrane preparation

#### 3.1.1. Nafion®/PBI binary membranes

When Nafion® in its protonated form (Nafion®–H) was mixed with a PBI/DMAc solution, a turbid suspension was formed as a result of the instant acid-base reaction between Nafion® ($pK_a$ −6 [37]) and PBI ($pK_{aH}$ 5.5 [22]). A set of experiments was designed where the Nafion® counter-cation was systematically varied during membrane casting, since it is well known that polymer miscibility can be strongly dependent on the present cations [28]. Membrane composition M088 was used for the ionomer screening. The resulting membranes were subsequently evaluated according to their visual appearances as listed in Table 1.

Complete phase separation occurred during membrane casting when any of the $K^+$, $N(CH_3)_4^+$, $Rb^+$ or $Cs^+$ Nafion® ionomers were used. The resulting membranes had agglomerates of PBI dispersed in a continuous opaque Nafion® phase. The $Na^+$ and $Li^+$ ionomers gave transparent blend membranes. However, texture and irregularities were observed in the membranes indicating miscibility problems.

As the ion size increases from $H^+$, $Li^+$ and $Na^+$ to $K^+$, $Rb^+$ or $Cs^+$, the Lewis acidity and therefore the charge coordination ability of the cations decreases. The $H^+$ form of Nafion® is involved in a strong acid-base interaction with PBI forming insoluble polymeric salt from which a membrane cannot be cast. $K^+$, $Rb^+$ or $Cs^+$ Nafion® ionomers are non-acidic and forms stable solutions when mixed with PBI. However, phase separation occurred during membrane casting. Compared with $K^+$, $Rb^+$ and $Cs^+$, $Li^+$ and $Na^+$ are weakly acidic allowing for limited charge coordination.

In this context, $NH_4^+$ is special. It has an ionic radius similar to that of $K^+$ but is significantly more acidic ($pK_{aH}$ 9.2). In addition, $NH_4^+$ has the inherent potential to form hydrogen

**Table 1 – Visual appearances of M088 (88 wt% Nafion® and 12 wt% PBI) prepared from different cation exchanged Nafion® ionomers.**

| Nafion® ionomer | $H^+$ | $Li^+$ | $Na^+$ | $K^+$ | $NH_4^+$ | $N(CH_3)_4^+$ | $Rb^+$ | $Cs^+$ |
|---|---|---|---|---|---|---|---|---|
| Membrane visual appearance | Poor | Reasonable | Reasonable | Poor | Homogeneous | Poor | Poor | Poor |

bonds with imine groups in the benzimidazole rings of PBI and O atoms in the sulfonic acid groups of Nafion®.

The weak acidity and the hydrogen bond formation capability of $NH_4^+$ facilitate the coordination between Nafion® and PBI. The interaction is not strong enough to form precipitation, which means that the polymer blends are soluble and stable in DMAc. This discussion seems supported by the observation that complete phase separation occurred during casting when the Nafion® ionomer with a completely non-acidic and aprotic cation ($N(CH_3)_4^+$) was employed.

Based on these results, blend membranes covering the whole composition range could easily be cast from the Nafion®–$NH_4$ ionomers. After casting, the membranes were boiled in dilute $H_2SO_4$ and treated with boiling water in order to wash out $NH_4^+$ and to restore the protonated form of Nafion® to give an ionically cross-linked blend membrane. A schematic illustration of the ionic cross-linking of the polymer blend is given in Figure 1.

The degree of ionic cross-linking was dependent on membrane composition. In M088 the amount of acidic groups in Nafion® equals the amount of basic groups in PBI, which according to Eq. (1) results in complete neutralization. 1100 corresponds to the equivalent weigh of Nafion® and 308 to the molecular weight per PBI repeating unit.

Acidic groups per PBI repeating unit

$$= \left(\text{Wt. fraction Nafion}^{®}/1100\right) \Big/ \left(\text{Wt. fraction PBI}/308\right) \quad (1)$$

It should be noted that each PBI repeating unit has 2 basic sites. Hence, M094, M097 and M100 membranes are acidic while M082, M060, M030, M005 and M000 have an excess of basic groups. The blend membrane casting procedure based on Nafion®–$NH_4$ could without modifications be scaled up to prepare 800 $cm^2$ homogeneous membranes throughout the whole composition range.

### 3.1.2. *PA doping*

PA doping was performed at temperatures ranging from 50 to 150 °C. The PA doping results are summarized in Fig. 2. The membranes with an excess of basic groups were partly soluble in phosphoric acid at temperatures higher than 50 °C. Those PBI-rich membranes displayed lower doping level at 80 °C than at 50 °C, apparently due to the loss of the polymer. The PA uptake for membrane M000 (pure PBI) doped at 50 °C

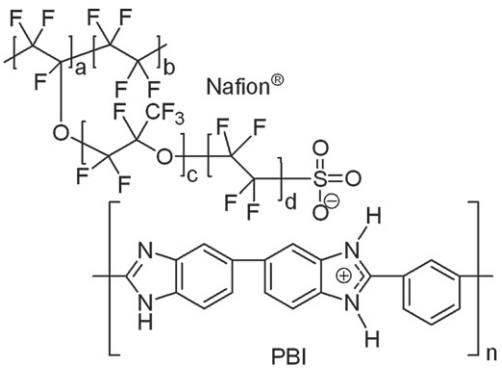


**Fig. 1 – –Illustration of ionically cross-linked recast Nafion®/PBI complex.**

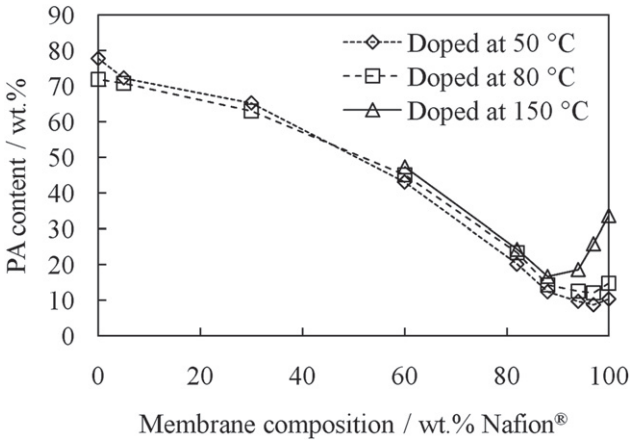


**Fig. 2 – The PA uptake for Nafion®/PBI blend membranes doped in 85 % PA at different temperatures.**

corresponds to around 11 PA molecules per PBI repeating unit, whereas the PA uptake for membrane M100 (pure Nafion®) doped at 150 °C corresponds to around 5 PA molecules per sulfonic acid group. These results corresponds well with previously reported results for pristine PA doped PBI and Nafion® membranes treated under similar conditions [17,38]. A minimum in PA uptake was observed for M088, which could be explained by the complete ionic cross-linking reaction between the two polymers. The very coherent polymer matrix exhibits very high resistance to swelling. Since Nafion® is a stronger acid than PA, the ionic interaction between Nafion® and PBI will not be affected by PA and the Nafion®/PBI complex will remain intact.

### 3.2. *FTIR spectra*

FTIR spectra were recorded for membranes covering the whole composition range (Fig. 3), and the band assignments for the two polymers are summarized in Table 2.

A broad absorption band (1100–1370 $cm^{-1}$) was observed for the M100 and M094 membranes, which was assigned to C–F and sulfonic acid end group stretching. Two distinct absorption peaks were developed at 1230 $cm^{-1}$ and 1160 $cm^{-1}$ for the neutral membrane (M088) and for the blend

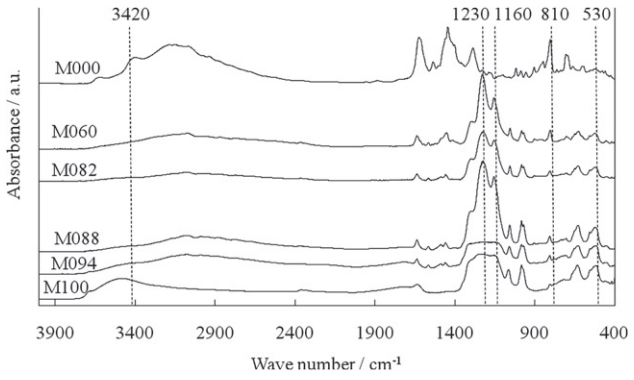


**Fig. 3 – FTIR spectra for Nafion®/PBI blend membranes. The weight percentages of Nafion® in the blend membranes are indicated in the figure.**

**Table 2 – FTIR spectra and absorption band assignments for Nafion®, PBI and their blends.**

| Wave number ($cm^{-1}$) | Assignment | | |
|---|---|---|---|
| | Nafion® [40,41] | PBI [28,41] | Nafion®/PBI blends [41] |
| 530 | $CF_2$–O–$CF_2$ | | |
| 640 | $CF_2$–O–, –$CF_2$– | | |
| 710 | | Benzene ring C–H bending | |
| 810 | | Benzene ring C–H bending | |
| 980 (s) | C–F stretching (–CF($CF_3$)) | | |
| | C–O–C stretch | | |
| 1070 (m) | S–O stretch | | |
| 1100–1370(s, broad) | $CF_2$ and $CF_3$ stretch, S–O stretch | | |
| 1160 (s, broad) | | | Ionic sulfonate |
| 1230 (vs, broad) | | | Ionic sulfonate |
| 1300 (s) | | N–H | |
| 1450 (vs) | | Aromatic C–C stretch | |
| 1630 (vs) | | C=C/C=N imine stretch | |
| 3160 (broad) | | Hydrogen bonded N–H | |
| 3420 (broad) | | Non-hydrogen bonded N–H | |
| 3500 (broad) | O–H stretch | | |

membranes with an excess of basic groups (M082 and M060). The appearance of these bands has previously been reported to be very sensitive to the local environment of the sulfonate group [28,39]. The changed appearance of the absorbance bands to a more distinct shape was likely due to formation of ionic sulfonate groups as a consequence of the acid-base reaction between Nafion® and PBI.

The high frequency FTIR showed an absorption band at 3420 $cm^{-1}$ for M000 which was assigned to non-hydrogen bonded N–H stretching. It has previously been reported that this band experiences a slight red shift to lower frequencies when PBI is blended with sulfonated polysulfone, indicating a more pronounced hydrogen bonding present [28]. For the Nafion®/PBI blend membranes (M094-M060) the intensity of the 3420 $cm^{-1}$ absorption band was very low while the 3160 $cm^{-1}$ absorption band was still present. This indicates, just like expected, that the fraction of free non-hydrogen bonded N–H protons is very low in the Nafion®/PBI membranes since they are participating in the ionic cross-linking between the two polymers.

Two characteristic absorption peaks in the FTIR fingerprint region (810 $cm^{-1}$ for PBI and 530 $cm^{-1}$ for Nafion®) were chosen and integrated in order to obtain the area under the peaks. The relative areas are plotted as a function of the membrane composition in Fig. 4. A linear correlation between the relative peak intensity and blend membrane composition was observed, which confirmed the blend membrane composition homogeneity after casting and washing.

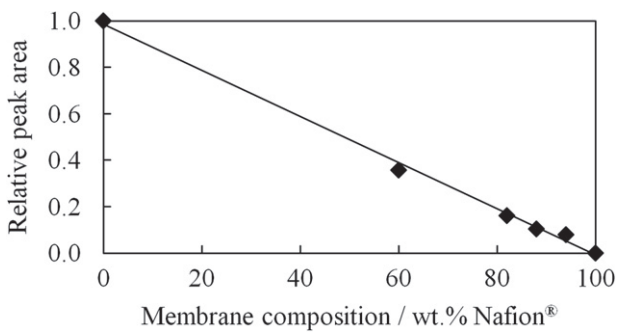


**Fig. 4 – Relative peak areas for the absorption bands at 810 $cm^{-1}$ and 530 $cm^{-1}$ in Figure 3.**

### 3.3. TGA

Onset temperatures of decomposition and water uptake data for non-doped membranes were obtained from TGA measurements. The water uptake was calculated from the total weight loss at 250 °C on the dry polymer basis. Water uptake data and onset temperature of the major decomposition are plotted as functions of membrane composition in Fig. 5. Mass-spectrometry confirmed that the major weight loss at temperatures of up to 250 °C was due to evaporation of water. The hydrophilicity of PBI is due to intermolecular hydrogen bonding between water and N and N–H groups in PBI [38]. In this work PBI and recast Nafion® showed water uptakes of 22% and 33%, respectively, which was in agreement with previously reported results for solution cast PBI and Nafion® 117 [42]. The water uptake decreased from 33% for M100 to around 18% for M097. It reached a minimum at the neutral composition (M088) which could possibly be explained by the lack of free hydrogen bonding sites and reduced swelling capability. Going toward

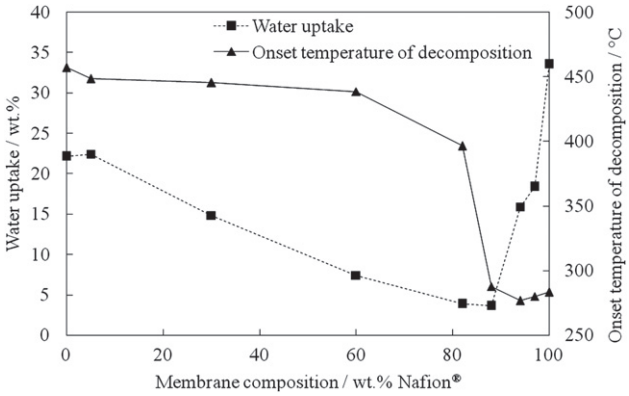


**Fig. 5 – Water uptake and onset temperature of major decomposition.**

higher PBI contents (membranes M082-M000) increased the amount of hydrophilic N or N–H sites available for hydrogen bond interaction with water, resulting in increased water uptake. The water uptake showed a trend that was similar to the PA uptake during membrane doping.

The onset temperature of the major decomposition was around 280 °C for the membranes with an excess of acid groups (M100-M094). At the neutral composition (M088) the onset temperature was found to be slightly higher (288 °C). For blend membranes with an excess of basic groups (M082, M060, M030, M005 and M000), the onset temperature of the major decomposition increased to above 400 °C.

### 3.4. Mechanical strength

Mechanical data at 130 °C and ambient humidity for pristine as well as PA doped membranes is summarized in Table 3. For the non-doped membranes the resistance to deformation was improved as the PBI content in the membranes increased, indicated by a Young's modulus increase from 2.9 MPa for M100 (pure Nafion®) to about 2,700 MPa for M000 (pure PBI). The engineering tensile stress at break data followed the same trend and increased gradually from about 0 for M100 to about 126 MPa for M000. This corresponds well to previously reported mechanical data for PBI membranes [43]. The measuring temperature was above the glass-transition temperature of Nafion® which explains the very poor mechanical properties for M100. The elongation at break was more than 800% for M100 and dropped to 9% for M082 and then increased to about 40% for M000. This further illustrates how the acid-base interactions between the two polymers make the polymer matrix very coherent.

Stress-strain curves were also recorded for the PA doped membranes. Membranes M100, M094, M088 and M082 were doped in 85% PA at 150 °C whereas membrane M060 and M000 were doped at 50 °C. It is well known that PBI membranes suffer from poor mechanical stability at high acid doping levels due to the plasticizing effect of PA [43]. This was also confirmed in this investigation and illustrated by a dramatic decrease in Young's modulus as well as engineering tensile stress at break and an increase in elongation at break. On the other hand, the mechanical properties for the pure recast Nafion® membrane (M100) were improved after acid doping. This could eventually be connected to a shift in the glass-transition temperature after PA doping. After acid doping, a minimum in elongation at break and a maximum in Young's modulus and stress at break were observed close to the neutral composition (M088). This could primarily be explained by the lower PA doping level for these membranes. On the other hand, the lower PA doping level for these membranes originates from the strong acid-base interaction between the two polymers.

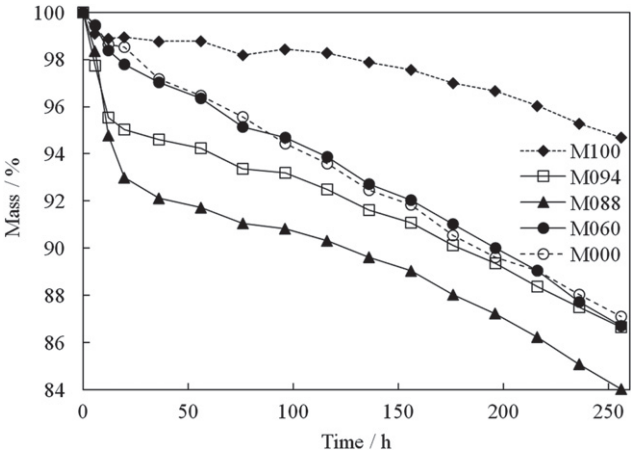


**Fig. 6 – Chemical degradation expressed as the membrane remaining mass after certain durations.**

### 3.5. Fenton test

The relative chemical stability of the membranes was evaluated in an accelerated degradation test (Fig. 6). The polymer samples were immersed in aqueous solutions of hydrogen peroxide (3 wt.%) and 4 ppm Fe(II) to catalyze the decomposition of hydrogen peroxide into hydroxyl radicals.

The chemical degradation mechanism of Nafion® has been subject for extensive investigation. Radical attack on the sulfonic acid end groups have been suggested as a starting point, followed by an unzipping mechanism according to Equations (2) and (3) [44].

$$-(CF_2)SO_3^- + R^\cdot \rightarrow -(CF_2)SO_3^\cdot + R^\cdot \quad (2)$$

$$-(CF_2)SO_3^\cdot \rightarrow -(CF_2)^\cdot + SO_3 \quad (3)$$

**Table 3 – Summary of Young's modulus, elongation at break and engineering tensile stress at break for Nafion®/PBI blend membranes at 130 °C and ambient relative humidity. The PA contents for the doped membranes are indicated in parentheses.**

| Membrane | Young's modulus (MPa) | | Elongation at break (%) | | Engineering tensile stress at break (MPa) | |
|---|---|---|---|---|---|---|
| | Pristine | PA doped | Pristine | PA doped | Pristine | PA doped |
| M100 (34%) | 2.9 ± 0.5 | 5.5 ± 0.8 | >800 | 732 ± 49 | ≈0 | 2.3 ± 0.2 |
| M094 (19%) | 64.5 ± 8.7 | 59.0 ± 3.4 | 70.8 ± 9.9 | 192 ± 29.3 | 5.1 ± 0.9 | 3.6 ± 0.4 |
| M088 (17%) | 313 ± 12.4 | 200 ± 13.7 | 14.1 ± 2.1 | 19.8 ± 5.0 | 16.9 ± 0.3 | 9.1 ± 0.7 |
| M082 (24%) | 722 ± 25.6 | 272 ± 11.7 | 9.3 ± 1.7 | 64.5 ± 11.0 | 30.9 ± 2.7 | 13.2 ± 0.5 |
| M060 (43%) | 1596 ± 145 | 127 ± 15.8 | 16.4 ± 6.5 | 109 ± 8.8 | 68.7 ± 3.4 | 8.4 ± 0.6 |
| M000 (78%) | 2708 ± 510 | 5.8 ± 1.7 | 39.8 ± 8.6 | 113 ± 17.8 | 126 ± 16.9 | 1.8 ± 0.2 |

$SO_3$ will in turn form an adduct ($^+OH_2{\bullet}SO_3^-$) with water followed by deprotonation to form sulfuric acid. $SO_3$ has also been reported to form zwitterionic adducts with ammonia ($^+NH_3{\bullet}SO_3^-$) with low energy barrier of formation [45]. The electron donating sites in PBI may form adducts with $SO_3$ in the same manner as ammonia and hence promote Nafion® oxidation by shifting the reaction towards the $SO_3$ formation. In this way PBI could act as a catalyst for the initiation of Nafion® oxidation. This could also explain why the highest initial rate of oxidation in the Fenton test was observed for the membrane with equimolar amounts of acidic and basic groups (M088).

On the other hand Kerres et al. reported improved chemical resistance for ionically cross-linked blend membranes of PBI and sulfonated partially fluorinated arylene polyethers [30]. These contradicting results could possibly be explained by a major distinction in the degradation mechanism between Nafion® and the sulfonated partially fluorinated arylene polyethers.

### 3.6. Through-plane conductivity

The through-plane conductivity data for the PA doped membranes is shown in Fig. 7. The measurements were made at 130 °C with a relative humidity in the 16–18% range. The blend membranes with Nafion® contents of 88% (M088), 94% (M094) and 100% (M100) were doped in 85% PA at 150 °C for about 16 h, while the blend membranes with Nafion® contents of 0% (M000) and 60% (M060) were doped in 85% PA at 50 °C. The PA contents of these membranes are indicated in the figure, also as shown in Fig. 2. It should be remembered that it is not straightforward to compare these results because of the large variation of the PA content. For M000 with an acid content of 78 wt.%, corresponding to an acid doping level of around 11, the conductivity was about 0.09 S $cm^{-1}$. For pure Nafion® membranes with an acid content of 34 wt.%, the conductivity was found to be 0.03–0.04 S $cm^{-1}$. Both are in good agreement with the literature data [17,23]. For the blend membranes, the conductivity was considerably lower. This is most likely due to the low PA content, which is apparently a major contributor to the proton conductivity in the membranes. More efforts are being made to improve the acid doping of these membranes.

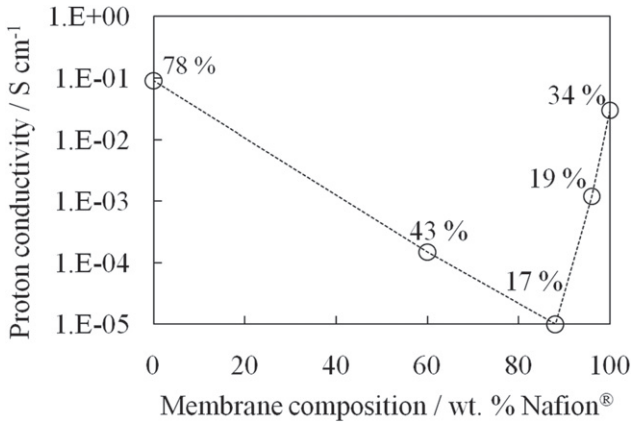


**Fig. 7 – Proton conductivity of PA doped membranes at 130°C and relative humidity of 16–18%. The PA contents of the membranes are indicated in the figure.**

### 3.7. Electrolysis test

It is well known that a membrane proton conductivity of at least $10^{-2}$ S $cm^{-1}$ is required for high temperature PEM fuel cells in order to get a reasonable performance [20]. Consequently, this should also be valid when the cell is operated in the electrolysis mode. Based on the results from the through-plane conductivity measurements it was clear that only the pure PA doped Nafion® (M100) and PBI (M000) membranes could fulfill the conductivity requirements for the electrolyte material. Hence, the tested membranes were PBI (M000) and Nafion® (M100 and 212) doped in 85% PA at 50 °C and 150 °C, respectively. The single cells were assembled directly from anode, cathode and membrane without previous hot pressing. Fig. 8 shows a set of typical polarization curves for three cells. It can be seen that at low current densities the voltages for the three different kinds of cells were more or less identical, indicating that the major difference in the cell performance was not due to a difference in the catalytic activity of the electrodes but rather a difference in the conductivity of the membranes.

The performances of the two different Nafion® cells were more or less identical. For the MEA based on PA doped M100 the current density reached 300 mA $cm^{-2}$ at 1.75 V. The current density was significantly higher for the PBI/PA (M000) MEA at 1.75 V (500 mA $cm^{-2}$). This can be compared with about 450 mA $cm^{-2}$ at 1.75 V for a Nafion®-$SiO_2$ based cell, obtained at 120 °C under ambient pressure by Antonucci et al. [9]. However, poor durability was observed for the MEA based on PA doped PBI. Most of the tested PBI/PA based MEAs lasted only for a couple of hours. The durability problems were apparently connected to severe membrane failure since a decrease in the cell voltage under a constant current, accompanied by a reduction of the gas evolution (both hydrogen and oxygen) was observed. On the other hand, fuel cell durability tests with acid doped PBI membranes have been demonstrated for more than 20,000 h with a degradation rate of 5–10 μV $h^{-1}$ [20,46]. The mechanism of PBI/PA membrane degradation under the electrolysis conditions is not understood and further efforts are being made in studies of it.

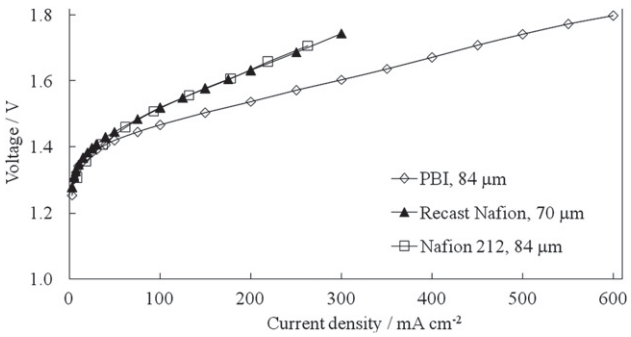


**Fig. 8 – Polarization curves for steam electrolysis cells with different membranes. The type of membranes and the corresponding membrane thickness are indicated in the figure.**

Nafion®/PA membranes exhibited better durability compared with PBI/PA membranes. During a continuous test of 90 h, the current density under a constant cell voltage of 1.7 V was varied with temperature and steam pumping, however, no evident membrane degradation was observed from the polarization as well as gas production at both electrodes.

Due to the insufficient proton conductivity of the blend membranes, polarization curves could not be recorded for the MEAs based on these membranes. Work is in progress to optimize the acid doping procedure in order to improve proton conductivity and the cell performance for steam electrolysis .

## 4. Conclusions

A novel procedure for solution casting of homogeneous Nafion®/PBI blend membranes was developed based on the Nafion®–$NH_4$ salt form. The moderate acidity of $NH_4^+$ in combination with its inherent ability to form hydrogen bonds prevented Nafion®/PBI phase separation during membrane casting. The homogeneity of the blend membranes through the whole composition range was confirmed by FTIR. FTIR further indicated a decreased fraction of non-hydrogen bonded N–H groups in the Nafion®/PBI blend membranes. The water uptake and the onset temperature of polymer decomposition of the blend membranes showed a strong dependence on the composition of the binary blend membranes, with a minimum at around 88 wt.% Nafion® and 12 wt.% PBI, where the complete neutralization occurs between the acidic Nafion® and basic PBI. Mechanical strength at 130 °C, i.e. the Young's modulus and tensile stress at break, of the non-doped blend membranes showed a gradual increase as the PBI content increased. The composition corresponding to the neutral blend membrane showed the highest weight loss as well as the highest initial rate of weight loss in the Fenton test. This indicated a chemical incompatibility between the two polymers in the oxidizing environment. The PA uptake during doping was strongly dependent on the membrane composition, exhibiting a minimum for the neutral blend membrane. A similar trend was observed for the water uptake of the pristine blend membranes and the proton conductivity of the PA doped membranes. Preliminary steam electrolysis tests were made at 130 °C, showing reasonable performance and stability for MEAs based on PA doped Nafion® membranes.

## Acknowledgments

Danish Power Systems ApS is thanked for providing PBI. Financial supports are acknowledged from the European Commission within the 7th Framework Programme (WELTEMP project 212903) and the Danish Council for Strategic Research (HyCycle).

## REFERENCES

[1] Banerjee S, Curtin DE. Nafion® perfluorinated membranes in fuel cells. J Fluorine Chem 2004;125:1211–6.

[2] Millet P, Andolfatto F, Durand R. Design and performance of a solid polymer electrolyte water electrolyzer. Int J Hydrogen Energy 1996;21:87–93.

[3] Heitner-Wirguin C. Recent advances in perfluorinated ionomer membranes: structure, properties and applications. J Memb Sci 1996;120:1–33.

[4] Mauritz KA, Moore RB. State of understanding of Nafion. Chem Rev 2004;104:4535–85.

[5] Linkous CA, Anderson HR, Kopitzke RW, Nelson GL. Development of new proton exchange membrane electrolytes for water electrolysis at higher temperatures. Int J Hydrogen Energy 1998;23:525–9.

[6] Li Q, He R, Jensen JO, Bjerrum NJ. Approaches and recent development of polymer electrolyte membranes for fuel cells operating above 100 °C. Chem Mater 2003;15:4896–915.

[7] Hauch A, Ebbesen SD, Jensen SH, Mogensen M. Highly efficient high temperature electrolysis. J Mater Chem 2008;18:2331–40.

[8] Millet P, Dragoe D, Grigoriev S, Fateev V, Etievant C. GenHyPEM: a research program on PEM water electrolysis supported by the European commission. Int J Hydrogen Energy 2009;34:4974–82.

[9] Antonucci V, Di Blasi A, Baglio V, Ornelas R, Matteucci F, Ledesma-Garcia J, et al. High temperature operation of a composite membrane-based solid polymer electrolyte water electrolyser. Electrochim Acta 2008;53:7350–6.

[10] Grigoriev SA, Millet P, Korobtsev SV, Porembskiy VI, Pepic M, Etievant C, et al. Hydrogen safety aspects related to high-pressure polymer electrolyte membrane water electrolysis. Int J Hydrogen Energy 2009;34:5986–91.

[11] Antonucci PL, Arico AS, Creti P, Ramunni E, Antonucci V. Investigation of a direct methanol fuel cell based on a composite Nafion®-silica electrolyte for high temperature operation. Solid State Ionics 1999;125:431–7.

[12] Watanabe M, Uchida H, Seki Y, Emori M, Stonehart P. Self-humidifying polymer electrolyte membranes for fuel cells. J Electrochem Soc 1996;143:3847–52.

[13] Alberti G, Casciola M. Composite membranes for medium-temperature PEM fuel cells. Annu Rev Mater Res 2003;33:129–54.

[14] Costamagna P, Yang C, Bocarsly AB, Srinivasan S. Nafion® 115/zirconium phosphate composite membranes for operation of PEMFCs above 100 °C. Electrochim Acta 2002;47:1023–33.

[15] Alberti G, Casciola M, Pica M, Tarpanelli T, Sganappa M. New preparation methods for composite membranes for medium temperature fuel cells based on precursor solutions of insoluble inorganic compounds. Fuel Cells 2005;5:366–74.

[16] Doyle M, Choi SK, Proulx G. High-temperature proton conducting membranes based on perfluorinated ionomer membrane-ionic liquid composites. J Electrochem Soc 2000;147:34–7.

[17] Savinell R, Yeager E, Tryk D, Landau U, Wainright J, Weng D, et al. A polymer electrolyte for operation at temperatures up to 200 °C. J Electrochem Soc 1994;141:L46–48.

[18] Li Q, Hjuler HA, Bjerrum NJ. Oxygen reduction on carbon supported platinum catalysts in high temperature polymer electrolytes. Electrochim Acta 2000;45:4219–26.

[19] Wainright JS, Wang JT, Weng D, Savinell RF, Litt M. Acid-doped polybenzimidazoles – a new polymer electrolyte. J Electrochem Soc 1995;142:L121–123.

[20] Li Q, Jensen JO, Savinell RF, Bjerrum NJ. High temperature proton exchange membranes based on polybenzimidazoles for fuel cells. Prog Polym Sci 2009;34:449–77.

[21] He R, Li Q, Jensen JO, Bjerrum NJ. Doping phosphoric acid in polybenzimidazole membranes for high temperature proton exchange membrane fuel cells. J Polym Sci Part A Polym Chem 2007;45:2989–97.

[22] Ma YL, Wainright JS, Litt MH, Savinell RF. Conductivity of PBI membranes for high-temperature polymer electrolyte fuel cells. J Electrochem Soc 2004;151:A8–16.
[23] Li Q, Rudbeck HC, Chromik A, Jensen JO, Pan C, Steenberg T, et al. Properties, degradation and high temperature fuel cell test of different types of PBI and PBI blend membranes. J Memb Sci 2010;347:260–70.
[24] He R, Li Q, Xiao G, Bjerrum NJ. Proton conductivity of phosphoric acid doped polybenzimidazole and its composites with inorganic proton conductors. J Memb Sci 2003;226:169–84.
[25] Li Q, Pan C, Jensen JO, Noyé P, Bjerrum NJ. Cross-linked polybenzimidazole membranes for fuel cells. Chem Mater 2007;19:350–2.
[26] Noyé P, Li Q, Pan C, Bjerrum NJ. Cross-linked polybenzimidazole membranes for high temperature proton exchange membrane fuel cells with dichloromethyl phosphinic acid as a cross-linker. Polym Adv Technol 2008; 19:1270–5.
[27] Kerres J, Ullrich A, Meier F, Häring T. Synthesis and characterization of novel acid-base polymer blends for application in membrane fuel cells. Solid State Ionics 1999; 125:243–9.
[28] Deimede V, Voyiatzis GA, Kallitsis JK, Li Q, Bjerrum NJ. Miscibility behavior of polybenzimidazole/sulfonated polysulfone blends for use in fuel cell applications. Macromolecules 2000;33:7609–17.
[29] Hasiotis C, Li Q, Deimede V, Kallitsis JK, Kontoyannis CG, Bjerrum NJ. Development and characterization of acid-doped polybenzimidazole/sulfonated polysulfone blend polymer electrolytes for fuel cells. J Electrochem Soc 2001;148: A513–519.
[30] Kerres J, Schönberger F, Chromik A, Häring T, Li Q, Jensen JO, et al. Partially fluorinated arylene polyethers and their ternary blend membranes with PBI and $H_3PO_4$. Part I. Synthesis and characterisation of polymers and binary blend membranes. Fuel Cells 2008;8:175–87.
[31] Li Q, Jensen JO, Pan C, Bandur V, Nilsson MS, Schönberger F, et al. Partially fluorinated arylene polyethers and their ternary blends with PBI and $H_3PO_4$. Part II. Characterisation and fuel cell tests of the ternary membranes. Fuel Cells 2008;8:188–99.
[32] Hobson LJ, Nakano Y, Ozu H, Hayase S. Targeting improved DMFC performance. J Power Sources 2002;104:79–84.
[33] Ainla A, Brandell D. Nafion®-polybenzimidazole (PBI) composite membranes for DMFC applications. Solid State Ionics 2007;178:581–5.
[34] Wycisk R, Chisholm J, Lee J, Lin J, Pintauro PN. Direct methanol fuel cell membranes from Nafion-polybenzimidazole blends. J Power Sources 2006;163:9–17.
[35] Zhai YF, Zhang HM, Zhang Y, Xing DM. A novel $H_3PO_4$/Nafion-PBI composite membrane for enhanced durability of high temperature PEM fuel cells. J Power Sources 2007;169:259–64.
[36] Marshall A, Borresen B, Hagen G, Tsypkin M, Tunold R. Preparation and characterisation of nanocrystalline $Ir_xSn_{1-x}O_2$ electrocatalytic powders. Mater Chem Phys 2005; 94:226–32.
[37] Yang YS, Siu A, Peckham TJ, Holdcroft S. Structural and morphological features of acid-bearing polymers for PEM fuel cells. In: Scherer GG, editor. Adv polym sci. Berlin Heidelberg: Springer Verlag; 2008. p. 55–126.
[38] Li Q, He R, Berg RW, Hjuler HA, Bjerrum NJ. Water uptake and acid doping of polybenzimidazoles as electrolyte membranes for fuel cells. Solid State Ionics 2004;168:177–85.
[39] Lu XY, Weiss RA. Specific interactions and ionic aggregation in miscible blends of nylon-6 and zinc sulfonated polystyrene ionomer. Macromolecules 1992;25:6185–9.
[40] Liang ZX, Chen WM, Liu JG, Wang SL, Zhou ZH, Li WZ, et al. FT-IR study of the microstructure of Nafion® membrane. J Memb Sci 2004;233:39–44.
[41] Section 9: molecular structure and spectroscopy. Infrared correlation charts. In: Lide DR, editor. CRC handbook of chemistry and physics. 90th ed. Boca Raton, FL: CRC Press/ Taylor and Francis; 2010. Internet version.
[42] Li Q, Hjuler HA, Bjerrum NJ. Phosphoric acid doped polybenzimidazole membranes: physiochemical characterization and fuel cell applications. J Appl Electrochem 2001;31:773–9.
[43] He R, Li Q, Bach A, Jensen JO, Bjerrum NJ. Physicochemical properties of phosphoric acid doped polybenzimidazole membranes for fuel cells. J Memb Sci 2006;277:38–45.
[44] Endoh E. Highly durable PFSA membranes. In: Vielstich W, Yokokawa H, Gasteiger HA, editors. Handbook of fuel cells – fundamentals, technology and applications. Chichester: Wiley; 2009. p. 361–74.
[45] Canagaratna M, Phillips JA, Goodfriend H, Leopold KR. Structure and bonding of the sulfamic acid zwitterion: microwave spectrum of $^{+}H_3N{-}SO_3^{-}$. J Am Chem Soc 1996; 118:5290–5.
[46] Schmidt TJ, Baurmeister J. Properties of high-temperature PEFC Celtec®-P 1000 MEAs in start/stop operation mode. J Power Sources 2008;176:428–34.

II

Accepted in International Journal of Hydrogen Energy 25th of April 2012

# PEM steam electrolysis at 130°C using a phosphoric acid doped short side chain PFSA membrane

Martin Kalmar Hansen[a,*], David Aili[a], Erik Christensen[a], Chao Pan[a], Søren Eriksen[b], Jens Oluf Jensen[a], Jens von Barner[a], Qingfeng Li[a] and Niels J. Bjerrum[a]

[a] *Energy and Materials Group, Department of Chemistry, Kemitorvet 207, Technical University of Denmark, DK-2800 Lyngby, Denmark*

[b] *Tantaline A/S, Nordborgvej 81, L3V108, DK-6430 Nordborg, Denmark*

* Corresponding author. Tel.: +45 45252413; Fax: +45 45883136 E-mail address: mkh@kemi.dtu.dk

**Abstract**

Steam electrolysis test with a phosphoric acid doped Aquivion™ membrane was successfully conducted and current densities up to 775 mA·cm$^{-2}$ at 1.8 V was reached at 130 °C and ambient pressure. A new composite membrane system using perfluorosulfonic acid membrane (Aquivion™) as matrix and phosphoric acid as proton conducting electrolyte was developed. Traditional perfluorosulfonic acid membranes do not possess sufficient dimensional stability and proton conductivity to be used at elevated temperatures and ambient pressures. The elevated temperature, high potentials and acidic conditions implied that a new and highly corrosion resistant construction material was needed. Tantalum coated stainless steel felt was tested and found suitable as the anode gas diffusion layer.

**Keywords:**

Water electrolysis; High temperature; Tantalum coating; Proton exchange membrane; PEMEC

## 1 Introduction

To meet the demand for a reduction in human created $CO_2$ (Kyoto Protocol and others [1]) a change from the fossil fuel based energy to sustainable energy is required. Water electrolysis can play an important role in this global strategy. Proton exchange membrane (PEM) water electrolysis has several advantages compared with the conventional alkaline technology, including higher gas purity (99.99%) [2], higher gas production rates (due to higher current densities of 1-2 $A \cdot cm^{-2}$) [3] and the ability to work under higher pressures (70 bar [4] and even up to 130 bar [5] and 138 bar [6] have been reported) and even differential pressurisation (systems with approximately 20 bar [7] and 70 bar [8] pressure difference have been reported). PEM electrolysers are generally based on perfluorosulfonic acid (PFSA) type membranes [9] such as Nafion®. The proton conductivity of PFSA type membranes is generally highly dependent on the water content, which implies that its operation temperature is limited to under 100 °C [10] unless the system is pressurised in order to keep the membrane well hydrated. However, for a number of reasons it has been proposed that elevating the temperature to above 100 °C would be beneficial [10]. First of all, the elevated temperature will improve the electrode kinetics and thus reduce the overpotentials which are connected to kinetic limitations. Secondly, the total thermodynamic energy requirement for the water splitting ($\Delta H$) is lowered from 284 $kJ \cdot mol^{-1}$ (liquid water, 80 °C) to 243 $kJ \cdot mol^{-1}$ for steam electrolysis at 130 °C. Furthermore, the reversible voltage, as calculated from the Gibbs free energy change ($\Delta G$), is reduced slightly by raising the temperature from 80 °C (1.18 V, liquid water) to 130 °C (1.16 V, steam).

An elevated temperature is also advantageous for PEM systems operated in fuel cell mode [11]. In fuel cell technology the challenge with an increase in operation temperature was solved by replacing water as the proton conducting phase in the membrane with phosphoric acid (PA), which exhibits high anhydrous proton conductivity and has very low vapour pressure [12]. For example, PA doped polybenzimidazole (PBI) can be used at operation temperatures up to 200 °C [11, 13, 14] since its proton conductivity mechanism is not (like in traditional PFSA membranes) completely dependent on the presence of water within the membrane matrix. In a recent work within our group, PA doped PBI was investigated for its ability to work as an electrolyte in electrolysis [15]. The PA doped PBI membrane based MEAs showed relatively good performance in steam electrolysis mode but suffered from severe durability limitations. The PA doped Nafion® based MEA, on the other hand, showed considerably better durability but slightly lower performance. The moderate performance could

eventually be explained by a large membrane-electrode interfacial contact resistance and uneven current distribution as discussed by Millet *et al.* [9]. This could eventually be connected to the limited dimensional stability of the PA doped Nafion® membrane under the operating conditions, it is known from literature that PA has a plasticising effect on PBI membranes likely due to membrane swelling [16]. Limited dimensional stability of traditional Nafion® membranes are known to be due to increased water swelling with reduced elastic modulus of the membrane *i.e.* at higher temperatures [17, 18].

Another way to improve the electrolysis performance of PFSA membranes at elevated temperatures is to improve their hydration characteristics through the incorporation of hygroscopic inorganic fillers, such as $SiO_2$ [19, 20], $TiO_2$ [21] or zirconium phosphates [22] or by pressurising the system in order to keep the membrane well hydrated [19-21, 23].

Aquivion™ is another type of polymer in the PFSA family, which differs from Nafion® in terms of the equivalent weight and the length of the sulfonic acid terminated side groups. Compared with the conventional Nafion® membranes, this type of PFSA membranes exhibits considerable higher softening temperatures [24] which naturally should facilitate the electrolysis operation at elevated temperatures. Its high elastic modulus has also been identified as important for its superior performance in $H_2/O_2$ PEM fuel cells [25, 26].

Increasing the temperature and replacing water as the proton carrier with PA naturally result in harsher conditions within the cell. Hence highly corrosion resistant materials are needed for the cell hardware. Traditionally, titanium is used for this purpose in low temperature PEM electrolysis [2, 27]. However recent work within our group [28] has shown that titanium has a very high corrosion rate in PA at elevated temperatures. In order to simulate the conditions in an operating electrolysis cell based on a PA doped membrane, the corrosion currents were determined in 85 wt% PA at 120 °C and potentials up to 1.1 V vs. SHE. Under these conditions the corrosion current of titanium was determined to be 6.3 $mA \cdot cm^{-2}$, which according to Faradays Law corresponds to a corrosion rate of 73 $mm \cdot year^{-1}$ [28]. For comparison, the corrosion current density of Ta under these conditions was determined to $6.3 \cdot 10^{-5}$ $mA \cdot cm^{-2}$ which gives a corrosion rate of under $1 \cdot 10^{-3}$ $mm \cdot year^{-1}$ [28]. Similar extremely low corrosion rates of less than $1 \cdot 10^{-2}$ $mm \cdot year^{-1}$ for Ta have been determined at temperatures up to 150 °C in 85 wt% PA and at potentials as high as 2.27 V vs. SHE [29]. The excellent corrosion resistance of tantalum in aggressive acidic media is due to a protective oxide surface layer, $Ta_2O_5$, that is naturally formed on the surface but only in very thin layers (3 nm [30]). However such oxide layers have a low

electronic conductivity, hence the performance of the tantalum coated cell components may be dramatically reduced if too thick oxide layers are formed.

Aiming at better performance and longer durability especially for high temperature operation, tantalum was in the present study selected as a coating material for both the flow plates and anode gas diffusion layer (GDL). PA doped Aquivion™ membranes were tested in steam electrolysis mode and some parameters were investigated including flow pattern design, the assembly procedure and the importance of the gas diffusion layer characteristics.

## 2 Experimental

### 2.1 Tantalum coated flow plates and gas diffusion layers

The flow patterns were machined in-house from stainless steel (316L) on a CNC milling machine. Three different flow patterns were tested after being coated with tantalum by chemical vapour deposition by the company Tantaline. The anode GDL was made from 316L stainless steel felt (Swiit Metallic Fiber Co. Ltd) coated with tantalum (Tantaline). Two different types of felt were tested: a single layer felt with a fibre diameter of 12 μm and a double layer felt where one half of the felt was made from 8 μm fibres and the other half of 12 μm fibres. The difference in the fibre diameter gave rise to a felt with a more dense structure on one side (the 8 μm side). Both types of stainless steel felts had a total thickness of 0.5 mm.

### 2.2 Characterization of gas diffusion layer.

On the cathode side a wet-proofed non-woven carbon cloth (Freudenberg H2315 C2) was used as GDL, which was not further examined in this work. The stainless steel felt was examined by porosity measurements before and after tantalum coating. The porosity measurements were carried out on a Micromeritic AccuPyc 1330 pycnometer on samples of ca. 0.3 $cm^3$. The surface topology of the tantalum coatings and the cross sections of coated felt were examined using scanning electron microscopy (SEM) which was performed on a Carl Zeiss EVO MA10 microscope. Cross sections of the felts were made using a Hitachi E-3500 ion mill. Resistance measurements were performed in an in-house designed four point experimental setup allowing resistance measurements at different compression forces. The GDL compression force could be varied between approximately 0.1 and 3.0

MPa by a vertical hand screw where the force was measured by a Nordic Transducer MD1010R Strain gauge.

The measurements were performed by applying a constant direct current (100 mA) while measuring the voltage as a function of the applied compression force. The contact resistance was measured for a quadratic 1 $cm^2$ piece of the GDL material sandwiched between two rectangular strips of tantalum foil (0.3 mm thick, 99.9% Goodfellow) with a width of 1.5 cm laying perpendicular to each other giving a contact area 1 $cm^2$. The metal pieces were fixed by a PTFE holder, and kept electrically insulated from the pressure setup by PTFE spacers. All the measurements were performed at room temperature. The voltages were measured at the peak force, which was raised in intervals of approximately 0.1 MPa.

## 2.3 Electrode preparation

The anodes were made individually for each MEA. The anode had a geometric area of 11.6 $cm^2$. The ink was manually air sprayed directly onto the GDL which was kept at 130 °C. The spraying procedure was optimised (stepwise spraying, keeping the GDL as dry as possible) to prevent the ink from deep penetration into the GDL. The ink consisted of $IrO_2$ (made in a thermolysis process similar to the work by Hu *et al.* [31] (BET surface area 23 $m^2 \cdot g^{-1}$), and provided from Norwegian University of Science and Technology), a 6 wt.% ionomer binder (Aquivion™ D83-06A, Solvay Solexis) and 2-propanol (puriss, Riedel de Häen) as dispergent. The weight ratio between $IrO_2$ and the 2-propanol was kept constant *i.e.* there was approximately 100 times more 2-propanol than $IrO_2$. After spraying the catalyst onto the GDL the anode was doped with a solution consisting of 1.5 wt% aqueous PA and glacial acetic acid in a 1:1 weight ratio, to give a PA loading of approximately 0.1 $mg \cdot cm^{-2}$. The loadings of $IrO_2$ were between 1.0 and 3.5 $mg \cdot cm^{-2}$ and the ionomer binder content was either 5 or 15 wt%.

The cathodes were prepared in large sheets with a typical area of 600 $cm^2$. The ink was manually air sprayed onto the pre-treated non-woven carbon cloth at 110 °C in steps in order to avoid deep penetration of the ink into the GDL. The ink consisted of an in-house made 40 wt% Pt/C catalyst, a Nafion® ionomer (D521 Dispersion DuPont™) and ethanol (96 Vol%, KEMETYL) as dispergent. The platinum loading was about 0.8 $mg \cdot cm^{-2}$ and the Nafion® ionomer loading about 0.3 $mg \cdot cm^{-2}$. The cathodes were punched out in to discs with a geometric area of 11.6 $cm^2$ using a hydraulic press.

## 2.4 Membrane Electrode Assemblies

Commercially available Aquivion™ E79-05S - 50 μm (Solvay Solexis) membranes were pre-treated by boiling in 3% $H_2O_2$ for 1 h, rinsing in demineralised water and boiling in a 0.5 M $H_2SO_4$ solution for 2 h, followed by extensive boiling and rinsing in demineralised water. The membranes were doped in 85 wt% PA for 16 hours at 150 °C in a glass container covered with a glass plate [15, 32], to give a PA content of about 44 wt% which corresponds to about 6 PA molecules per sulfonic acid group. The membrane electrode assemblies (MEAs) were made in two different ways, either by assembling directly in the cell, or by hot pressing for 2 minutes at 155 °C and 5 MPa before cell assembly.

2.5 Electrolysis test

The MEAs were tested in an in-house designed test cell. It consisted of flow plates with a circular flow area of 10 $cm^2$. Three different flow patterns were tested. An asymmetric spiral (A) and two patterns with straight channels (B and C) as shown on figure 1. The depths of the channels are colour coded and darker colour corresponds to a deeper channel. The land (ribs) is white, whereas the inlets and outlets are black in the figure. In all three cases the inlets and outlets were in the outer perimeter of the flow area located at the top and bottom. The dimensions of the patterns are given in table 1.

**Table 1:** Summary of the physical characteristics of the different flow patterns

| | | Channel dimension [mm] | | | Land [mm] | Area [$mm^2$] | |
|---|---|---|---|---|---|---|---|
| # | Flow design | Width | Depth | Max. Length | Width | Channel | Land |
| A | Asym. spiral | 2 | 2 | ~290 | 2 | 608 | 387 |
| B | Straight | 2 | 1 | 34 | 2 | 594 | 401 |
| C | Straight | 1 | 1 | 34 | 1 | 593 | 402 |

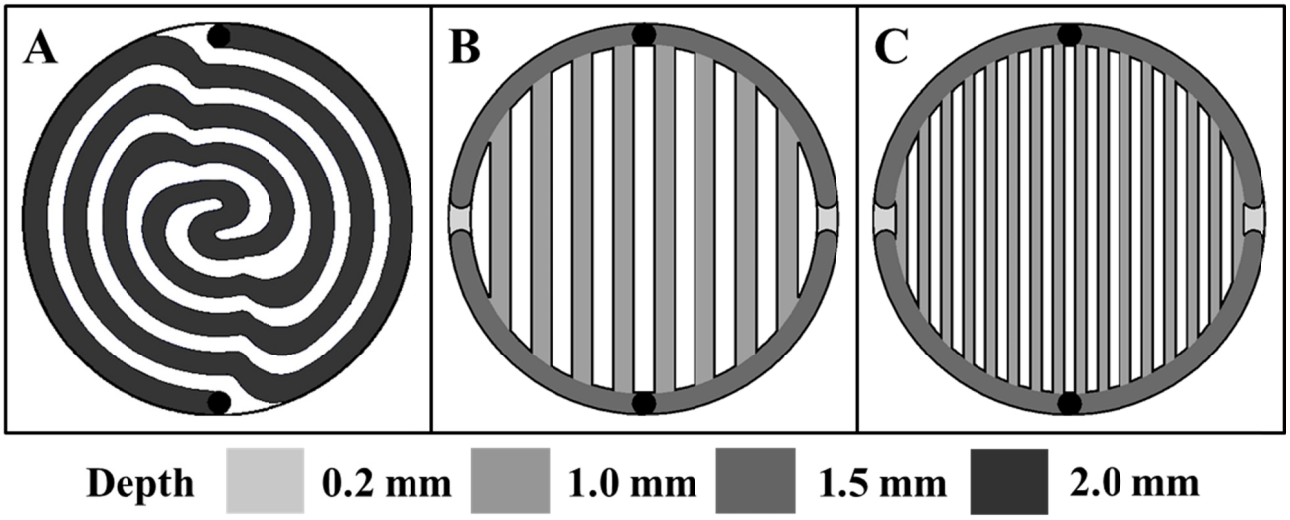


**Figure 1:** Schematic illustrations of the flow patterns. The depth of the channels is indicated with a grey scale. The black circles are inlet and outlet.

The flow plates were made of tantalum coated stainless steel (Tantaline®). The flow plates were fixed to aluminium end plates containing electrical heating elements. Eight bolts with disc springs were used to assemble the cell. The clamping force for the cell was 5 Nm, which in this system was calculated (from spring constant and compression) to be equivalent to 7 MPa. The distribution of force between the electrodes and the gaskets is not known.

The electrolysis tests were performed at 130 °C under ambient pressure. Water was fed by a peristaltic pump (Alitea –XV) through an evaporator at 180 °C. Water from the exit flows was collected in condenser flasks at 5°C and the remaining flow of hydrogen and oxygen were monitored by mass flow meters (Brooks 4800 Series). The cell was powered by an in-house made current source.

The cell was heated to the operating temperature before steam was supplied to the cell in order to avoid condensation of water in the cell. To achieve steady state behaviour an upstart period of 20 minutes was applied. Measurements for the polarisation data were then done by current step potentiometry with the steady state voltage recorded 10 minutes after each current were set.

The characteristics for the tested MEAs are listed in table 2, where they are grouped after the parameters varied.

**Table 2:** MEA characteristics for the tested MEAs

| | Anode | | | | |
|---|---|---|---|---|---|
| MEA # | $IrO_2$ [mg·cm$^{-2}$] | Binder [wt%] | GDL Batch # | Flow pattern | Hot pressed |
| Variation of anode GDL | | | | | |
| MEA1 | 0.98 | 5 | 1 | C | Yes |
| MEA2 | 1.06 | 5 | 1 | C | Yes |
| MEA3 | 0.93 | 5 | 2 | C | Yes |
| MEA4 | 1.22 | 5 | 2 | C | Yes |
| Variation of assembly procedure | | | | | |
| MEA5 | 1.01 | 15 | 1 | C | No |
| MEA6 | 1.02 | 15 | 1 | C | Yes |

## 3 Results and discussion

### 3.1 Tantalum coated stainless steel felt

Important aspects for GDLs in fuel cells and electrolysers are their porosity [2] and surface topology [33]. Zhou *et al.* [33] mentioned the surface topology as one of the important factors of the GDL since it defines the number of contact points between the GDL and the bipolar plate (BPP). One of the key points in the GDL is that it should offer an optimal trade-off between high porosity and low electrical resistance.

The stainless steel felt had a measured porosity of 82 % before coating with tantalum which was in agreement with the specification from the supplier. After the tantalum coating of the stainless steel felt, the porosity was reduced. The porosity of the double layer felt with the thicker coating (batch 1) was 45 % and the single layer felt with the thinner coating (batch 2), was 72%. Grigoriev *et al.* [2] reported that the optimal porosity for a liquid electrolyser should be between 30% and 50%. However, their experiments and calculations were done on sintered spherical titanium particles which pack in a very ordered way. The felts in the present study were much less ordered which undoubtedly affected the pore sizes, which was another important parameter [2]. Pore sizes might be of less importance in case of steam electrolysis compared to liquid electrolysis since blockage of the pores is less likely in the steam case than in the liquid case. The surface topology and cross sections of the felts investigated by SEM, are shown in figure 2.

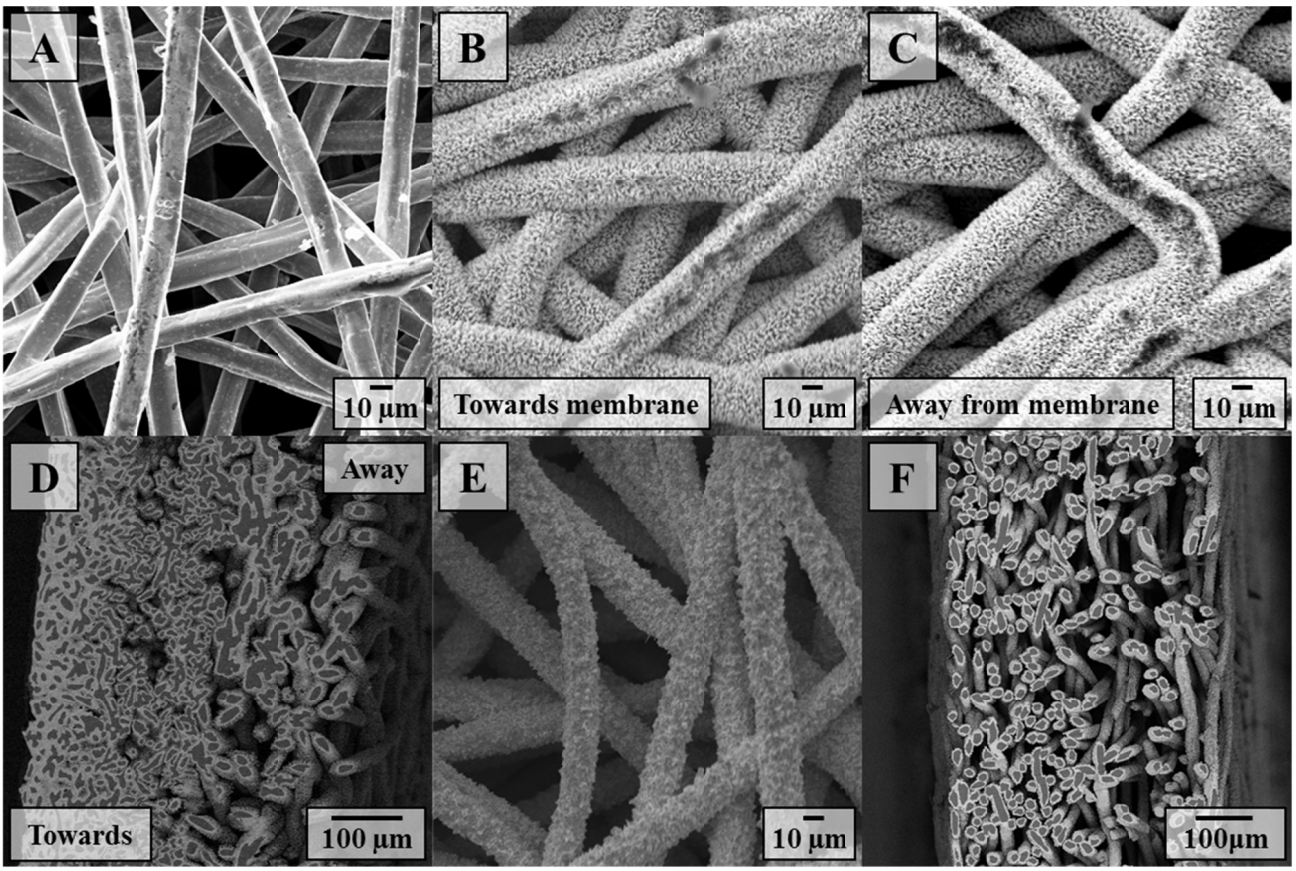


**Figure 2:** SEM images of: A: Pristine single layer felt. B: Ta coated double layer felt dense side. C: Ta coated double layer felt less dense side. D: Cross section of Ta coated double layer felt, dense side left, less dense side right. E: Ta coated single layer felt. F: Cross section of Ta coated single layer felt.

The porosity data were clearly supported by the images in figure 2. The single layer felt with the thinner coating (2-E and 2-F) obviously had a much more open structure than the double layer felt with the thicker tantalum coating (2-B to 2-D). Another apparent difference between the two felt batches was the surface topology of the tantalum coating on the stainless steel fibres. A combination of the differences in porosity and surface topology can possibly have a big influence on the penetration depth of catalyst ink into the felt. It must be expected that the ink penetrated deeper into the single layer felt which had a more open structure. The fibres of the single layer felt also had a smoother surface than those of the double layer felt. Moreover the combination of a denser structure (the individual fibres are closer together) and the rougher surface of the fibres (the dendrites) would give rise to an increased

number of contacts points between the GDL and the membrane and between the GDL and the flow plate. This increase in contact points resulted in a better interfacial contact.

High electronic conductivity of the GDL and the flow plate and good interfacial contact between them are of great importance in order to reach good performance [34]. In order to investigate if tantalum coated stainless steel felt can be used as gas diffusion layer in an electrolysis cell the resistance of the felt was measured. In figure 3 the measured resistance is shown as a function of clamping pressure. The resistance was the sum of the bulk resistance of the felt and the two interfacial resistances between the coated felt and tantalum foils. Two batches of tantalum coated felts were tested where the amount of coating was varied. Batch 1 was a double layer felt with a thicker tantalum coating than batch 2 (a single layer felt). The resistance of three samples of each batch was measured and the averages and the corresponding standard deviations for both batches are depicted in figure 3.

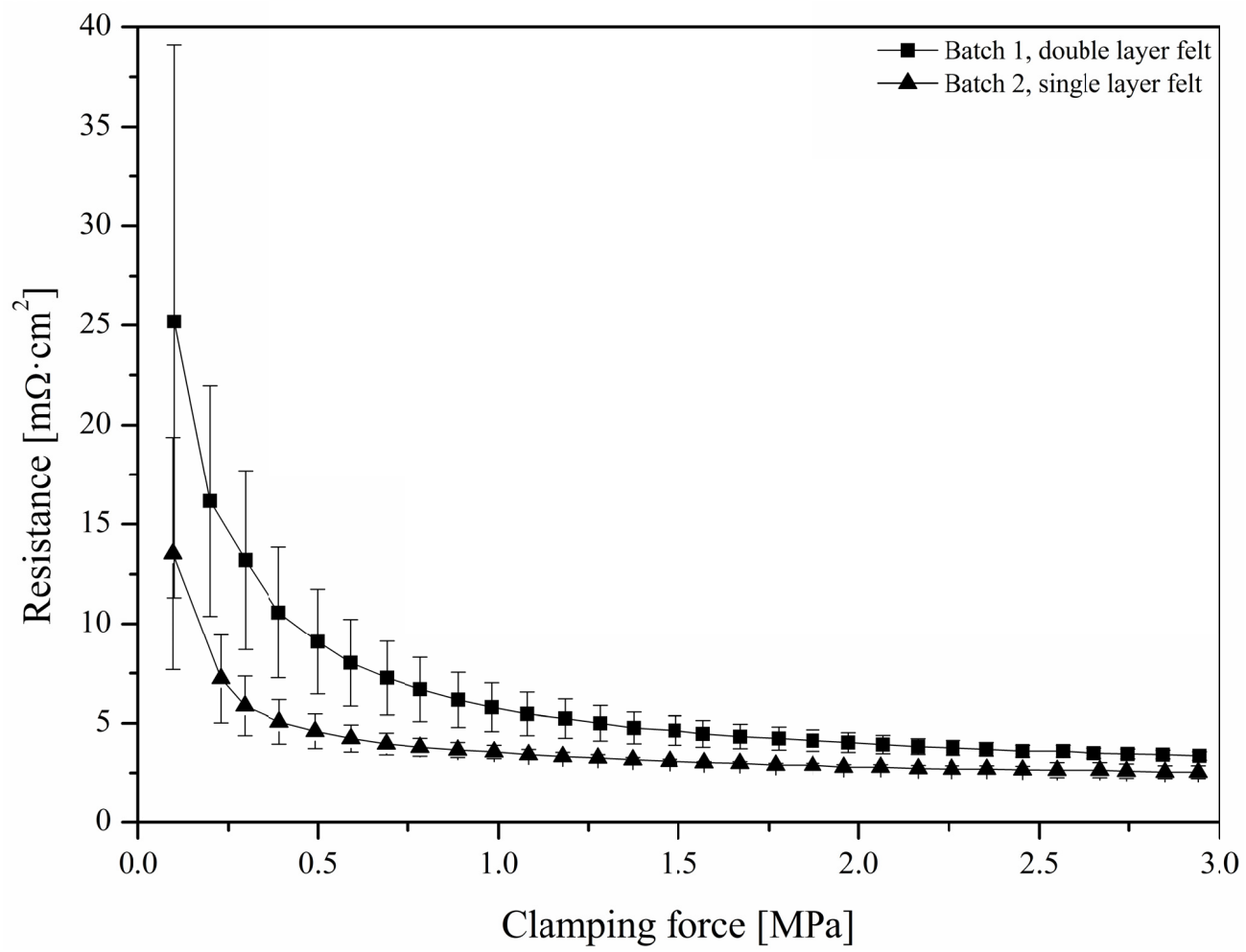


**Figure 3:** Resistance as function of clamping force for two different types of Ta coated stainless steel felt. Double layer felt with a thicker Ta coating and single layer felt with a thinner Ta coating.

The total resistance of the single layer felt (thinner Ta coating) was lower than for the double layer felt (thicker Ta coating), which can be explained by the fact that the fibres with the thicker tantalum coating are stiffer and more rigid. Consequently, the higher total resistance of the double layer felt can be explained by a higher interfacial contact resistance since fewer fibres were in contact with the tantalum foils. As the clamping force was increased the resistance difference diminished as more fibres came into contact with the Ta foil.

At clamping forces above 2 MPa both types of tantalum coated felts exhibited a very low resistance (in the 3 mΩ·cm$^2$ range). For comparison, DOE has proposed a maximum limit of 10 mΩ·cm$^2$ for the

bipolar plates (in fuel cell systems) including the contact resistance between GDL and BPP [35]. Hence the values for the resistance found in this work are well below the DOE target. Thus the natural occurring oxide layer of $Ta_2O_5$, which gives tantalum its excellent corrosion resistance, was not limiting the electrical conductivity of the GDL and the tantalum coated felt is therefore suitable for use as GDL in acidic steam PEM electrolysis.

3.2 Cell performance with different GDLs

As mentioned above and shown in figure 1 three different flow patterns were tested. However, only small differences were observed and all measurements presented in this work were performed with flow pattern C, which had given rise to marginal lower cell voltages during polarisation tests than the two other patterns in the initial experiments. The reason for this marginal improvement in performance could be explained by the shorter channel length compared to the asymmetric spiral pattern, and due to a marginally better flow- and electrical distribution between the GDL and the flow pattern compared to the two other flow patterns.

Some variations in the polarisation measurements were observed and ascribed to the fact that the electrodes were hand-made. The polarisation curves of some of the best performing MEAs in the present study based on a PA doped Aquivion™ membrane are shown in figure 4. The importance of the properties of the coated felt was examined in real electrolysis applications and polarisation curves for single cells with anode GDL from the two different types of felts are shown in figure 4. It is clear that the performance of the two double layer felt MEAs (MEA1 and MEA2) is better than the performance of the MEAs (MEA3 and MEA4) with single layer felt.

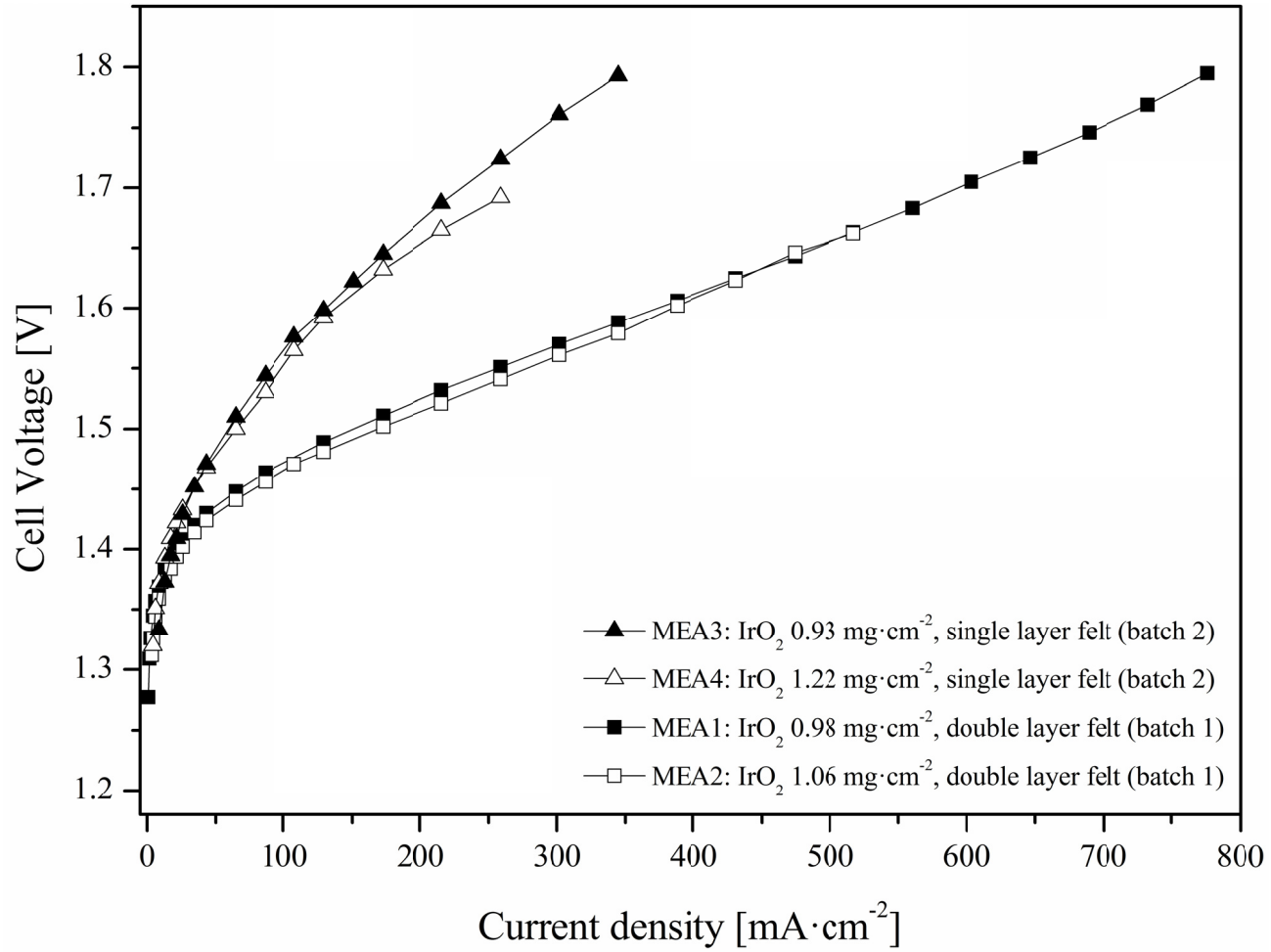


**Figure 4:** Polarisation curves for PA doped Aquivion™ based MEAs at 130 °C and ambient pressure. Two different felts were used as anode GDL.

From the polarisation curves in figure 4 it is seen that the surface topology of the GDL plays a very important role for the performance of the MEA. Polarisation curves can be divided into different regions, an activation governed region at low current densities, an ohmic resistance governed region at intermediate current densities and (not important here) a mass transport governed region at high current densities. It can be seen in figure 4 that the performance differs in both the activation controlled current density range and in the ohmic resistance controlled current density range of the polarisation curve. The activation and the ohmic contributions to the polarisation curves are separated according to equation 1 [36, 37] (by regression) and plotted in figure 5.

$$E = a + b \cdot \log(i) + iR \qquad \text{(Eq. 1)}$$

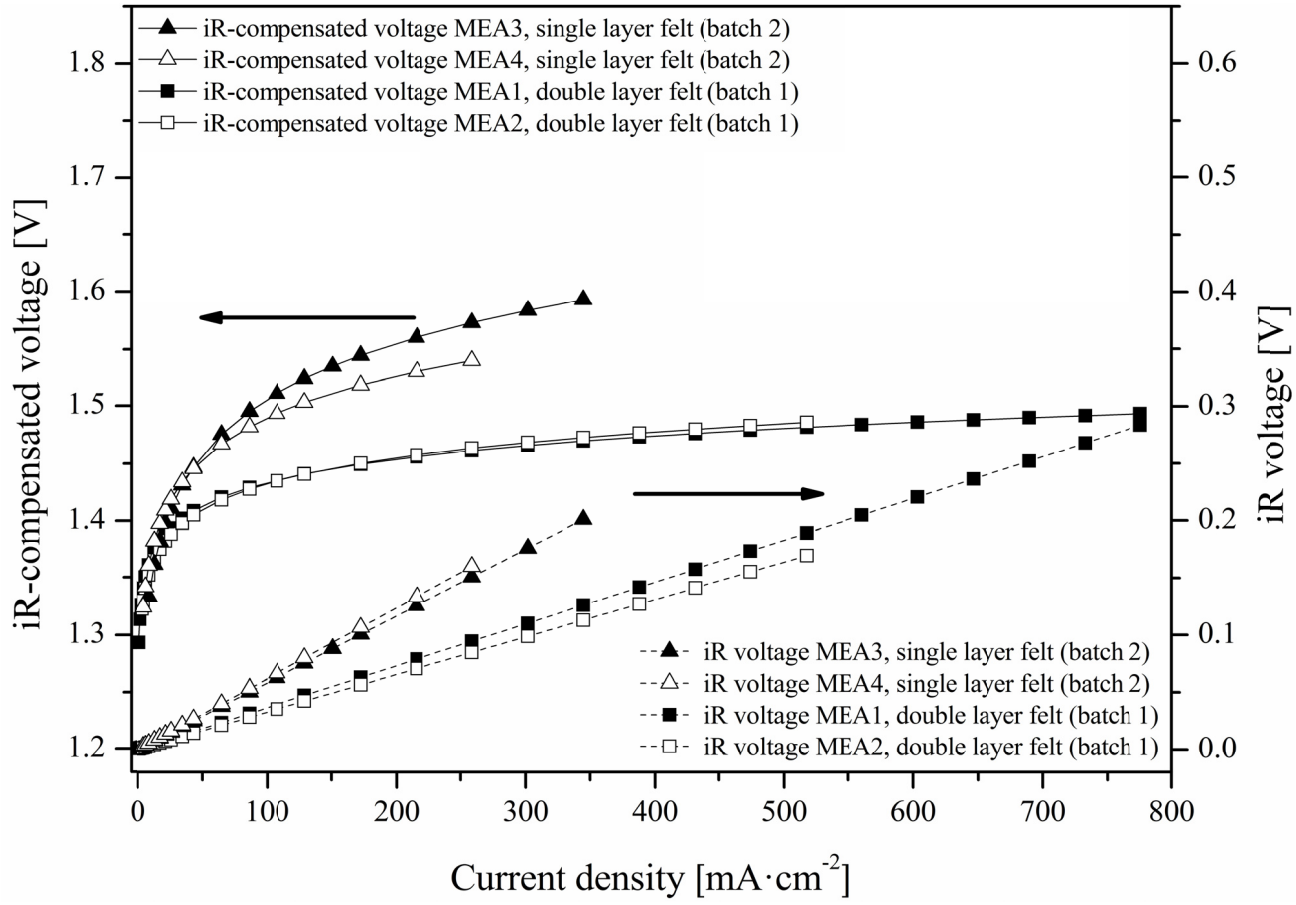


**Figure 5:** iR-compensated voltages and ohmic voltages for measurements with variation of anode GDL. Solid lines correspond to the iR-compensated voltage and dashed lines correspond to the iR-voltage.

From figure 5 it can be seen that the MEAs with the single layer felt anode (MEA3 and MEA4) clearly shows higher activation overvoltage as well as higher ohmic resistance compared to the MEAs using double layer felt (MEA1 and MEA2).

Since all MEAs had been hot pressed under the same conditions they should have similar interfacial contact resistance between the membrane and the electrode. However, since the topology of the tantalum coating was strikingly different between the two batches of felt (see figure 2) there is an obvious difference in the interfacial contact resistance between the membrane and the electrode. For

the difference in the activation overvoltage range there are two obvious explanations. Firstly due to the more open structure of the single layer felt with smoother Ta coating the catalytic ink penetrates deeper into the felt which limits the catalyst utilisation. Another reason for the better catalytic performance of double layer felt could be better dispersion of the $IrO_2$ particles on the rougher surface of the fibres. The better dispersion gives rise to a higher active catalytic area and thus a higher catalytic performance, much like the strategy of using supported catalyst to increase the catalytic active area as discussed by Nikiforov *et al.* [38]. The lower resistance in the system can also be explained as a combination of the rougher topology of the tantalum coating of the double layer felt and the fact that the fibres of the double layer felt facing the membrane is closer together, which gives shorter distance between the contact points. A rougher surface on the GDL will as mentioned above give rise to a larger total surface area and thus more contact points between the membrane and gas diffusion layer leading to a lower total resistance [2, 33].

The low values found from the resistance measurements (see figure 3) indicates that the contact resistance between the GDL and the flow plates are more uniform than between the GDL and the membrane, and of less importance for the total resistivity in the electrolysis setup tested in the present work.

### 3.3 Variation of assembly method

Two different ways of assembling the MEA were investigated, direct assembly of the MEA in the cell without prior hot pressing and hot pressing the MEA before cell assembly.

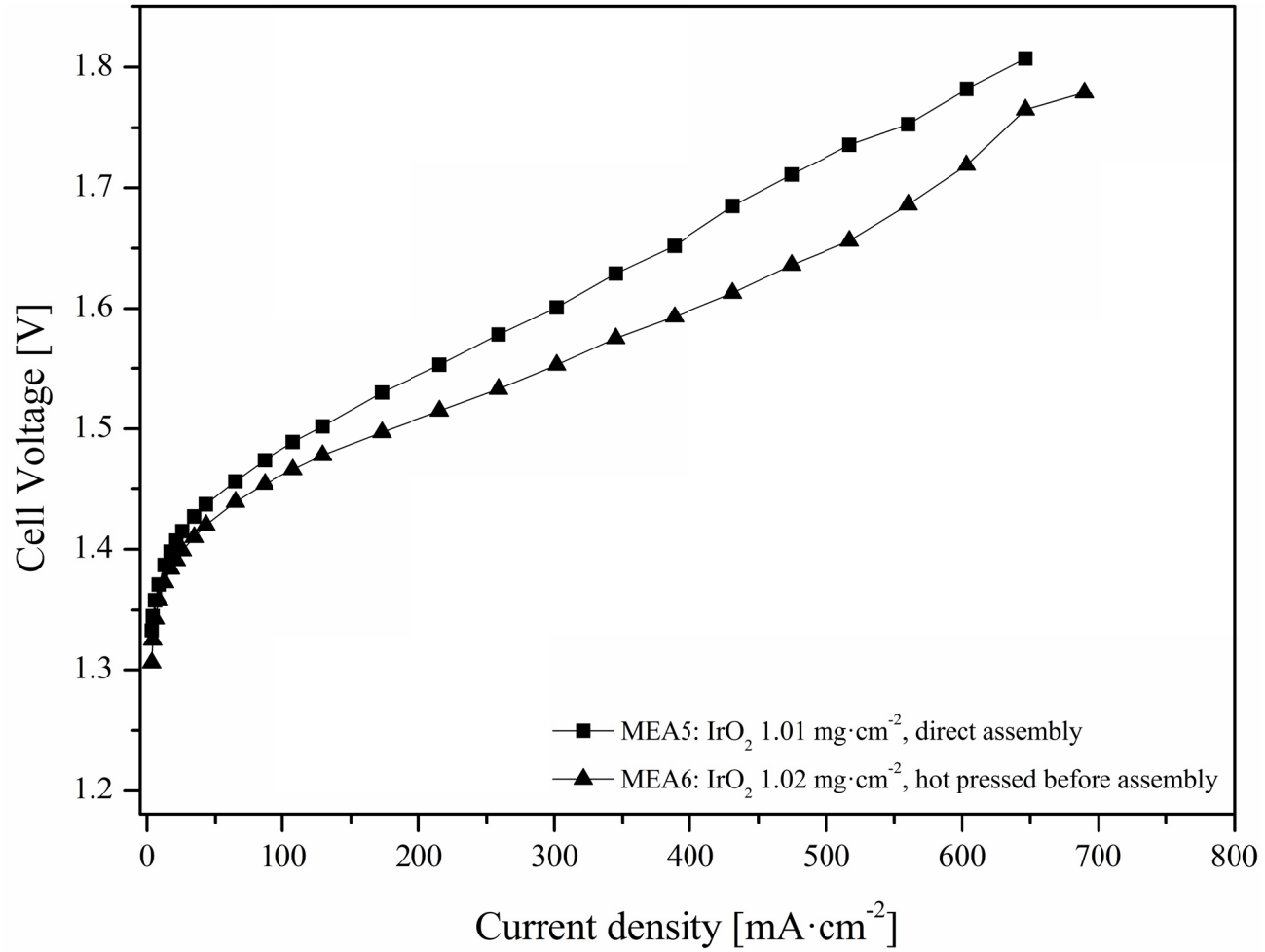


**Figure 6:** Polarisation curves for MEAs assembled directly in the cell or with prior hot pressing.

From figure 6 it can be seen that hot pressing the MEA before the cell assembly gives a better performance. Throughout the whole current density range the hot pressed MEA (MEA6) showed lower voltages than the MEA that had been assembled directly in the cell (MEA5). This was most likely due to lower contact resistance between the electrodes and the membrane and better utilisation of the catalyst. The increase in the voltage at current densities above 520 $mA \cdot cm^{-2}$ for the hot pressed MEA (MEA6) is more likely to be due to problems with the temperature stability of the evaporator used to feed the steam to the cell and condensation of water in the gas outlet tubing on the anode side than an actual effect of mass transport limitations. Fluctuations in the evaporator temperature and droplets of condensed water bursting out from the outlet gas tubing were observed to correspond with the fluctuations in the cell voltage.

During the work, MEAs with higher anode catalyst loading, 3.5 $mg \cdot cm^{-2}$, were tested (not presented here). A slightly improved performance (at high current densities) was observed by going down in catalyst loading to approximately 1 $mg \cdot cm^{-2}$, but more investigations need to be carried out before a firm conclusion can be drawn for the optimal anode loading. The ionomer loading in the anode was either 5 wt% or 15 wt% in this work, no significant difference was found by varying the ionomer content with this range. On the other hand it was earlier reported by Ma *et al.* [39] that lower overvoltages were obtained by lowering the Nafion® ionomer content from 40 wt% to 10 wt%. Xu *et al.* [40] found an optimal anode binder loading of 25 wt.% Nafion® ionomer, testing between 5 and 40 wt.%. In fuel cells the optimal binder content in the electrodes has been reported to be around 33 wt.% [41, 42]. Further work should be devoted to investigate the influence of varying the catalyst loading and the binder content in the anode.

### 3.4 Discussion and comparison with literature

The result for PA doped Aquivion™ is quite promising compared to the relatively few previous published steam electrolysis studies at elevated temperatures and ambient pressures. For example, Antonucci *et al.* [20] used a Nafion®-$SiO_2$ composite membrane based system and operated the cell in steam electrolysis mode at 120 °C and ambient pressures. The best performance for this system was 450 $mA \cdot cm^{-2}$ at 1.8 V. Furthermore, also at 120 °C and at ambient pressures, Baglio *et al.* [21] used a Nafion®-$TiO_2$ composite membrane based system, and obtained a current density of 700 $mA \cdot cm^{-2}$ at 1.8 V. Both inorganic filler composite systems had an anode catalyst loading of 5 $mg \cdot cm^{-2}$. The best result obtained in the present work was 775 $mA \cdot cm^{-2}$ at 1.8 V and 130 °C, with an anode loading of 1 $mg \cdot cm^{-2}$ $IrO_2$, see table 3. However, the performance is still considerable lower than that of the state-of-the-art low temperature PEM electrolysers. Though, it is encouraging with these improvements in performance for high temperature PEM electrolysers with respect to future work. The result demonstrates proof of concept of using PA instead of water as proton conducting phase in steam electrolysis.

A good fix point to compare electrolysis performances from different systems is the so-called thermoneutral (TN) voltage (1.48 V at standard conditions). This is the voltage where the cell neither is consuming heat from nor emitting heat to the surroundings. Hence at current densities corresponding to voltages above this value heat will be released to the surroundings. Compared to other PFSA composite

MEAs at comparable voltages, the best performing MEA in this work had a current density of 75 $mA \cdot cm^{-2}$ higher than a Nafion®-$TiO_2$ composite system [21], and 325 $mA \cdot cm^{-2}$ higher than a Nafion®-$SiO_2$ composite MEA [20] at 1.8 V, even though the operating temperature was higher and the anode catalyst loading in the present work was considerably lower.

**Table 3:** Comparison of current densities with literature values at the thermoneutral (TN) voltage (1.48 V) and at 1.8 V.

| | Electrolyte | Anode loading $[mg \cdot cm^{-2}]$ $IrO_2$ | Temperature [°C] | $i_{TN}$ $[mA \cdot cm^{-2}]$ | $i_{1.8\ V}$ $[mA \cdot cm^{-2}]$ |
|---|---|---|---|---|---|
| Antonucci *et al.* [16] | Nafion®-$SiO_2$ | 5 | 120 | 250 | 450 |
| Baglio *et al.* [18] | Nafion®-$TiO_2$ | 5 | 120 | 350 | 700 |
| Present work (MEA1) | Aquivion/PA | 1 | 130 | 130 | 775 |

As it can be seen from table 3, both the inorganic filler systems [20, 21] have considerable better performance at the thermoneutral voltage. This could eventually be explained by the considerable larger $IrO_2$ loading on the anode, which would give a much larger active catalytic area and the fact that the catalyst layer is deposited directly to the membrane and not on the GDL like in the present work. Furthermore it is known that PA is inhibiting the catalytic performance for $IrO_2$ in the oxygen evolution reaction [43]. However, these experiments were done in a liquid electrolyte where the influence of the phosphate anion is believed to be much larger than for PA in a PFSA matrix. The long term durability of the MEAs still needs to be examined, the leaking of PA from the membrane to the anode under electrolysis conditions is unknown. However for PA doped fuel cells the total acid loss has been reported to be as low as 0.5 $\mu g \cdot m^{-2} \cdot s^{-1}$ [44]. Furthermore lifetimes of approximately 18.000 hours have been reported for PA doped fuel cells at 160 °C [44]. Finally it can be seen from table 3 that the current density for MEA1 at 1.8 V is considerable higher than the two inorganic filler composite systems [20, 21], hence it is very clear that the ohmic resistance (most likely due to enhanced proton conductivity) of the PA doped system is much lower than in the $TiO_2$ and $SiO_2$ systems.

## 4 Conclusions

This work has shown that it is possible to use PEM electrolysers based on PA doped PFSA composite membranes at temperatures above 100 °C at ambient pressure and still reach reasonably high current densities at cell voltages under 2 V.

Tantalum coated stainless steel felts showed sufficient corrosion resistance and electronic conductivity and approved suitable as GDL materials in the acidic steam PEM electrolysers. It was found that hot pressing the MEAs before cell assembly improved the cell performance, thus the cell voltage was lowered with up to a 100 mV at 520 $mA \cdot cm^{-2}$. Further investigations are necessary in order to reach conclusions of the influence of ionomer binder in the anode and the optimal anode catalyst loading.


## Acknowledgements

The Electrochemical Energy Group at Norwegian University of Science and Technology is thanked for providing the $IrO_2$ used in the experiments. Financial support is acknowledged from the European Commission within the 7th Framework Programme (WELTEMP project 212903) and the Danish Council for Strategic Research (HyCycle).


## References


[1] *A roadmap for moving to a competitive low carbon economy in 2050*. European Commision; **2011** [COM(2011) 112/F]

[2] Grigoriev SA, Millet P, Volobuev SA, Fateev VN. *Optimization of porous current collectors for PEM water electrolysers*. Int. J. Hydrogen Energy **2009**;34:4968-73.

[3] Rasten E, Hagen G, Tunold R. *Electrocatalysis in water electrolysis with solid polymer electrolyte*. Electrochim. Acta **2003**;48:3945-52.

[4] Grigoriev SA, Millet P, Korobtsev SV, Porembskiy VI, Pepic M, Etievant C, et al. *Hydrogen safety aspects related to high-pressure polymer electrolyte membrane water electrolysis*. Int. J. Hydrogen Energy **2009**;34:5986-91.

[5] Grigoriev SA, Porembskiy VI, Korobtsev SV, Fateev VN, Auprêtre F, Millet P. *High-pressure PEM water electrolysis and corresponding safety issues*. Int. J. Hydrogen Energy **2011**;36:2721-8.

[6] Narayanan SR, Kindler A, Kisor A, Valdez T, Roy RJ, Eldridge C, et al. *Dual-feed balanced high-pressure electrolysis of water in a lightweight polymer electrolyte membrane stack*. J. Electrochem. Soc. **2011**;158:B1348-B57.

[7] Hamdan M, Norman T. *2010 Annual Progress Report - DOE Hydrogen Program*. Section II.E.2 - PEM Electrolyzer Incorporating an Advanced Low-Cost Membrane, U.S. Department of Energy; **2010**

[8] Marangio F, Pagani M, Santarelli M, Calì M. *Concept of a high pressure PEM electrolyser prototype*. Int. J. Hydrogen Energy **2011**;36:7807-15.
[9] Millet P, Andolfatto F, Durand R. *Design and performance of a solid polymer electrolyte water electrolyzer*. Int. J. Hydrogen Energy **1996**;21:87-93.
[10] Linkous CA, Anderson HR, Kopitzke RW, Nelson GL. *Development of new proton exchange membrane electrolytes for water electrolysis at higher temperatures*. Int. J. Hydrogen Energy **1998**;23:525-9.
[11] Li Q, He R, Jensen JO, Bjerrum NJ. *Approaches and Recent Development of Polymer Electrolyte Membranes for Fuel Cells Operating above 100 °C*. Chem. Mater. **2003**;15:4896-915.
[12] Macdonald DI, Boyack JR. *Density, Electrical Conductivity, and Vapor Pressure of Concentrated Phosphoric Acid*. J Chem & Eng Data **1969**;14:380-4.
[13] Wainright JS, Wang JT, Weng D, Savinell RF, Litt M. *Acid-doped polybenzimidazoles: A new polymer electrolyte*. J. Electrochem. Soc. **1995**;142:L121-3.
[14] Li Q, Jensen JO, Savinell RF, Bjerrum NJ. *High temperature proton exchange membranes based on polybenzimidazoles for fuel cells*. Prog. Polym. Sci. **2009**;34:449-77.
[15] Aili D, Hansen MK, Pan C, Li Q, Christensen E, Jensen JO, et al. *Phosphoric acid doped membranes based on Nafion®, PBI and their blends - Membrane preparation, characterization and steam electrolysis testing*. Int. J. Hydrogen Energy **2011**;36:6985-93.
[16] He R, Li Q, Bach A, Jensen JO, Bjerrum NJ. *Physicochemical properties of phosphoric acid doped polybenzimidazole membranes for fuel cells*. J. Membr. Sci. **2006**;277:38-45.
[17] Bauer F, Denneler S, Willert-Porada M. *Influence of temperature and humidity on the mechanical properties of Nafion® 117 polymer electrolyte membrane*. Journal of Polymer Science, Part B (Polymer Physics) **2005**;43:786-95.
[18] Alberti G, Casciola M, Massinelli L, Bauer B. *Polymeric proton conducting membranes for medium temperature fuel cells (110-160°C)*. J. Membr. Sci. **2001**;185:73-81.
[19] Xu W, Scott K, Basu S. *Performance of a high temperature polymer electrolyte membrane water electrolyser*. J. Power Sources **2011**;196:8918-24.
[20] Antonucci V, Di Blasi A, Baglio V, Ornelas R, Matteucci F, Ledesma-Garcia J, et al. *High temperature operation of a composite membrane-based solid polymer electrolyte water electrolyser*. Electrochim. Acta **2008**;53:7350-6.
[21] Baglio V, Ornelas R, Matteucci F, Martina F, Ciccarella G, Zama I, et al. *Solid Polymer Electrolyte Water Electrolyser Based on Nafion-$TiO_2$ Composite Membrane for High Temperature Operation*. Fuel Cells **2009**;9:247-52.
[22] Rodgers MP, Shi Z, Holdcroft S. *Ex situ Characterisation of Composite Nafion Membranes Containing Zirconium Hydrogen Phosphate*. Fuel Cells **2009**;9:534-46.
[23] Millet P, Dragoe D, Grigoriev S, Fateev V, Etievant C. *GenHyPEM: A research program on PEM water electrolysis supported by the European Commission*. Int. J. Hydrogen Energy **2009**;34:4974-82.
[24] Ghielmi A, Vaccarono P, Troglia C, Arcella V. *Proton exchange membranes based on the short-side-chain perfluorinated ionomer*. J. Power Sources **2005**;145:108-15.
[25] Kreuer KD, Schuster M, Obliers B, Diat O, Traub U, Fuchs A, et al. *Short-side-chain proton conducting perfluorosulfonic acid ionomers: Why they perform better in PEM fuel cells*. J. Power Sources **2008**;178:499-509.

[26] Aricò AS, Di Blasi A, Brunaccini G, Sergi F, Dispenza G, Andaloro L, et al. *High Temperature Operation of a Solid Polymer Electrolyte Fuel Cell Stack Based on a New Ionomer Membrane*. Fuel Cells **2010**;10:1013-23.

[27] Hwang CM, Ishida M, Ito H, Maeda T, Nakano A, Hasegawa Y, et al. *Influence of properties of gas diffusion layers on the performance of polymer electrolyte-based unitized reversible fuel cells*. Int. J. Hydrogen Energy **2011**;36:1740-53.

[28] Nikiforov AV, Petrushina IM, Christensen E, Tomás-García AL, Bjerrum NJ. *Corrosion behaviour of construction materials for high temperature steam electrolysers*. Int. J. Hydrogen Energy **2011**;36:111-9.

[29] Kouřil M, Christensen E, Eriksen S, Gillesberg B *Corrosion rate of construction materials in hot phosphoric acid with the contribution of anodic polarization*. Mater. Corros. **2011** DOI: 10.1002/maco.201006021.

[30] Lecuyer, Quemerais, Jezequel. *Composition of natural oxide films on polycrystalline tantalum using XPS electron take-off angle experiments*. Surf. Interface Anal. **1992**;18:257-61.

[31] Hu J-m, Zhang J-q, Cao C-n. *Thermolytic formation and microstructure of $IrO_2$ + $Ta_2O_5$ mixed oxide anodes from chloride precursors*. Thermochim. Acta **2003**;403:257-66.

[32] Savinell R, Yeager E, Tryk D, Landau U, Wainright J, Weng D, et al. *A Polymer Electrolyte For Operation at Temperatures up to 200 °C*. J. Electrochem. Soc. **1994**;141:L46-8.

[33] Zhou Y, Lin G, Shih AJ, Hu SJ. *A micro-scale model for predicting contact resistance between bipolar plate and gas diffusion layer in PEM fuel cells*. J. Power Sources **2007**;163:777-83.

[34] Kraytsberg A, Auinat M, Ein-Eli Y. *Reduced contact resistance of PEM fuel cell's bipolar plates via surface texturing*. J. Power Sources **2007**;164:697-703.

[35] *Hydrogen, Fuels Cells and Infrastucture Technologies - Program Multi-Year Research, Development and Demonstration Plan - Planned program activities for 2005-2015*. Section 3.4, U.S. Department of Energy; **2007** [DOE/GO-102007-2430]

[36] Slavcheva E, Schnakenberg U, Mokwa W. *Deposition of sputtered iridium oxide - Influence of oxygen flow in the reactor on the film properties*. Appl. Surf. Sci. **2006**;253:1964-9.

[37] Da Silva LM, Franco DV, De Faria LA, Boodts JFC. *Surface, kinetics and electrocatalytic properties of Ti/($IrO_2$ + $Ta_2O_5$) electrodes, prepared using controlled cooling rate, for ozone production*. Electrochim. Acta **2004**;49:3977-88.

[38] Nikiforov AV, Tomás García AL, Petrushina IM, Christensen E, Bjerrum NJ. *Preparation and study of $IrO_2$/SiC-Si supported anode catalyst for high temperature PEM steam electrolysers*. Int. J. Hydrogen Energy **2011**;36:5797-805.

[39] Ma L, Sui S, Zhai Y. *Investigations on high performance proton exchange membrane water electrolyzer*. Int. J. Hydrogen Energy **2009**;34:678-84.

[40] Xu W, Scott K. *The effects of ionomer content on PEM water electrolyser membrane electrode assembly performance*. Int. J. Hydrogen Energy **2010**;35:12029-37.

[41] Passalacqua E, Lufrano F, Squadrito G, Patti A, Giorgi L. *Nafion content in the catalyst layer of polymer electrolyte fuel cells: effects on structure and performance*. Electrochim. Acta **2001**;46:799-805.

[42] Litster S, McLean G. *PEM fuel cell electrodes*. J. Power Sources **2004**;130:61-76.

[43] Owe L-E, Tsypkin M, Sunde S. *The effect of phosphate on iridium oxide electrochemistry*. Electrochim. Acta **2011**;58:231-7.

[44] Mader J, Xiao L, Schmidt TJ, Benicewicz BC. *Polybenzimidazole/Acid Complexes as High-Temperature Membranes*. Adv. Polym. Sci. **2008**;216:63-124.